

Tesi di dottorato in Scienze e ingegneria per l'uomo e l'ambiente, di Daniela Lo Presti,
discussa presso l'Università Campus Bio-Medico di Roma in data 9/04/2021.
La disseminazione e la riproduzione di questo documento sono consentite per scopi di didattica e ricerca,
a condizione che ne venga citata la fonte.



Università Campus Bio-Medico di Roma

Corso di dottorato di ricerca in
SCIENZE E INGEGNERIA PER L'UOMO E
L'AMBIENTE/SCIENCE AND ENGINEERING FOR
HUMANS AND THE ENVIRONMENT
Curriculum Bioingegneria/Bioengineering
XXXIII ciclo a.a. 2017-2018

**Wearables based on fiber Bragg grating sensors for
applications in Smart Healthcare: from design to test**

Daniela Lo Presti

Coordinatore
Prof. Giulio Iannello

Tutore
Prof. Emiliano Schena

Tesi di dottorato in Scienze e ingegneria per l'uomo e l'ambiente, di Daniela Lo Presti,
discussa presso l'Università Campus Bio-Medico di Roma in data 9/04/2021.
La disseminazione e la riproduzione di questo documento sono consentite per scopi di didattica e ricerca,
a condizione che ne venga citata la fonte.

Dedication

*To my parents, who supported me whatever I wanted to do and
love me whoever I will become.
I will never say enough how grateful I feel for the love
and support I received throughout my life.*

Acknowledgements

I would like to thank my supervisor, Prof. Emiliano Schena for guiding me through the Ph.D. and even more for being a living example of passionate scientist dedicated to carrying out high quality research. His knowledge and passion have been an inspiration for me.

I would also like to say a big thank you to all the members of the Unit of Measurements and Biomedical Instrumentation for teaching me the technical skills I was lacking, for their inputs throughout the years on several fronts, and for the cheerful coffee breaks and lunches.

I would like to express my gratitude to people at ENEA research center of Frascati for their insights into fiber optics. In particular, my sincere gratitude to Michele Caponero for sharing with me his knowledge about fiber optic sensors, it has been a pleasure to work with him and all the team (a special thanks to Andrea, Rosaria, Valerio, and Aurora). I hope that the deep discussions, as well as the collaborations with all of them will continue in the coming years.

I would like to sincerely say thanks to Prof. Domenico Formica for giving me the opportunity of being part of an amazing project which will improve my technical skills and my self-confidence in the next future.

Good company and sport were essential for me to survive the stress of work, therefore a word of thanks goes to my friends, especially to Grazia, Chiara, Daria, Renata, my cousins Alessia and Alessandra, and my gym partners who sweeten my life with chats, delicious dinners, and pilates.

Thanks to my big family, my aunts, my uncles, all my cousins, and the little ones Felice, Maria Rita and Pietro, for their presence. Always ready to enjoy with me and congratulate for my achievements in life and work.

I am very thankful for Davide, who supported me with immense love and taught me how to disconnect from work stress outside working time. Thanks for loving my quirks and bearing my mood swings.

Last but not least, my family, dad, mum and Filippo. They deserve an immense thanks for the constant support, always with me even if far away, ready to push me up when I felt down, under pressure and not enough. I will feel eternally grateful for having them by my side.



Abstract

Recently, the healthcare system has undergone a prospective transition by bringing patient-centeredness to the forefront.

A lot of effort has been made to identify ways in which care could become more patient-centered and reach out into every corner of the community to adequately deal with the most significant phenomena of the 21st century: the increasing lifespan of the population and their more active lifestyle.

Although people are living longer, they are not necessarily healthier than before. The Global Burden of Disease, a study conducted by the World Health Organization, predicts a very large increase in disability caused by age-related chronic diseases (e.g., cardiovascular diseases, stroke, and neurological diseases) which require long-term treatments and, in turn, cause a considerable economic burden on the healthcare management and the social insurance programs.

In this context, a healthcare system that begins to look into smart technologies can promptly respond to these urgent health needs.

The Smart Healthcare (SH) is an innovative way to provide care by allowing higher empowerment of patients, facing fragmentations in the health system, and fostering greater coordination and collaboration with organizations and providers across care settings. This approach relies on the use of a new generation of information technologies to transform the traditional medical system in an all-round way, making healthcare more efficient, more convenient, and more personalized.

The present work positions itself within the stream of research on wearables based on fiber optics for SH framework and addresses the topic of developing medical wearables for clinical applications. Among several smart technologies, the attention mainly goes to wearable devices since they are already revolutionizing care delivery by enabling continuous, unobtrusive, and longitudinal health monitoring outside of the hospital. Wearables have evolved to become one of the biggest industries in the world: their market is expected to grow by 89 million by 2022, connecting over 900 million, confirming how these devices are becoming a life necessity. In a few words, wearables have paved their way into everything we use in our daily life.

Usually, consumer wearables are made of electronic sensors but suffer from electromagnetic interferences, electrical safety issues (such as current leakage), and harsh conditions (such as high working temperature - T and pressure - P). These issues are dampening their usage as medical devices.

This thesis proposes an innovative approach in the development of wearables for SH applications involving attractive optical alternatives based on fiber Bragg gratings (FBGs) due to their intrinsic advantages, among others, the immunity to electromagnetic interferences, the inherent electric safety, the high performance in terms of metrological properties, and the multiplexing ability.

The remainder of this work is structured as follows:

Chapter 1 presents the background of this work and establishes the context of the research topic.

Chapter 2 proposes a description of the measuring principles of the FBG-based systems applied to medicine and healthcare and gives an overview of the state-of-the-art about the gratings employments in the development of wearables, innovative smart surgical tools, robotic devices, and biosensors.

Chapter 3 includes a description of the physiological sources and how these signals can be transduced into physiological measurements. Attention will be mostly given to wearables for cardiorespiratory monitoring, joint motion detection, and sensorimotor behavioral assessment.

Chapter 4 proposes the design, the fabrication, and the feasibility assessment of the FBG-based wearables developed during these three years of research.

Chapter 5 discusses the main issues, challenges, and future trends of FBGs-based systems for SH applications.

Keywords

Flexible and soft sensors; Fiber Bragg gratings, Healthcare 4.0; Joint motion detection; Measuring systems development and assessment; Physiological monitoring, Sensorimotor behavioral assessment; Smart Healthcare; Smart textiles; Wearables.

List of Acronyms, Symbols, and Abbreviations

A Cross Section Area	EMI Electromagnetic Interferences	MAE Mean Absolute Error
A/A Abduction/Adduction	ENEA Agency for New Technologies, Energy and Sustainable Economic Development	MIS Minimally Invasive Surgery
AB Abdomen	F Force	MAPE Mean Absolute Percentage Error
AR Axial Rotation	FBGs Fiber Bragg Gratings	MC Mitral Valve Closure
AO Aortic Valve Opening	F/E Flexion/Extension	MCF Multicore Fiber
AC Aortic Valve Closure	fMRI Functional Magnetic Resonance Imaging	MF Mass Fraction
BCG Ballistocardiogram	f_r Respiratory Frequency	MIS Minimally Invasive Surgery
BP Body pressure	F_r Resulting Force	MO Mitral Valve Opening
BT Body temperature	GO Graphene Oxide	MoCap Motion Capture
C Bending Curvature	GOD Glucose Oxidase	MOD Mean of Difference
CFBG Chirped fiber Bragg gratings	HA Hydroxyapatite	MPE Mean Percentage Error
CFRP Reinforced carbon fiber	h_{err} Hysteresis Error	MR Magnetic Resonance
CK17 Cytokeratin	HiBi Highly Birefringent	MV Minute Volume
CP Cerebral Palsy	HR Heart Rate	P Pressure
Cp Specific Heat	HRV Heart Rate Variability	PAH Polycyclic Aromatic Hydrocarbon
CP Calcium Phosphate	ICL Imperial College London	p_e Effective Photoelastic Coefficient
CT Computer Tomography	ICR Instantaneous Center of Rotation	PE Polyethylene
D Diffusion Coefficient	IoT Internet of Things	PEP Pre-ejection Period
d Distance	IVD Intervertebral Disc	PI Polyimide
DoF Degree of Freedom	K Thermal Conductivity	PLA Polylactic acid
E Young Modulus	K-Tape Kinesio Tape	PMMA Poly (methyl methacrylate)
ECG Electrocardiogram	L Length	PPG Photoplethysmography
EDC Carbodiimide	LOA Limit of Agreement	PR Pulse Rate
EFBG Etched Fiber Bragg Gratings	LVET Left Ventricular Ejection	PSD Power Spectral Density
EGFR Epithelial Growth Factor Receptor		

List of Acronyms, Symbols and Abbreviations

PTT Pulse Transit Time	SSSA Sant'Anna School of Advanced Studies	WHO World Health Organization
PWA Pulse Wave Analysis	S/P Supination/Pronation	wt% Weight Percent
PVC Polyvinyl Chloride	SPR Surface Plasmon Resonance	x_b Breathing Displacement
Q Heat Flux	S_T Thermal Sensitivity	x_h Heartbeat Displacement
QS2 Electromechanical Systole	t Time	%e Percentage Error
r Radius	T Temperature	α Fiber Thermal Expansion Coefficient
R Reaction Force	t_{BB} beat-to-beat Interval	β Hygroscopic Expansion Coefficient
R² Root Mean Square	T_E Expiratory Period	ΔL Axial Elongation
RC_p Pulmonary Rib Cage	TFBG Tilted Fiber Bragg Gratings	ε Strain
RC_a Abdominal Rib Cage	T_I Inspiratory Period	ξ Fiber Thermo-Optic Coefficient
RI Refractive index	tk Thickness	η_{eff} Effective Refractive Index
RH Relative Humidity	TPU Thermoplastic Polyurethane	θ Eulerian Angle of A/A
ROM Range of Motion	T_R Respiratory Period	Λ Grating Period
SCG Seismocardiogram	u Velocity	v Plank Constant
SD Standard Deviation	UCBM University Campus Bio-Medico of Rome	λ_B Bragg Wavelength
S_e Strain Sensitivity	u_L Linearity Error	μ Viscosity
SGD Smart Graspable Device	V Volume	ρ Density
SH Smart Healthcare	V_C Compartmental Volume	σ Stress
SiO₂ Silicon Dioxide	V_T Tidal Volume	τ Response Time
S_P Pressure Sensitivity	W Water Flux	Φ Eulerian Angle of F/E
S_{RH} Relative Humidity Sensitivity	WDM Wavelength Division Multiplexing	Ψ Eulerian Angle of AR
S_{RI} Refractive Index Sensitivity		

Contents

Acknowledgements	v
Abstract	vi
Keywords	vii
List of Acronyms, Symbols, and Abbreviations.....	viii
List of Figures.....	xii
List of Tables	xviii
List of Equations	xix
Chapter 1 Introduction.....	21
1.1 The concept of Smart Healthcare.....	21
1.1.1 The Smart Healthcare Framework	23
1.1.2 The Smart Healthcare Stakeholders.....	24
1.1.3 The enabling technology.....	26
1.2 The use of wearables in the Smart Healthcare.....	27
1.2.1 Medical vs. Consumer wearables	29
1.2.2 Key factors which drive the wearables acceptance	29
1.2.3 Wearable technology: where-to-wear-it.....	31
1.2.4 A new way for medical wearables: from soft close-contact to stick-to-skin devices.....	33
1.3 Ph.D. candidate's contribution.....	35
Chapter 2 Fiber Bragg gratings in medicine and healthcare	37
2.1 Theoretical background and principles of measuring.....	38
2.2 Applications in medicine and healthcare : a literature overview.....	41
2.2.1 Biomechanics.....	41
2.2.2 Minimally Invasive Surgery	49
2.2.3 Physiological Monitoring.....	57

2.2.4 Medical Biosensing.....	64
Chapter 3 Wearable systems based on FBGs: from physiological sources to physiological measurements.....	71
3.1 Wearables for cardiorespiratory monitoring.....	71
3.1.1 The importance of cardiorespiratory monitoring.....	71
3.1.2 The mechanical coupling between wearables based on FBGs and chest	73
3.1.3 Thermo-hygrometric conditions of respiratory gases	80
3.2 Wearables for joint motions detection.....	90
3.2.1 The importance of detecting articular joints movements.....	90
3.2.2 The mechanical coupling between wearables and joints.....	91
3.3 Wearables for sensorimotor behavioral assessment.....	96
3.3.1 The importance of primitive reflexes	96
Chapter 4 Wearable systems based on FBGs: design, fabrication, and feasibility assessment	101
4.1 Wearables for cardiorespiratory monitoring.....	102
4.1.1 The mechanical coupling between wearables and chest	102
4.1.2 Thermo-hygrometric conditions of respiratory gases	148
4.2 Wearables for joint motion detection.....	170
4.3 Wearables for sensorimotor behavioral assessment.....	192
Chapter 5 Conclusion.....	207
References	212
Ph.D. candidate publications	235

List of Figures

FIGURE 1:1 The pillars of SH framework.....	22
FIGURE 1:2 The main blocks of the SH framework.....	24
FIGURE 1:3. The SH stakeholders.....	25
FIGURE 1:4. The enabling technology [7].....	27
FIGURE 1:5. The wearables Market.....	28
FIGURE 1:6 The determinants of human health.....	30
FIGURE 1:7 The BODY MAP: wearable sensors for respiration, heart rate, blood pressure, and body temperature[29].....	31
FIGURE 1:8 The BODY MAP: wearable sensors for movement and forces/pressure (i.e., the impact of movement), blood glucose, active and passive touch, and stimulation/hydration[29].....	32
FIGURE 1:9 A schematic representation of a flexible sensor (blue) conformed to the curved soft human skin.....	33
FIGURE 1:10 Stretchable, soft and skin-like wearables: from textile-mountable to stick-to-skin sensors.....	34
FIGURE 2:1. (A) The main configurations of FBGs: uniform FBG, CFBG, TFBG, EFBG, and FBG array. The spectral responses and measured parameters (ϵ , T, and RI) are also reported. (B) A schematic representation of the interrogation unit with all the components used to interrogate and read the FBGs. An FBG array is shown by way of example. The data acquisition hardware -DAQ- in the receiver block is used to maintain the synchronization between the swept laser source and the array of photodetectors.....	40
FIGURE 2:2. The main application scenarios where FBGs have been employed for medical and clinical purposes.....	41
FIGURE 2:3. Applications in biomechanics. Examples of systems for soft and hard tissues are highlighted in green, for the musculoskeletal system in bright blue, and for prostheses, orthoses, and bone cement in pink.....	42
FIGURE 2:4. Applications in MIS and robot-assisted MIS. Examples of tissue manipulations are highlighted in straw yellow, tissue ablation in red and tool shaping in bright green.....	50
FIGURE 2:5. Applications in physiological monitoring. Examples of systems for monitoring f_R are highlighted in light blue, for HR in light red, for BP in purple, and for BT in acid green.....	58
FIGURE 2:6. Applications in medical biosensing. Examples of the main binding typologies are highlighted.....	66
FIGURE 3:1. A 10s-lasting window of typical BCG (blue) and ECG (magenta) signals on the left. A zoom on a single heart beating-related mechanical and electrical on the right with fiducial points. As evident, the electrical cardiac activity (e.g., systole) triggers the mechanical one (aortic valve opening) as the systolic complex with the R-peak in ECG signal is followed by the AO peak in BCG.....	75
FIGURE 3:2. Sensors location on the chest [306].....	75
FIGURE 3:3. The modeled chest wall contributions with a zoom on a single breath and a single heartbeat displacement.....	78
FIGURE 3:4. A dumbbell-shaped flexible sensor with a zoom on the FBG sensor inside. During inspiration, the chest wall expansion causes a displacement on the matrix resulting in a grating ϵ and in turn, in a positive shift of $\Delta\lambda_B$	79

List of Figures

FIGURE 3:5. A typical FBG output during cardiorespiratory activity. The $\Delta\lambda_B$ vs. time of single respiratory and cardiac contribution is highlighted.....	80
FIGURE 3:6. Thermo-hygrometric exchanges during inspiration and expiration [319]......	81
FIGURE 3:7. A simplified psychrometric chart [318].....	82
FIGURE 3:8 Structure of nasal cavity wall [322].....	83
FIGURE 3:9. Model of heat exchange on nasal cavity wall [322].....	84
FIGURE 3:10. Model of water exchange using bilayer film theory [322].	84
FIGURE 3:11. The working principle of a functionalized FBG sensor during coating swelling and deswelling. A volumetric expansion of the coating causes a positive $\Delta\lambda_B$, otherwise a shrinkage a negative $\Delta\lambda_B$	86
FIGURE 3:12 The bilayer model of an active coating.	88
FIGURE 3:13. A typical trend in time of a functionalized wearable FBG sensor in the breathing zone together with the chest volumes. As evident, an opposite trend is shown between the two signals: during expiration, the chest volume (V_{Chest}) on the bottom reduces while RH and T increase. Otherwise, λ_B on the top, increases; during inspiration, the chest volume increases, and RH and T are at ambient conditions. Otherwise, λ_B on the top decreases. Three different airflow velocities are underlined by green, blue, and red color lines.	89
FIGURE 3:14. The body movements [337]......	91
FIGURE 3:15. Joint types and allowed movements. Some examples are listed in the table [337].92	
FIGURE 3:16. The planes of motions [340]......	93
FIGURE 3:17. Model of tibial on femoral F/E motion.	94
FIGURE 3:18. (A) The transverse section of an FBG-encapsulated flexible sensor for finger F/E; (B) the flexible sensor placed on the index finger and the sensor neutral axis; (C), the FBG output changes $\Delta\lambda_B$ over time during F/E movements: an increase of $\Delta\lambda_B$ due to grating ε during F and a decrease of $\Delta\lambda_B$ during E [94]......	96
FIGURE 3:19. The brain development with potential delays in milestones attainment in preterm infants.	97
FIGURE 3:20. Examples of primitive reflexes.	98
FIGURE 3:21. The forces F_1 , F_2 , and F_3 (and their resultant F_T) applied by the fingers and the reaction force R applied by the palm during grasping [352]......	99
FIGURE 3:22. The FBG-based graspable/greppable device working principle: an increase of $\Delta\lambda_B$ occurs during object squeezing while a reduction during object releasing [353].	100
FIGURE 4:1. Wearables for cardiorespiratory monitoring: bare, encapsulated, and functionalized FBG have been used for their sensorization.....	102
FIGURE 4:2. The experimental setp and protocol.....	104
FIGURE 4:3. The design of the proposed smart textile. Each compartment (left and right) is identified by a specific color.....	105
FIGURE 4:4. (A) the smart textile output of all the FBGs and the FBGs sum over a 30s-lasting window of quiet breathing; (B) The $\Delta V_{global}^{Mocap}$ and $\Delta\lambda_B^{global}$ signals over time.	106
FIGURE 4:5. Steps of data analysis followed to obtain temporal parameters.....	107
FIGURE 4:6. Steps of data analysis for the estimation of the volumes.	109
FIGURE 4:7 Volumes estimated by the Mocap (blue lines) and the FBGs (red lines).	110
FIGURE 4:8. Bland-Altman plots and the linear regression.....	113

List of Figures

FIGURE 4:9. (A) Bland-Altman plot and linear regression of V_T ; (B) Mean and SD values of V_T estimated by the smart textile (red bar) and MoCap (blue bar) of all the eight volunteers..... 114

FIGURE 4:10. Compartmental percentage contributions %RCp, %RCa, and %AB calculated by the two instruments 114

FIGURE 4:11. The experimental setup. 116

FIGURE 4:12. Bland-Altman plots for f_R and V_T 117

FIGURE 4:13. The setup used for carrying out the tests during cycling. 119

FIGURE 4:14. Example of a 30 s-window. (A) The signal recorded by the reference instrument (black). (C) The signal obtained summing all the FBG signals (i.e., t-shirt SUM signal - red). (B) The power spectrum related to the reference and (D) The power spectrum related to t-shirt SUM signals. The maximum peaks are around 0.4 Hz (i.e., average f_R of 24 bpm) 120

FIGURE 4:15. MAE values for the different sensors, the t-Shirt SUM, RCp, RCa, AB, Anterior, and Posterior, per each volunteer 120

FIGURE 4:16. The 30 s - window f_R values of this signal and of the reference instrument. 121

FIGURE 4:17. (A) The CAD of the mold used for the rectangular-shaped flexible sensor, (B) the one for the dumbbell-shaped sensor, and (C) the mold for the dumbbell-shaped sensors with 4 FBG. 125

FIGURE 4:18. Results of metrological characterization: response to ϵ (a), T (b), RH (c), and water immersion (d). 127

FIGURE 4:19. Hysteresis loops at velocities simulating 10 bpm (black loops) and 20 bpm (blue loops). 128

FIGURE 4:20. The experimental setup. 131

FIGURE 4:21. Signals collected during the experimental protocol by the FBG on(A) the abdomen, (B) THE thorax, and (C) the flowmeter. 132

FIGURE 4:22. The peaks detection. 133

FIGURE 4:23. The Bland-Altman plots with the linear regression for breath-by-breath f_R estimation. 133

FIGURE 4:24. A zoom on the apnea stages collected by FBGs and PPG sensor. 134

FIGURE 4:25. The peak detection. 135

FIGURE 4:26. The Bland-Altman plots with the linear regression for beat-by-beat HR estimation 135

FIGURE 4:27. The experimental setup during shooting. 137

FIGURE 4:28. Shooting actions performed by archer 1 and archer 2. 138

FIGURE 4:29. The phases of a single shooting action and the collected signal..... 138

FIGURE 4:30. The wearable system with a zoomed detail of the anchoring system. The front rectangular plate is highlighted, the back-pad plate with U-shaped loops in dotted line, hooks in yellow. .. 141

FIGURE 4:31. The experimental setup. 141

FIGURE 4:32. From top to bottom, the five designed protocols. Each box is colored as the icon representing the activity performed by the volunteer during the execution of the protocol. The activities are: A) standing, B) sitting, C) supine, D) walking, E) lateral lifting of the arms, F) front lifting of the arms, G) maximum arms up, H) maximum right torsion of the trunk, I) maximum left torsion of the trunk, J) front bending of the trunk, K) lifting an item from the ground on the left, L) moving the item from left to right, M) lifting an item from the ground on the right and N) moving the item from right to left. 143

FIGURE 4:33. The moving window used to estimate f_R 144

FIGURE 4:34. (A) The positioning of the ECG electrodes (RA, LA, and RL) and the flexible sensor (in the three positions: horizontally along the left side of the sternum, above the umbilicus, and vertically between the xiphoid process and the umbilicus). The ECG signal with the corresponding SCG signals

List of Figures

recorded by the 4 FBGs is shown on the right with a zoom on two consecutive beats related to the ECG signals and the corresponding SCG signal with the proper fiducial points. (B) the signals collected when the sensor is placed vertically (on the left) and horizontally over the umbilicus (on the right). 147

FIGURE 4:35. A digital microscope picture of the coated FBG sensor. All the coatings features are listed in the table. 150

FIGURE 4:36. The experimental set-up. The optical spectrum analyzer (A), the climatic chamber (B), the molds (C), the capacitive-based RH sensor (D), the bare FBG (E), the humidifier (F), the laptop to check RH reference in LabVIEW environment inside the chamber during tests (G), the computer to check the FBG outputs during tests (H), DAQ (I), and the mass flow controller (L). 150

FIGURE 4:37. The RH step response of the four functionalized FBG with the reference. 151

FIGURE 4:38. The 4 FBGs spectra before and after the functionalization. 152

FIGURE 4:39. Plots show the agar-based FBGs responses to RH increase after the T compensation. 152

FIGURE 4:40. The reference ΔRH on the left and the bare FBG output (expressed as ΔT [°C]) over time on the right. 153

FIGURE 4:41. The fitting model of the step responses of all the four FBG sensors. 154

FIGURE 4:42. The developed needle instrumented with a functionalized FBG sensor. 156

Figure 4:43. Experimental set-up of the first and third phases: the ventilator (a), the FBG-based needle (b), the capacitive RH sensor (c), the lung simulator (d), the Y-piece (e), the optical spectrum interrogator (f) and the DAQ (g). in fig. 3b experimental set-up of the second phase in which the humidifier (h) is added. 157

FIGURE 4:44. Data analysis workflow. Example of experiment performed at $MV= 4L \cdot min^{-1}$. The 120s lasting signal which peak detection is applied on, refers to $5^{th}f_{R4}$ 158

FIGURE 4:45. Whiskers plots: the red line is the red line in the middle of each box is the sample median, and the whiskers, above and below, extend from each box to boundary lines at the 25th and the 75th percentiles. 160

FIGURE 4:46. RH changes recorded by the reference instrument (blue line) and the FBG sensor (orange line). 161

FIGURE 4:47. Data collected by the spirometer. W is a part of the warming-up stage (60 seconds in total), A is the apnea stage. Then, the quiet breathing stage is shown, together with the synchronization point at the end of the first expiration after the apnea. 163

FIGURE 4:48. A 30-s window showing the signals collected by the spirometer (blue line, ΔV) and by the proposed probe (orange line, $\Delta \lambda_B$). 163

FIGURE 4:49. Bland-Altman plot. A colored symbol represents each volunteer. The black line represents the MOD value, while the upper and lower red line the upper and lower LOA, respectively. 164

FIGURE 4:50. The MR-compatible wearable device. Block A shows the FBG (1), the agar-based matrix (2), the Dragon-Skin brick (3), and the PLA-based case (4). Block B shows the sliding covers (5), the heat-shrink sheath (6), and the flexible tube (7). 165

FIGURE 4:51. (A) The experimental setup; (C) the IR markers protocol; (D) the developed wearable system worn below the nostrils. 166

FIGURE 4:52. Results collected during the experiments on one of the volunteers: (A) the output of the wearable system and (B) the output of the MoCap system (V_{Chest}). The green line is related to the slow breathing stage, the blue one to normal breathing stage, and the red one to the fast breathing stage. In black, the apnea stages. 167

FIGURE 4:53. Bland-Altman plots related to slow breathing, normal breathing, and fast breathing. Each color represents one volunteer. The continuous black line is the MOD, while the dashed lines delimited the LOAs interval. 168

List of Figures

FIGURE 4:54. Wearables for joint motion detection: encapsulated FBGs have been used for the sensorization of wearable systems for neck and low back movements. 170

FIGURE 4:55. The flexible FBG-based sensing element. (A): Shape and size of the sensor in frontal view (up), lateral view (middle), and warped configuration (bottom); (B): Details of the sensor in frontal view (up), lateral view (middle), and warped configuration (bottom). 171

FIGURE 4:56. The FBG working principle when (A) attached to the neck for detecting (B) F/E and (C) left and right AR movements. 173

FIGURE 4:57. The experimental setup and performed protocol for (A and B) neck movements and (C and D) respiratory activity. 174

FIGURE 4:58 (A) The α_{FE} and (B) the θ_{AR} angles formed in the sagittal and transverse plane; (C) reference output changes over time during F/E and (D) AR repetitions; (E) FBGs outputs changes over time during F/E and (F) AR repetitions. 175

FIGURE 4:59. (A) The peak detection during the first group 5 F/E, (B) the second group 5 F/E right, (C) right AR repetitions, (D) left AR repetitions. 176

FIGURE 4:60. The output changes of both the wearable (black line) and the MoCap system (blue line) collected during F/E and AR repetitions. 177

FIGURE 4:61. Signals collected by the flowmeter (blue trend) and by the FBGs (black trend) during both quiet breathing (light blue box) and tachypnea (red box). 178

FIGURE 4:62. An example of signals processing performed for the f_R estimation from data recorded by the flowmeter and the wearable systems, during quiet breathing. The PSD spectra over frequency [Hz] and the peak detection over time [s] are shown for both the reference system and the proposed wearable system based on two flexible sensors (FBG1 and FBG2). The $S_n^f(t)$ signals are filtered and normalized. 180

FIGURE 4:63. (A) signals collected by the flowmeter (blue line) and the FBGs (black line) for each volunteer during quiet breathing and (B) during tachypnea. All the signals are synchronized, filtered, and normalized. The detected peaks are highlighted by using red markers. 181

FIGURE 4:64. (A) the markers placement and (B) the experimental setup. 185

FIGURE 4:65. The distance $d_{L3 - L1}$ (left image) and the lumbar angle θ (right image) retrieved from markers' trajectories. 187

FIGURE 4:66. (1) The wearable output ($\Delta\lambda_B$), (2) the distance between L1 and L3 ($\Delta d_{L3 - L1}$) and (3) the lumbar angle (θ) trends obtained per each trial. (a): Trial 1; (b): Trial 2; (c): Trial 3; (d): Trial 4; (e): Trial 5; (f): Trial 6; (g): Trial 7; (h): Trial 8. 189

FIGURE 4:67. (1) The distance between L1 and L3 evaluated by the MoCap ($\Delta d_{L3 - L1}$) and (2) the reconstructed distance ($\Delta d_{\Delta\lambda B}$) obtained per each trial. (a): Trial 1; (b): Trial 2; (c): Trial 3; (d): Trial 4; (e): Trial 5; (f): Trial 6; (g): Trial 7; (h): Trial 8. 190

FIGURE 4:68. Wearables for sensorimotor behavioral assessment: for grasping investigations, encapsulated FBG are used to fill greppable/graspable tools. 192

FIGURE 4:69. (A) The geometrical features of SGD; (B) the main manufacturing steps: the FBG sensor positioning (step 1), the silicone mixture pouring (step 2), and the SGD removed from the mold after the rubber vulcanization (step 3). 195

FIGURE 4:70. (A) A detail of the anchoring system elements designed to allow fitting of the SGD within an already existing robotic interface; (B) the SGD together with the robotic interface. 196

FIGURE 4:71. Setup of the compression tests: the cylinder-shaped sample between the lower and the upper plates of the Instron machine and the initial sample length before (l_0) and during the compression (l) are illustrated. The top plate moves at constant speed parallel to the x-axis. 197

FIGURE 4:72. The σ - ϵ relationships for Dragon Skin™ 10, 20, and 30 are shown in blue, red, and green, respectively. In particular, the continuous lines represent the average σ_{exp} values, the shaded areas the

List of Figures

related uncertainties, and the black dotted lines the σ_{th} values obtained by the best linear fitting model.	198
FIGURE 4:73. The SGD in the blocking system, the load cell, and the mechanical indenter are shown in the picture. A schematic representation of the SGD between the lower and the upper plates of the Instron machine is illustrated. The top plate moves at constant speed parallel to the x-axis.	199
FIGURE 4:74. The $\Delta\lambda_B$ vs. F_{ext} of SGD ¹ and SGD ² : in continuous magenta lines the average $\Delta\lambda_B$ vs. F_{ext} responses, in the shaded magenta area the related uncertainties and in dotted black lines the best linear fitting.	200
FIGURE 4:75. (A) Video frames of grasping actions identified by the clinicians; (B) the related signals collected by the SGD. Grasps actions are enumerated from 1 to 5.	201
FIGURE 4:76. Experimental set-up of fMRI trial with the data flow: the MRI scanner (a), the patient (b) and the robotic interface instrumented by the SGD (c) in the scanner room, and the workstation (d), the FBG interrogator (e) and the laptop (f) in the control room. Digital and analogue data flows between the scanner and control rooms are shown using blue and red arrows, respectively.	202
FIGURE 4:77. (A) The flow of data analysis. The peaks in $\Delta\lambda_B$ coming from the SGD were used to infer the timing of the action and create a boxplot MRI design. This was convolved with the HRF to generate the design model for the GLM. (B) Significant clusters of functional response to the task (in red and yellow) overlaid onto the subject's T1-weighted brain image.	203
FIGURE 5:1. The TRL level of FBG-based systems for medical and healthcare applications.	209

List of Tables

TABLE 4:1.....	112
TABLE 4:2.....	112
TABLE 4:3.....	116
TABLE 4:4.....	117
TABLE 4:5.....	121
TABLE 4:6.....	122
TABLE 4:7.....	129
TABLE 4:8.....	130
TABLE 4:9.....	133
TABLE 4:10.....	136
TABLE 4:11.....	136
TABLE 4:12.....	139
TABLE 4:13.....	153
TABLE 4:14.....	154
TABLE 4:15.....	155
TABLE 4:16.....	159
TABLE 4:17.....	160
TABLE 4:18.....	168
TABLE 4:19.....	168
TABLE 4:20.....	173
TABLE 4:21.....	182
TABLE 4:22.....	182
TABLE 4:23.....	183
TABLE 4:24.....	188
TABLE 4:25.....	188

List of Equations

Equation 2:1	38
Equation 2:2	39
Equation 2:3	39
Equation 3:1	76
Equation 3:2	76
Equation 3:3	77
Equation 3:4	77
Equation 3:5	80
Equation 3:6	82
Equation 3:7	82
Equation 3:8	82
Equation 3:9	83
Equation 3:10	83
Equation 3:11	84
Equation 3:12	84
Equation 3:13	85
Equation 3:14	85
Equation 3:15	86
Equation 3:16	87
Equation 3:17	87
Equation 3:18	87
Equation 3:19	87
Equation 3:20	87
Equation 3:21	88
Equation 3:22	88
Equation 3:23	88
Equation 3:24	94
Equation 3:25	94
Equation 3:26	95
Equation 3:27	95
Equation 3:28	95
Equation 3:29	96
Equation 3:30	100
Equation 3:31	100

List of Equations

Equation 4:1	108
Equation 4:2	110
Equation 4:3	110
Equation 4:4	111
Equation 4:5	112
Equation 4:6	119
Equation 4:7	128
Equation 4:8	132
Equation 4:9	135
Equation 4:10	145
Equation 4:11	159
Equation 4:12	168
Equation 4:13	179
Equation 4:14	179
Equation 4:15	179
Equation 4:16	186
Equation 4:17	186
Equation 4:18	186
Equation 4:19	187
Equation 4:20	187
Equation 4:21	196
Equation 4:22	198

Chapter 1 Introduction

1.1 The concept of Smart Healthcare

The advancement of healthcare mainly relies on technological innovations for disease prevention, diagnosis, and treatment to establish new strategies for care delivery and management. All these transformations are clearly reshaping the doctor-patient relationship and pushing a paradigm shift in the healthcare system.

Recently, the traditional doctor/hospital-centered health management has undergone a prospective transition. A lot of effort has been made to identify ways in which care could become more patient-centered and reach out into every corner of the community to adequately deal with the most significant phenomena of the 21st century: the increasing lifespan of the population and their more active lifestyle [1]–[3].

Population aging is the dominant demographic phenomenon of the 21st century: people worldwide are living longer, and by 2050, the world's population aged 60 years and older is expected to rise up to 2 billion, according to the current projection of the World Health Organization (WHO) [4], [5]. Living longer represents one of the crowning achievements of the last century but also a significant challenge. The Global Burden of Disease, a study conducted by WHO and the World Bank, with partial support from the U.S. National Institute on Aging, predicts a considerable increase in disability caused by age-related chronic diseases (e.g., cardiovascular diseases, stroke, and neurological diseases, diabetes, and pulmonary disorders) [6]. Chronic conditions require long-term treatments and, in turn, cause a considerable economic burden on the healthcare system and on the social insurance programs. To make matters worse, a sudden shift in demand like the ones due to the COVID-19 pandemic may cause an additional unpredictable burden on healthcare resources. The experience of the current pandemic pushed health systems to their limits and brought out the vulnerability and fragility of the actual model of healthcare delivery and management as well as the preparedness of existing structures to handle human health hazards and to truly place patients at the center of their care. For this reason, although over the last decades, steps forward have been taken towards the modernization of the current health ecosystem, the situation we are living in showed the need for a strengthen health digitalization in order to: ensure people receive continuous health

monitoring, better manage even remotely diseases, treatments, and care services according to the patients' needs, lower health-related costs and reduce strain on the hospital capacity.

According to the WHO, a well-functioning healthcare system requires a steady financing mechanism, a properly trained workforce, accurate and precise health monitoring, and easy access to reliable information [4]. Evidence shows that the healthcare system may accomplish these requirements by becoming truly smart.

The Smart Healthcare (SH) is an innovative way to provide care by allowing patients' higher empowerment, facing fragmentations in the health system, and fostering greater coordination and collaboration with organizations and providers across care settings to deliver health services aligned with the patient s' needs [1]. Fig. 1:1 summarizes the pillars of SH revolution.

The main scope of the SH is exploiting the technological advancement to allow a daily health check in conjunction with the conventional clinical monitoring for improving the quality of care while lowering the related costs and the strain on the hospital capacity [7], [8]. To accomplish this aim, the establishment of an innovative framework is necessary for addressing the determinants of human health through: *i*) a person-facing perspective to ensure health gains through a proactive provision of care [9], *ii*) a continuous, long-term, and unobtrusive health monitoring tailored on the individual's needs [10], *iii*) a shift in the patient-doctor relationship from one-to-one to a multidisciplinary approach [1] and *iv*) a hospital not confined behind the walls of a single building, but distributed over the whole territory [11].



FIGURE1:1 The pillars of SH framework.

This approach relies on the use of technologies such as wearables, implantable sensors, Internet of Things (IoT), Big Data, and mobile devices, the establishment of innovative

structures to manage and deliver care person-centered and the setup of a multidisciplinary team working to coordinate care and meet the needs of individual [12],[13].

As evident, in this unique framework, various stakeholders with different needs are engaging and work together to find out the optimal trade-off between an improvement in the quality of delivered care and a reduction of the socio-economic burden caused by the public management of health [14].

The following sections firstly described the SH framework with the engaging stakeholders; then, an overview on the innovative technological solutions which enable such a digital revolution in care management and delivery is presented with a particular focus on the wearable systems. Lastly, the thesis aims and objectives are shown by underlining its position within the stream of SH-focused research.

1.1.1 The Smart Healthcare Framework

The framework of the new SH system can be split into two main settings: in-hospital and in-home care, according to the scenario in which care services occur. New technologies like Big Data, the Internet of Things (IoT), artificial intelligence, wearables, and implantable sensors may provide seamless care delivery and health management across the hospital-home boundary (Fig. 1:2).

In-Hospital care. The SH framework aims at decentralizing and making care patient-centric. In this context, hospitals will continue to play a crucial but less central role than in the past, attempting to do not manage all services under “one roof” but deliver a narrower set of high-value services within a broader ecosystem of entities. To accomplish this aim, a redesign of the existing infrastructures and a build of new clinical management systems is mandatory, fostering the rise of smart hospitals [11]. A smart hospital still offers treatments for acute, severe, and complicated conditions while embracing a digital transformation in the health management and delivery. In this scenario, innovative technologies are provided and exploited to better suit the users’ needs, to improve the daily management of medical staff and the quality of the delivered care with a lower human error rate and cost-effective operations. Information and communication technology-based infrastructures, especially those based on IoT optimization and automated processes, will contribute to improve existing in-hospital care procedures, reduce staff burnout, and optimize workflows making a hospital truly smart [15].

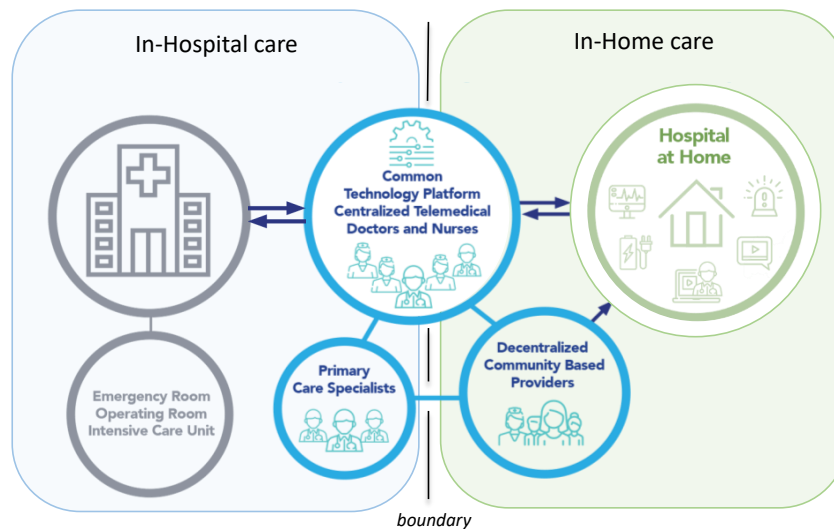


FIGURE 1:2 The main blocks of the SH framework.

In-Home care. Smart technologies for unobtrusive and remote monitoring and virtual health services, are key elements for increasing access to care from home and reducing the strain on hospital resources. In-home care monitoring may be extremely useful to check patients' health status after their hospital discharge, shorten hospital length of stay, and prevent readmissions. At the same time, it is a valuable solution to manage ongoing chronic conditions and establish preventive health strategies [16]. In this scenario, wearables and unobtrusive sensors are the principal sensing solutions used to enable the shift of healthcare services from hospital to home, improving the quality of delivered care and lowering health-related costs [17]. These technologies track users' health status encouraging an active role in managing personal healthcare and wellness, while cloud-based server databases enable data storage and remote accessibility by care professionals to support patients in a more targeted way during daily activities. In this context, the role of a home even smarter in conjunction with smart technologies such as wearables and is fundamental for providing automated services and assistance to patients (especially useful for elderly and disabled people) while collecting health data, reducing their reliance on healthcare providers and improving their quality of life during their daily activities [16].

1.1.2 The Smart Healthcare Stakeholders

Improved health outcomes are not attributable to health systems alone but also to individual as well as socioeconomic and environmental determinants. The main healthcare stakeholders can be categorized into three groups with different needs and perspectives: hospitals,

governments (e.g., ministry of health and education) in conjunction with health decision-making institutions (e.g., civil protection and research institutions), and patients [14], as shown in Fig. 1:3.

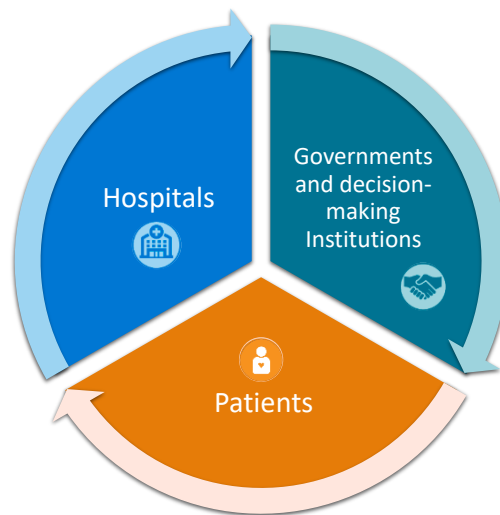


FIGURE 1:3. The SH stakeholders.

Hospitals. As previously described, in-hospital care is one of the main blocks on which the SH framework grounds. Key figures in this setting are the hospital administrators and the medical staff. An administrator oversees the organizational side of health services. In a rapidly changing healthcare system, hospitals' administrative responsibilities need to be managed following a multi-disciplinary approach. All the professionals involved in the hospital administration should have the knowledge of the regulatory framework and understand the complexities in the new way of providing care: the different entities involved in the health management and their roles, the technological update, the issues for data privacy, and security and the overall health management policies. Thus, hospital administrators work with both public and private sectors on matters of policy, research, and cooperation [1].

Another key category that belongs to the hospital settings and is primarily involved in the health system revolution is the medical staff. In particular, the centrality of patients in the SH framework is impacting the doctors' place in the health care ecosystem. At the same time, technological updates are forcing doctors to embrace new technology-enabled care for improving the quality of services delivered to patients. Through the integration of technology into their practices (within areas like disease prevention, surgical procedures, better access to information, and medical telecommunications), the role of doctors is changing from a dominant to

a guidance-cooperation model in terms of clinical decision making focused on the patient needs [18].

Governments and decision-making Institutions. The governance role is becoming of paramount importance given the increasing complexity of health systems and changing epidemiological and demographic scenarios. Governments act to strengthen health systems, financial aspects, and other resources to establish the new healthcare framework facing globalizations, population aging, and lifestyle changes. The government ministries cooperate with decision-making institutions (e.g., academia, professional associations, and private sector organizations) to set the context within which the healthcare system operates and to maximize the health of the population within the country's financial and resource constraints [19],[20]. Moreover, during public health emergencies like COVID-19 pandemic, cooperation with research institutes may also serve as a good basis to add significant value to decisions by providing evidence to characterize threats and forecast outcomes.

Patients. The SH framework grounds on the idea of the patient-centeredness since people who are engaged in the decision-making about their own care tend to have better outcomes than those who are not. In this scenario, the use of innovative technological tools and resources may help in improving both the patient engagement and the hospital distribution over the territory by assessing the specific level of health and goals reached by each patient during their continuous and remote monitoring. To better target the patient efforts, lower the public health-related costs, and improve the telemonitoring, it is important to understand which patients are most at risk of developing a costly condition and/or seeing a pre-existing healthcare condition worsen [21]. Therefore, risk stratification is fundamental to define how patients should be engaged in accordance with their level of health. For instance, in the case of high-risk patients, the engagement is primarily achieved through in-home care management by sharing data with the medical staff and family members. Otherwise, the engagement of rising-risk and low-risk patients deals more with managing risk factors; thus, this category should be able to identify determinants of risk during their daily life activities, and doctors' interventions are often focused on prevention of disease and promotion of health [22]. For all these conditions, smart technologies such as wearables and smart systems play a pivotal role [17].

1.1.3 The enabling technology

The concept of SH is transforming healthcare to a 4.0 version, and the smart technology represents both the brain and the hands to enable such a revolution and translate the focus of medicine from curative to preventive measures [7],[23].

The new technological brain consists of some essential components: precision medicine, telemedicine, artificial intelligence, IoT, and Big data to refine the diagnosis, allow sharing of sensible information between medical staff and patients and personalize treatment procedures; the new hands include robots, artificial organs, wearable devices, customized materials and three dimensional printing to improve the quality of delivered care, collect useful data and information about the health state of the patients, and improve strategies and treatments tailored on the patient's needs. A representation of the new hands and brain of healthcare 4.0 is proposed in Fig. 1:4.

In a few words, we can say that smart technologies are capable of recording health information, storing and computing information, and delivering personalized advice or automated actions from the collected data throughout various solutions for both *in-hospital* and *in-home* care. From now on, this Chapter mainly focuses on the new technology, which represents the most emerging and popular trend of the 21st century: wearable devices.

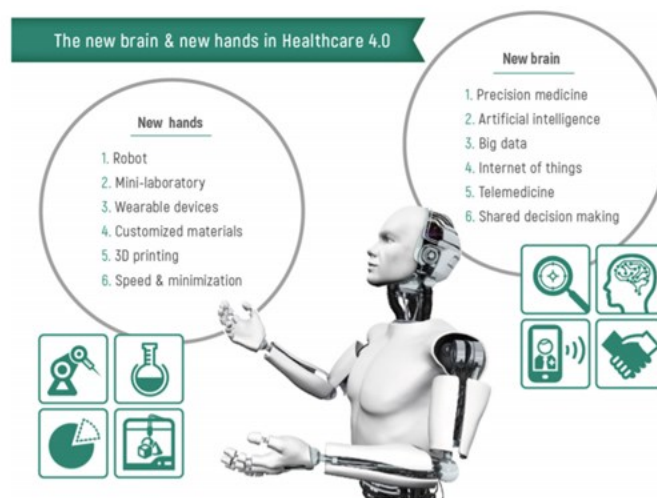


FIGURE 1:4. The enabling technology [7].

1.2 The use of wearables in the Smart Healthcare

Digitalization is changing all areas of human life, from social settings to basic needs, like personal healthcare, triggering an unprecedented impact of smart technology in the healthcare sector. The digital revolution brings out a demand for devices that can monitor an individual's physiological functions 24 hours a day, remotely and comfortably. Among several devices, wearables have recently reached a renewed and larger interest from our community since they

have the power to enhance human health simply by connecting technology to the skin [17],[24].

Wearable devices have evolved to become one of the biggest industries globally, thanks to the fascinating innovations that have continued to keep this technology lively. As a matter of fact, a study conducted by Statista shows that the wearable market is expected to grow by 89 million by 2022, connecting over 900 million, confirming how these devices are becoming a life necessity [25].

Today, people have integrated wearable technology into their lives to stay connected: from wristbands that track the steps, heart rate (HR), and body fat measuring scales to blood pressure (BP) checkers and sleep trackers. In a few words, wearables have paved their way into everything we use in our daily life.

At present, most wearable manufacturers (e.g., Apple, Samsung, Fitbit, and Xiaomi; see Fig. 1:5) promote the use of their device for improving physical performance and fitness and promoting healthy habits, but many have not been approved for medical uses.

2019 competitive landscape: Market shares of the wearable systems

(Source: Wearables in Consumer and Medical Applications 2020 report, Yole Développement, 2020)

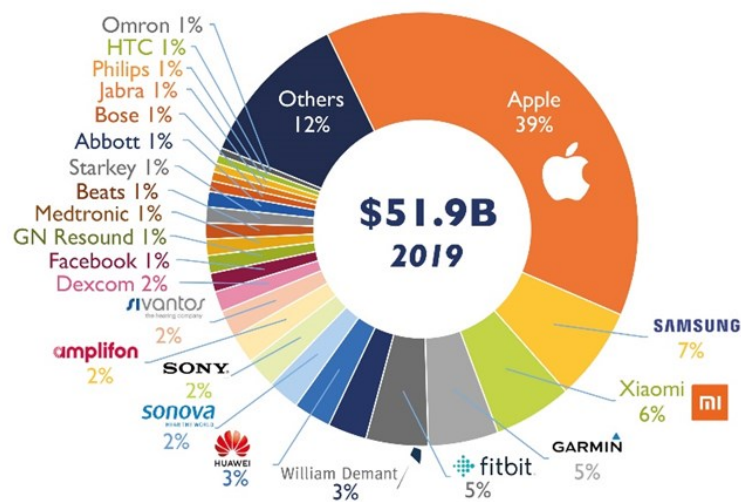


FIGURE 1:5. The wearables Market.

Considering the crucial role of such a technology in the SH framework, the main requirements and challenges around wearable devices potentially used for clinical purposes (i.e., medical wearables) are underlining in the following sections.

1.2.1 Medical vs. Consumer wearables

In the last decades, the line between consumer and medical wearables is beginning to blur since practitioners and researchers are working together and opening a constructive dialogue on how to approach and accommodate technological advances in a way that ensures consumer wearable technology to become a valuable asset for healthcare and medicine. Unfortunately, there are still some concerns that are dampening the use and spread of wearables for clinical aims [26]. The main ones are the following:

1. While medical and consumer wearables are based on the same premises – the products need to be comfortable, easy-to-use, and not cumbersome, their functions serve a different purpose. Medical wearables are of vital importance: they can detect life-threatening conditions and collect data to help medical staff with patient diagnoses; hence, high reliability is necessary;
2. Medical wearables need to comply with stringent safety and accuracy standards before being considered for clinical applications. Patients may become over-reliant on the devices; thus, a false sense of safety and misdiagnosis must be avoided;
3. As any medical product, they must be approved by regulatory authorities and certified in compliance with ISO standards.

1.2.2 Key factors which drive the wearables acceptance

The success of the use of wearables in medicine and healthcare has a high relationship with the determinants of human health. It is known that the combination of many factors affects the health of individuals and communities. Commonly, the main considered factors are the access and use of health care services, but often they have less of an impact than where we live, the surrounding environment, genetics, education, and relationships with friends and family. To a large extent, the context of people's lives determines their health (Fig. 1:6).

These determinants can be grouped into the person's individual characteristics and behaviors, the physical environment, and the socio-economic context [27].

The person's individual characteristics and behaviours. There are two main kinds of health determinants related to the individual sphere. Some features, such as age, sex, and genetic disease, are fixed and not under our control. Other characteristics, otherwise, are modifiable to improve our well-being. These include behavioral things like diet, exercise, washing, drinking, and smoking, which may potentially increase the risk of both chronic and infectious diseases.

The physical environment. These factors are related to the physical conditions in which we live and work. The surrounding environment dramatically impacts on our health. For instance, clean water, pure air, and healthy workplaces contribute to healthy living. At the same time, we are exposed daily to various occupational risks for health in the workplace. Among others, these include neurological and musculoskeletal injuries due to fatigue experienced after working long hours, insufficient rest, moving workloads without adequate protective equipment, mental work-related load, and occupational burn-out.

The socio-economic environment. Many factors affecting health lie beyond the healthcare system in the broader social and economic systems. They include education, health services, employment, community safety, and social support. For instance, a healthy standard of living, such as adequate income and housing, is associated with many positive health outcomes. At the same time, high levels of education may increase the awareness of racial and ethnic disparities and promote equal access to health services.

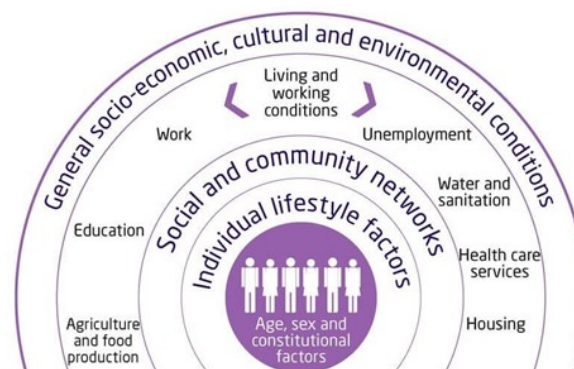


FIGURE 1:6 The determinants of human health.

Novel technologies for data collection such as the use of medical wearables should provide a global measure of the health status by capturing data across several domains and detecting changes of human health states as well as the variation of physical factors (including the ones related to environmental changes and/or occupational scenario) that may also affect fluctuations in physiology, mood, behaviors, thoughts, and feelings. To enhance the technology acceptance, the identification of the perceived barriers and the patient-specific health determinants should be performed in order to improve the adherence to medical plans and ensuring that the benefits of treatment are understood by each patient. In this way, the design of these

technological solutions will be tailored to the patient's needs, resulting in lowered cost of care and optimized health outputs [28].

1.2.3 Wearable technology: where-to-wear-it

In the SH frameworks, a wearable device could effortlessly provide detailed longitudinal data to monitor individuals' progress without involving more uncomfortable and expensive measuring equipment. A clear description of functional, technical, and social consideration in on-body locations for wearable technologies potentially used in healthcare is proposed in [29].

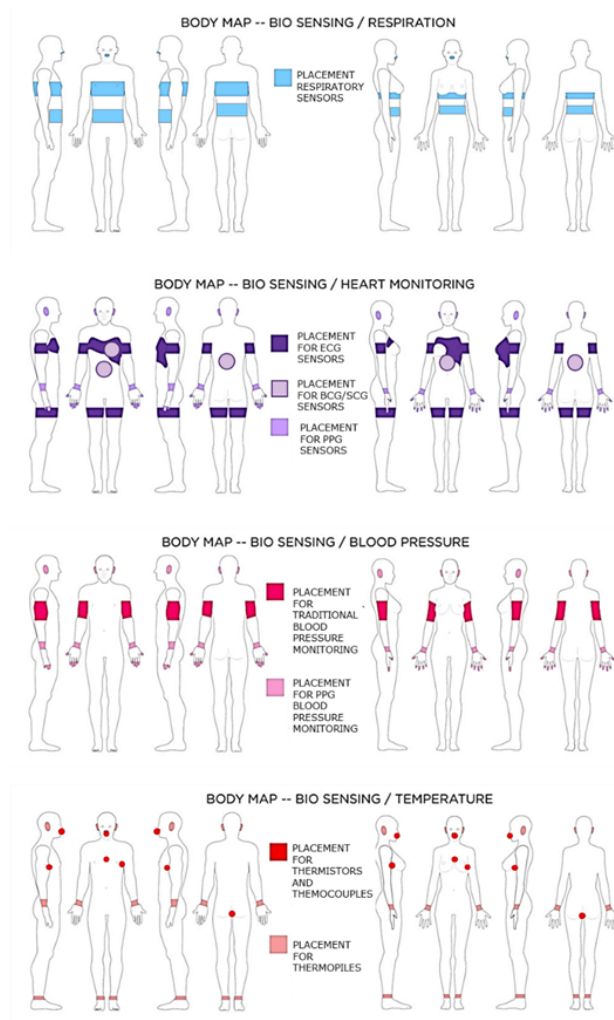


FIGURE 1:7 The BODY MAP: wearable sensors for respiration, heart rate, blood pressure, and body temperature[29].

When designing medical wearables for healthcare, it is crucial to consider several issues summarized into proxemics, weight distribution, motion impedance, thermal tolerance, and social acceptability [29].

A wearable device placed on the body should measure important information such as vital signs (i.e., HR, the respiratory frequency - f_R , BP, and the body temperature - BT), body motion (e.g., joint movements), tactile sensing, blood glucose level and stressful conditions without exceeding the body's natural perceived size, hindering the wearer's movement or balance, and overheating. In Fig. 1:7 and 1:8, the sensors placement locations according to the measuring parameters proposed in the literature.

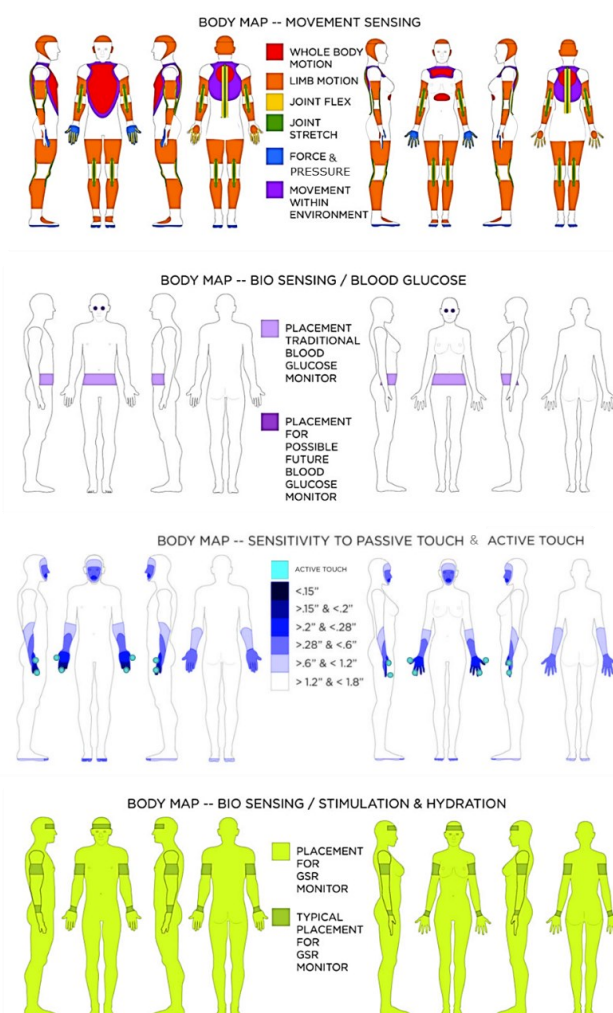


FIGURE 1:8 The BODY MAP: wearable sensors for movement and forces/pressure (i.e., the impact of movement), blood glucose, active and passive touch, and stimulation/hydration[29].

1.2.4 A new way for medical wearables: from soft close-contact to stick-to-skin devices

The hot trend in wearables is moving towards flexible and soft devices since they provide better contact with the skin and the natural contours of the human body [30] (Fig. 1:9). Otherwise, the performance of conventional bulky and rigid wearables in contact with the human tissues can be affected by the weak compliant and an incomplete connection with the body.

For this reason, over the last decades, researchers have mastered materials and device design approaches to enable high performances and functionalities in biocompatible, soft and stretchable sensing elements that can be worn on the body and, in some cases, directly stick to the skin to overcome the aforementioned issues.

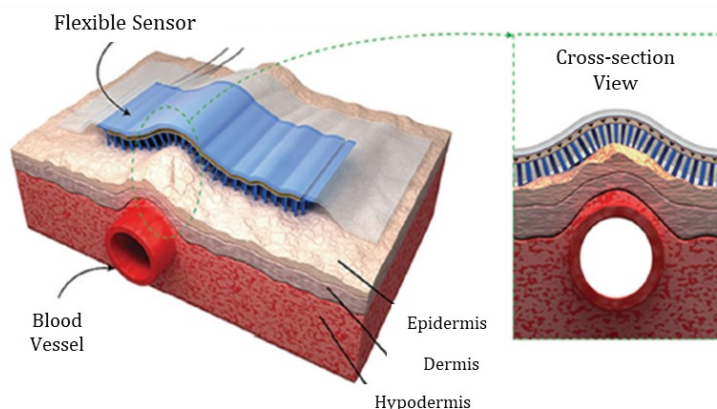


FIGURE 1:9 A schematic representation of a flexible sensor (blue) conformed to the curved soft human skin.

Various attempts have been made to develop stretchable and flexible sensors that could endure large deformation and conform to the curved soft human skin. This research activity is leading to a transition in the wearables from bulky devices and systems with sensors permanently glued on artificial textiles up to wearable strain sensors with skin-like sensing capacity [31]. These solutions go from soft sensors mountable on textiles (e.g., smart garments equipped with flexible sensors) up to soft devices directly stick to the skin (e.g., e-tattoo) (Fig. 1:10). In all these systems, the polymer matrices act as skin-like support materials thanks to their stretchability, human friendliness, and biocompatibility [30],[32]. Focusing on the SH scenario, soft sensors are used to instrument wearables for several applications: the monitoring of physiological parameters, the detection of human motion, the development of human-machine interfaces, and soft robotics.

In the literature, the majority of works related to flexible wearables consist of strain sensors based on conductive nanomaterials such as metal nanowires [33], carbon nanotubes [34], and graphene [35], which respond to mechanical deformations by changes of their electrical resistance or capacitance. When encapsulated into a soft matrix, those electronic sensors are capable of skin-comfortable monitoring of human health. Still, they suffer from electromagnetic interferences (EMI) and electrical safety issues (such as current leakage).

To overcome these limitations, recently, an innovative approach in the development of wearables for SH applications involved attractive optical alternatives based on fiber Bragg gratings (FBGs) due to their intrinsic advantages, among other, the immunity to EMI, the inherent electric safety, the high performance in terms of metrological properties, and the multiplexing ability. Methods of inscriptions of FBGs in polymeric optical fibers (for instance, polyimide - PI or ORMOCER rather than acrylate) [36],[37], and embedding FBGs in stretchable elastomers [38],[39] have been demonstrated to improve the softness and elasticity of FBGs from a small range of strain (ϵ) ($\epsilon < 1\%$ [40]) due to the rigidity of the silica fiber to large strain (e.g., $\epsilon > 30\%$ for instance, reaching during joint bending [41]).

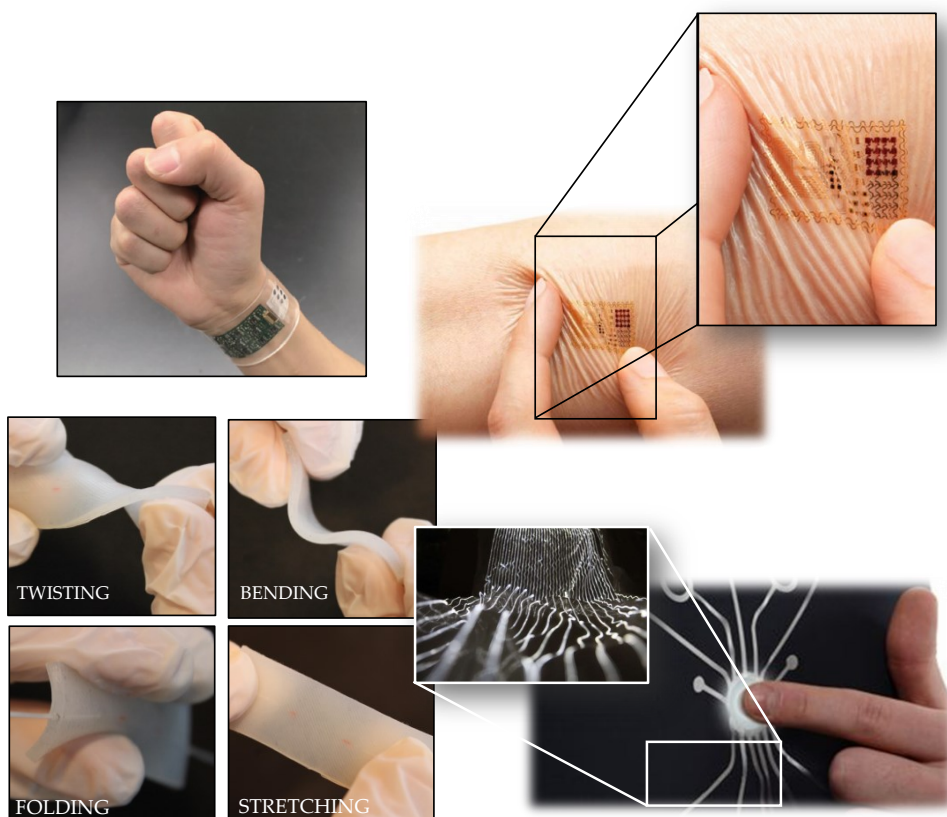


FIGURE 1:10 Stretchable, soft and skin-like wearables: from textile-mountable to stick-to-skin sensors.

1.3 Ph.D. candidate's contribution

The present work positions itself within the stream of research on smart technologies based on fiber optics for SH framework and addresses the topic of developing medical wearables for clinical applications.

This thesis aims at providing original contributions to the emerging FBGs applications for healthcare in several ways. Chapter 2 proposes a description of the theoretical background and measuring principles of the FBG-based systems applied to medicine, and it gives an overview of the state-of-the-art about FBGs employments in the development of wearables, innovative smart surgical tools, robotic devices, and biosensors. Chapter 3 includes a description of the physiological sources, their modelling, and the FBGs working principles to understand how these sources can be transduced into a signal easily detectable by sensing solutions. Attention will be mostly given to respiratory and cardiac activity, joint movements, and sensorimotor behaviors. Chapter 4 proposes the design, the fabrication, and the feasibility assessment of the main FBG-based wearables developed during this Ph.D.: a description of the design and the fabrication methods is included to underline ways to combine the FBG advantages with innovative methods of gratings encapsulation into soft skin-like materials, the feasibility assessment of the wearables capability for monitoring useful health-related information is described underlining tests carried out to investigate the metrological properties (both static and dynamic) of the proposed solutions and to obtain the related statistical measurement errors by comparing the system performances with benchmarks (usually gold standards in clinical practice).

Following this path, the present work answers the following leading questions around such a research topic:

<p>1) <i>What are the key elements to consider for the development of FBG-based wearables usable for SH applications?</i></p>

<p>2) <i>Which main steps should be accomplished to translate such optical technology from laboratory environments to clinical and everyday settings?</i></p>

Considering the complexity of the scenario which this thesis ground on, three main applications of FBGs-based wearables have been identified: the physiological monitoring (with particular regards to cardio-respiratory activity), the joint movements detection (especially joints flexion-extension – F/E), and the sensorimotor behavioral investigations (i.e., grasping reflex

in newborn infants). The belonging scenario guided the design, the fabrication, and the assessment of the proposed custom measuring systems based on FBGs to accomplish both clinical and technical requirements relevant to the specific application.

Chapter 2 Fiber Bragg gratings in medicine and healthcare¹

In the previous chapter, an extensive discussion about the direct relationship between the increase in life expectancy and the quality of systems for healthcare delivery and management has been proposed [42], [43]. Moreover, the recent scientific breakthroughs and technological advancements that can potentially change the way in which diseases are diagnosed and treated and a healthy lifestyle is promoted have been underlined [44]. Among others, powerful novel approaches based on smart systems, including wearables, have been presented as key enablers of the SH framework [42].

As an emerging technology, FBGs are becoming increasingly attractive for sensing applications showing several advantages over the competitors [45], [46]. FBGs are small, light, chemically inert, non-toxic, immune to electromagnetic interferences, and easily multiplexable [45], [47]. All these distinctive features combined in a single unit make FBGs important alternatives to electrical sensors. Besides, the FBGs intrinsic sensitivity to ε (S_ε) and T (S_T) enables their use in the measurement of clinically relevant parameters and in several medical branches [47]. Moreover, the increasing attention given to this technology by several publications and its growing usage in healthcare field underlines the strong interest to fulfill the gap between research and clinical practice [48], [49].

In this Chapter, an overview of the FBGs-based sensing solutions, their principle of work, and their most recent applications in medicine are presented. A similar overview of the current state-of-the-art offers the reader a better understanding of the FBGs great potentialities for SH applications while underlining the strengths and weaknesses of this technology.

The remainder of Chapter 2 is divided as follows: Section 2.1 provides a description of the theoretical background and the measuring principles of the FBGs, Section 2.2 gives an overview of the state-of-the-art of the FBGs applications in biomechanics, minimally invasive surgery

¹ This Chapter is an excerpt from the paper "Fiber Bragg Gratings in medical application and future challenges: a review" of which the Ph.D. candidate is main author" doi: 10.1109/ACCESS.2020.3019138

(MIS), physiological monitoring, and medical biosensing underlining wearables solutions when proposed.

2.1 Theoretical background and principles of measuring

Before describing the applications of FBGs-based systems in medicine and healthcare, a brief overview of the theoretical background and the basic working principles of different FBG configurations is proposed.

An FBG sensor is an optical resonator inscribed into the core of a fiber optic [50], [51]. The key principle of operation is to induce, by means of an external laser and an interferometer or a diffractive element, a periodic perturbation of the refractive index of the core of a single-mode optical fiber along the longitudinal direction (z). The inscription of such a perturbation in the fiber core induces light coupling between the forward propagating mode and a backward propagating mode at the resonant wavelength λ_B (the so-called Bragg wavelength).

Fig. 2:1 A shows the main configurations of FBGs proposed for medical applications, their spectral response, and the parameters they can directly measure [52], [53]. A schematic representation of the interrogation unit with all the components used to interrogate and read an FBG is illustrated in Fig. 2:1 B.

The simplest configuration is the uniform FBG [51], in which the modulation of the refractive index has a constant period (Λ) along z . This structure resonates at λ_B equal to:

$$\lambda_B = 2 \eta_{eff} \Lambda$$

Equation 2:1

with η_{eff} the mean effective refractive index of the fiber core at the location of the grating. The spectrum reflected by the FBG shows a steep peak centered around λ_B , with reflectivity usually within 10% and 90% in FBGs having a length ranging from 3 mm to 10 mm. For FBGs operating around 1550 nm, the reflected bandwidth is typically in the order of 0.3 nm; hence, an FBG sensor behaves similarly to a microwave notch filter having a quality factor ~ 5200 [9].

The measurement principle of the FBGs relies on the dependence of both η_{eff} and Λ on ϵ and T [50]–[53]: a grating tension or compression along its z -axis, as well as a T variation ΔT , cause a shift of the λ_B ($\Delta\lambda_B$), and of the whole spectrum as reported in:

$$\frac{\Delta\lambda_B}{\lambda_B} = (1 - p_e)\varepsilon + [(1 - p_e)\alpha + \xi]\Delta T$$

Equation 2:2

The $\Delta\lambda_B$ has a linear dependence on both ε and ΔT , with p_e the effective photoelastic coefficient, α the fiber thermal expansion coefficient, and ξ the fiber thermo-optic coefficient.

For glass fibers operating in the infrared, typical S_e values are around 1 pm/ $\mu\varepsilon$ for ε and 10 pm/ $^\circ\text{C}$ for ΔT . The optical fiber embedding the FBG needs a physical connection to a channel of a dedicated device (i.e., optical interrogator) using a standard connector (see Fig. 2:2 B). The commercially available interrogators have a number of channels ranging from 1 to 16. Typically, FBGs are interrogated through a rapid scanning tunable laser coupled to a photodetector followed by a transimpedance amplifier or a broadband source like a superluminescent LED connected to a spectrometer [53]. These systems allow the detection of the whole reflection spectrum, and using a peak-tracking method; it is possible to estimate the λ_B with an accuracy ≤ 1 pm. A schematic of the experimental setup used to interrogate FBGs is illustrated in Fig. 2:2B.

A chirped FBG (CFBG) is characterized by a non-uniform modulation $\Lambda = \Lambda(z)$; noteworthy in a linear CFBG, the period of the grating increases at a constant rate through the grating length [54]. As a result, the CFBG does not reflect a single wavelength, but the spectrum has a broad bandwidth. Each portion of the grating reflects a different Bragg wavelength:

$$\lambda_B(z) = \lambda_B(0) + \zeta z$$

Equation 2:3

where ζ is the chirp rate [54], [55]. Since the CFBG behaves as a broadband reflector, in which each section has its own dependence on T and ε , CFBG sensors have been used to measure either T or ε distributions along the grating length z . The main approach, called spectral reconstruction, is based on an optimization technique [55]–[57]. This method estimates the distribution of these parameters along the grating length (from 15 mm to 50 mm) by reading the spectral deformations from the reference conditions.

To make the grating sensitive to refractive index (RI) changes for biosensing applications, two main configurations have been exploited. The first approach is the use of a tilted FBG (TFBG), whereas the refractive index modulation plane is tilted with respect to the fiber axis by angles usually lower than 10° [58]–[60]. This grating has a λ_B similar to a standard FBG sensor, but also excites several cladding modes at the boundary between the cladding and the outer medium, that propagate out of the fiber. These modes are visible in reflection by coating

the fiber with an end-reflector, such as a gold mirror, and appear as a comb of narrow linewidths at wavelengths smaller than λ_B [59]. The second approach is the etched FBG (EFBG), in which a uniform FBG is modified by chemically etching the fiber cladding along the grating [61], [62]. In EFBG, the poor light confinement causes a change of η_{eff} term as a function of the RI, depending on the fiber thickness. As a result, we observe both a $\Delta\lambda_B$ and a variation of the optical intensity when the grating is exposed to RI changes [61].

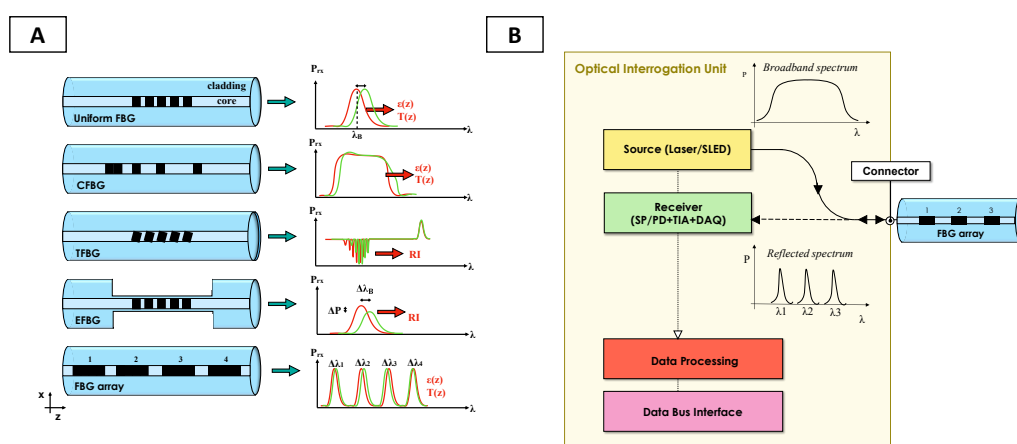


FIGURE 2:1. (A) The main configurations of FBGs: uniform FBG, CFBG, TFBG, EFBG, and FBG array. The spectral responses and measured parameters (ϵ , T , and RI) are also reported. (B) A schematic representation of the interrogation unit with all the components used to interrogate and read the FBGs. An FBG array is shown by way of example. The data acquisition hardware -DAQ- in the receiver block is used to maintain the synchronization between the swept laser source and the array of photodetectors.

The reflected bandwidth of FBGs is much smaller than the operating range of the interrogators. Hence, it is possible to fabricate several grating elements along the fiber, in an array format, each having a different λ_B . In this principle, called wavelength division multiplexing (WDM), multiple FBGs are stacked in a single fiber. The use of this solution allows resolving the parameter of interest (e.g., T , ϵ , and RI) along the fiber, isolating each FBG sensor contribution [63]. The FBG arrays can be fabricated with a custom density of sensors and to achieve high resolution (i.e., sub-centimeter) for lengths up to several meters. Moreover, their behavior can be described by exploiting finite element models (FEMs) and combining experimental data with machine learning methods [64], [65].

All the aforementioned FBG configurations are designed as short-length distributed sensors which resonate at wavelengths that correspond to the propagation within the FBG pitch.

2.2 Applications in medicine and healthcare : a literature overview

In the following sections, the state-of-the-art of FBGs applications in medicine and healthcare is grouped into biomechanics, minimally invasive surgery – MIS, physiological monitoring, and medical biosensing, as shown in Fig. 2:2.

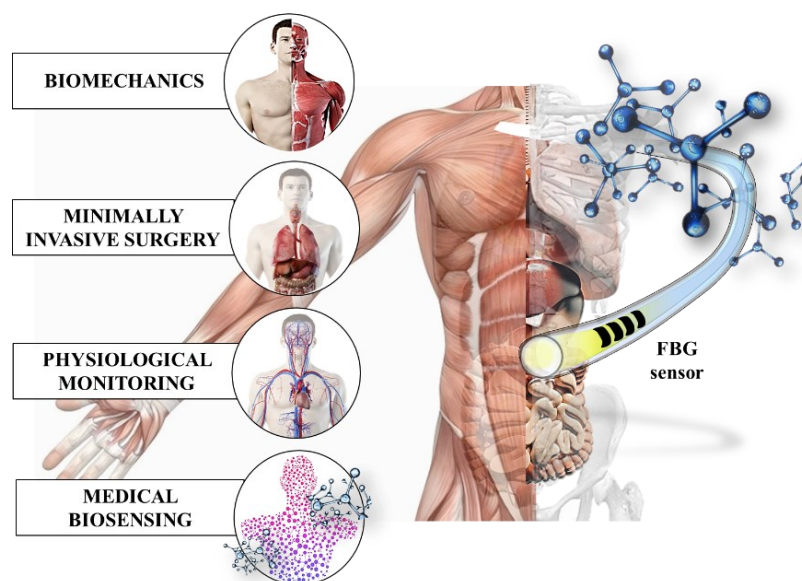


FIGURE 2:2. The main application scenarios where FBGs have been employed for medical and clinical purposes.

2.2.1 Biomechanics

The term biomechanics involves the application and the extension of mechanics to the human body at different levels of increasing complexity. In this section, an overview of FBGs-based systems for biomechanical applications will be given, tracing the body structural organization, from the tissue level up to the system level [66]. The description will start with studies concerning soft and hard tissue responses to mechanical stimuli. Then, FBGs involved in musculoskeletal applications in terms of joint kinematics and P mapping will be reviewed. Lastly, works related to the interaction between native biological tissues and foreign materials (i.e., prostheses and orthoses) in terms of load transfer mechanisms and pressure (P) distributions will be described. Fig. 2:3 shows the body parts involved in the following studies grouped into three main categories (i.e., Soft and Hard Tissue, Musculoskeletal System, and Prostheses,

Orthoses, and Bone Cement). Each category is coded by a different color (i.e., green, bright blue, and pink, respectively).

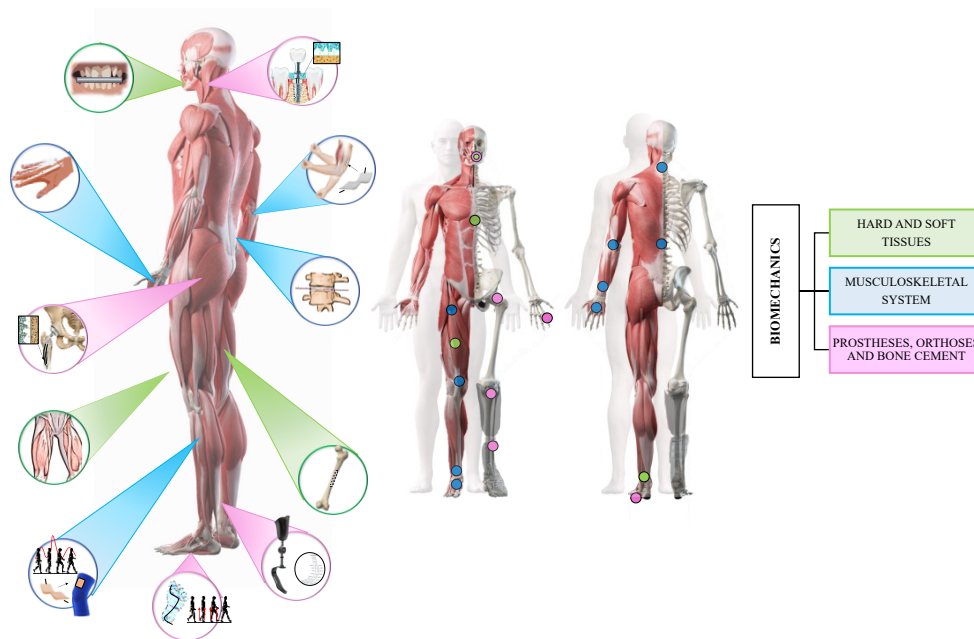


FIGURE 2:3. Applications in biomechanics. Examples of systems for soft and hard tissues are highlighted in green, for the musculoskeletal system in bright blue, and for prostheses, orthoses, and bone cement in pink.

Soft and Hard tissues. In the last decades, FBGs have been used to measure stress-strain (σ - ϵ) fields in soft and hard tissue biomechanics, where conventional sensors are not technically feasible [46]. The principal aim is to extend the knowledge about the tissue mechanical properties useful to develop detailed analytic models and optimized sensing solutions. The term soft tissues mainly refer to ligaments, tendons, and muscles. In the literature, most of FBG-based applications in this field have concerned the measurement of ϵ and force (F) of ligaments and tendons from both animals and cadavers [67],[68]. Gratings have been embedded into micro-fabricated encapsulations made of shape memory alloys [68], stainless steel [69], or directly attached to the tissue [28]. The systems' response to applied loads and controlled strains have been monitored during static and dynamic conditions to find out the systems' metrological characteristics. For instance, an FBG sensor housed into a micro-fabricated encapsulation made of shape memory alloy in [68] and of stainless steel in [69] was fabricated for ϵ and F sensing. Tests in static and dynamic conditions (e.g., at different loads and during loading-unloading cycles to simulate various postures and locomotion) were performed on a femoral cadaveric tendon and a ligament in [68] and on a bovine tendon in [69]. Results demonstrated

good sensitivity, accuracy, and repeatability of the proposed systems that added to an easily implantability make these technological solutions adaptable for minimally invasive measurements. In other studies presented in [67] and [70], similar tests were performed to validate FEMs. In [67], a good correlation was found between the tendon distribution of ϵ simulated by the proposed FEM and the one measured by an E-shaped buckle transducer (with an FBG sensor glued on its central arm). However, better results may be achieved using an array of multiplexed FBGs to allow distributed ϵ measurements. Not only the biomechanics of soft tissues from the lower limbs but also from other body districts have been studied in the literature. Recently, an FBG encapsulated in a protective sheath was used for measuring chordae tendineae tension in the cardiac mitral valve [71]. The sensor shape and movement mimicked the ones of the native biological tissue. Results of tests performed on both a 3D-printed left heart simulator and six independent chordae of a porcine mitral valve showed good performances and no interferences among chordae, during normal and hypertension-simulated conditions. Lastly, also in-vivo measurements of longitudinal and transverse ϵ and changes in the muscle-tendon unit were performed in [72]–[74]. In all these applications, FBGs were directly attached to the skin, and Magnetic Resonance (MR) images of the inner tissues were acquired.

Research efforts have also been dedicated to studying the biomechanics of hard tissues: bones and teeth. Bone deformations were investigated in response to applied loads [75]. Moreover, the influences of simulated fractures, bone decalcification, and sensor positioning layout on the ϵ measurements were studied [76], [77]. Synthetic and cadaveric femurs were employed, and strain gauges were often used as reference instruments. For instance, a total of four FBGs and four strain gauges were placed around the circumference of an acrylic tube and a cadaveric femur bone of the same length. Results showed a loss of linearity by comparing results from sensors placed on the tube with the ones on the tissue. These findings reflect the genuine non-linearity in the bone segment. The measurement of ϵ as a quantitative evaluation of the effect of simulated fractures was presented in [76] and [77]. In [76], a total of seven FBGs were glued along a stainless-steel plate used to fix the fracture. FBGs were easier to use than strain gauges sensors, with higher feasibility to monitor the evolution of the ϵ in the bone. In [77], an array of FBGs was directly attached over fractured synthetic femur sawbones, and the influence of fiber orientation and gratings location on the ϵ measurements was investigated. Results suggested that a straight layout works better than a coiled one for ϵ sensing. Also, bone decalcification over time was analyzed as an influencing factor in the ϵ measurement [78].

The comparison of FBG's output changes detected on an untreated sample and on a partially decalcified one showed a linear increase of ϵ with the calcium loss. In the literature, other applications of FBG-based systems in hard tissue biomechanics have concerned the

measurement of deformations of teeth and mandible during mastication [79], [80]. In particular, the capability of monitoring clinically relevant bite F in thirty-six volunteers, as well as detecting different masticatory patterns associated with the chewed food in animals, was investigated. Results showed good performances for both the proposed systems. In [79], the bite F of males experienced higher values than females with the maximum F at the molar region; in [80], the output of an FBG sensor embedded in a titanium mesh showed a high signal-to-noise ratio useful to easily determine the magnitude and the frequency contents associated to the chewing process.

Precisely at the halfway between soft and hard tissues, it is located the articular cartilage. The mechanical properties of this tissue were studied in [81]–[83]. In all these works, the cartilage has been modeled using a viscoelastic model, and micro-indenters with an FBG sensor located at the tip were used to study changes in tissue relaxation times and stiffness. In [81] and [82], results showed an increase of all these parameters with the indentation depth. The spherical tip showed advantages in terms of shorted indenter length and risk minimization of tissue surface damage. The spherical indenter was also able to distinguish healthy cartilage from artificially degenerated in [83] and from osteoarthritic tissue of seven patients who underwent knee replacement in [84]. Higher F in [83] and higher stiffness in [84] were exhibited by the healthy cartilage. Otherwise, no significant differences were found in terms of relaxation time of tissues with different grades of degeneration [84].

Musculoskeletal system. The inherent connectivity between soft and hard tissues is essential for musculoskeletal motion and stability. Indeed, at a higher level of complexity, the human body can be considered a whole-joint organism where bones meet and are functionally integrated with soft tissues to constitute a kinematic chain. In the literature, a lot of biomechanical studies focused on FBG-based systems for human joint kinematics. The principal clinical aims are the prompt detection of bad postural habits, which may lead to musculoskeletal diseases, and the quantitative assessment of the rehabilitation programs to provide even more personalized treatments. Optical goniometers have been proposed for monitoring knee, elbow, and ankle range of motions (ROMs) [79], [85], [86], during static and dynamic conditions (e.g., static postures and walking). In all these works, cantilevers-based systems and different transmission mechanisms (e.g., stiff arms and rubber belts) were used for de-amplifying the ϵ transmitted to the grating, according to the ROM of the joint under investigation. The influence of the distance between a pin mechanism and a cantilever on the sensitivity of a custom optical goniometer was investigated in [84]. Results showed the bigger the distance, the higher the ϵ induced on the grating. Moreover, tests on twenty-six volunteers wearing the proposed device

on the knee showed a good agreement between the output of the FBG-based goniometer and the one of the reference system in monitoring F/E movements. Moreover, good accordance in the measurement of gait parameters during walking on either leg was achieved. Similar results were found in [87], where F/E movements of elbow and ankle were monitored by using an optical goniometer with rubber-based transmissions. However, all these solutions are bulky thus should be re-evaluated in terms of the user's comfort and ability to keep its rotation axis during gait trials.

For this reason, most of the studies for joint kinematics focused on the development and assessment of wearables based on FBGs [88]–[90]. Usually, to improve their robustness and performances, FBGs have been housed into more flexible structures made of polymers such as Polyvinyl chloride - PVC [88]–[90], Dragon Skin™ silicone families [91], [92], polylactic acid - PLA [93], and Thermoplastic Polyurethane (TPU) [94]. Buttons, belts, Velcro® strips, and tapes have been used as bonding elements.

ROMs and movement patterns have been monitored on both lower and upper limbs and spinal cord segments. Goniometers and motion capture systems have been often used as benchmarks. Several works focused on lower limbs to study their kinematics and understand the complex dynamics associated with the gait. Usually, the metrological characteristics of the wearable systems have been reported, followed by tests on a treadmill during walking, jogging and/or running. Among others, a wearable solution comprising a Kinesio Tape® (K-Tape) embedding an FBG sensor was proposed in [95] to monitor the angular displacement of the knee joint during gait cycles. Results showed the consistency of this solution to perform gait analysis and perceive the pick activity movements of the quadriceps. Some concerns of the proposed system are related to its fragility because the FBG was embedded bare. Thus, a step forward was done in [96], where an epoxy resin matrix was used to house the FBG, and two 3D-printed hooks were used to guarantee the sensor compliance with the K-Tape on the ankle. Another study proposed FBGs embedded in PVC strips to be worn on the elbow, knee, wrist, and back, in static angle posture maintenance and jogging tests [89]. Results showed stable output changes in response to step-by-step angular variations, and the elbow was the joint most affected by disturbances. During jogging, the sensor mounted on the knee showed the highest values of ϵ and a signal amplitude reduction with speed. In this context, an innovative fabrication technique was proposed to develop a smart ring for knee and elbow joints in [93]. The FBGs were encapsulated in the system made of PLA during the printing process. Then, different bend angles were performed to retrieve the FBG sensitivity and to assess the capability of monitoring movement patterns.

Wearables were also proposed for monitoring the mobility of phalanges of hands and feet. An instrumented rubber cable for monitoring plantar dorsiflex was fabricated in [97], whereas a smart glove in [98] and a smart TPU guide in [94] were used for interphalangeal joints movement detection. In [98], an array of fourteen FBGs embedded in PVC was glued in a coiled layout over the interphalangeal joints on the glove upper surface. Results reported minimum and maximum ϵ for fully opened and closed hands, respectively, with the need for a pre-calibration when worn by different subjects [98]. The capability of accurately distinguishing among metacarpophalangeal, distal, and proximal interphalangeal was confirmed in [98], but slight losses of linearity in the system response were found with finger size reduction. In [94], an array of thirty-six FBGs in a TPU guide was worn, assuring the contact with each finger by a tape on the nail on one side, a Teflon flattener on the opposite side, and a silicon ring structure around the guide. Results of the angular displacements response vs. torques (calculated by multiplying applied F and moment arm) allowed the evaluation of the joint quasi-stiffness. Lastly, some studies investigated the use of FBG-based flexible sensors directly attached to the skin or taped on stretchable belts for spinal motion detection [92], [99]. In [92], the movements of F/E and axial rotation (AR) of the cervical segment of nine volunteers were detected by using two custom flexible sensors based on FBGs showing good performances when compared to a Motion Capture (MoCap) system used as a reference, with potentiality in preventing neck pain.

Another function of the musculoskeletal system regards body stability. In this arena, FBG-based systems were used to monitor intravertebral discs (IVDs) P [100]–[103]. The IVDs are the main joints of the spinal segment, and an understanding of the P distribution is an essential indicator of disc mechanics, injuries, and degeneration aetiology. In [101], the IVD nucleus P was measured by an optical probe with the grating at the tip. The optical system exhibited good repeatability in monitoring P and an easier insertion than strain gauges, which often causes interferences with the vertebral endplates and potential damages. Also, the influence of the insertion depth and the diameter of the probe on the measured P was described in [102], [103]. The probe was constituted by two segments joined together by means of a bar with an FBG glued above. At the same level of insertion, results showed that the bigger the diameter, the higher the F , while at different levels, the deeper the insertion, the higher the F value.

Prostheses, orthoses, and bone cement. Other applications of FBGs for human biomechanics are related to the study of the interaction between human inner/outer tissues and foreign materials. The main aims are the recovery optimization of lost musculoskeletal functions by replacing body parts (i.e., prostheses) and the improvement of residual functions through

the application of external devices designed to fit with the outer body components (i.e., orthoses).

The P mapping and ϵ distribution at the prosthetic joints have been measured to study malalignments and/or unbalanced contact areas [104]–[106]. For instance, two arrays of five CFBGs each were embedded in a tibial spacer to map the P on cadaveric condylar grooves during a total knee replacement. Results of non-uniform P mapping suggested a failure of knee arthroplasty with risky long-term degradation of the bones in in-vivo applications. Moreover, the fiber diameter, the presence of bone cement, and the use of press-fit prophylactic stems were investigated as influencing factors on load transferring and ϵ distributions at the implant-femur interfaces in [100] and [107], respectively. Results showed that: a small fiber diameter improved the sensing element performance, a cemented prosthesis allowed a more uniform distribution of the P, and a press-fit prophylactic stem limited the risk of fracture in the immediate postoperative care for patients with notch depth larger than 5 mm.

As suggested in [100], bone cement plays a crucial role in the implant stabilization and uniform load and ϵ distributions; thus, the mechanical properties of various bonelike materials have been investigated in the literature. The curing processes of Poly(methyl methacrylate) - PMMA [108], [109], Hydroxyapatite (HA) [110], and Calcium Phosphate (CP) [111],[112] cements were monitored by embedding FBGs in blocks made of such materials. The ϵ profiles and T were measured over the whole duration of the material shrinkage to check the presence of values out of physiological range, particularly dangerous for tissue necrosis and implant instability. Results in [109] and [111] showed that differences in ϵ pattern are related to the cement porosity (i.e., the number of voids which occurs after the monomer evaporation), and that a high number cause cement weakness and implant failure. Moreover, according to the porosity level, the immersion of cement specimen in liquid solutions until the saturation allowed the determination of the material expansion coefficients [112].

Once the prosthesis fits perfectly, the evaluation of body movements' mechanism has been assessed to study the recovery of lost musculoskeletal functions. For instance, FBGs embedded into a carbon fiber-reinforced transtibial prosthesis were proposed in [113], [114] to evaluate the recovery of the user's gait. Eight FBGs were placed in a vertical position and nine FBGs in a horizontal position to enable the measurement of vertical ϵ and mechanical F/ ϵ non-perpendicular to the ground direction, respectively. An additional FBG sensor was placed at the distal end of the prosthesis and used for the T compensation. Results of static tests showed a linear response of the proposed system to applied loads with values twice the mass of the volunteer enrolled in the study. Then, three walking tests at three different velocities (i.e., 0.5 m/s, 1.1 m/s, and 2.2 m/s) were performed by attaching the instrumented prosthesis on the knee,

showing promising results especially for the FBGs attached to the regions where the prosthesis stores and releases energy during walking. Such a study, combined with other ones focused on robotic manipulators equipped with FBGs for tactile sensing [115],[116] opens up to future applications of FBGs in bionics. Indeed, FBG-based sensory feedback could enable closed-loop control of the prosthesis, improving its embodiment, amputee's recovery functions, and engagement with the surroundings going beyond the results achieved with MEMS sensors [117], [118].

In the literature, the main orthoses instrumented by FBGs. have been developed in the form of amputee sockets, wheelchairs, fixed platforms, plantar insoles, and orthodontic apparatus. The monitor of P at the amputee sockets-stump and skin-wheelchairs interfaces were investigated in studies concerned with the FP7 IASiS projects [119]–[121], whose aim was bringing optical fiber technology in rehabilitation applications, and more recently in [122]–[124]. In all these studies, the sensing element was encapsulated into flexible matrices. Moreover, the influences of the matrix thickness in [121], [122], and the grating embedding depth [122] on the sensor performances have been investigated. For instance, in [122], the amputee sockets-stump interfacial P were measured by using an epoxy material sensor pad based on the FBG sensor embedded in a silicone matrix. Results showed that the system with the FBG sensor on the top of the pad encapsulated into the thickest matrix exhibited the highest sensitivity. Foot plantar P and ground reaction forces (R) were detected by fixed platforms in [125], [126], and orthotic insoles in [127]–[134] instrumented by single or multiple FBGs. In [131], both shear and plantar P were discriminated during gait, using an array of ten FBGs. Other exciting approaches were proposed in [86] and [87], where the two FBGs-based solutions were developed to monitor the ground R: a fixed platform instrumented by five multiplexed FBGs in [133] and a cork-based insole with an array of six FBGs in [134]. Both the proposed solutions were able to monitor vertical ground R during gait, as well as the body center of mass displacements in static positions. Moreover, corks allowed the gratings thermal isolation. The most recent smart insole was proposed in [132]. The system was wholly 3D-printed, and the FBGs were encapsulated into the insole during the printing process with promising during both standing position and walking cycles.

Another important application in orthotics regards the study of dental biomechanics by measuring the properties of teeth and mandible in response to the installation of dental implants and orthodontic apparatus. In dental implants, the main aim is to study σ - ϵ patterns on the temporomandibular joint due to the implantation. In all these studies, the sensing elements were directly placed on the outer surface of a mandible equipped with a dental implant [135], [136]. In some cases, strain gauges were used as reference instruments to assess the system

capability of measuring a high level of static and dynamic ϵ , and these measurements were also used to validate FEM [137], [138]. Results in [137] showed a good agreement between the measuring method and FEM when teeth are subjected to symmetrical loads. At the same time, the marked differences during non-symmetric configurations suggested the hardness in replicating the complex dental structure. Moreover, research efforts have also been devoted to study the influence of the sensor positioning on the ϵ measurement in [139]. Results showed the highest values for sensors positioned in the molar region.

To fix dental implants, often dental cement is required. Thus, FBGs were also used to monitor T, ϵ , and σ built-up during the curing process of gypsum products [140] and dental resin [141]. The most interesting sensing solution was described in [141], where two FBGs in highly birefringent (HiBi) fiber were employed to monitor the multi-axial stress build-up with promising results. Several studies also reported on the application of FBGs in the presence of dental orthosis involving splints [142] and brackets [143]–[145]. The proposed systems were used to measure T, ϵ patterns, and P distributions. Both T and F sensing were carried out during the splint positions in [142], showing an increment of both these parameters with small variation in the F values due to the patient self-adjusting. The orthodontic F applied by a bracket on the dental arch was measured by the custom solutions proposed in [91] and [92]. In [91], an FBG sensor written in a HiBi fiber was bonded on the orthodontic bracket between the orthoses and the incisor outer surface with good ability in detecting longitudinal and transversal F applied on the teeth, in the range corresponding to clinical applications. Lastly, the influence of grating positions on the ϵ distribution was investigated in [92], where seven FBGs were placed along three teeth roots and transversally along four teeth apex. As expected, the maximum ϵ was experienced by the gratings at the molar tooth's cervical position.

2.2.2 Minimally Invasive Surgery

The MIS and the associated tools are becoming increasingly relied upon across the healthcare industry. The term MIS describes all kinds of surgery that minimize injury to the patient with reductions of tissue trauma, pain, and recovery time. Recently, the advent of robotic in MIS imposed an increasing burden on the surgeon's manual dexterity and visual-motor control [105]. However, the use of handheld/robotic tools between the surgeon's hand and the tissue, as well as the physical separation in teleoperated surgery, limit the haptic feedback to the surgeon with potential tissue trauma or unintentional damage to healthy tissue [103]. To overcome these limitations, FBGs-based tools have been proposed for tasks of tissue manipulation and ablation to restore tactile and T sensations fundamental for providing haptic

feedback to the surgeon during MIS and robot-assisted MIS [146], [147]. Moreover, to access the surgical target sites along tortuous anatomical paths, several surgical flexible tools have been equipped with FBGs to guide and track the tool positioning by monitoring its shape and location [148]. Fig. 2:4 shows the body parts involved in the following studies grouped into three main categories (Tissue Manipulation, Tissue Ablation, and Tool Shaping). Each category is coded by a different color (i.e., straw yellow, red, and bright green, respectively).

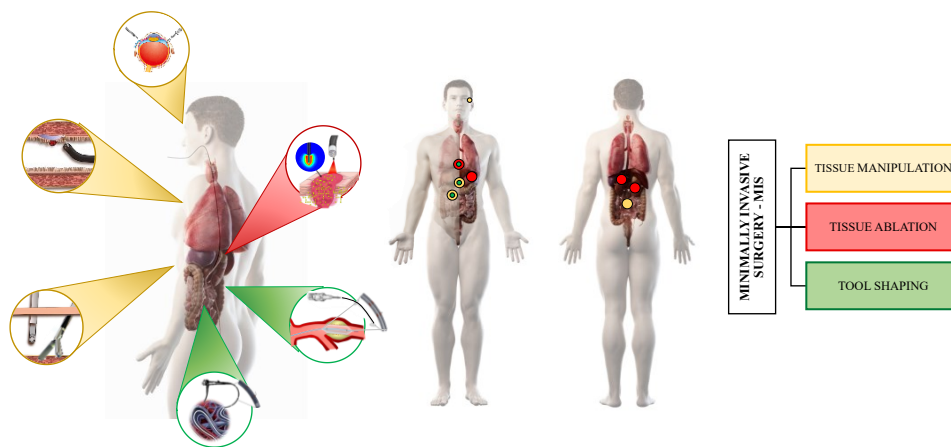


FIGURE 2:4. Applications in MIS and robot-assisted MIS. Examples of tissue manipulations are highlighted in straw yellow, tissue ablation in red and tool shaping in bright green.

Tissue Manipulation. Tissue manipulation includes surgical maneuvers to grasp, clip, suture, and palp outer and inner tissues. These tasks establish tool-tissue interactions to allow unprecedented functionality including, automated robotic responses, recognition of tissue force signatures, ability to minimize tool-to-tissue forces during microsurgery, and potentially improve the safety and efficacy of the surgical procedures. As a result, the surgeon can control the applied F avoiding any tissue damage, and distinguish between hard and soft, healthy, and unhealthy palpated tissues [146], [149]. In the literature, several surgical tools as graspers, clipper, needles, and catheters have been instrumented with FBGs for applications of retinal microsurgery, laparoscopy, endoscopy, and percutaneous procedures, including epidurals and biopsy [146].

Retinal microsurgery is one of the most technically challenging micron-scale maneuvers performed on delicate tissues [150]. Surgeons need to operate on very small and delicate eye tissue with the magnification of a surgical microscope and fine control of the surgical motion, discharging hand tremor. The proposed solutions ranged from 1 degree-of-freedom (1-DoF) [151] to 2-DoF [152] and 3-DoF [153] tool-tip force sensors based on single and multiple FBGs,

with and without T compensation. Evaluation experiments with the proposed instruments were conducted on different epiretinal membrane models with manual [154] and handheld robotic control [155]. In [151], the first attempt to develop a 1-DoF FBG-based intraocular force sensor was carried out instrumenting a 25 Gauge (~ 0.5 mm diameter) micro-pick instrument with a single FBG embedded in a Nitinol wire. Subsequently, by employing three FBGs, the concept was extended to a 2-DoF tool for F-sensing with T compensation, and tests on different epiretinal membrane models with manual [154] and handheld robotic control [155] were performed. In a follow-up work [153], the first sub-millimetric 3-DoF F sensing pick instrument employing four FBGs was proposed to maximize the decoupling between axial and transverse F sensing. Besides assisting with membrane peeling, some FBGs-based tool-tip F sensing devices were developed to detect puncture F in retinal vein cannulation. Generally, these instruments employ three longitudinal FBGs for 2-DoF F sensing capabilities attached to a cannulation needle with a distal tip bent at around 45° relatively to tool shaft axis [156]–[158] to ensure puncture F in the direction of the needle tip. An $80\text{-}\mu\text{m}$ needle tip F sensing cannulation tool was proposed and assessed during the cannulation of synthetic retinal vessel models [156] and cadaver pig eyes [157]. Similarly, in [158], [159], a $70\text{ }\mu\text{m}$ needle tip tool was attached to a handheld robotic device and cannulated vessels in the chorioallantois membranes of chicken embryos. A step forward has been done in [160], where a new control method to compensate unintended movements of the operator's hand actively and to keep the cannulation device securely inside the vein following cannulation was proposed. Experiments in fertilized chicken eggs vasculature, shown 100% success in venous puncture detection and significantly reduced cannula position drift via the stabilization aid of the robotic system [161].

Several studies introduced micro-forceps with integrated FBG-based F sensing [160], [162], [163]. For instance, in [160], a 3-DoF F sensing motorized forceps was proposed employing an additional sensor to capture the tensile F along the tool axis. Moreover, a nonlinear F computation method was proposed to ensure that grasping does not affect the axial F reading. Validation experiments, including random samples, showed that the method could predict 3-DoF in the axial direction. Lastly, FBG-based force sensors integrated into the tool shaft outside the eye were described in [164]–[166]. This is a highly desired functionality in robot-assisted retinal surgery because the stiffness of the robotic system attenuates the user's perception of the scleral F with the potential for eye injury. In [164], a tool able to sense the scleral F in transverse directions and the location of the sclera contact point on the shaft was developed. This solution allowed a robot control framework based on variable admittance using the sensory information to reduce the scleral interaction F exceeding a safe level. Furthermore, in [165], a control method was proposed to enable the robot to perform autonomous motions

reaching desirable sclera F and/or insertion depth and pre-defined safe trajectories. Moreover, robotic systems, FBG-based F sensing instruments, and a recurrent neural network were combined to develop intelligent assistive solutions to predict excessive F instances and augment the performance of the user [166], [167].

Other surgical applications regard laparoscopic and endoscopic procedures, where FBGs have been extensively used to provide tactile feedbacks inferred from either the exerted F during surgical tasks or the distal contact F during tissue palpation. Solutions based on one-point and distributed measurements have been proposed using uniform single or multiple FBGs, directly mounted on the tip, in the proximity of the tip or onto a transmission mechanism connected to the tool (e.g., Steward [168], Sarrus [169], and cantilever-beams [170] structures). Moreover, FEMs have been often used to drive the system development in terms of optimized sensor positioning and miniaturized tool dimensions to achieve the best performances. T compensation, axial F decoupling, bending outward effects, and creep resistance were also evaluated to validate the feasibility of the proposed designs in MIS applications. In [171], a laparoscopic needle driver to measure axial and grasping F at the grasper tip was presented. The lower jaw of the grasper was equipped with two FBGs. The FBG sensor used to measure axial ε was embedded in the flexure structure of the jaw, as the deflection of this element during object pulling induces ε on the grating. The FBG sensor used for measuring grasping F was mounted on the jaw proximally after the flexure segment. This device is an updated version of a previous prototype proposed to overcome some issues related to grasping repeatability and axial sensor hysteresis error in [172]. The novelty lies in the use of a T-shaped grasper made of stainless steel instead of an I-shaped one made of plastic. These features improved the system biocompatibility and sterilizability. The higher rigidity of the steel resulted in a reduction of the system sensitivity in favor of higher repeatability and accuracy with negligible bending and F coupling effects.

However, systems equipped with an FBG sensor directly attached in the proximity to the tip often undergo either limited resolution or operating range. Trade-offs between the F sensing resolution and proximity of the sensors to the tool tip can be optimized by adequately choosing the sensor locations. To overcome these issues, some studies proposed the use of FBGs incorporated onto the tool shaft [173] or a transmission mechanism between the end-effector and the joint [170], [174], [175]. For instance, in [173], a 2-DOF needle driver based on four FBGs was developed to be compatible with the Da Vinci Surgical System. Three robot-assisted MIS tasks were carried out by novice and expert surgeons. Results showed different F profiles according to the level of expertise and improvement in the task execution for both the group thanks to the F feedback. Recently, two interesting solutions based on transmission

mechanisms were proposed in [169] and [175]. The same research group focused on two FBG-based systems for grasping and palpation tasks using Stewart and Sarrus linkage mechanisms in [175] and [169], respectively. The adopted structures were optimized on the basis of finite element analysis. In both the studies, the rigid kinematic parts of the proposed mechanism were substituted with flexural hinges to provide effective F interaction between tool and tissue and prevent damages to tissues during laparoscopic applications. Moreover, an FBG sensor in a tight suspension configuration was mounted at the flexure's central line. In [175], FEM results suggested the need for an additional cantilever-beam structure to improve the system sensitivity even if sacrificing its axial stiffness and F decoupling. Results in [175] showed an excellent linear response to applied static loads with high sensitivity. A consistent agreement with a commercial F sensor used as a reference was also reported during dynamic loading experiments (the average error between the two measuring systems was 0.26 N). Results in [169] showed that in both static and dynamic F loading experiments, excellent consistency was found in terms of simulated and experimental sensitivity and linearity. Then, two simulated cylindrical cancer nodules were buried in the samples at different depths of a silicone phantom and a porcine liver, and the achieved results validated the effectiveness of the proposed sensor to detect tumors from the F distribution map during tissue palpation.

Although laparoscopic surgery was considered the greatest revolution in MIS and robot-assisted MIS over the past two decades, another surgical revolution for tissue manipulation involved FBGs in natural orifice transluminal endoscopic surgery [176]. In contrast to laparoscopy, no superficial incisions are necessary to reach the target. In the literature, flexible catheters and tubes were equipped with FBGs and inserted through natural cavities [177]. Distal contact F, P mapping, and tactile distributions were some of the main measured parameters. For instance, nitinol tubes equipped with two FBGs for detecting the distal F of tendon-sheath mechanisms in flexible endoscopic robotic surgery were proposed in [178], [179]. The main differences between the two versions are related to the overall length of the nitinol tube (reduced from 6 mm to 3mm) and to the grating length (reduced from 4 mm to 1 mm). Evaluations of F calibration, hysteresis, and T compensation were carried out. Results showed linear responses of the two FBGs to F and T. Issues related to T compensation and creeping effect, as well as signal noise associated with improper glues, were fulfilled in [178] and ex-vivo and in-vitro tests were performed to assess its functionality. Results showed a stable response with good linearity within the range of 0.1 N - 0.5 N with a percentage error of approximately 4.2 % between the measured and the theoretically estimated values.

An interesting application of two FBGs arrays with thirty-two gratings each, for P mapping in gastroscopy was proposed in [180]. A flexible catheter was inserted through the nasal hole

with a sensing length covering the path from the pharynx to the stomach for monitoring the gastrointestinal mobility. Firstly, controlled in-vivo clinical trials were carried out to directly compare the system performance with a commercially available solid-state manometry catheter showing a substantially equivalent response. Then, a volunteer was intubated and asked to perform controlled swallows. Results demonstrate the ability of the FBGs-based catheter to record peristalsis running from pharynx to stomach by measuring muscle contraction (P increments) and retraction (P decrements). Abnormal values can allow measuring early symptoms of diseases related to the upper digestive apparatus. Another FBG-based system suitable to work inside the digestive apparatus was proposed in [181]. An endoscopic instrument was developed for palpation of the inner colonic wall for future applications in colorectal cancer screening. The device was equipped with three silicone encapsulated FBGs. A FEM guided the system development, demonstrating the proposed tool's capability to measure contact F along its axis with a linear response between ε and applied F .

Other percutaneous procedures for tissue manipulation involved FBGs-based needles for biopsies and epidural punctures [182]–[184]. Solutions for tissue-tool tip F sensing have been proposed in the form of a needle equipped with FBGs. In [182], an 18 Gauge needle stylet was provided with three optical fiber embedding four FBGs each. The needle was mechanically connected to a device with a pen-like knob grasped by the users, and information of tool-tissue contact was rendered via a haptic display that uses ultrasonic motors to convey directional cues to users. An amount of twenty puncture trials were performed by each of the ten subjects involved in the study. Results showed that subjects could easily determine the direction in which haptic feedback was guiding them, improving their task performance. Lastly, an optical guidance system for epidural space identification was proposed in [183]. An FBG sensor was placed inside the lumen of an 18 Gauge epidural needle and tested on a lumbar phantom used to train clinical procedures for epidural space identification. Intentionally wrong punctures without achieving the epidural space were also performed. Results showed the system capability of discriminating the most significant tissue interfaces from the detection of the P state experienced by the needle tip during the penetration inside the phantom model. Moreover, the correct and wrong punctures were clearly distinguished.

Tissue Ablation. Another important application of MIS is the cancer removal through tissue thermal ablation. Localized measurement of T distributions inside the organs may improve the clinical outcomes reducing the probability of damaging surrounding healthy tissue. Tissue ablation by thermal treatments (e.g., laser ablation, radiofrequency ablation, microwave ablation, high intensity focused ultrasound, and cryoablation) have an immense potential for the

removal of cancer and have already gained broad clinical acceptance [185]. The main advantages are related to their minimal invasiveness since these treatments can be performed either via a percutaneous insertion of a small needle-like applicator or through a natural orifice under endoscopic ultrasound guidance. Thermal treatments involve the use of different types of energy to induce a cytotoxic T increment in the target organ in order to destroy all the tumors with an additional safety margin while sparing the surrounding healthy tissue. Although these techniques have been performed for decades, there are some open challenges. The high T induced to destroy tumors inevitably damage healthy cells. Besides, the difficulties to accurately monitor the effects of the treatment in real-time can cause either an incomplete tumor removal or the damage of surrounding healthy structure. FBGs have immense potential for improving the clinical outcome in this field since the knowledge of T during the treatment can be beneficial to target the thermal damage to tumor cells minimizing the harm of healthy tissues [186], [187]. The possibility to resolve T along with the fiber by fabricating FBG arrays facilitates the 3D reconstruction of tissue T. This unique characteristic makes FBGs better than other temperature sensors (e.g., thermocouples, thermistors) for this application. In 1997, the first attempts to monitor T during thermal ablation by FBGs were presented in [188]. In the last decades, FBGs usage in this field has grown tremendously, and these sensors have been applied in phantoms and during the treatments of different organs (e.g., liver, bone, kidney, pancreas, biliary tree) in animal models (ex-vivo and in-vivo) and clinical trials [188]–[196]. During the first attempts, the majority of the studies have been performed by using one or more fiber optics embedding a single FBG sensor, while recent investigations have employed arrays of FBGs to perform high-resolved measurements and to reconstruct the whole map of T within the organ. Recently, studies have proposed highly dense FBGs with spatial resolution better than 1 mm with ten or more FBGs embedded within a single fiber. For instance, recently, a configuration using an array of twenty-five FBGs with a grating length of 0.9 mm was proposed in [197]. Regarding other performances of these sensors, it is worth noting that they can measure T with accuracy in the order of 0.1 °C, with short response time, and data can be collected at sampling frequency higher than 1 kHz [63], [193], [197]. Other advantages are related to the absence of artifacts due to the direct absorption of the energy delivered to perform the treatment, while this problem can significantly affect different types of sensors [198]–[200]. An important advantage is that these sensors can be used in Computed Tomography (TC) and MR room. This can be crucial since several thermal treatments are performed under either CT or MR guidance. Also, this feature makes FBGs an optimal tool for assessing the performance of new non-invasive protocols for monitoring T maps during thermal treatments by CT or MR images (i.e., CT thermometry and MR thermometry [201], [202]). A potential problem can be related to the

cross- S_e , especially during in-vivo experiments. In this scenario, movements caused by the patients' respiratory activity can strain the sensors causing measurement errors. This concern involves applications during lungs' treatments and all the organs that experience movements during respirations (e.g., liver, pancreas, and kidney). Experiments have shown measurement errors up to some $^{\circ}\text{C}$, but they can be minimized by filtering the recorded data [193]. Recently, CFBGs have been applied to this field to estimate the thermal gradient, particularly significantly close to the applicator used to deliver the energy during the treatment [203]. The recent developments of highly dense FBGs allowing measurements with high resolution could discourage future use of CFBGs in this application, also considering the complexity of the data analysis to retrieve information from their spectrum.

Tool Shaping. For the correct manipulation of surgical tools inside the patient's body, it is essential to track their position and shape during a surgical procedure dynamically. Despite the availability of commercial FBGs-based shape sensors certified EN60601 (a series of standards for the safety and the effectiveness of medical electrical equipment) [204], the 3D real-time shape reconstruction is still challenging. Indeed, the complex morphologies of the targeted sites and the tortuous path access under constrained spaces require high embedding capability of the sensing system and inherent tool deformability. To overcome these issues, optical fiber technology has gained attention for curvature estimation and shape reconstruction. The main configurations of FBGs-based shape sensors can be grouped into multiple single-core fibers, epoxy-molded or fastener to a support, and multicore fibers (MCFs), having several cores integrated into a single fiber. The most widely used configurations for shape sensing are: triangular with three outer cores [205], [206], square with four outer cores [207], [208], and hexagonal with one central core and six outer core [166] (typical configuration for MCFs). The more cores are exploited, the higher is the accuracy of the shape sensor at the equal value of core spacing (core-to-core distance) [209]. Besides, some studies investigated the multi-sensitive capability of shape sensors for simultaneously detecting the interaction F between the instrument and the surrounding environment, while reconstructing shape [210], [211]. Needles, catheters, endoscopes, and continuum robots for MIS and robot-assisted MIS applications (e.g., in neurosurgery, otolaryngology, biopsy, colonoscopy, and intravascular surgery) have been equipped with FBGs, showing enormous potentialities in tool shaping. Among the instrumented tools, better performances have been found in the shape reconstruction of systems that undergo small deformations (e.g., steerable needle for biopsy and ablation). Indeed, their inherent higher stiffness in comparison to catheters and endoscopes induced a perfect ϵ transmission to the attached FBGs.

Referring to multiple single-core fibers, the triangular configuration has been the most exploited in medical applications since it can be interrogated using only three channels of the interrogation unit and ensures a simpler assembly than the other configurations. Furthermore, when employing a central core, such configuration allows twist angles detection in addition to T compensation, axial ϵ removal, and curvature sensing [212]. For instance, in [205] and [206], a surgical needle was equipped with a triplet of single-core optical fibers in a triangular configuration. Each fiber embedded four FBGs glued along the shaft grooves for shape sensing during a biopsy. Results in free space and gelatin phantom insertion showed maximum errors in needle shape reconstruction and tip positioning (about 2.23 mm and 1.91 mm in free space, and 0.79 mm and 0.57 mm, in gelatin), higher in out-of-plane deflections than in in-plane ones. Improvements in target accuracy and precision of the proposed system were reached by combining a robot-assisted needle steering method with FBGs-based shaping feedback [213]. Attempts have also been made toward the shape sensing of endoscopes and catheters. Their length and flexibility higher than those of needles require more FBGs to provide useful and accurate curvature information. Moreover, research efforts have been dedicated to the implementation of shape sensors in endoscopes. For instance, in [207] and [208], a square configuration of four single core fibers, each consisted of five FBGs, was proposed. Results showed the system capability of reconstructing the tool shape but with large errors during in-vivo tests [207]. This configuration allows the T compensation and curvature profile measurement but suffers from low resolution in twist angle detection [208]. Recently, a step forward to the accuracy improvement of shape reconstruction has been done exploiting MCFs arranged in a hexagonal configuration, as reported in [214]. Such a system resulted in a valid alternative to fluoroscopy for endovascular navigation. The shape sensor was obtained using three of the seven cores of the MCFs, inscribing thirty-eight multiplexed FBGs each, to sense curvature and shape from the ϵ detected by the gratings. Results showed high accuracy in the 3D shape reconstruction over the whole sensing length (380 mm).

2.2.3 Physiological Monitoring

The monitoring of physiological parameters is at the cornerstone of medicine and surgery since it is a relatively non-invasive measure of human health. The baseline indicators of a patient's health status are often known as vital signs [215]. This section is devoted to describing the FBG-based systems used to detect vital signs routinely checked by healthcare providers: f_R , HR, BP, and BT). Fig. 2:5 shows the body parts involved in the following studies grouped into four main categories (named Respiratory frequency, Heart Rate, Blood Pressure, and Body

Temperature). Each category is coded by a different color (i.e., light blue, light red, purple, and acid green, respectively).

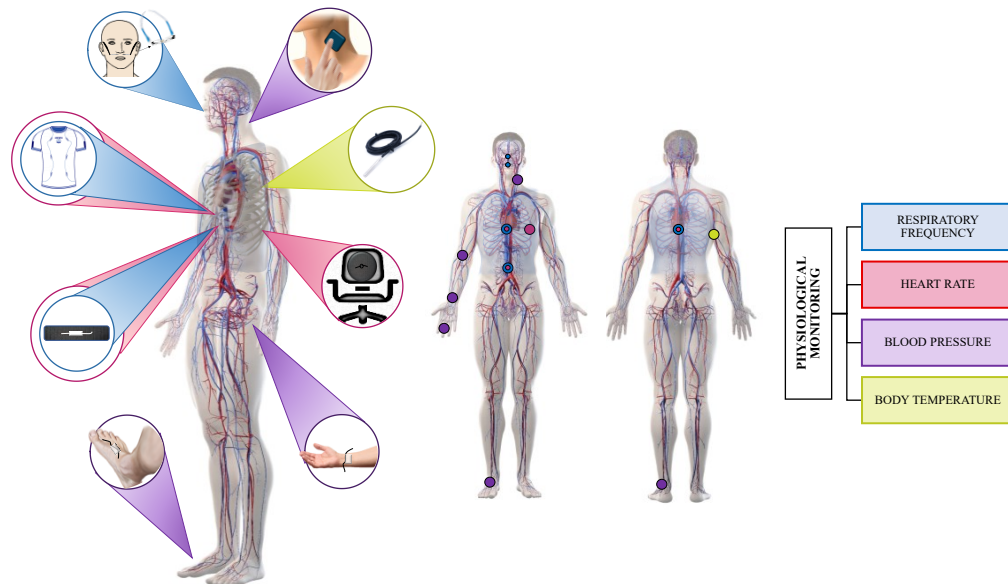


FIGURE 2.5. Applications in physiological monitoring. Examples of systems for monitoring f_R are highlighted in light blue, for HR in light red, for BP in purple, and for BT in acid green.

Respiratory frequency. The f_R has been extensively monitored by using FBGs-based technologies in clinical (e.g., respiratory rehabilitation and MR examination) and sports settings (e.g., cycling and archery) [216]. The majority exploited the grating intrinsic S_ϵ for developing wearable and non-wearable systems able to monitor f_R from the respiratory-induced chest wall deformations. In this kind of application, FBGs have been either bare or housed into passive flexible matrices, bonded on textiles (e.g., elastic bands and stretchable T-shirts) or on synthetic surfaces the body skin comes into contact with (e.g., cushions, wheelchairs, flatbeds [217], [218]). Spirometers, flowmeters, and MoCap systems have been often used as benchmarks [219]–[222]. The first study concerning the monitoring of f_R by thoracic cage deformations was described in [223]. An FBG sensor was embedded in an elastic band to hold it in place during breathing. Good signal-to-noise ratio, not fully linear response to ϵ , and capability of triggering external devices for artificial ventilation, was demonstrated. FBGs used to instrument wearable systems were also proposed in [224]–[226], in the framework of the financed OFSETH FP6 EU project. Both thoracic and abdominal movements were detected by smart elastic bands. One band was instrumented by a single FBG in a coiled-layout fiber. Once the S_ϵ and fatigue strength have been studied, the system assessment was performed on healthy adults

and using a simulator inside the MR scan. The capability of measuring ϵ elongation up to 3% and to be a golden solution for MR vital signs monitoring was demonstrated. Smart T-shirts based on a different number of FBGs (from two up to twelve gratings) have been proposed as innovative technologies enabling unobtrusive respiratory monitoring in terms of f_R , respiratory (T_R), inspiratory (T_I) and expiratory (T_E) periods, tidal (V_T) and compartmental (V_C) respiratory volumes in [221], [222], [227]. Indeed, a high number of gratings allows investigating the behavior of different chest compartments. For the first time, the MoCap system was used to drive both the system fabrication and assessment. Tests in standing and prone positions and MR scan and cycling were carried out to investigate the system response to different working conditions. The promising results showed that the system performances increased with the number of gratings, their location, and orientation (for instance, percentage errors in f_R estimation $\leq 0.38\%$ [227] rather than 1.59% [222] and 1.14% [221]). Moreover, the smart textile based on twelve FBGs, a half located in specific positions on the front of the cage and a half on the backside, showed high accuracy in estimating breath-by-breath T_R , T_I and T_E values (for instance, T_R bias of 0.001 s rather than 0.14 s [222] and 0.04 s [221]) with good capability of monitoring V_T after a pre-calibration (bias of 0.09 L). Such a prototype was also involved in studies where influences of sex and sensor positioning have been considered to drive further optimization in terms of the number of FBGs, robustness, and more adaptability to different body shapes [228].

In this regard, two different branches of research have been proposed: *i*) the instrumentation of synthetic surfaces in contact with the skin (e.g., cushions, wheelchairs, flatbeds [217], [218]), and *ii*) the rise of flexible wearable sensors based on FBGs, high compliant to the skin [229]–[231]. Some examples belonging to the first branch are FBGs taped on a cushion [217] and a plexiglass board [232], placed between the backside of the chest and the backrest of the seat or the MR flatbed, respectively. Results showed good performance in measuring dynamic ϵ caused by breathing (in both cases, percentage errors $<12\%$).

Regarding the second branch, an amount of novelty has been brought by studies based on flexible sensors to be comfortably worn by the subject. In these works, often, a metrological characterization is firstly required to find out the sensor S_ϵ and other parameters (e.g., T and relative humidity - RH) since the properties of the 3D matrix influence the FBG response. For instance, in [231], a rectangular-shaped flexible sensor based on FBG technology was calibrated to retrieve static and dynamic metrological characteristics showing S_ϵ one order of magnitude bigger than the T ones, negligible RH-induced contributions, and acceptable hysteresis errors. Then, the proposed sensor was used to instrument two elastic bands for monitoring

mean and breath-by-breath f_R values from the thorax and abdomen movements during tests in the lab and out-of-lab (i.e., during simulated archery races) [220].

A different approach for the f_R monitoring involved the measurement of nasal/oral airflow. Techniques for a direct measure of the respiratory airflow or based on different thermo-hygrometric conditions between inspiration and expiration have been proposed. The main difference between these two techniques is related to the presence of active polymer coatings for the grating functionalization. This configuration allows variations in the surroundings (i.e., in the content of water vapor and so in RH and T) to activate the coating volumetric or refractive index changes responsible for FBG wavelength shifts and coupling intensity variations.

Focusing on the direct monitoring of respiratory airflows, both bare and metal-coated FBGs have been used to develop flowmeters (e.g., orifice meters and hot wire anemometers) and spirometers. Cantilever-based mechanisms and external energy sources (e.g., laser) have been often required for the transduction of the airflow into FBG output changes. For instance, in [233], an isosceles triangle cantilever with a couple of FBGs at either side was pushed/pulled by the flow F transmitted on it. The cantilever bending caused grating tensions/compressions, showing a non-linear relation between wavelength shifts, $\Delta\lambda_B$ and measured flowrates with a high S_e . Another cantilever-based approach was proposed in [234], where a spirometer based on FBG technology was proposed for pulmonary function tests. The FBG sensor was glued lengthwise along a cantilever beam mounted transversely to the upper section of an aluminum plate. During inspiration/expiration, the cantilever was pushed/pulled by the plate swiveling, and in turn, the FBG sensor was tensioned/compressed. Comparing some crucial respiratory parameters (i.e., forced expiratory volume in the first second, FEV1, forced vital capacity, FVC, and peak expiratory flow, PEF) obtained by the FBG outputs and the reference one measured by a commercial spirometer showed promising results.

Research efforts have also been made in the use of metal-coated FBGs to develop hot wire anemometers, where an external source of energy has been often used to ensure the sensing element thermal equilibrium. Recently, examples of this kind of solution were described in [235], [236], where graphene and silver layers were used as coatings, respectively. Their measurement principle is underpinned by the metallic layers, which absorb the power of pumping light. Usually, an external source heats the metallic layer causing a red shift of the coated FBG sensor. When the airflow hits the sensing element, part of the heat is taken away from the layer, and the FBG undergoes a blue shift. All these works showed an effective improvement of the system flowrates sensitivity thanks to the metallic layer, with a non-linear relationship between FBG wavelength shifts and measured flowrates.

As previously described, differences in airflow thermo-hygrometric conditions can also be exploited for f_R monitoring. Few studies proposed devices with bare FBGs to estimate f_R by detecting ΔT between inhaled and exhaled airs [237],[238]. The most used solutions are based on the FBG functionalization for RH sensing [239]. To accomplish this aim, several coatings have been exploited. Among others, synthetic and natural polymers (e.g., PVA, PMMA, and Agar) and nanostructured films of Graphene oxide (GO) and Polycyclic aromatic hydrocarbon/Silica nanoparticles (PAH/SiO₂). The matrix thickness (t_k) and coating polymer concentration (wt%) have been investigated as influencing factors of the RH sensitivity of functionalized FBGs suggesting higher sensitivity and response times for thicker matrices and higher polymer concentration [240].

Heart Rate. The HR has been monitored simultaneously to f_R by most of sensing FBG-based solutions previously described to measure chest displacements [217], [227], [229]–[231]. Indeed, the heart's mechanical activity causes vibrations smaller and faster than the respiratory ones on the chest surface. The graphical representation of the heartbeat-induced displacements is known as seismocardiogram (SCG) when measured as vibrations on the chest, and ballistocardiogram (BCG) when referred to the ballistic forces generated by the heart and measured at the center of mass of the human body. FBGs are very suitable for non-invasive cardiac monitoring since they are small and light, highly sensitive to ϵ , with long-term stability and proper frequency response. These features allow the recording of cardiac-induced displacements, typically ranging from 0.2 mm to 0.5 mm, and frequency components, mainly ranging from 0.6 Hz and 40 Hz [241]. The majority of the proposed studies investigated the cardiorespiratory monitoring describing wearable and non-wearable solutions made of polymers and composite materials such as Polydimethylsiloxane - PDMS [230], PVC [229], [242], Dragon Skin™ 20 [231], Plexiglass [243], Fiberglass [244] and reinforced carbon fiber (CFRP) [218]. Electrocardiogram (ECG) and photoplethysmography (PPG) have been often used as benchmarks [243]. Despite the use of different measurement principles and various casing materials, all the studies agreed that the proposed systems show more accuracy in the estimation of f_R than HR values. This finding is justified by the smaller amplitude of the signal related to the heart activity than the one due to respiration, by the need for more sophisticated filtering stages required to extract the cardiac contributions masked by the respiratory one, and by the lack of standardized fiducial measuring points for the SCG detection. Such harnesses are still limiting the clinical use of SCG/BCG signals for HR monitoring.

Recently, a first effort in the definition of fiducial points has been made in [220], [231] where an elastic based instrumented by a flexible sensor based on a single FBG was positioned

on three measurement sites (i.e., xiphoid process, umbilicus and below the left mammilla) of 3 volunteers to investigate the site influence on the signal amplitudes. During both inter- and intra-volunteer analysis, significant differences were found, suggesting the influence of anthropometry and sensor pre-stretching. However, the low values of standard deviation measured during each test indicated the high repeatability of the system once worn and the capability of measuring HR. A step forward has been done in [167], where HR was measured by two nominally identical FBGs, one sensor worn on the xiphoid process and the other one above the umbilicus of 9 volunteers. The FBG sensor at the xiphoid process resulted more accurate than the one above the umbilicus in estimating HR values when compared to the reference one, both in terms of mean and beat-by-beat values (e.g., mean absolute percentage errors around $\sim 5.74\%$).

Other exciting solutions for potential SCG clinical applications have exploited the FBG MR-compatibility. In [243] and [244], HR during the MR scan was measured, placing the sensor in contact with the backside of enrolled volunteers and the thorax (i.e., in the form of a wearable system), respectively. Despite the strong electromagnetic field generated inside the MR scanner, the signal propagated in the fiber was not distorted, and a good agreement (percentage errors $< 7\%$ for both the proposed systems) was found between mean and beat-by-beat HR values measured by the FBG-based system and the reference instrument. The same system in [243], was used to instrument a chair and a footplate. Results of 3 volunteers showed differences always lower than 2.68 bpm between HR values obtained by the FBG and the ECG sensors. Similar approaches were proposed in [218] and [242]. In [218], a smart bed equipped with 12 FBG in a single fiber was presented. Results showed that the HR detected by the smart bed was very close to the one measured by a pulse oximeter. Lastly, in [242], a conic-shaped device was instrumented by an FBG sensor and used to measure HR when positioned in contact with the left upper thorax of five volunteers. A comparison between mean HR values measured by the FBG sensors and a digital oscilloscope showed good agreement.

Blood Pressure. The BP calculated from the pulse wave using FBGs is one of the most challenging measuring techniques concerning vital signs monitoring. Indeed, a low-pass filtering stage (e.g., 0.5Hz-5Hz), the identification of each pulse wave, the signal normalization along the y-axis and standardization along the x-axis, and a calibration curve built using partial least squares regression analysis are necessary before being able to calculate BP [245]. Usually, when the heart beats, the pulse wave moves through the circulatory system. In the literature, several FBGs-based solutions were proposed to perform the pulse wave analysis (PWA), detecting the arterial pulse at different peripheral pulsatile sites. The PWA has been extensively

used for monitoring BP (and the pulse rate, PR) starting from the peaks in the pulse wave patterns. The advantage of PWA also relies on monitoring pulse variability in terms of pulse transit time (PTT) to retrieve an estimation of the arterial stiffness and of the waveform and to improve the quantification of the systolic load on the heart and other central organs [246]. Sphygmomanometers placed on the arm/wrist, pulse oximeters on the finger, and stethoscopes have been often used as benchmarks. Systems based on FBGs for BP monitoring have been fabricated to be directly attached to the skin [245], encapsulated into wearables [247],[248], or embedded into probes in contact with the skin surface [249]–[251]. The pulse wave has been detected on several body parts (i.e., temple, finger, ankle, neck, foot, elbow and wrist [247], [248], [252]–[255]), at the level of the peripheral pulsatile sites (i.e., brachial, carotid, radial, ulnar and tibial arteries). In [245],[256], an FBG sensor was used for BP monitoring. It was taped perpendicularly to the direction of the blood flow in the radial artery of the right wrist. A sphygmomanometer around the left upper arm was used as a reference system. Moreover, influences of individual differences, measurement site height and assumed postures on the accuracy of the BP monitoring have been investigated in [245], [256]. Tests were carried out on elderly and young subjects in supine posture in [245] and in supine, sitting, and standing positions with increasing height differences between the FBG sensor and the reference instrument in [256]. Results showed the good capability of the proposed sensor to calculate BP in several postures at fixed heights (error < 4 mmHg) with a reduction of accuracy according to individual differences and height (errors < 6 mmHg in both cases).

Attempts have also been devoted to the employment of wearable solutions for the BP monitoring. They have been developed in the form of skin-like systems [247] and hollow boxes [248], [257], [258] with a flexible diaphragm. The most recent solution has been proposed in [248], where an FBG-based hollow tube was developed to detect pulse waves from the volumetric changes of the finger. The results of eighteen volunteers showed the capability of the proposed device to monitor BP, PR, and PTT, using an electronic stethoscope as reference. Moreover, repeatable morphologies between followed pulses have been demonstrated. Lastly, among optomechanical probes based on FBGs, two studies proposed spring- and lever-based mechanisms to improve the systems' sensitivity to the small ε caused by the pulse wave [249], [251]. Both the works showed highly performant solutions for BP monitoring. Indeed, such mechanisms improved the S_ε around ten and twenty times compared to the ones obtained without transmission elements.

Body Temperature. The BT has been monitored in some studies reported on FBGs-based systems. Needle-based systems and wearables have been proposed. Commercial

thermometers have been often used as benchmarks. In [259], polymer packaging was used to improve the sensitivity of bare FBGs. In particular, an unsaturated polymer resin encapsulating the grating allowed an increment of S_T around 15 times higher than the bare one. Then, five prototypes of the proposed sensor were embedded into an upper body intelligent cloth, on the right and left chest and armpit, and on the upper back. A weighted FEM was proposed to obtain the final BT from the five sensors placed on the upper body. Indeed, the contribution of each body part to the final BT values is different and should be weighed. A good agreement was found between the last BT values measured by the proposed system and the ones measured by a medical mercury thermometer. A Teflon-based capillary structure was proposed in [260]. First, the capillary was filled with epoxy resin. Then, tests were carried out by placing the proposed system and a mercury thermometer into a water bath at identical positions, when T ranges from 35 °C to 45 °C. A nonlinear input-output relationship was found presumably related to the resin solidification process. Thus, another structure was proposed to improve the system performance by fixing the FBG sensor only at two endpoints. Results showed a linear response with S_T 23 times higher than a bare FBG sensor. Lastly, a prototypal FBG probe consisting of a hypodermic needle has been recently proposed in [261] and subjected to cyclic sterilization processes. The aim was to investigate the influence of such a process on the FBG-based probe performances compared to a commercial thermistor. Results showed that the optical probe was not harmed from thermal stress cyclically induced by the sterilization while the thermistor was affected. Moreover, the S_T of the FBG-based needle showed no significant changes with the accumulation of sterilization cycles (up to 250), and the standard deviation remained low and stable over the cycles as compared to those determinates by the commercial system. These findings are considered very promising for clinical practice.

2.2.4 Medical Biosensing

The need for even more accurate diagnosis and personalized medicine is leading to a growing understanding of disease pathological pathways through the detection of biomarkers. Biomarkers are considered efficacious indicators for several pathologies such as cancers, neurodegenerative disorders, and cardiovascular disease [262]. For this reason, researchers have invested a lot of effort in medical biosensing to promptly assess the stage of the disease and design the most effective treatments tailoring to the patients' individual needs [262], [263]. A biosensor is a compact device that incorporates a high-affinity biological receptor (e.g., enzymes, aptamers, cells, and antibodies) for the recognition of a specific analyte (e.g., proteins, DNA/RNA sequences, virus, and bacteria)[264]. Among others, medical biosensing based on

optical fiber gratings presents good performances in detecting biological components since the recognition of the analyte is transduced into a measured optical signal with high sensitivity, immune to external disturbance, stable, and with high signal-to-noise ratio [263]. Although TFBG is the principal grating configuration used in optical biosensing, also EFBGs have attracted recent interest as biosensors [61]. However, some hurdles are still limiting their use.

In biosensing applications, all the proposed sensing solutions should be able to detect changes in the surrounding refractive index caused by the biochemical receptor-analyte reaction. Thus, the first step forwards in the fabrication of EFBGs-based biosensors is the partial or full exposition of the core-inscribed sensing part to the surrounding medium obtained by etching, polishing, or tapering the fiber [263]. Usually, the chemical etching has been performed before the grating functionalization to improve the biosensors' surrounding RI sensitivity (S_{RI}). Unfortunately, although a smaller diameter results in a higher S_{RI} , an improvement in the fiber fragility during the functionalization steps is observed. Some studies have focused on the influence of EFBG diameters on the system performance to find out a good trade-off between S_{RI} and robustness [265], but challenges still exist. Otherwise, TFBGs can be directly used for biosensing purposes exploiting their intrinsic sensitivity to surrounding RI changes.

The most widespread optical configuration for medical biosensing is represented by the surface plasmon resonance (SPR) based biosensors. Numerous studies reported on pure and localized SPR excitations obtained by coating the grating with noble metal films and nanoparticles (e.g., gold and silver). Moreover, silane chemistry has often been performed as an additional biofunctionalization strategy to allow an appropriate immobilization of bio-receptors on the sensor surface. Lastly, the blocking of the uncovered sections to avoid non-specific analytic bindings and additional depositing of nanoparticles (e.g., gold and GO) have been proposed to improve the sensor selectivity and sensitivity [266]–[268].

The choice of reagents depends on the final target applications. EFBGs- and TFBGs- based biosensors have been used to detect metabolic pathways, cellular growth and proliferation, proteins, bacteria, and viruses to allow diseases and disorders detection, drug testing, and cellular regeneration. Most of the proposed detection technologies have not required fine labeling procedures, and the binding process could be assessed and monitored in real-time. Confocal and fluorescence microscopy-based approaches have been used to assess the effectiveness in modifying the fiber surface [269], [270]. Biosensors based on FBG sensors have been extensively used for applications in medical diagnostics, ranging from the detection of cancers, viruses, and bacterial infections to cardiovascular, neurological, and endocrine disorders and diseases. According to the biological reagent in charge of capturing the analyte, the proposed EFBG/TFBG-based biosensors can be grouped into antibody-, nucleic acids-, enzyme- and

whole cell-based biosensors. The most popular biosensing technique for pathologies diagnosis is based on the immobilization of a bio-receptor (e.g., antibody, aptamer) on the fiber surface to capture a specific biological target (e.g., protein, virus, bacteria, whole-cell, and small molecules) [271]. Fig. 2:6 shows the main diagnostic areas targeted by the following studies grouped into three main categories (i.e., Cancers, Viral and Bacterial Infections, Genetic Diseases, and Neurodegenerative and Endocrine Disorders).

These solutions allow f_R monitoring from the oral or nasal airflow in the form of needle-like probes and temporary wearable devices (e.g., face masks and plates below the nostrils), with uniform FBGs and TFBGs working in reflection or in transmission [272], [273]. An FBG sensor inserted in a metallic needle and coated by agar was proposed in [219], [274], [275] for f_R monitoring during both mechanical ventilation and human breathing. The measured f_R values were compared with the ones set on the mechanical ventilator and measured by using a commercial spirometer in [274], [275], and [219], respectively, showing promising results (percentage error <3%).

Among temporary wearable devices, a respiratory mask instrumented by an FBG sensor coated by GO was used in [272] and by 23 PAH/SiO₂ layers in [276]. Both the devices showed a high capability of monitoring f_R , but only the one in [276] was tested on humans. A more comfortable solution was recently proposed by [277], where a completely MR-compatible plate made of PVC was instrumented by an agar-coated FBG sensor encapsulated into a Dragon Skin™ matrix. The assessment was carried out on six volunteers during slow, normal, and fast breathing, placing the plate below the nostrils. Promising results were testified by values of absolute percentage errors $\leq 2.29\%$.

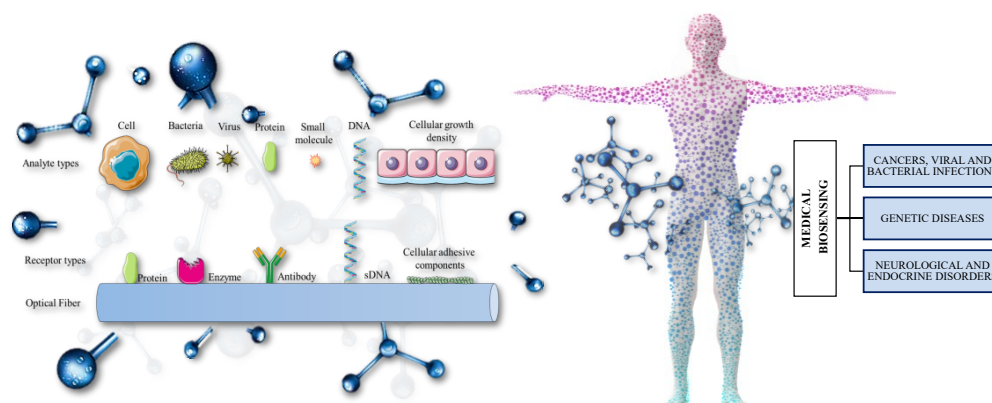


FIGURE 2:6. Applications in medical biosensing. Examples of the main binding typologies are highlighted.

Cancers, Viruses, and Bacterial Infections. Systems for a prompt diagnosis of cancers and infections caused by viruses and bacteria have been proposed starting from the EFBG/TFBG detection of changes in RI due to the antibody-antigens reaction binding. In [266], the diagnosis of lung cancer in the distal bronchial tree was proposed. The group manufactured a minimally invasive gold film-coated SPR-TFBG sensor. The biosensor was embedded inside a catheter and designed to detect a cancer cell biomarker (i.e., Cytokeratin, CK 17) by the surface immobilization of a specific antibody (i.e., anti-CK17). Ex-vivo studies on freshly resected human lobectomies showed that the device detected the biomarker and distinguished healthy samples from tumoral ones. Moreover, additional information about the tissue stiffness allowed the right positioning of the catheter. Recently, nucleic acid aptamers (DNA or RNA) have been emerged as attractive alternatives to antibodies, leading to the development of nucleic acid-based biosensors based on FBGs. Cancer biomarkers were detected by DNA-based biosensors in [266]. A specific DNA aptamer (i.e., MAMA2) was immobilized on the fiber surface (50 nm gold film-based SPR-TFBG sensor) for the detection from the tissue surface of mammaglobin proteins, expression of circulating human breast cancer cells. Moreover, additional gold nanoparticles were used as amplifier labels of the biosensor response. Results showed the capability of detecting a low concentration of cancer cells (10cells/mL) with a good specificity as compared to other control cell lines.

Other studies have focused on the diagnosis of cancers and inflammatory processes from the detection of the cell growth density in response to cancer biomarkers drugs and other stimuli using whole cell-based biosensors. Among others, in [278] and [279], the detection of the epithelial growth factor receptor (EGFR) was performed. The EGFR is an important biomarker that is over-expressed by numerous cancer cells [280]. In [278] and [279], the functionalization of the fiber surface with specific monoclonal antibodies was performed to quantify extracellular membranes receptors in native human epithelial cells. In both the studies, the sensor architecture lay on a gold-coated SPR-TFBG with monoclonal mouse immunoglobulin G antibody (anti-EGFR) immobilized using Dojindo's carboxylic acid. The interaction between the proposed immunosensor and EGFRs (intact and with an overexpressed receptor) was investigated by measuring changes in transmission spectrum amplitude and wavelength as cellular binding events occurred. Specific bindings of cells were detected for concentration $\geq 3.0 \cdot 10^6$ cell/mL with linear binding relation over time.

In the field of cell growth density, another application has focused on the investigation of drugs and microenvironments-cell interactions in cell culture equipment. The effect of trypsin, serum, and sodium azide on the NIH-3T3 fibroblast cells response was studied by using a gold-coated SPR TFBG [281]. Results showed that such stimuli induced detachment of cells from the

sensor surface, serum uptake, and cellular metabolism inhibition, respectively. The resulting signal indicated a regeneration capability under repetitive stimuli and the possibility of detecting biofilm formation and drugs on the fiber surface.

Genetic Diseases. Another innovative field of application in medical diagnostics relies on the detection of genetic diseases performed by biosensors based on DNA hybridization [269], [270]. Indeed, the discovery of imperfect matches of DNA sequences is the leading cause of specific genetic mutations. Although innovative efforts have been assayed towards the development of such biosensors, the development of high performant sensing solutions is still challenging. In [269], micro-structured FBGs were functionalized by single-stranded DNA (ssDNA) aptamer to bio-recognize complementary base sequences and form a stable double-stranded region. Results showed high specificity to detect low target concentration in real-time. The main issues are related to difficulties in performing reproducible fabrication processes. Indeed, the washing process with a phosphate buffer saline solution followed by a re-hybridization led to a different number of active sites occupied by DNA molecules. Considering that the optical response depends on the location of such binding sites on the fiber surface, a different value of local sensitivity was achieved.

Neurodegenerative and Endocrine disorders. DNA and enzyme-based biosensors have been developed for the diagnosis of neurodegenerative disorders (e.g., depression, Parkinson's disease, and dementia), often caused by the abnormal value of small molecules such as S-adenosyl-L-homocysteine (AdoHcy) and dopamine. For instance, in [268], a gold-coated SPR TFBG was functionalized with ssDNA aptamer anchored on the graphene layer. The sensor showed a linear response with a dopamine concentration increment with high resolution. A similar study was proposed in [282], where the enzyme named Lysine methyltransferase (Set7) was used to functionalize the surface of the gold film-coated SPR-TFBG fiber to detect AdoHcy. Results showed the capability of detecting surrounding refractive index changes from the transmitted spectrum, allowing low concentrations measurements.

Another field of application in medical diagnostics regards endocrine disorders starting from the detection of the blood glucose level. Several studies proposed glucose oxidase (GOD)-based TFBG biosensors. In [283], GOD was immobilized on a GO-coated TFBG via the cross-linker 1-ethyl-3-(3-dimethylaminopropyl) carbodiimide (EDC) and N-hydroxyl succinimide (NHS). The glucose level was measured starting from the refractive index changes, which occurred during the catalytic reaction of GOD. A sensitivity of 0.25 nm/mM was found in the range of low glucose concentrations between 0 nM and 8nM. Another TFBG sensor was used in [284], where the GOD enzyme was immobilized on a silanized optical fiber surface. The

strong adhesion of GOD to the optical fiber due to the silanization process enabled the detection of low glucose concentration (0.013-0.02 mg/ml).

Tesi di dottorato in Scienze e ingegneria per l'uomo e l'ambiente, di Daniela Lo Presti,
discussa presso l'Università Campus Bio-Medico di Roma in data 9/04/2021.
La disseminazione e la riproduzione di questo documento sono consentite per scopi di didattica e ricerca,
a condizione che ne venga citata la fonte.

LL

Chapter 3 Wearable systems based on FBGs: from physiological sources to physiological measurements

The new concept of SH aims at providing continuous monitoring of patient vital signs, physical activities, musculoskeletal parameters, and other internal and external factors that contribute together to the global health state and human wellness. As described in Chapter 1, the paradigm shift introduced by the SH framework grounds on technologically driven disease prevention and prompt medical interventions to establish a person-centered health system. Advances in sensing technology, communication, and data transmission, constitute some of the main pillars on which such a new framework consolidates itself. At the same time, tools designed to be minimally invasive for clinical and surgical applications, systems based on flexible and smart technologies for cumbersome monitoring, and biosensors for personalized treatments foster consistent improvements in the quality of the delivered care and the level of patients' engagement. Among various sensing technology, Chapter 2 focuses on FBGs which are considered by the research community very attractive over the competitors thanks to their inherent characteristics. These advantages make FBGs extremely useful for several applications in medicine and healthcare.

3.1 Wearables for cardiorespiratory monitoring

3.1.1 The importance of cardiorespiratory monitoring

Monitoring both respiratory and cardiac activities is fundamental since the cardiovascular and ventilatory systems regulate several vital functions of the human body and adapt themselves in response to various stressors.

Cardiorespiratory variables can be monitored to inform on the occurrence of relevant pathological or stress conditions that may be responsible for unhealthy states. The regulation of the

cardiovascular and ventilatory systems is very complex, and each variable may be a crucial indicator of severe clinical events [285].

The f_R and HR are the two physiological parameters of vital importance related to respiratory and cardiac activities. The f_R , defined as the times of respiration observed during a minute (expressed in breaths min^{-1} or bpm), is a vital sign whose abnormal values are predictors of breathing dysfunctions but also chronic heart failure, cardiopulmonary arrest, and admission to an intensive care unit [286]. Moreover, evidence showed that f_R responds to various non-metabolic stressors, including environmental-induced stress, cognitive load, pain, and emotional stress [287], [288]. Recently, f_R appears to be a useful marker of physical effort during exercise, with important implications for different sporting activities [289], [290]. However, although f_R results in a strong indicator of serious events, its measurement has been often considered negligible [291] or not recorded routinely, even when the patient's primary problem is a respiratory condition [292] [293] due to the lack of a reliable automated f_R monitor system contributes.

Not only f_R but also V_T is a crucial component of ventilation. The term V_T , defined as the volume of air delivered to the lungs at each inspiration, may increase under conditions that cause metabolic acidosis (e.g., abdominal pathology or sepsis) as well as any hypoxia and hypercapnia [294], [295].

Different from respiration, cardiac monitoring has always played a crucial role in the clinical scenario. According to the WHO, cardiovascular diseases are the principal cause of death globally, taking an estimated 17,9 million lives each year [296]. Thus, many technologies have been proposed for providing information about heart health and supporting clinical decision-making. Among several cardiac parameters, HR is the most frequently measured since its changes are directly associated with pathological abnormalities (e.g., cardiovascular diseases and cardio-metabolic factors) as well as behavioral factors and lifestyles (e.g., diet and physical exercises) [297]. The HR is the number of times the heart beats per minute (often expressed as bpm or $\text{beat}\cdot\text{min}^{-1}$), and its reliable monitoring made this vital sign one of the most popular also for fitness and sport application. Indeed, it is considered an important indicator of the state of an athlete's body during physical activity [297].

Another specific variable derived from HR is the HR variability (HRV). The HRV is defined as the physiological variation in the duration of intervals between sinus beats and serves as a measurable indicator of cardiovascular integrity and prognosis [298] [299], [300].

In the following subsections, two different methods for monitoring respiratory and cardiac activities based on FBGs are proposed:

1. The mechanical coupling between the chest and the FBG sensor for monitoring both respiratory and cardiac parameters.
2. Thermo-hygrometric exchanges between the human body and the surrounding atmospheric environment (i.e., the breathing zone) where the FBG is located for monitoring respiratory parameters.

3.1.2 The mechanical coupling between wearables based on FBGs and chest

The description of the wearable systems for monitoring respiratory and cardiac activity based on the mechanical coupling between the measuring systems and the chest starts with the description of the physiological sources of the signals collected by the proposed sensing solutions. Then, the model of the chest wall displacements associated with these physiological sources and the principles of work of the proposed FBG-based sensing solutions designed for these aims are presented.

3.1.2.1 Physiology

Exchanging the air inside the lungs as well as pumping blood through the vascular system are physiological mechanical functions achieved by organs (i.e., lungs and heart) deformation, and fluid (e.g., blood) displacement [285].

The process in which air moves in and out of the lungs is known as breathing. The breathing mechanism involves two processes: inspiration and expiration. During the inspiration, there is a contraction of muscles attached to the ribs on the outer side, which pulls out the ribs and results in the expansion of the chest cavity. Then, the diaphragm contracts, moves downwards, and expands the chest cavity resulting in the contraction of the abdominal muscles. During the expiration, muscles attached to the ribs contract, the muscles of the diaphragm and the abdomen relax, which leads to a decrease in the volume of the chest cavity and increases the P of the lungs, causing the air in the lungs to be pushed out through the nose [301].

Pumping blood through the cardiocirculatory system is the primary function of the heart beating. This pumping activity needs rhythm generators (the sinoatrial node) to produce the

electrical sequence of depolarization and repolarization carried by conductive pathways (e.g., the atrioventricular node, the bundle of His, the right and left bundle branches, Purkinje fibers) toward contractile cells (myocardium). When the electrical signal of a depolarization reaches the contractile cells, they contract; when the repolarization signal reaches the myocardial cells, they relax. Synchronized contraction of the myocardium generates P to drive the blood flow in arteries to distal organs, and the constant repetitive pumping action maintains the circulation to all organs [302].

The results of these two mechanical activities can be subcategorized into: *i*) deformations of the chest wall during the respiratory cycles and *ii*) displacements and vibrations caused by the heart beating and the pulse wave traveling through the body. These contributions are different: the one of breathing is macroscopic and thus, easily detectable by using sensors sensitive to ϵ and in contact to the chest; the contribution of the heart beating is microscopic and masked by the respiratory one because of its smaller amplitude. Moreover, although faster, the signal induced by the heart beating to the chest surface spectrally overlaps with the higher respiratory harmonics (3rd or 4th harmonics [17]), making very challenging the separation of the cardiac components from the dominant respiratory harmonics.

The detection of chest wall displacements due to breathing was extensively investigated, and several contact-based techniques have been proposed over the years. A deeper description of these wearable technologies was proposed in [288], where also FBGs are presented as an alternative to common electrical and mechanical ϵ sensors. Their short response time (approximately 10 ms) and high S_ϵ (typically 1-1.2 pm/ $\mu\epsilon$) allow easy monitoring of chest wall deformations (with an amplitude of 4 mm to 12 mm and a frequency range of 0.2 Hz – 0.34 Hz in normal activity) by positioning a sensor on the thorax or the abdomen.

The detection of the cardiac mechanical activity was performed as early as the turn of the 20th century [8] using two main approaches [303]: *i*) the measurement of whole-body recoil forces in response to cardiac ejection, usually termed BCG signal [304]; and *ii*) the local chest surface measurement of cardiac-induced vibrations, typically referred to as SCG signal [305]. These vibrations are usually measured in the form of accelerations by using accelerometers and gyroscopes on the body, while the use of strain sensors as FBGs for BCG/SCG monitoring is often limited to devices installation on bed mattresses and chair supports [243] [218]. The recent development of FBG-based smart garments for cardiorespiratory monitoring has led to a growing interest in the measurement of SCG signals aiming at improving its reliability and clinical use. A typical SCG signal along with the corresponding ECG signal on a window of 10 s

is shown together with ensemble-averaged SCG and ECG in Fig. 3:1. The peaks in the SCG signal correspond to the opening and closing of the aortic (AO/AC) and mitral (MO/MC) valve, while the IM point occurs during the period of rapid change in ventricular P. The intervals PEP, LVET, and QS2 illustrated in Fig 3:1 are: pre-ejection period, left ventricular ejection time, and electro-mechanical systole. Any deviation of these intervals can correspond to an abnormality of the heart function. For instance, increased PEP and decreased LVET are visible in heart failure patients compared to healthy subjects.

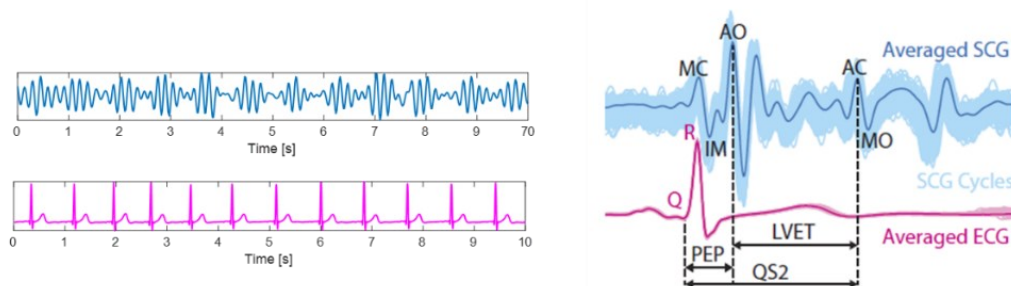


FIGURE 3:1. A 10s-lasting window of typical BCG (blue) and ECG (magenta) signals on the left. A zoom on a single heart beating-related mechanical and electrical on the right with fiducial points. As evident, the electrical cardiac activity (e.g., systole) triggers the mechanical one (aortic valve opening) as the systolic complex with the R-peak in ECG signal is followed by the AO peak in BCG.

Unfortunately, both BCG and SCG failed to prove their feasibility, and some limitations are still dampening their spread in clinical evaluations. The main issues related to their use are:

- A lack of standard measurement methods: various methods in several locations detect slightly different signals. In Fig. 3:2, the sensors' location distribution proposed in [306] is shown. A widely used placement has been on the sternum or its left lower border. Other locations include the heart apex (lateral left lower chest) and the aortic valve listening area at the right upper sternal border.

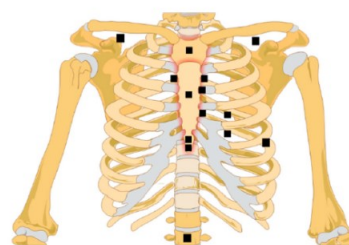


FIGURE 3:2. Sensors location on the chest [306].

- A lack in understanding the exact physiologic origin of the BCG/SCG waveforms;

- Insufficient clear guidelines for the interpretation of results;
- Clinical diagnosis of myocardial infarction, angina pectoris, and coronary heart disease required a high level of specificity and reliability that the BCG and SCG had not reached yet;
- A large inter-subject variability, mainly due to the limited tools available at that time for signals analysis;

3.1.2.2 Model

To better describe the chest wall displacements detectable by strain sensors in contact with the chest surface, the model in [307] is summarized.

The chest wall displacement $x(t)$ may be described as a sum of the displacement due to breathing $x_b(t)$ and the much smaller ones caused by the heartbeat $x_h(t)$.

$$x(t) = x_b(t) + x_h(t)$$

Equation 3:1

Each component can be modeled as follows:

- the displacement due to breathing $x_b(t)$ as the lowpass filtered periodic sequence of quadratic inspiration and exponential expiration waveforms $w(t)$, expressed as:

$$w(t) = \begin{cases} \frac{-K_b}{T_I T_E} + \frac{K_b T_R}{T_I T_E} t; & t \in [0, T_I] \\ \frac{K_b}{1 - e^{-\frac{T_E}{\tau}}} t^2 (e^{-\frac{-(t-T_E)}{\tau}} - e^{-\frac{-T_E}{\tau}}); & t \in [T_I, T] \end{cases}$$

Equation 3:2

Where K_b is the model constant used for adjusting the breathing displacement amplitude, T_I is the inspiration period, T_E is the expiration period, and T_R is the respiratory period ($T_R = T_I + T_E$), whereas τ is the time constant.

The $x_b(t)$ signal has an amplitude ranging from 4 mm to 12 mm with a frequency range of 0.2 Hz – 0.34 Hz in normal activity [308].

- Regarding $x_h(t)$, several models have been proposed in the literature. The first ones modeled this displacement as a sine wave [309], half-cycle sine pulses [310], and Gaussian pulse train [311]. However, although the cardiac displacement due to the heart beating is characterized by a pulsatile nature, the related waveform is more complex. Several mechanical contributions caused by two main electrical events: the ventricular depolarization (QRS complex in the ECG) and the ventricular repolarization (T wave in the ECG) should be considered. Therefore, a single heartbeat displacement $x_{hs}(t)$ is modeled by two distinct pulses as

$$x_{hs}(t) = \eta \cos(\omega t + \gamma \sin(\Omega t)) e^{-\frac{(t-b)^2}{c}}$$

Equation 3:3

Where b , c , η , ω , γ , and Ω are constant parameters. The total displacement $x_h(t)$ can be expressed as:

$$x_h(t) = \sum_{i=1}^{N_{BBI}} x_{hs} \left(t - \sum_{j=1}^i t_{BB}[j] \right)$$

Equation 3:4

where $t_{BB}[j]$ is the j -th beat-to-beat interval.

These motions are faster and weaker than the ones due to breathing. To better quantify, the heart-induced vibrations $x_h(t)$ have an amplitude ranging from 0.2 mm – 0.5 mm and frequency from 1 Hz – 1.34 Hz (i.e., from 60 bpm to 80 bpm) in quiet conditions [308].

An example of simulated chest wall displacements $x(t)$ considering both the contributions are shown in Fig 3:3 with a zoom on a single breathing displacement $x_{bs}(t)$ and a single heartbeat displacement $x_{hs}(t)$. Usually, to better analyze and discriminate these contributions low, high and/or bandpass filters are applied on the raw signals $x(t)$.

Generally, the respiratory component is located in a frequency range of less than 0.5 Hz; thus, Butterworth lowpass filters with cut-off frequency of 0.5 Hz are applied [312]. Regarding the descriptions of the cardiac component, a deeper consideration should be made. SCG signal details two main frequency domains. Measurements of frequency components from 0.6 Hz to 20 Hz are related to vibrations induced by the blood flow ejection into the vascular bed can be used to identify heart malfunctioning [312]. The second frequency domain from 20 Hz up to 2 kHz is mainly used in investigations of positional and shape changes of the heart and intracardiac events such as the closure of the mitral and tricuspid valves, which can produce

frequencies up to 200 Hz [312]. Thus, several filters have been used in the literature, but the most used has been the Butterworth bandpass filter with a lower cut-off frequency of 0.6 Hz or 1 Hz and a higher cut-off frequency of 10 Hz, 15 Hz, 20 Hz, or 25 Hz [313]. Once filtered, the processed signal relates to peaks and valleys on the SCG and can be used for cardiac investigation.

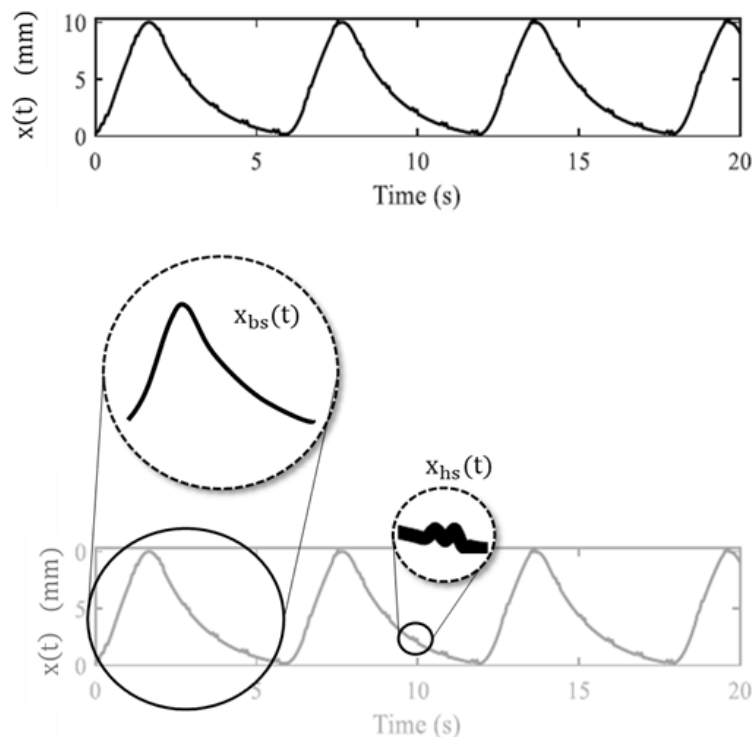


FIGURE 3.3. The modeled chest wall contributions with a zoom on a single breath and a single heartbeat displacement.

3.1.2.3 FBG-based wearables for cardiorespiratory monitoring by chest displacement: working principles

As described in Chapter 2, FBGs are intrinsically sensitive to ϵ . This feature can be exploited to develop wearables where good adhesion and compliance between the sensor and the chest surface must be achieved to detect the chest wall displacement and in turn, its deformation.

Focusing on the respiratory activities, when the subject inhales, the diaphragm contracts, and the stomach inflates, the sensor that is positioned in contact with the chest is strained.

Conversely, during the exhalation, when the diaphragm expands, and the stomach depresses, the sensor is compressed.

According to the model previously described, the displacement related to the respiratory activities are not the only ones detectable on the chest, but many events originated by the cardiac mechanical activity such as the cardiac valves opening and closing, isovolumic contraction, cardiac filling, and blood injections induce vibrations/displacements onto the chest surface.

All these respiratory and cardiac activities are detected by the FBGs in terms of $\Delta\lambda_B$ over time, exploiting the FBGs intrinsic S_ϵ and their short response times. As described in Chapter 2, an FBG works as a strain and temperature sensor; thus a variation of ϵ and T affects both Λ and η_{eff} resulting in a $\Delta\lambda_B$ [52] following Eq 2:2.

For improving the adhesion to the skin/garments and the mechanical coupling between the FBG sensor and the chest, flexible polymeric matrices have been often used to encapsulate the grating [314]–[316]. When the FBG is housed in the matrix, its ϵ and thermal sensitivities are largely influenced by the polymer's elastic and thermal properties, much thicker than the silica fiber. Hence, changes in the constitutive characteristics of the casing material and in bonding strength at the fiber-matrix interface are the main influencing factors.

To optimize the S_ϵ , silicones are often used as polymer matrices since they shield the gratings from environmental perturbations resulting in negligible influences of ΔT , ΔRH , and sweater on the FBG output [52].

In Fig. 3:4, an example of FBG-based flexible sensor in a soft dumbbell-shaped matrix is proposed.

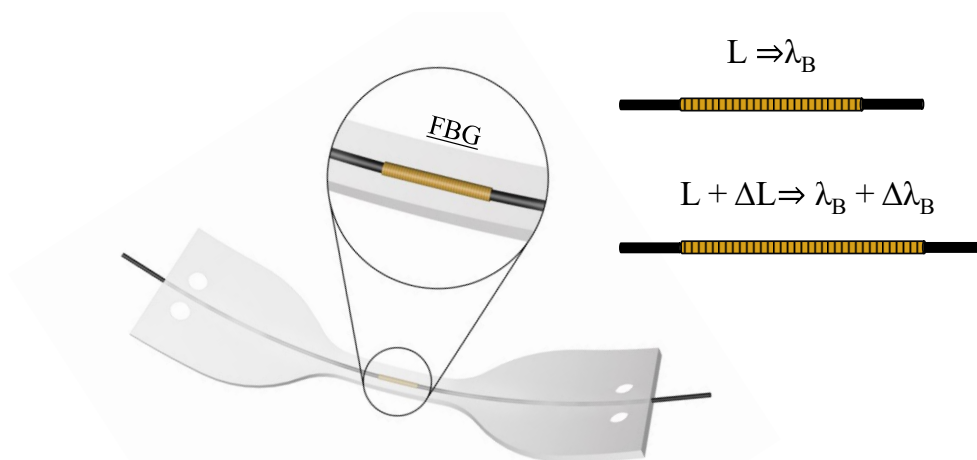


FIGURE 3:4, A dumbbell-shaped flexible sensor with a zoom on the FBG sensor inside. During inspiration, the chest wall expansion causes a displacement on the matrix resulting in a grating ϵ and in turn, in a positive shift of $\Delta\lambda_B$.

Typically, in these applications, FBG mainly works as a strain sensor, and the $\Delta\lambda_B$ caused by chest wall displacements during breathing and cardiac activity may be described as the sum of two contributions:

$$\Delta\lambda_B(t) = \Delta\lambda_B^b(t) + \Delta\lambda_B^h(t)$$

Equation 3:5

with $\Delta\lambda_B^b(t)$ the contribution related to the ε induced by the breathing and $\Delta\lambda_B^h(t)$, the one related to the heart activity.

A typical $\Delta\lambda_B(t)$ detected by a strain sensor based on FBG and placed on the chest surface is shown in Fig 3:5. It is evident the influences of both the activity and the similarities in the pattern already showed in Fig 3:3.

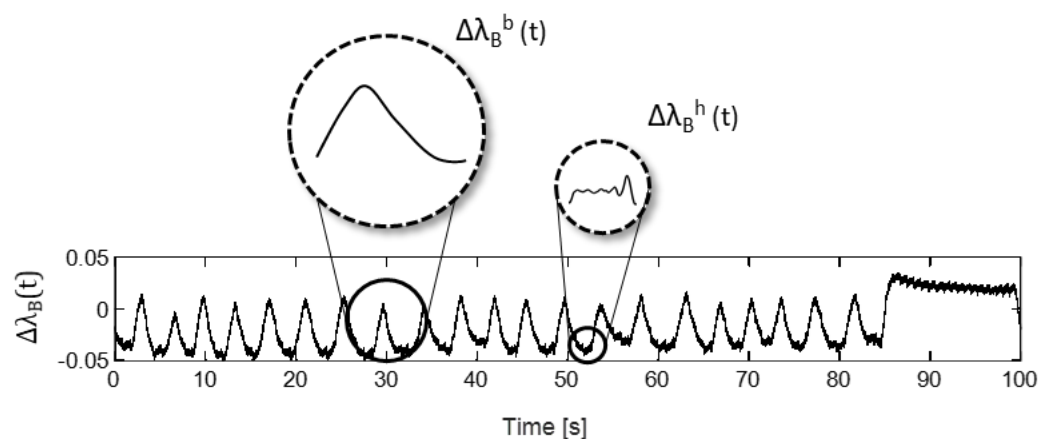


FIGURE 3:5. A typical FBG output during cardiorespiratory activity. The $\Delta\lambda_B$ vs. time of single respiratory and cardiac contribution is highlighted.

3.1.3 Thermo-hygrometric conditions of respiratory gases

Before starting with the description of studies based on this approach, the description of the air exchange processes in breathing is provided. In particular, the physiology behind the generation of breathing airflow is proposed, focusing on the heat and moisture exchanges that occurred during inspiration and expiration in the breathing zone.

3.1.3.1 Physiology

Extra-thoracic airways (nasal passages, mouth-throat, larynx, pharynx) are the gateway of the respiratory system as inhaled and exhaled air passes through the nose or the mouth [317]. During normal breathing, the extra-thoracic airways implement several mechanisms for respiratory heat and transfer and water vapor exchanges. As air is inspired, it is heated and humidified, resulting in cooling and drying of the mucosa. A healthy person reaches that equilibrium during nasal breathing at the bifurcation of the trachea. Therefore, the air which reaches the alveoli is at body T ($\sim 37^{\circ}\text{C}$) and fully saturated with water vapor (RH $\sim 100\%$). During exhalation, the expiratory airflow passes over the cooler upper airway mucosa, and this cooling effect causes a regain of heat energy by the mucosa together with the condensation of a portion of moisture in the air coming from the lungs (at RH = 100% T = 37°C) on the mucous membranes, whereby the mucous membranes are moisturized again [317], [318] (see Fig. 3:6).

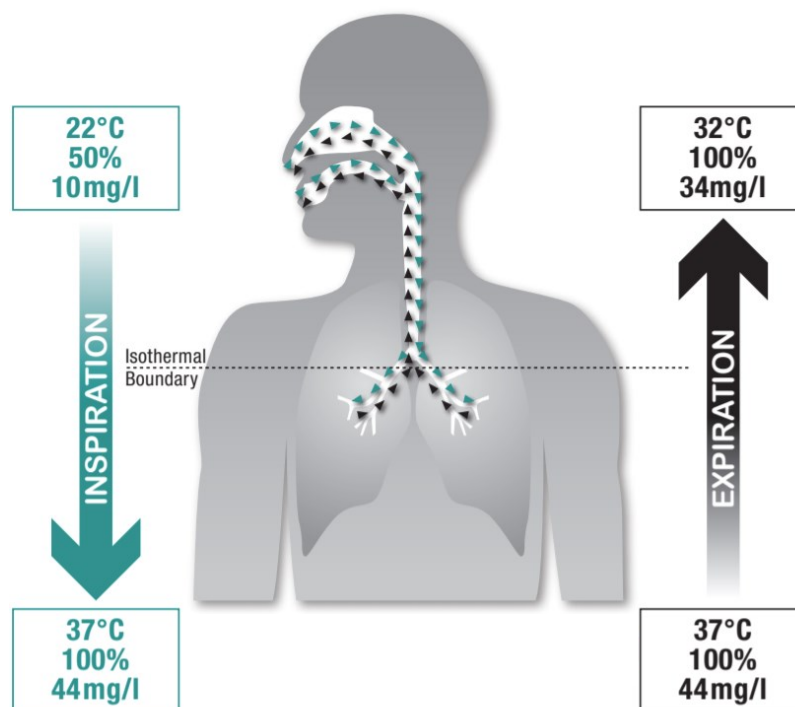


FIGURE 3:6. Thermo-hygrometric exchanges during inspiration and expiration [319].

Expired air reaches the nares at $\sim 32^{\circ}\text{C}$ and the net content of water loss is affected by the surrounding environment: the cooler the ambient air, the more moisture is reclaimed by the process of condensation as shown in Fig. 3:7.

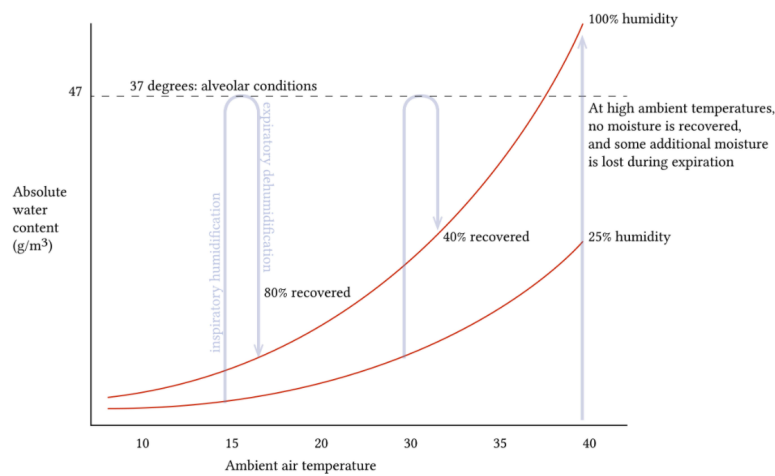


FIGURE 3:7. A simplified psychrometric chart [318].

Thus, the measurement of ΔRH may be useful for investigations on respiratory activity using sensors not in contact with the chest but worn close to the nose/mouth in the breathing zone.

3.1.3.2 Model

The human upper airway's airflow structure is quite complicated, and the flow ranges from laminar to turbulent. In this section, a simple model of the nasal airflow is proposed considering that in a healthy person, 75% of respiratory gas conditioning takes place in the nasopharynx. The remaining part is taken over by the trachea.

The governing equations of the model of flow in the nasal cavity are described in [320] and consist of: the equation of conservation of mass (Eq. 3:6), momentum (Eq. 3:7), transport equation of energy (Eq. 3:8), and transport equation of the mass fraction of water (Eq. 3:9) under the assumptions of laminar airflow:

$$\nabla \cdot u = 0$$

Equation 3:6

$$\rho \left(\frac{\partial u}{\partial t} + u \cdot \nabla \right) u = -\nabla P + \mu \nabla^2 u$$

Equation 3:7

$$\rho C_p \left[\frac{\partial T}{\partial t} + (u \cdot \nabla) T \right] = \frac{k}{P C_p} \nabla^2 T$$

Equation 3:8

$$\frac{\partial MF}{\partial t} + (u \cdot \nabla)MF = D\nabla^2 MF$$

Equation 3:9

Here t , u , P , K , T , and MF denote time, velocity, pressure, temperature, and mass fraction of water vapor, respectively. Material properties ρ , μ , C_p , K , and D are density, viscosity, specific heat, thermal conductivity, and the mass diffusion coefficient, respectively [321].

To incorporate the T and humidity adjustment performed by the nasal cavity functions, appropriate boundary conditions should be introduced to represent the heat and water exchanges occurring at the nasal cavity wall for solving the transport equations of energy (Eq. 3:8) and mass fraction of water (Eq. 3:9) [322].

The nasal cavity wall has a layered structure consisting of a mucous membrane and a capillary layer consisting of capillaries located on the organ side (see Fig. 3:8). The inhaled air's T and humidity are adjusted by heat and water exchanges between the organ side and the air side via the mucous membrane.



FIGURE 3:8 Structure of nasal cavity wall [322]

To determine the heat flux from the organ to the airflow, the following equation is proposed

$$Q_{memb} = K_{memb} \frac{\partial T}{\partial n} = K_{memb} \frac{T_0 - T_s}{\delta_{memb}}$$

Equation 3:10

With T_0 the temperature of the organ side (constant because the organ is provided with sufficient heat by the capillary layer), T_s the temperature of the membrane surface (not constant), Q_{memb} (red arrow in Fig 3:9) represents the heat flux from the organ to the air via the membrane, K_{memb} and n denote the thermal conductivity of the membrane and the normal

vector of the nasal cavity wall surface. If $T_0 > T_s$, Q_{memb} is transmitted into the air side from the organ, otherwise from the air to the organ side, and the inhaled air is cooled.

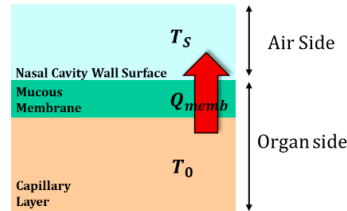


FIGURE 3:9. Model of heat exchange on nasal cavity wall [322].

Regarding the computation of the mass fraction of water F in Eq 3:9, a two-film theory is used to model the water exchange between organ and air sides. This theory describes water transport between the nasal mucus layer (liquid phase) and inhaled air (gas phase) via a thin film constituted of the membrane layer and an additional layer called the boundary layer next to the nasal cavity wall surface on the air side (Fig. 3:10).

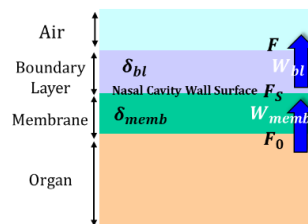


FIGURE 3:10. Model of water exchange using bilayer film theory [322].

The governing equation of the water fluxes between the organ side and the boundary layer via the membrane (W_{memb}) and the water flux between the membrane and the air side via the boundary layer (W_{bl}) are the following.

$$W_{memb} = D_{memb} \frac{\partial F}{\partial n} = D_{memb} \frac{F_0 - F_s}{\delta_{memb}}$$

Equation 3:11

$$W_{bl} = D_{bl} \frac{\partial MF}{\partial n} = D_{bl} \frac{MF_0 - MF_s}{\delta_{bl}}$$

Equation 3:12

where MF_0 is the vapor mass fraction on the organ and mucous membrane side, which is a constant value because the mucous membrane is supplied with sufficient water by the capillary layer; MF_s is the vapor mass fraction on the surface of nasal cavity wall; MF is the vapor

mass fraction on the air side; D_{bl} and D_{memb} are the mass diffusion coefficient of boundary layer and mucous membrane respectively [321] [323], δ_{bl} and δ_{memb} are the thickness of boundary layer and mucous membrane layer [324].

Moreover, this theory assumes that the fluxes in both layers should be equal because the species transported to the gas phase from the liquid phase pass through the two layers:

$$W_{memb} = W_{bl}$$

Equation 3:13

By solving all these equations, the species mass fraction on the nasal cavity is:

$$MF_S = \frac{(D_{memb}/\delta_{memb}) MF_0 + (D_{bl}/\delta_{bl}) MF}{D_{memb}/\delta_{memb} + D_{bl}/\delta_{bl}}$$

Equation 3:14

Starting from this model, several studies in the literature investigated thermohydrimetric exchanges in the so-called breathing zone for monitoring respiratory activity and breathing patterns. Such a zone is the micro-environment close to the nose and mouth where a stream of inspired particles from the ambient to the nasal/oral cavity and of the expired ones from the human body to the ambient takes place. Hence, a sensor worn in the proximity of the nasal/oral cavity is reached by gases at different thermohydrimetric conditions ranging repetitively from environmental T and moisture values to $\sim 37^\circ\text{C}$ and 100% of RH. These differences between the inspired airflow and the one already expired can be detected by wearable sensors located in the breathing zone in order to perform respiratory monitoring.

3.1.3.3 FBG-based wearables for respiratory monitoring from thermohydrimetric conditions of respiratory gases: working principle

The main solutions for detecting changes in T and RH in the respiratory flow based on FBGs exploit hygroscopic materials as active coatings to functionalize the gratings [239]. As described in Chapter 2, synthetic (e.g., PVA, PMMA) and natural polymers (e.g., Agar, Agarose, and Chitosan) have been proposed in the literature [325].

When a hygroscopic material coats the grating, its volumetric expansion due to the trapping of water vapor droplets into the coating matrix causes changes in Λ_B ($\Delta\Lambda_B$) and η_{eff} and, in turn, $\Delta\lambda_B$. Thus, Eq. 2:2 is modified as follows [326]:

$$\frac{\Delta\lambda_B}{\lambda_B} = (1 - p_e) \cdot \varepsilon_{RH} + (1 - p_e) \cdot \varepsilon_T + \alpha_n \cdot \Delta T$$

Equation 3:15

With ε_{RH} , the strain induced by the RH changes (ΔRH) and ε_T , the strain induced by ΔT .

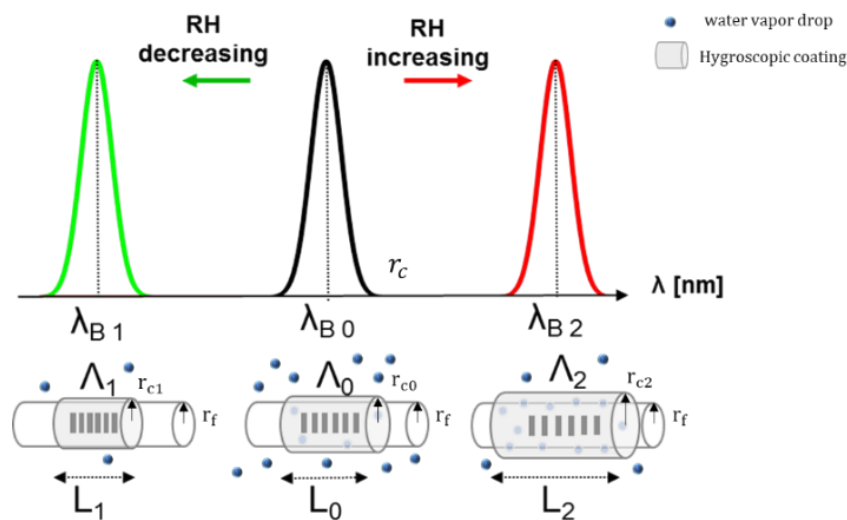


FIGURE 3:11. The working principle of a functionalized FBG sensor during coating swelling and deswelling. A volumetric expansion of the coating causes a positive $\Delta\lambda_B$, otherwise a shrinkage a negative $\Delta\lambda_B$.

The FBG principle of work, when exposed to RH changes, is shown in Fig. 3:11. During the water absorption, the hygroscopic material (coating radius of r_{c0}) surrounding the fiber (fiber radius r_f) swells; thus, the coating radius increases ($r_{c2} > r_{c0}$). Otherwise, during the water desorption, the coating deswells, and its radius decreases, $r_{c1} < r_{c0}$.

Two models can be used for describing the static and dynamic behavior of a functionalized FBG.

In a first analysis, the coated FBG can be modeled by neglecting the radial ε and using a 1D theoretical model of an infinitely long rod made of two materials with a perfect adherence: the hygroscopic material and the fiber glass [326].

At the equilibrium, the stresses induced by these materials on the axial direction must be balanced, and the axial elongation must be the same:

$$\sigma_c A_c = \sigma_f A_f; \Delta L_c = \Delta L_f$$

Equation 3:16

With σ_c and σ_f , the stresses, and ΔL_c and ΔL_f the axial elongations, induced on coating (cross-section area A_c) and fiber (cross-section area A_f), respectively. Assuming the behavior of fiber and coating linear, isotropic, and elastic, the generic σ - ε relationship is:

$$\varepsilon_c = \frac{\sigma_c}{E_c}; \varepsilon_f = \frac{\sigma_f}{E_f}$$

Equation 3:17

Where ε_c and ε_f are the axial strains induced on coating (Young modulus E_c) and fiber (Young modulus E_f), respectively.

Assuming linear relationships both $\Delta\lambda_B$ - ΔRH and $\Delta\lambda_B$ - ΔT [327], the FBG sensitivity can be split into two components:

$$\frac{\Delta\lambda_B}{\lambda_B} = S_{RH} \cdot \Delta RH + S_T \cdot \Delta T$$

Equation 3:18

Where S_{RH} and S_T are the humidity and thermal sensitivity coefficients, respectively. Considering all the assumptions above, these coefficients can be expressed as:

$$S_{RH} = (1 - p_e) \cdot \left(\frac{A_c E_c}{A_c E_c + A_f E_f} \right) \cdot (\beta_c - \beta_f)$$

Equation 3:19

$$S_T = (1 - p_e) \cdot \left[\alpha_f + \left(\frac{A_c E_c}{A_c E_c + A_f E_f} \right) \cdot (\alpha_c - \alpha_f) \right] + \alpha_n$$

Equation 3:20

Where β_c and α_c are the hygroscopic and thermal expansion coefficients of coating and β_f and α_f are the hygroscopic and thermal expansion coefficients of the fiber. As the glass does not

absorb water β_f can be assumed zero [326]. Moreover, if the T contribution can be considered negligible, the FBG behavior and the S_{RH} coefficient may be expressed as follows:

$$\frac{\Delta\lambda_B}{\lambda_B} = S_{RH} \cdot \Delta RH \rightarrow S_{RH} = (1 - p_e) \cdot \left(\frac{A_c E_c}{A_c E_c + A_f E_f} \right) \cdot \beta_c$$

Equation 3:21

As expected, S_{RH} increases according to both geometrical and mechanical properties. In the literature, the FBG sensitivity to RH is expressed in two different ways: in term of S_{RH} [%⁻¹] as shown in Eq 3:21 and in term of K_{RH} [nm·%⁻¹] as shown in Eq. 3:22:

$$\Delta\lambda_B = K_{RH} \cdot \Delta RH$$

Equation 3:22

Regarding the transient analysis and dynamic characteristics of a coated FBG, the bilayer model is presented. Considering the mass transfer inside a coating modeled by a bilayer (i.e., the surface and the inner layers of coating), two response times are considered: the fast response time τ_f , which describes the surface layer response to RH step change, and the slow response time τ_s which is the inner layer response time [328]. The constant τ_f is faster than τ_s because it is the first layer that the water vapor reaches during the absorption process (see Fig. 3:12).

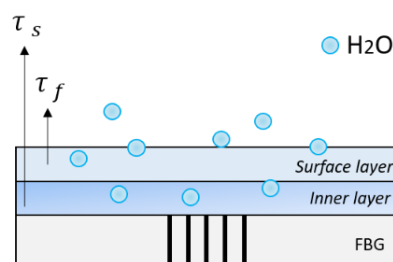


FIGURE 3:12 The bilayer model of an active coating.

Following this model, the layers response to a step change can be described by using the sum of two exponential functions, as reported in Eq 3:23:

$$\Delta\lambda_B^{norm} = 1 - (w_f \cdot e^{-t/\tau_f} + w_s \cdot e^{-t/\tau_s})$$

Equation 3:23

Where w_f and w_s represent the weights of the surface and the inner layers, respectively. The absorption process is influenced by the coating radius [329]. In particular, the bigger the radius, the longer the time constants. At the same time, the polymer concentration wt% influences the coating porosity, which decreases with wt%. As a consequence, the higher wt%, the longer the time constants [330].

A global response time may also be evaluated to describe the system's step response as the time needed to reach a specific value (usually τ_{63} , which is the time required for a first-order system to achieve 63.2% of the step change magnitude).

A typical example of the output changes of a functionalized FBG sensor for RH measurement, when placed in the breathing zone close to the nostrils, is shown in Fig. 3:13. A comparison with the chest wall volume changes is proposed to underline that the FBG output trend is the opposite of the ones of the chest volume. Indeed, during expiration, the chest volume is reduced while the exhaled airflow hits the sensor at higher T and RH. Otherwise, during inspiration, when the chest expands itself, the inspired air is at ambient conditions; thus, a flow at ambient T and RH moves from the environment to the body.

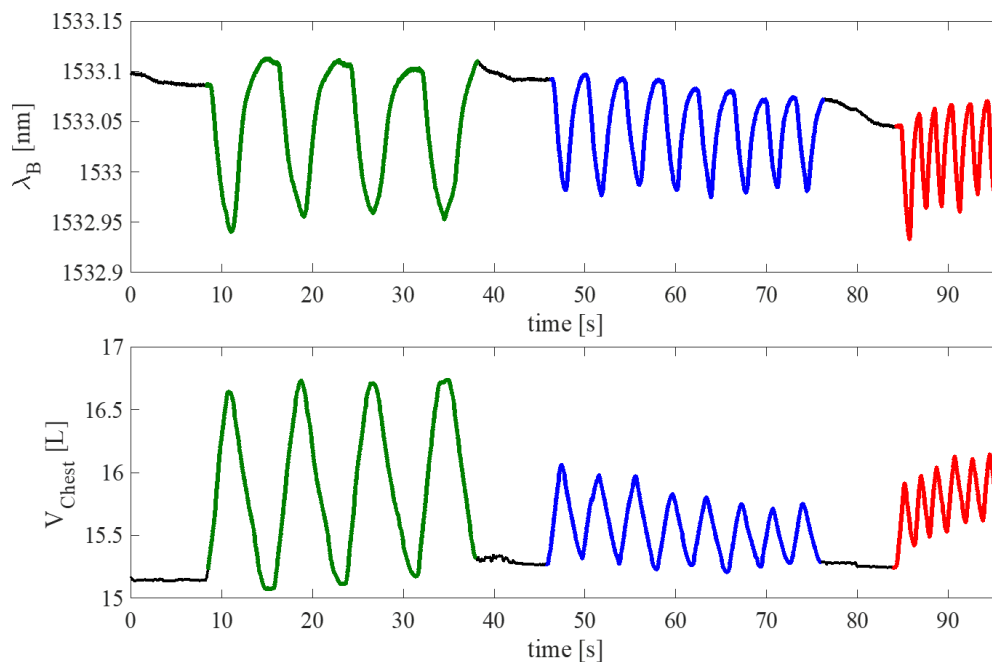


FIGURE 3:13. A typical trend in time of a functionalized wearable FBG sensor in the breathing zone together with the chest volumes. As evident, an opposite trend is shown between the two signals: during expiration, the chest volume (V_{chest}) on the bottom reduces while RH and T increase. Otherwise, λ_B on the top, increases; during inspiration, the chest volume increases, and RH and T are at ambient conditions. Otherwise, λ_B on the top decreases. Three different airflow velocities are underlined by green, blue, and red color lines.

3.2 Wearables for joint motions detection

3.2.1 The importance of detecting articular joints movements

Human motion monitoring has gained attention in many research and clinical areas, such as medicine, ergonomics, and sports. Through this analysis, the deviations from normal movement in terms of the altered kinematic, kinetic, or patterns can be identified and used to evaluate neuro-musculoskeletal conditions, establish optimized treatment planning, and assess the efficacy of rehabilitation programs for various patients [66].

A joint is a location where bones meet each other to give the skeleton stability and mobility. Three types of joints are present in the body: immovable (the fibrous joints), semi-movable (the cartilaginous joints), and freely movable (the synovial joints) [66]. Among them, the synovial ones are the key joints because they provide mobility by allowing load-bearing, low-friction, wear-resistant smooth movement between articulating bone surfaces. Each movement at a synovial joint result from the contraction or relaxation of the muscles that are attached to the bones on either side of the articulation. Movement types are generally paired, with one being the opposite of the other such as flexion/extension (F/E), left /right (L/R) and superior/inferior (S/I) rotation (R), abduction/adduction (A/A), and supination/pronation (S/P) [331].

Wearable devices that provide continuous monitoring of joint activity are gaining growing attention [332]. These devices are extremely useful in the SH framework since with aging, synovial fluid production is reduced, the cartilage wears, and the articulating bones come into direct contact, causing irregular articular surface and loss in bone density, which are commonly known as musculoskeletal damage. Worldwide, musculoskeletal disorders have become a serious threat to healthy aging. Musculoskeletal disorders are one of the major causes of work loss and early retirement, lost retirement wealth [333], and reduced productivity [334]. At the same time, wearables can enable home rehabilitation crucial for optimization planning therapies and patient outcomes. The general approach proposed in the literature for monitoring joint movements via FBG-based wearable systems is based on the mechanical coupling between the sensor and the joint under investigation [335]. Systems in the literature can be grouped into garments instrumented by flexible sensing elements and flexible sensors directly stick to the skin, as previously described in Chapter 2.

3.2.2 The mechanical coupling between wearables and joints

3.2.2.1 Physiology

Each movement at a synovial joint results from the contraction or relaxation of the muscles that are attached to the bones on either side of the articulation. During the contraction, changes in the magnitude of muscle length result in different joint angles, motions, and postures. From measuring the range of motion (ROM) of a joint, it is possible to estimate the maximum F generated by the muscle, which indicates the health condition of a joint. Similarly, joint angles, number of repetitions, and orientations at different activity levels also depict muscle strength and endurance [336]. Movement types of joints are various and generally paired (see Fig. 3:14), with one being the opposite of the other such as F/E, L/R and S/I R, A/A, and S/P. Each joint has optimal angles and ROM according to the type of movement and a physiological repetition frequency according to the activity in which the joint is involved [66],[337].

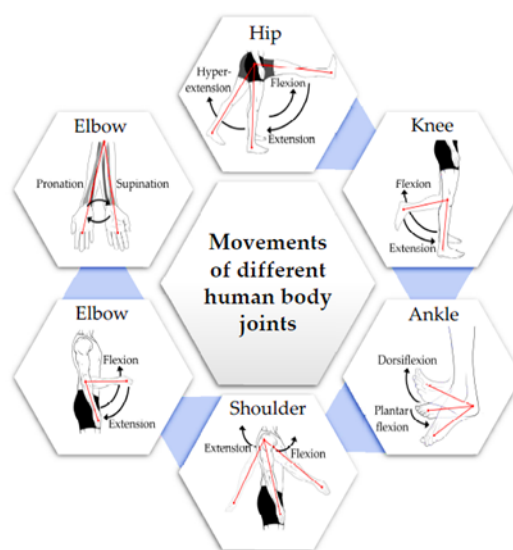


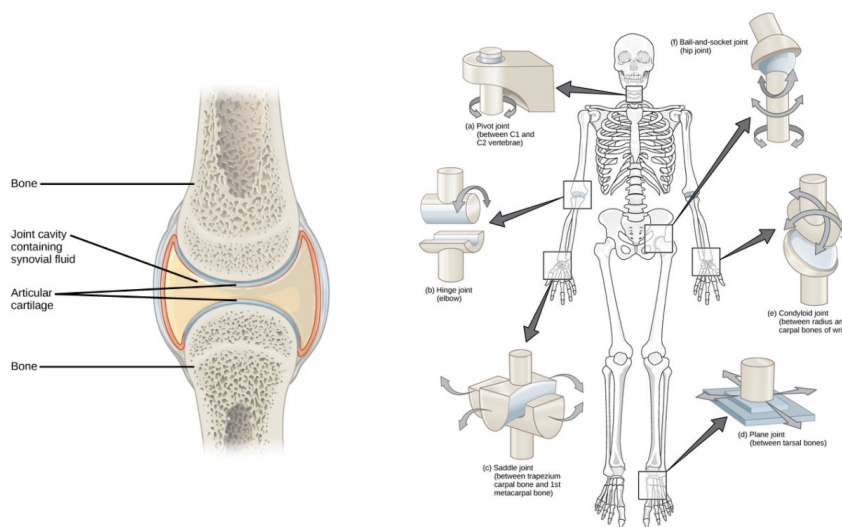
FIGURE 3:14. The body movements [337].

3.2.2.2 Model

The human body is a well-developed mechanical structure made up of more than 200 differently shaped bones, which serve as a framework of the body. All synovial joints have six degrees of freedom (DOF) in which six independent parameters must be measured and

described if the relative positions of the attached body segments are to be defined [338]. However, depending on analysis objectives and degree of accuracy requirements, simplified mechanical structures are usually adopted [338].

The simplest model of the human body considers it constituted of rigid links, connected by geometrical joints categorized by the types of movement permitted: pivot, hinge, saddle, plane, condyloid and ball-and-socket joints [339]. (see Fig 3:15)



Joint Type	Joint Movement	Examples
Pivot	Rotation of one bone around another	Top of the neck
Hinge	Flexion/Extension	Elbow/Knee/Ankle
Saddle	Flexion/Extension/Adduction/Abduction/Circumduction	Thumb
Plane	Gliding movements	Inter-carpal/Tarsal bones
Condyloid	Flexion/Extension/Adduction/Abduction/Circumduction	Wrist
Ball-and-socket	Flexion/Extension/Adduction/Abduction/Rotation	Shoulder/Hip

FIGURE 3:15. Joint types and allowed movements. Some examples are listed in the table [337].

For a description of the general planar motion of the articular surfaces, the terms sliding, spinning, and rolling are commonly used. Sliding motion is defined as the pure translation of a moving segment against the surface of a fixed segment [340]. The contact point of the moving segment does not change, while its mating surface has a continually changing contact point. If the surface of the fixed segment is flat, the instantaneous center of rotation (ICR) is located at infinity; otherwise, it will be located at the center of the curvature of the fixed surface. Spinning motion is the exact opposite of sliding motion, where the moving segment rotates, and the contact point on the fixed surface does not change. The ICR is, in this case, located at the center of the spinning body that is undergoing pure rotation. Rolling motion is a motion between moving and fixed segments where the contact points on each surface are constantly changing.

However, the arc length of the moving surface matches the path on the fixed surface so that the two surfaces have point-to-point contact without slippage. The relative motion of rolling is a combination of translation and rotation. The ICR is located at the contact point.

Most of the planar motion of anatomical joints can be described using a combination of any two of the above three basic types of motion. Still, in practice, the determination of the ICR is highly sensitive to error.

The analysis of anatomical joint kinematics commonly uses a spherical joint model. This type of joint allows 3 DOF rotation; thus, it needs three angles to specify the relative position between moving and fixed segments. Given a proper selection of axes of rotation in which one is fixed to the fixed segment and another is fixed, it is possible to make the finite rotation sequence-independent or commutative. In the knee joint, for example, the F/E angle (Φ) occurs about a mediolaterally directed axis fixed to the femoral condyle, and the angle of axial R (ψ) is measured about an axis along the shaft of the tibia (Fig. 13:3). The third axis (i.e., the floating axis) is orthogonal to them and defines the angle of A/A (ϑ).

The Eulerian angle system describes these joint motions. Indeed, if a unit vector triad (I, J, K) is fixed to the fixed segment along X, Y, Z axes and another triad (i, j, k) is fixed to the moving segment, along x, y, z axes, the relationship between them can be expressed by a rotational matrix in terms of the Eulerian angles (Φ, ψ, ϑ) in terms of sine and cosine as shown in Fig. 3:16.

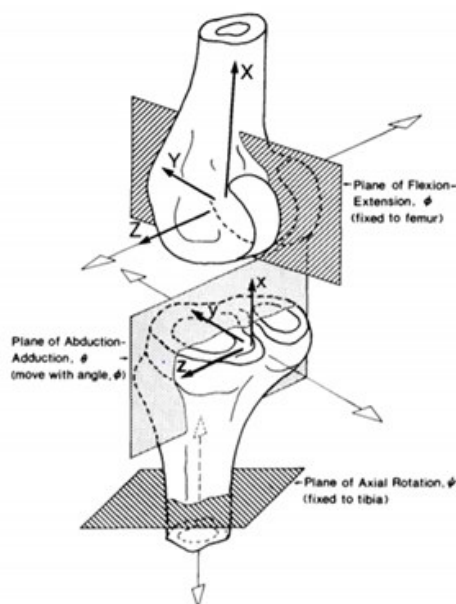


FIGURE 3:16. The planes of motions [340].

These motions are normally accompanied by the stretching of tissues such as skin and muscle. Wearables coupled to the skin strained according to the type of joint movement, and the ϵ which can occur at the skin surface are axial, bending, shear, and torsional. The sensor location should be carefully evaluated to guarantee comparable measurements and optimize the sensor's capability in detecting joint movement. Strain sensors can only measure the amount of stretch on the opposite sides of the joint in the case of rotation or along the bending curvature in the case of F/E [341] [342].

$$\begin{bmatrix} \frac{I}{J} \\ \frac{J}{K} \\ \frac{K}{L} \end{bmatrix} = \begin{bmatrix} c\phi c\vartheta & s\phi c\vartheta & -s\vartheta \\ -s\phi c\psi + c\phi s\vartheta s\psi & c\phi c\psi + s\phi s\vartheta s\psi & c\vartheta s\psi \\ s\phi s\psi + c\psi s\vartheta c\psi & -c\phi s\psi + s\psi s\vartheta c\psi & c\vartheta c\psi \end{bmatrix} \begin{bmatrix} \frac{I}{J} \\ \frac{J}{K} \\ \frac{K}{L} \end{bmatrix}$$

Equation 3:24

By way of example, during the tibial on femoral F/E, the most common ϵ that occurred on the skin surface are the axial and bending ones. In the case of small ROM, the displacement ΔL between two generic aligned points belonging to the same circumference on the sagittal plane may be described by the following relationship:

$$\Delta L = r \cdot \alpha$$

Equation 3:25

With r the circumference radius and α the angle on the sagittal plane (see Fig. 3:17).

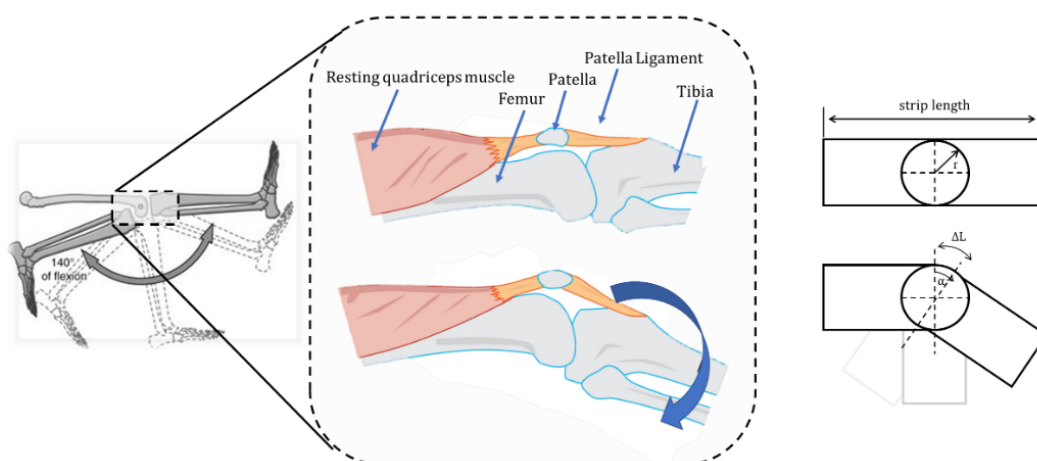


FIGURE 3:17. Model of tibial on femoral F/E motion.

3.2.2.3 FBG-based wearables for monitoring joint movements: working principles

During joint movements, several types of ε may occur on the sensing element in contact with the skin: axial, bending, shear, and torsional ε . The proposed FBG-based systems consist of gratings encapsulated into flexible polymeric matrices and have been commonly designed to be axially strained and bent. The axial ε occurs when the flexible matrix is stretched or compressed by a linear F in the horizontal direction due to the joint movement. Bending ε occurs when the matrix is stretched on one side and compressed on the opposite side due to the linear F applied in the vertical direction when the joint moves [94],[335].

The FBG principle of work in this scenario is similar to the one described for detecting chest wall displacement due to breathing and cardiac activity. Still, in this case, the input which causes $\Delta\lambda_B$ is often the bending due to the joint movement. Assuming no negligible shears between the sensor and the garments/skin and environmental perturbations in terms of T and RH , the $\Delta\lambda_B$ vs. ε relationship is the following:

$$\Delta\lambda_B = S_\varepsilon \varepsilon$$

Equation 3:26

The ε -induced on the FBG is defined by a beam bending theory, in which the ε is proportional to the curvature of bending (C) and also to the distance offset (d_o) of the optical fiber from the system neutral axis:

$$\varepsilon = C \cdot d_o$$

Equation 3:27

When the sensor is encapsulated into a flexible matrix, an offset d_o from the neutral axis may be present according to the deepness of the fiber within the polymer. This distance d_o may be expressed in function of the thickness of the polymeric matrix (ht) and the distance of the fiber from the upper surface (t_1) (see Fig. 3:18):

$$d_o = t_1 - t/2$$

Equation 3:28

C is not a value we can designate, but an external factor that can be estimated by measuring the $\Delta\lambda_B$ from the previous two equations as follows:

$$C = \frac{1}{d_o(1 - p_e)} \frac{\Delta\lambda_B}{\lambda_B}$$

Equation 3:29

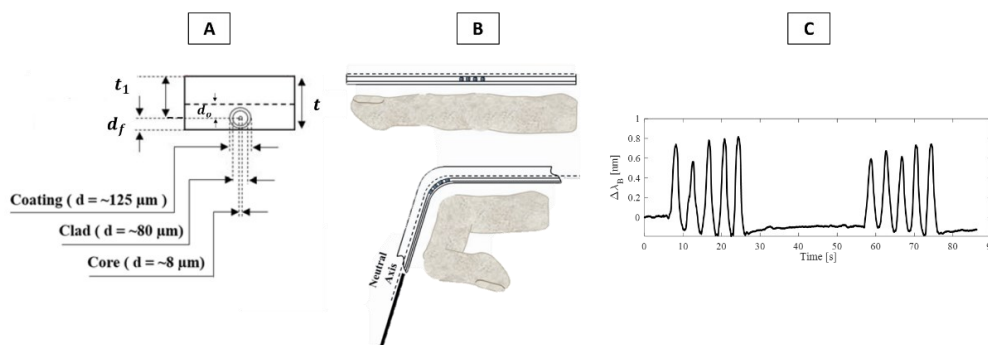


FIGURE 3:18. (A) The transverse section of an FBG-encapsulated flexible sensor for finger F/E; (B) the flexible sensor placed on the index finger and the sensor neutral axis; (C), the FBG output changes $\Delta\lambda_B$ over time during F/E movements: an increase of $\Delta\lambda_B$ due to grating ϵ during F and a decrease of $\Delta\lambda_B$ during E [94].

3.3 Wearables for sensorimotor behavioral assessment

The term “*sensorimotor system*” describes the sensory, motor, and central integration and processing components involved in maintaining joint homeostasis during bodily movements [343]. Briefly, sensorimotor circuits simultaneously process multiple different somatosensory stimuli and create many different patterns of muscle contractions to produce innate behaviors adapted for environmental conditions.

3.3.1 The importance of primitive reflexes

The sensorimotor system develops in the perinatal period, and the attainment of both gross and fine motor skills depends on it. Within the first few post-natal months, infants rapidly acquire new patterns of posture, muscle tone, and motor behavior. Spontaneous but seemingly non-goal-orientated movements known as “primitive” reflexes are replaced by purposeful goal-directed and skillful movements. This occurs parallel by increasing the motor cortex's maturation and the traditional explanation for the disappearance of this “primitive” reflex that is suppressed with the maturation of inhibitory tracts from the cortex [343]. As a result, the

developing infant starts to interact in an increasingly active manner with the enclosing environment by exploration, early learning, communication, as well as maintaining musculoskeletal integrity [344]. An understanding of child development focusing on the over lasting presence of primitive reflexes constitutes a key prerequisite to promptly highlight injuries in the sensorimotor systems at different ages.

For instance, a preterm birth (delivery before the full 37 weeks of gestation) has the potential to alter the natural process of infant motor development and may represent a critical window of vulnerability for altered sensorimotor cortex development responsible for abnormal reflexes patterns (see Fig. 3:19). This may be an explanation of the high incidence of functional motor and sensory difficulties in the adult population [345].

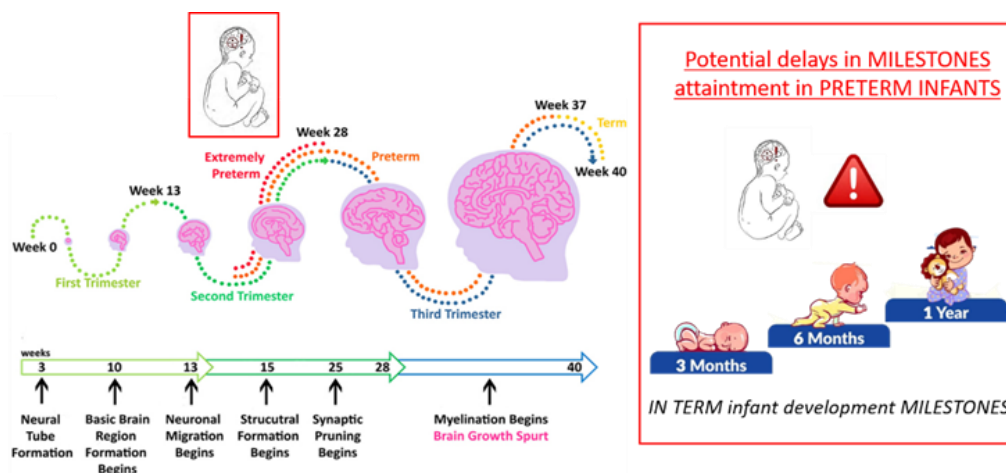


FIGURE 3:19. The brain development with potential delays in milestones attainment in preterm infants.

Primitive reflexes are a group of key behavioral motor responses to particular sensory stimuli in a specific place (e.g., the palm) that commence during pregnancy and are fully present at birth in term infants. They are natural reactions that start a developmental process that releases a neural circuit for a specific function. The neurological connections necessary are at a subcortical level located in the brain stem [346].

These movements are highly stereotyped; indeed, human infants exhibit spontaneous movements and primitive reflexes elicited by proper stimulations, such as Moro reflex, tonic neck reflex, step/walking reflex, plantar reflex, and palmar grasp reflex (Fig. 3:20).

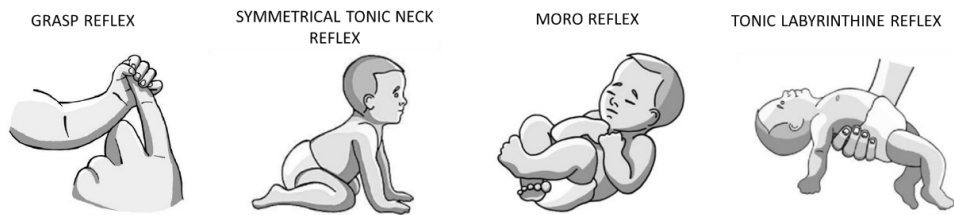


FIGURE 3:20. Examples of primitive reflexes.

Among the primitive reflexes, grasping is considered a key behavior that enables the infant first interactions with the surroundings. Atypical grasping patterns are considered predictive of neuromotor disorders and injuries but unfortunately, its clinical assessment suffers from examiner subjectivity, and the neuropathophysiology is poorly understood. Clinical assessment of palmar grasp is currently performed by applying light P on the infant's palm with an object or the examiner's finger to induce hand closure. This approach is entirely qualitative and based on the use of functional scales and the examiner's expertise [347] and is therefore potentially affected by inter-rater variability [348]. Furthermore, whilst clinicians and physiotherapists may develop discriminative experience about the quality of this reflex, they will still lack the sensitivity to identify subtle features that are not perceivable by a human observer (e.g., the discrimination of active/passive touch or the quantitative measurement of grasping strength and holding time). Therefore, a quantitative measure of grasping actions may provide new and valuable information about infant motor behavior. For this reason, clinical assessment tools, including wearables for neurodevelopment disorders and brain abnormalities in the infant period (particularly for those born preterm or at high risk of developing later CP) together with functional Magnetic Resonance Imaging (fMRI) are gaining a growing interests to help in precisely mapping the brain activity associated with motor tasks and thus provide important insights into how functional outcomes can be improved following cerebral injury [349], [350].

3.3.1.1 Physiology

Grasping is one of the first dominant motor behaviors that enable the interaction of a newborn infant with its surroundings. To elicit the palmar grasp reflex, the examiner inserts his or her index finger into the palm of the infant from the ulnar side and applies light pressure to the palm. Tactile without P and nociceptive stimulation of the palm are both inadequate. The response of the reflex comprises flexion of all fingers around the examiner's finger, which is composed of two phases: finger closure and clinging. The latter occurs as a reaction to the

proprioceptive stimulation of the tendons of the finger muscles due to slight traction after the application of pressure to the palm.

3.3.1.2 Model

The simplest model to approximate the infant's grasping actions is described in [351]. This model is based on the equilibrium translational and rotational reached between the object/hand systems. No friction forces are considered, and mechanical coupling between the hand and the object is achieved in terms of F/P . The grasping F exerted by each finger can be divided into three contact F for each phalanx of the finger (F_1, F_2, F_3), orthogonal to the phalanxes areas, and acting on the object surface with the direction passing through the center of the object.

The resultant F (F_T) passes through the center of the object due to the rotational equilibrium, and an equal R opposite to F_T is applied by the palm (see Fig. 3:21). For each finger, the effective contact surface is the grasped object surface divided for the four fingers and distributed along each of three phalanxes. Hence, the grasping action can be modeled in terms of two forces acting on the grasped object that are the resultant of the fingers forces F_1, F_2 , and F_3 (i.e., F_T) applied on the contact surface and the reaction force (R) applied by the palm.

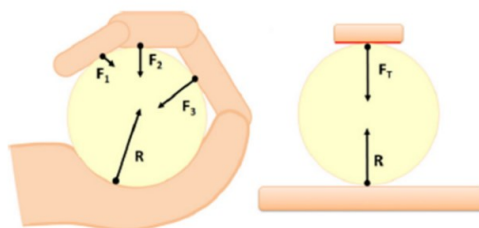


FIGURE 3:21. The forces F_1, F_2 , and F_3 (and their resultant F_T) applied by the fingers and the reaction force R applied by the palm during grasping [352].

3.3.1.3 FBG-based wearables for the assessment of grasping

The linear relation between the $\Delta\lambda_B$ and the axial ϵ applied to grating has been described in Eq. 2:2.

During palmar grasping, the ϵ induced on the grating is the result of transduction of the vertical F or P applied by the fingers and the palm on the polymeric matrix housing the FBGs.

If the FBG is coated by a thick polymer and E_f is close to polymer E (E_p), the axial ε along the FBG due to an applied pressure P is given by:

$$\varepsilon = P (2\nu - 1) / E$$

Equation 3:30

Considering a typical configuration of an FBG encapsulated at the mid-section of a cylinder-shaped polymeric matrix, the transduction of pressure into the axial ε of the grating is described by following the equation:

$$\frac{\Delta\lambda_B}{\lambda_B} = S_p \cdot P$$

Equation 3:31

With P the pressure applied by the fingers during grasping and S_p , the P sensitivity calculated as $(1 - \nu_e) \frac{\nu AP}{a E_f - \frac{L_{FBG}}{L_p} (A - a) E_p}$, where a is the cross-section area of the FBG, L_{FBG} is the grating length, and L_p is the axial length of the cylinder filled by the polymer [352].

A typical trend of FBG output changes $\Delta\lambda_B$ over time during grasping is proposed in Fig. 3:22. When the hand is closed around the object, the polymer squeezes, and the grating inside is strained; and is then unstrained once the object is released again [353].

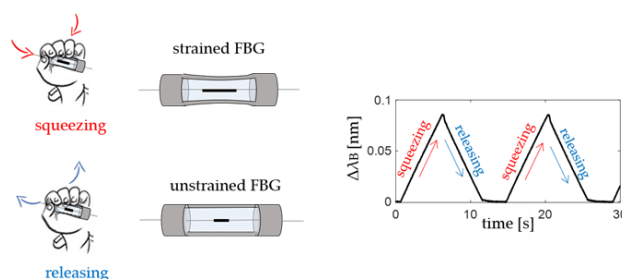


FIGURE 3:22. The FBG-based graspable/greppable device working principle: an increase of $\Delta\lambda_B$ occurs during object squeezing while a reduction during object releasing [353].

Chapter 4 Wearable systems based on FBGs: design, fabrication, and feasibility assessment

In the present Chapter, particular attention will be given to the scientific contributions provided by the Ph.D. candidate in the field of wearable devices for applications in healthcare. In all these contributions, FBGs are involved as the key sensing elements and used to instrument garments and wearable devices or to be directly stuck to the skin. Applications of FBG-based systems for cardiorespiratory monitoring and joints motion detection will be described. Lastly, the recent use of an innovative FBG-based interface for sensorimotor behavioral assessments will be presented. In all these studies, different populations have been targeted: healthy volunteers, adult patients, neonates, and athletes of different disciplines. Experiments were performed in various scenarios, from laboratories to hospitals and sport centers.

The main institutions and research groups involved in this work are:

- The unit of Measurements and Biomedical Instrumentation of UCBM where this Ph.D. has been carried out;
- The Neurophysiology and Neuroengineering of the Human-Technology Interaction of UCBM, where I carried out several activities of my Ph.D.;
- The Italian Agency for New Technologies, Energy and Sustainable Economic Development (ENEA), where I carried out several activities of my Ph.D.;
- The Neuro-Robotic Touch Laboratory at The BioRobotics Institute of Sant'Anna School of Advanced Studies (SSSA), where I spent some short visiting periods during my Ph.D.;
- The Department of Movement, Human and Health Sciences, University of Rome "Foro Italico", where I carried out several activities of my Ph.D.;
- The Department of Bioengineering of the Imperial College London (ICL), where I spent a 3-months visiting period during my Ph.D.

4.1 Wearables for cardiorespiratory monitoring

In this section, the wearables developed for monitoring both respiratory and cardiac activity are presented. These systems are grouped into the ones based on the mechanical coupling between the FBG sensor and the chest wall surface and based on changes in thermohygrometric conditions of respiratory gases.

As shown in Fig. 4:1, wearables belonging to the first group consists of bare or polymer-encapsulated FBGs for cardiorespiratory investigations. In contrast, the ones belonging to the second group are based on functionalized FBGs for respiratory monitoring.

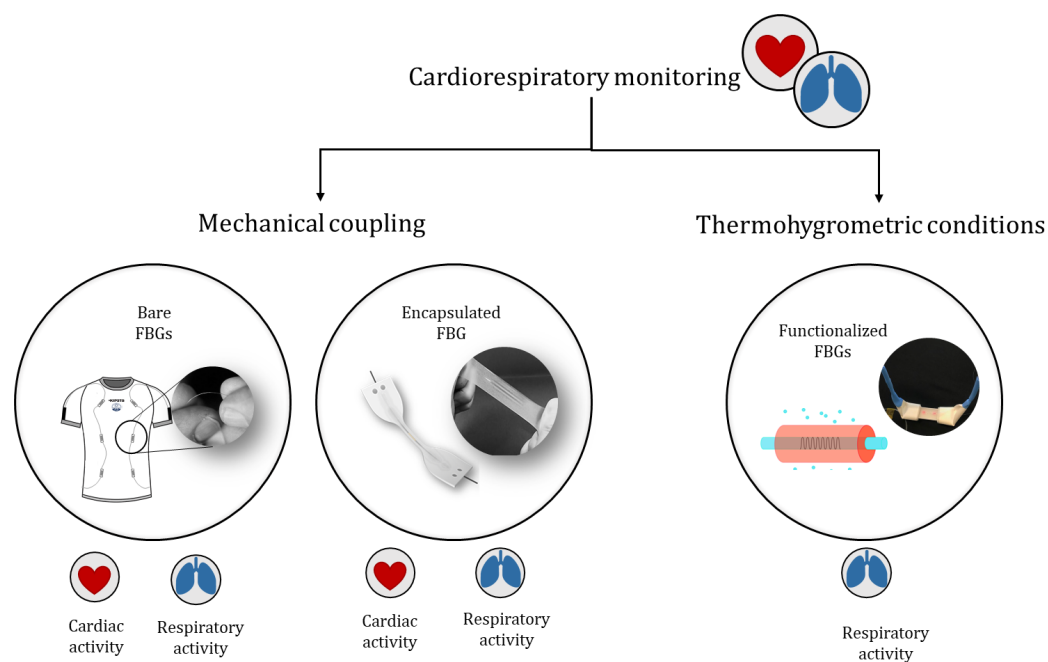


FIGURE 4:1. Wearables for cardiorespiratory monitoring: bare, encapsulated, and functionalized FBG have been used for their sensorization.

4.1.1 The mechanical coupling between wearables and chest

The mechanical coupling between the FBG sensors embedded into the proposed wearables and the chest wall surface was achieved by:

- Sticking bare FBGs directly to a smart textile.
- Encapsulating FBGs into polymeric flexible matrices with different shapes and dimensions for the sensorization of elastic bands.

4.1.1.1 Smart textile based on an array of 12 FBGs for cardiorespiratory monitoring

The use of wearable systems in the form of smart textiles for monitoring vital parameters has gained wide popularity in several medical, sport, and occupational settings since smart textiles can act as a “tech” second skin.

The proposed wearable system consists of a smart textile based on 12 bare FBGs stuck to an elastic t-shirt. This system was developed for respiratory monitoring and thoraco-abdominal motion pattern analysis. The feasibility of the proposed smart t-shirt was assessed by performing three main trials:

Trial 1: the use of the smart textile on healthy male volunteers for monitoring several temporal respiratory parameters (i.e., T_R , f_R , T_I , and T_E), V_T and volume variations of the chest wall compartments during quiet breathing.

Trial 2: the use of the smart textile on healthy female volunteers for monitoring temporal T_R , f_R , T_I , T_E , and V_T during quiet breathing.

Trial 3: the use of the smart textile for monitoring f_R during physical activity (i.e., cycling).

The system performances have been evaluated by using reference instruments (i.e., a motion capture system - Mocap in Trial 1 and Trial 2 and Quark b²metabolic cart during cycling in Trial 3).

To broader understand the findings achieved in each trial, the design and fabrication processes of the proposed system are first described.

Design and fabrication

The developed smart textile is the garment based on 12 FBGs, well-described in [354]. Typically, in the literature, single FBGs have been used to instrument garments and monitoring f_R . The novelty of this system relies on the use of 12 sensors according to the chest wall biomechanics. Indeed, from a mechanical point of view, the chest wall can be considered a twelve compartmental structure since the different muscles and physiological systems that contribute to the ventilatory pump. The model is composed of the left and right side of the pulmonary rib cage (RCp), abdominal rib cage (RCa), and abdomen (AB). Besides, each side of each compartment can be functionally split into the frontal and back contributions. The 12-compartment model allows considering that RCp and RCa are exposed at different pressures during the

inspiration, that the diaphragm acts directly only on RCa and non-diaphragmatic inspiratory muscles influence largely the RCp and not the RCa. The smart textile was designed by following this compartmentalization, so it embeds 12 FBGs. A further important novelty is that the FBGs positions have been chosen in accordance with the results of a breathing mechanics analysis carried out using a MoCap system (Smart-D, BTS Bioengineering Corp., Milan, Italy). The experimental protocol included ten infrared cameras set up following a circular pattern around each volunteer who stood at the center of the optoelectronic system (OS) room with 89 photo-reflective markers attacked on his skin (see Fig. 4:2). Data were collected during 120 s of quiet breathing at the sampling rate of 60 Hz, and seven participants (all male, mean \pm SD: age 28 ± 7 years, stature 181 ± 5.7 cm, body mass 72 ± 5 kg) were enrolled for these aims. The positions of the 12 sensors were selected with the purpose of optimizing the smart textile sensitivity to chest wall displacements following these main steps: *i)* the markers 3D trajectories were imported into MATLAB environment; *ii)* for each couple of markers, the maximum distance change (Δd_{max}) was calculated as the distance between its maximum value and the minimum one, and the average distance value (d_{mean}) was calculated as the mean distance between the two markers during the 120 s of quiet breathing; *iii)* the ratio between Δd_{max} and d_{mean} was considered the maximum ϵ (ϵ_{max}); *iv)* the couple of markers with the highest ϵ_{max} for each compartment was selected; *v)* lastly the FBGs were placed on the t-shirt along the 12 segments joining the selected markers. The 12 λ_B values (6 related to the sensors on the left side: FBG1_L, FBG2_L and FBG3_L on the front and FBG4_L, FBG5_L, and FBG6_L on the back, and 6 related to the ones on the right side: FBG1_R, FBG2_R, and FBG3_R on the front and FBG4_R, FBG5_R and FBG6_R on the back) were chosen to avoid any overlapping choosing a minim difference of 4nm. All FBGs have a grating length of 10 mm, 90% of reflectivity, and a S_ϵ of $\sim 1.2 \text{ pm} \cdot \mu\epsilon^{-1}$.

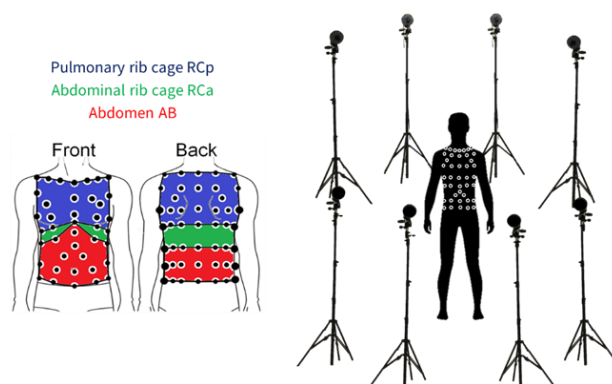


FIGURE 4:2. The experimental setp and protocol.

Two optical fibers were fabricated, each one with 6 FBGs spaced by 15 cm to allow the t-shirt to fit different anthropometric sizes. An optical fiber was placed on the front of the chest and the other one on the back. Then, the fiber extremities were looped into two small termination boxes placed on the sleeves of the t-shirt with the MU connectors necessary for connecting the FBGs to the interrogation unit necessary to send light along the fiber and collect the FBG output changes during the respiratory activity of the wearer.

All the FBGs used to instrument such a system are bare and directly stuck on the t-shirt using a commercial polymeric glue (3145 RTV MIL-A-46146, DOW CORNING, Michigan, MI, USA). Fig. 4:3 shows the design of the smart t-shirt based on 12 FBGs and their positioning.

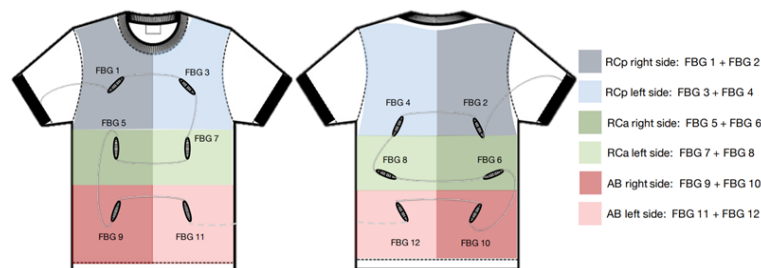


FIGURE 4.3. The design of the proposed smart textile. Each compartment (left and right) is identified by a specific color.

The capability of monitoring respiratory activity has been assessed at rest on both males (Trial 1) and females (Trial 2) and during cycling (Trial 3).

Trial 1: Smart textile assessment on males during quiet breathing²

The aim of this trial was the feasibility assessment of the developed 12 FBG-based smart t-shirt for monitoring T_R , f_R , T_I and T_E , V_T , and other volume variations of the chest wall compartments during quiet breathing.

Eight healthy male volunteers (age 24 ± 2 y.o. height 173 ± 5 cm, weight 69 ± 7 kg) with no history of respiratory disorders were enrolled in this study. Each volunteer was invited to wear the smart textile and to assume a standing posture. Then the 89 infrared photoreflexive

² This work is an excerpt from "Smart textile for respiratory monitoring and thoraco-abdominal motion pattern evaluation" in which the Ph.D. candidate is main co-author. doi: <https://doi.org/10.1002/jbio.201700263>

markers were placed on the t-shirt for enabling the MoCap data collection. Each volunteer was instructed to perform two different trials of self-paced quiet breathing lasting 60 s each, after a brief forced inspiration used to synchronize the signals of smart textile and MoCap in the post-processing phase. The 12 FBG outputs were collected simultaneously by using the optical spectrum interrogator (si425, Micron Optics Inc., Atlanta, USA) at a sampling rate of 250 Hz. A dedicated Virtual Instrument in LabVIEW environment running on a notebook provides the data visualization and saving.

From the markers trajectories, the volumes enclosed into the thoraco-abdominal surface were obtained through the connection of markers in a net of triangles. For each triangle obtained, the area and direction of the normal vector were determined. Thus, the internal volume of each shape was calculated using Gauss's theorem, which converts a surface integral into a volume integral. This procedure allows computing the volume enclosed by the 12 compartments of the thoraco-abdominal surface (left and right sides of ΔV_{RCp}^{MoCap} , ΔV_{RCa}^{MoCap} , ΔV_{AB}^{MoCap}). The volume enclosed by the whole chest wall ($\Delta V_{global}^{MoCap}$) is mathematically obtained by the sum of these 6 compartmental volumes.

Data collected in the first trial by the MoCap and by the smart textile were used to: *i)* calculate the temporal breathing parameters (T_R , f_R , T_I , T_E) from the $\Delta V_{global}^{MoCap}$ and the $\Delta \lambda_{B global}$ and to compare the two systems. The values of $\Delta \lambda_{B global}$ were obtained by summing all the $\Delta \lambda_B$ of the 12 FBGs and removing the mean value (see Fig. 4:4); *ii)* calibrate the smart textile in the calculation of the global volume ($\Delta V_{global}^{smart textile}$) and compartmental volumes ($\Delta V_{RCp}^{smart textile}$, $\Delta V_{RCa}^{smart textile}$, $\Delta V_{AB}^{smart textile}$), hereinafter called training phase.

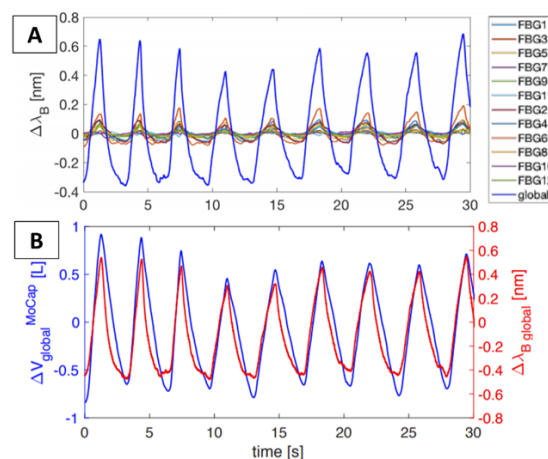


FIGURE 4:4. (A) the smart textile output of all the FBGs and the FBGs sum over a 30s-lasting window of quiet breathing; (B) The $\Delta V_{global}^{MoCap}$ and $\Delta \lambda_{B global}$ signals over time.

The second trial was used to test the calibrated smart textile in the estimation of compartmental ($\Delta V_{RCp}^{\text{smart textile}}$, $\Delta V_{RCa}^{\text{smart textile}}$, $\Delta V_{AB}^{\text{smart textile}}$) and global volume ($\Delta V_{\text{global}}^{\text{smart textile}}$) changes by using the compartmental ($\Delta V_{RCp}^{\text{MoCap}}$, $\Delta V_{RCa}^{\text{MoCap}}$, $\Delta V_{AB}^{\text{MoCap}}$) and $\Delta V_{\text{global}}^{\text{MoCap}}$ volume changes obtained by the MoCap used as a reference.

Focusing on the temporal parameters, the signal obtained by summing the 12 FBG output changes (ie, $\Delta \lambda_{B \text{ global}}$) and the $\Delta V_{\text{global}}^{\text{MoCap}}$ were used to extract all the above-mentioned temporal parameters from the smart textile and the MoCap, respectively. The steps followed are reported here below and schematically summarized in Fig. 4:5:

1. The minimum peak at the end of the forced inspiration in the signal was identified on both the $\Delta \lambda_{B \text{ global}}$ and $\Delta V_{\text{global}}^{\text{MoCap}}$: these two points were used to synchronize the signals;
2. The signals were resampled at 60 Hz (i.e., the lower sampling frequency between the two systems), and then their mean values were removed by the signals;
3. Maximum and minimum peaks were identified on both the zero-mean signals by a custom-made algorithm based on both a setup time window and signal threshold.

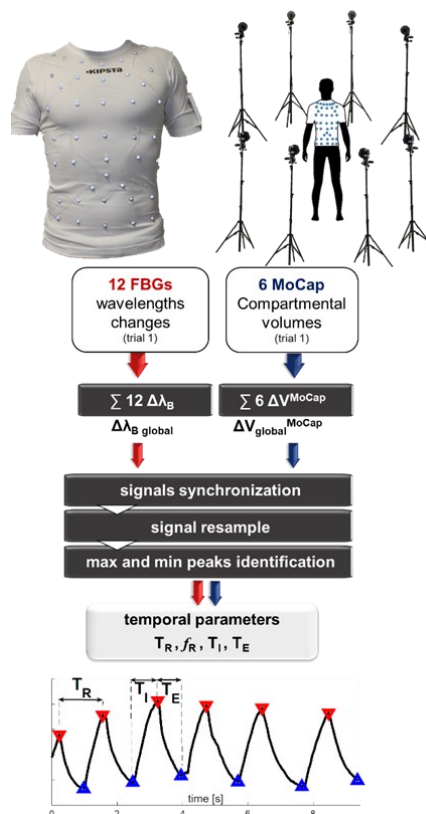


FIGURE 4:5. Steps of data analysis followed to obtain temporal parameters.

Thus, each T_R value was calculated as the time elapses between two consecutive maximum peaks, T_I , as the time interval between a maximum and its previous minimum, and T_E , as the time interval between the same maximum and the following minimum. Then f_R - expressed in bpm - was calculated as the ratio between 60 and T_R values. The comparison between all the T_R , f_R , T_I , T_E values obtained by using the two measurement systems was performed using three approaches: *i)* Bland–Altman analysis carried out to evaluate the mean of difference (MOD), as well as the limits of agreements (LOAs), calculated as the $MOD \pm 1.96 SD$ where SD is the standard deviation; *ii)* linear regression was used to evaluate the relationships between values; *iii)* a statistical test was used to investigate the hypothesis that there is no linear relationship between each parameter of interest estimated by the two different measuring systems (P values close to 0 correspond to a significant correlation between parameters). A significance level of 0.05 was set. Then, from T_R and f_R values, the percentage differences between the two instruments ($\%e_{T_R}$ and $\%e_{f_R}$, respectively) were calculated as in Eq. 4:1:

$$\%e_{T_R} = \frac{\overline{T_R}^{\text{smart textile}} - \overline{T_R}^{\text{MoCap}}}{\overline{T_R}^{\text{smart textile}}} \cdot 100; \quad \%e_{f_R} = \frac{\overline{f_R}^{\text{smart textile}} - \overline{f_R}^{\text{MoCap}}}{\overline{f_R}^{\text{smart textile}}} \cdot 100$$

Equation 4:1

being the $\overline{T_R}^{\text{smart textile}}$, $\overline{T_R}^{\text{MoCap}}$, $\overline{f_R}^{\text{smart textile}}$, $\overline{f_R}^{\text{MoCap}}$ the mean value of T_R and f_R calculated for each volunteer using the two systems, respectively.

Regarding the chest wall volumes, the reconstruction of the compartmental volume changes from the FBG signals was performed as follows:

1. By summing the signal outputs of two FBG sensors that monitor the same compartment according to Fig. 4:3 (i.e., 1 and 2, 3 and 4, 5 and 6, 7 and 8, 9 and 10, 11 and 12), the six wavelength changes relative to the left and right sides of each compartment were obtained as shown in Fig. 4:6;
2. The peak at the end of the forced inspiration in the signal was identified on both the $\Delta\lambda_{B \text{ global}}$ (obtained summing the six wavelength changes signals) and $\Delta V_{\text{global}}^{\text{MoCap}}$: since all the FBG signals are synchronized as well as all the volume changes, this peak was used as starting points of both the six wavelength changes signals and of the six compartmental volumes;

3. All the signals were resampled at 60 Hz (i.e., the lower sampling frequency between the two systems), and then their mean values were removed;
4. Minimum peaks were identified on the six smart textile signals and the six-volume signals by the same custom-made algorithm used in the temporal parameter calculation.

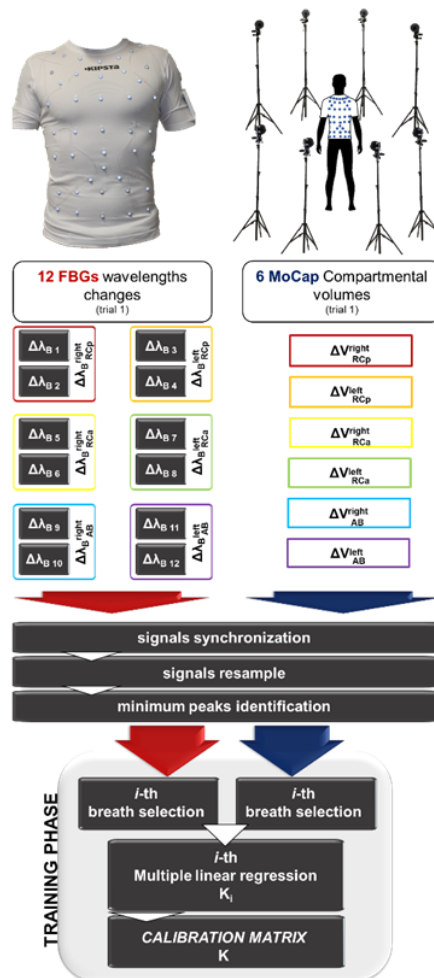


FIGURE 4:6. Steps of data analysis for the estimation of the volumes.

To reconstruct the compartmental volume changes from the FBG signals, multiple linear regression was performed on each breath included between two consecutive minimum peaks using MATLAB function *regress*. The six smart textile signals and the six-volume signals of the *j*-th breath were used in the multiple linear regression to obtain the *j*-th square matrix K_j (6×6 size) that contains the different weights of the 6 FBG outputs in the six compartmental volume changes reconstructions as reported in Eq. 4:2:

$$(\Delta V_i^{MoCap})_j = K_j \cdot (\Delta \lambda_{B_i})_j$$

Equation 4:2

where i represents the six compartments ($right_{RCp}$, $left_{RCp}$, $right_{RCa}$, $left_{RCa}$, $right_{AB}$, $left_{AB}$). Then the calibration matrix K of each volunteer was obtained by averaging the values of j square matrix K_j . Data collected in the second trial were used to test the smart textile in the volume estimations. The calibration matrix K - obtained by the training phase - was applied to the 6 FBG signals in order to estimate the compartmental volumes (ΔV_i^{FBG}) according to Eq. 4:3:

$$\Delta V_i^{smart\ textile} = \Delta \lambda_{B_i} \cdot K$$

Equation 4:3

Hence, from the six compartmental $\Delta V^{smart\ textile}$, left and right contributions of the same compartment were summed to obtain three compartmental volumes changes from the smart textile relative to the pulmonary rib cage ($\Delta V_{RCp}^{smart\ textile}$), the abdominal rib cage ($\Delta V_{RCa}^{smart\ textile}$), the abdomen ($\Delta V_{AB}^{smart\ textile}$). The global volume changes ($\Delta V_{global}^{smart\ textile}$) were calculated by summing the three compartmental volume changes.

Fig. 4:7 shows the zero-mean global and the three compartmental $\Delta V^{smart\ textile}$ obtained after the calibration process (training phase) by data collected on a volunteer, together with the ΔV^{MoCap} collected contemporaneously. So, the three compartmental and global volume changes obtained by the smart textile calibration were compared to the ones saved by the MoCap.

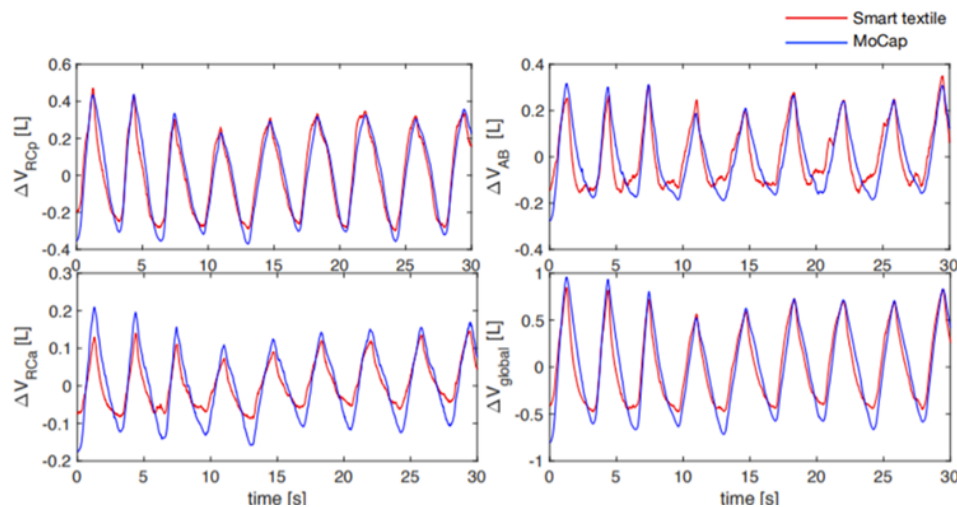


FIGURE 4:7 Volumes estimated by the Mocap (blue lines) and the FBGs (red lines).

First, similarly to the first trial, peak at the end of the forced inspiration in the signal was identified, on both the $\Delta V_{\text{global}}^{\text{smart textile}}$ and $\Delta V_{\text{global}}^{\text{MoCap}}$, to synchronize the four volumes of the smart textile with the ones of the MoCap; then all the signals were resampled at 60 Hz and the mean removed. Then maximum and minimum peaks were identified on the $\Delta V_{\text{global}}^{\text{smart textile}}$ and $\Delta V_{\text{global}}^{\text{MoCap}}$ signals: tidal volume - V_{T_i} values were calculated as the difference between two consecutive minimum (end-expiratory volume) and maximum (end-inspiratory volume) points, with i the quantity of the breaths selected between the two points. All the V_{T_i} values collected by the eight volunteers per each i -th breath obtained from the smart textile ($V_{T_i}^{\text{smart textile}}$) were compared against the $V_{T_i}^{\text{MoCap}}$ obtained by the MoCap system. Following the analysis performed on temporal parameters, the comparison between all the V_T values collected by the eight volunteers with the two measurement systems was performed using the same three approaches: *i)* Bland–Altman analysis; *ii)* linear regression analysis; *iii)* statistical test used to investigate the hypothesis that there is a linear relationship between $V_{T_i}^{\text{MoCap}}$ and $V_{T_i}^{\text{smart textile}}$ ($P < 0.05$).

By following the same procedure adopted to extract V_T from the global signals, the compartmental V_T were extracted by ΔV_{RCp} , ΔV_{RCa} , and ΔV_{AB} signals gathered by MoCap and calibrated smart textile. Then, average percentage contributions were calculated according to Eq. 4:4:

$$\left\{ \begin{array}{l} \overline{\%RCp} = \frac{\sum_i \%RCp^i}{N} = \frac{\sum_i \frac{VT_{RCp}^i}{VT^i} \cdot 100}{N} \\ \overline{\%RCa} = \frac{\sum_i \%RCa^i}{N} = \frac{\sum_i \frac{VT_{RCa}^i}{VT^i} \cdot 100}{N} \\ \overline{\%AB} = \frac{\sum_i \%AB^i}{N} = \frac{\sum_i \frac{VT_{AB}^i}{VT^i} \cdot 100}{N} \end{array} \right.$$

Equation 4:4

being i the i -th breath considered and N the number of breaths executed by the volunteer in the second trial. Moreover, SD was also calculated considering all the N values of V_T contributions obtained from each compartment. The SD values may be useful to evaluate the variability of the thoraco-abdominal contributions during the breathing activity. This procedure was carried out per each volunteer, separately.

To evaluate the quantitative differences between the two systems, raw differences ($\Delta\%$) between $\overline{\%RCp}, \overline{\%RCa}, \overline{\%AB}$ were calculated as in Eq. 4:5, by using the values gathered by the MoCap as reference:

$$\begin{aligned}\Delta\%_{RCp} &= \overline{\%RCp}^{\text{Smart textile}} - \overline{\%RCp}^{\text{MoCap}} \\ \Delta\%_{RCa} &= \overline{\%RCa}^{\text{Smart textile}} - \overline{\%RCa}^{\text{MoCap}} \\ \Delta\%_{AB} &= \overline{\%AB}^{\text{Smart textile}} - \overline{\%AB}^{\text{MoCap}}\end{aligned}$$

Equation 4:5

In order to investigate the statistical differences between the smart textile and the reference instrument in the percentage contributions, a statistical t-Student test was applied to investigate the hypothesis that there is a linear relationship ($P < 0.05$).

The mean and the SD values of each temporal parameter (T_I, T_E, T_R, f_R) obtained by the two systems for each volunteer are listed in Table 4:1. The SD was calculated by considering all the breaths in each signal collected during the trial. Table 4:2 shows the results of the Bland Altman analysis (expressed as bias \pm SD), the linear regression (R^2), and the statistical test (P-value).

TABLE 4:1

Volunteer	T_I [s]		T_E [s]		T_R [s]		f_R [bpm]	
	MoCap	Smart Textile	MoCap	Smart Textile	MoCap	Smart Textile	MoCap	Smart Textile
1	1.79 \pm 0.29	1.72 \pm 0.27	1.43 \pm 0.39	1.49 \pm 0.33	3.22 \pm 0.33	3.22 \pm 0.30	18.63 \pm 0.11	18.63 \pm 0.10
2	3.07 \pm 0.38	2.93 \pm 0.32	3.80 \pm 0.84	3.93 \pm 0.86	6.87 \pm 1.10	6.86 \pm 1.01	8.73 \pm 1.76	8.75 \pm 1.61
3	2.60 \pm 0.27	2.57 \pm 0.40	2.08 \pm 0.47	2.11 \pm 0.38	4.68 \pm 0.43	4.68 \pm 0.40	12.82 \pm 0.31	12.82 \pm 0.29
4	1.71 \pm 0.28	1.68 \pm 0.23	2.24 \pm 0.31	2.28 \pm 0.30	3.96 \pm 0.46	3.96 \pm 0.46	15.15 \pm 0.25	15.15 \pm 0.24
5	1.52 \pm 0.22	1.44 \pm 0.21	2.26 \pm 0.25	2.23 \pm 0.22	3.68 \pm 0.12	3.67 \pm 0.10	16.30 \pm 0.05	16.35 \pm 0.04
6	1.36 \pm 0.28	1.27 \pm 0.15	1.49 \pm 0.22	1.58 \pm 0.28	2.85 \pm 0.29	2.85 \pm 0.29	21.05 \pm 0.08	21.05 \pm 0.08
7	2.39 \pm 0.43	2.06 \pm 0.25	2.83 \pm 0.46	3.07 \pm 0.34	5.22 \pm 0.64	5.13 \pm 0.37	11.49 \pm 0.58	11.70 \pm 0.32
8	1.63 \pm 0.39	1.22 \pm 0.14	2.00 \pm 0.15	2.41 \pm 0.26	3.63 \pm 0.31	3.63 \pm 0.33	16.53 \pm 0.14	16.53 \pm 0.15

Mean and SD values are reported for both the MoCap system and the smart textile, for each volunteer.

TABLE 4:2

	R^2	P values	Bias \pm SD
T_I	0.75	<0.05	0.15 \pm 0.31 s
T_E	0.81	<0.05	-0.14 \pm 0.32 s
T_R	0.97	<0.05	0.01 \pm 0.19 s
f_R	0.93	<0.05	-0.02 \pm 1.04 bpm

Both T_R and f_R estimated by the smart textile showed a good agreement with the reference ones. This is testified by: *i*) the results of the linear regression (high R^2 values of 0.97 and 0.93, respectively, as well as the closeness to 1 of the slope of the best fitting line, 0.99 in both cases, as shown in Fig. 4:8); *ii*) the results of the Bland Altman analysis (the low value of the bias, 0.01 s for T_R and -0.02 bpm $^{-1}$ for f_R) as shown in Fig. 4:8; *iii*) the low value of the maximum $\%e_{T_R}$ and $\%e_{f_R}$, -0.09 s (1.72%) and -0.20 bpm $^{-1}$ (-1.75%), while the average values were 0.27% for both the systems. Finally, as expected, a linear relationship between the two parameters estimated by the two systems was statistically significant ($P < 0.05$).

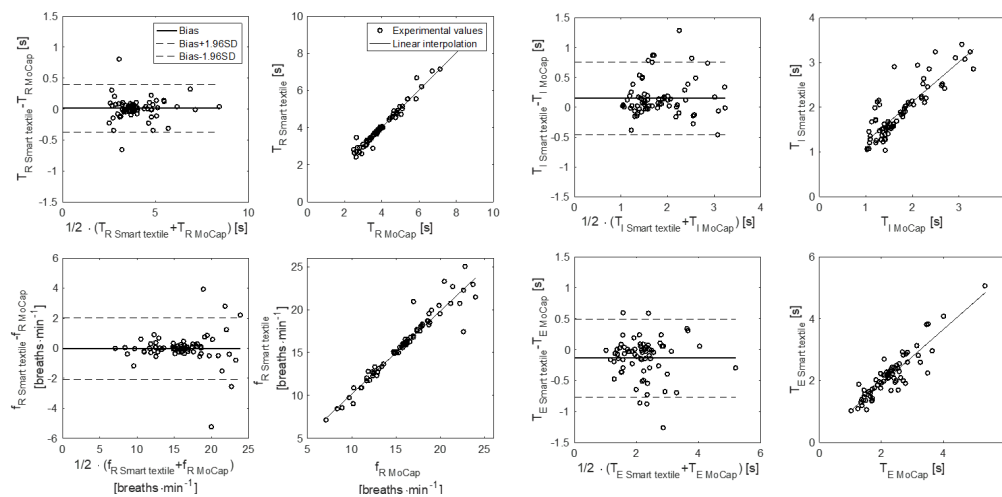


FIGURE 4:8. Bland-Altman plots and the linear regression

The performance of the smart textile in the calculation of global volume changes was evaluated by comparing the breath-by-breath tidal volume extracted by the $\Delta V_{\text{global}}^{\text{FBG}}$ ($V_{\text{Tsmart textile}}$) against the tidal volumes extracted by $\Delta V_{\text{global}}^{\text{MoCap}}$ ($V_{\text{Treference}}$), used as reference values.

Fig. 4:9 A shows the Bland-Altman plot (with MOD and LOAs) and the linear regression used to evaluate the relationships between V_T values measured by the smart textile and the reference system. The Bland-Altman analysis showed a mean bias value of -0.09 ± 0.15 L suggesting that the smart textile slightly underestimates V_T , pointing out the good agreement between the two systems ($R^2 = 0.90$, $P < 0.05$).

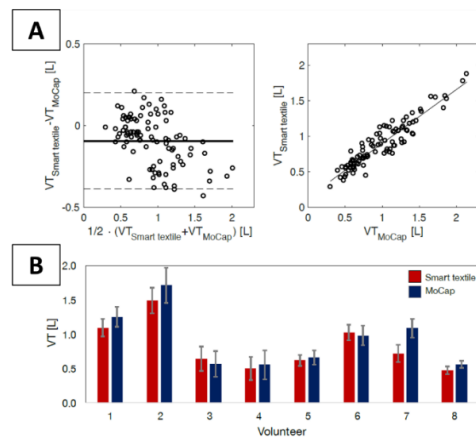


FIGURE 4:9. (A) Bland-Altman plot and linear regression of V_T ; (B) Mean and SD values of V_T estimated by the smart textile (red bar) and MoCap (blue bar) of all the eight volunteers.

The mean values of the $VT_{Smart\ textile}$ and $VT_{reference}$ values calculated per each volunteer are shown in Fig. 4:9 B, together with the SD calculated by all the V_T values of the same volunteer. A linear relationship was found between the mean values of V_T collected by the two instruments ($P < 0.05$).

Regarding the thoraco-abdominal patterns, Fig. 4:10 shows the compartmental percentage contributions (i.e., %RCp, %RCa, %AB) calculated by the two instruments per volunteer.

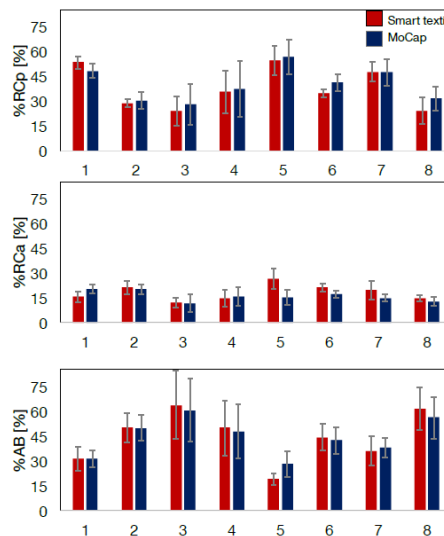


FIGURE 4:10. Compartmental percentage contributions %RCp, %RCa, and %AB calculated by the two instruments.

By considering all compartmental percentage values for all the volunteers enrolled, we found a linear relationship between values gathered by the two systems ($P < 0.05$ for %RCp, %RCa, and %AB).

These findings, together with biases found in the breath-by-breath inspiratory and expiratory phase durations values (up to 0.15 s), are similar to values reported in previous studies adopting fiber optic-based garments for the breathing rate monitoring [14],[13],[19],[24]. In addition, the f_R estimation shows that the results herein reported are similar to those shown in a previous paper focused on the smart textile under test [227]. These results highlighted that after one year of use, the performance of the proposed garment did not show any drift.

Regarding the monitoring of the respiratory volume, the proposed smart textile demonstrated an overall slight underestimation of breath-by-breath V_T values with a bias of -0.09 ± 0.15 L and a strong correlation with reference measurements ($R^2 = 0.90$). No statistical differences were found when the mean values of V_T collected by the two instruments were compared.

A significant linear relationship between smart textile and MoCap percentage contribution values was found ($P < 0.05$). It means that the proposed smart textile can be potentially used to identify abnormal breathing pattern and disorders within the respiratory system and help refine the differential diagnosis in clinical practice [358] by the analysis of thoraco-abdominal patterns, and it should be used to can indirectly measure the muscular involvement and the coordination of the breathing during the effort in sport science [359].

Trial 2: Smart textile assessment on females during quiet breathing³

Smart textiles are usually developed to fit a small range of body sizes since they are intended to be worn in close contact with the body for giving reliable information.

This trial aimed to evaluate the performances of the man-fit smart textile based on 12 FBG sensors, already described, in monitoring breath-by-breath temporal respiratory parameters (i.e., f_R , T_R , T_I , and T_E) and V_T when worn by women. On average, women are smaller than men for many body parts, for example, shoulder breadth, stature, and upper thorax circumference, while they are significantly larger than men in their hip breadth. Thus, when a woman wears a

³ This work is an excerpt from "Smart textile based on FBG sensors for breath-by-breath respiratory monitoring: tests on women" of which the Ph.D. candidate is the main author. doi: 10.1109/MeMeA.2018.8438721.

man suit, it will fit larger in her thorax and tighter in her hips. Presumably, its performances will be affected by these sex-related differences of body shape and anthropometry.

Eight young female volunteers (expressed in terms of mean \pm SD are: 22 ± 2 years old, 166 ± 5 cm of height, 58 ± 5 kg of weight) with no history of respiratory disorders were enrolled in this study and invited to perform the protocol previously described for male volunteers. The experimental setup of the proposed study is shown in Fig.4 :11.



FIGURE 4.11. The experimental setup.

Results of both Bland-Altman analyses for respiratory parameters are listed in Table 4.3. The Bland-Altman plots are shown in Fig. 4:12 for f_R and V_T .

TABLE 4:3

	MOD	LOAs
T_R [s]	0.002	± 0.251
f_R [bpm]	0.014	± 2.387
T_I [s]	-0.008	± 0.562
T_E [s]	0.010	± 0.577
V_T [L]	0.080	± 0.375

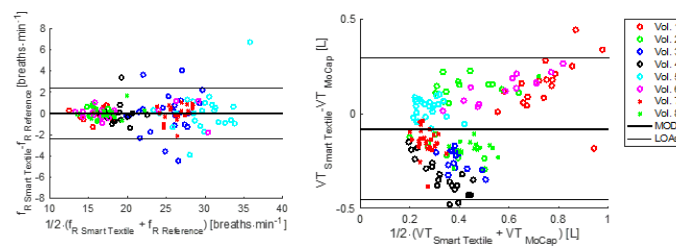


FIGURE 4.12. Bland-Altman plots for f_R and V_T .

The average percentage difference values $\%e_{f_R}$ and $\%e_{V_T}$ per each subject are listed in Table 4:4.

TABLE 4:4

Volunteer	$\%e_{f_R}$ [%]	$\%e_{V_T}$ [%]
1	0.20	-23.5 %
2	0.30	- 8.0 %
3	0.30	23.5 %
4	0.36	66.7 %
5	0.34	-13.9 %
6	0.11	-18.8 %
7	0.16	41.4 %
8	0.01	35.9 %

These findings suggest the high accuracy in the f_R estimation as it was found in male volunteers [360]. So, as expected, a not well fit does not affect the estimation of f_R because it is based on the distance between the following maximum peaks detected on the signal. Otherwise, regarding V_T monitoring, the proposed system demonstrated a high average percentage difference with respect to the reference value (with maximum differences of 66%). Moreover, the bias of 0.080 ± 0.375 L obtained by the Bland-Altman analysis demonstrated the weak capabilities of the proposed smart textile in the breath-by-breath analysis of volume changes on females. It means that anatomical dimorphism has an impact on the estimation of respiratory volumes. In particular, women tend to have smaller airways diameter, lung volumes, and upper thorax circumference while larger hip breadth. It results in a no well fit of the t-shirt necessary for accurate measurement of respiratory volume. In this case, data analysis is based on the calculation of signal amplitude between the minimum and maximum peaks. As expected, if the t-shirt fits too large, the mechanical coupling between the FBGs and the chest is not achieved, resulting in high errors in the V_T estimations.

Trial 3: Smart textile assessment during cycling⁴

The close contact to the body makes smart textiles performances affectable by any undesirable trunk movements, which may lead to noise on the desired signal. To distinguish between the sought-after signal and the movement noise, post-processing filtering methods are commonly used. However, the accommodation of a higher number of sensors (i.e., twelve FBGs) may improve the system redundancy and in turn, its reliability and accuracy of the measurement.

Thus, the aim of this trial was the assessment of the performances of the smart textile embedding twelve FBGs during a cycling incremental exercise test to identify the areas of the trunk which are most suitable for measuring f_R during activity and to verify if the sensors redundancy may improve the system performances with important implications for the design of sports respiratory wearables for respiratory monitoring.

Four volunteers were asked to wear the smart textile and using simultaneously a reference instrument based on airflow measurement with the purpose of validating the measure of f_R .

During the experiments, a gold standard reference system (i.e., Quark b², COSMED S.r.l., Rome, Italy) was used to collect reference respiratory airflow data. These data were recorded at 25 Hz (see Fig. 4:13) while an optical spectrum interrogator collected the t-shirt sensors outputs at 250 Hz. An electromagnetically braked cycloergometer (Lode Excalibur Sport, Groningen, the Netherlands) was used to carry out experiments during cycling exercises.

In the pilot tests, each volunteer wore the smart textile while ventilating into the mask of the reference instrument, and a ramp incremental exercise test to exhaustion [361] was performed. Prior to cycling tests, participants held their breath for 10 s to synchronize the signals from the t-shirt with those from the reference instrument.

For each subject, the 12 FBGs signals recorded by the smart t-shirt and the flow signal by the reference instrument (respiratory flow) were synchronized by using the first 10 s of apnea. Then, a band-pass filter between 0.05 Hz and 2 Hz was used to remove frequency content outside breathing bandwidth (up to 2 Hz) and to avoid the slow signal variations unrelated to respiratory movements. By summing all the twelve sensors signals (FBG1, ..., FBG12) in each time instant, a signal, hereinafter called t-shirt SUM signal, is obtained by considering all the information registered by all the sensors. Moreover, summing the signals recorded by the sensors positioned on the upper thorax (FBG1 and FBG7), those on the lower thorax (FBG 2, 8, 6,

⁴ This work is an excerpt from "Respiratory monitoring during cycling exercise: performance assessment of a smart t-shirt embedding fiber optic sensors" in which the Ph.D. candidate is co-author. doi: 10.1109/MetroInd4.0IoT48571.2020.9138307

12, 5, 11), and those on the abdomen (FBG3, 9, 4 and 10) the computation of the RCp signal, the RCa signal, and the AB signal was carried out. Additionally, the Anterior signal was computed (adding the outputs FBG signals related to the anterior part of the trunk, FBG 1,7, 2, 8, 3,9) and the Posterior signal (adding the outputs of FBGs on the posterior part of the trunk, i.e., 4,10, 5,11, 6,12).

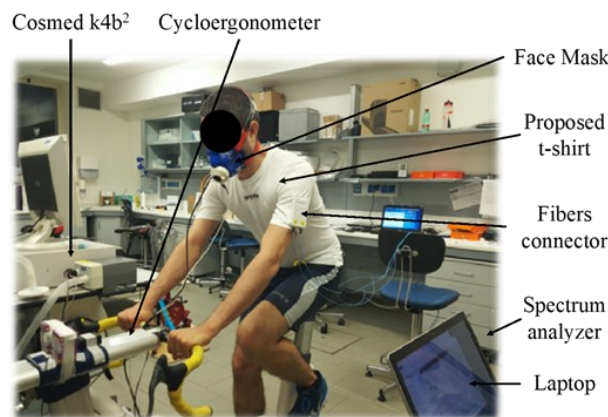


FIGURE 4.13. The setup used for carrying out the tests during cycling.

The performance of the proposed t-shirt in monitoring the average f_R was estimated every 30 s. To do this, the windowing of all the signals (reference, FBG1, ... FBG12, t-shirt SUM, RCp, RCa, AB, Anterior and Posterior) was computed to extract 30 s-lasting signals and their following post-processing (see Fig. 4:14). In each window, the power spectrum of each signal was obtained. Then, the maximum peak of each power spectrum was identified as the window average f_R .

To compare the data, the mean absolute error (MAE) was calculated as in Eq. 4:6 considering the f_R values obtained by FBG1, ... FBG12, t-shirt SUM, RCp, RCa, AB, Anterior and Posterior signals and those from the reference instrument:

$$MAE = \frac{\sum_{i=1}^n |f_{Ri} - f_{Ri}^{reference}|}{n}$$

Equation 4:6

being n the number of the windows of length 30 s, f_{Ri} the i -th window average respiratory value estimated by the signal (FBG1, ... FBG12, t-shirt SUM, RCp, RCa, AB, Anterior and

Posterior) and $f_{Ri}^{reference}$ the i -th window average respiratory value estimated by the reference signal.

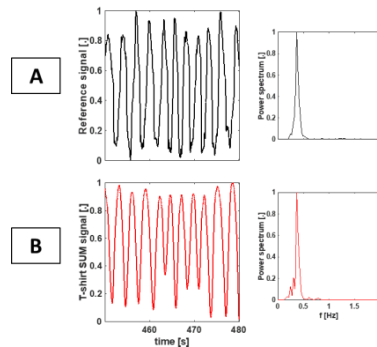


FIGURE 4:14. Example of a 30 s-window. (A) The signal recorded by the reference instrument (black). (C) The signal obtained summing all the FBG signals (i.e., t-shirt SUM signal – red). (B) The power spectrum related to the reference and (D) The power spectrum related to t-shirt SUM signals. The maximum peaks are around 0.4 Hz (i.e., average f_R of 24 bpm).

Lastly, the Bland-Altman analysis was carried out to identify MOD and LOAs values by using all the data recorded by the four volunteers [362].

Fig. 4:15 graphically reports the MAE values obtained using the different signals. Values always lower than 2 bpm were found estimating f_R from t-shirt SUM, RCa, and AB signals. Relatively high MAE values (up to 17 bpm) were found when f_R was estimated exclusively using FBG1, FBG2, FBG3, FBG4, FBG5, FBG6, FBG7, and FBG8.

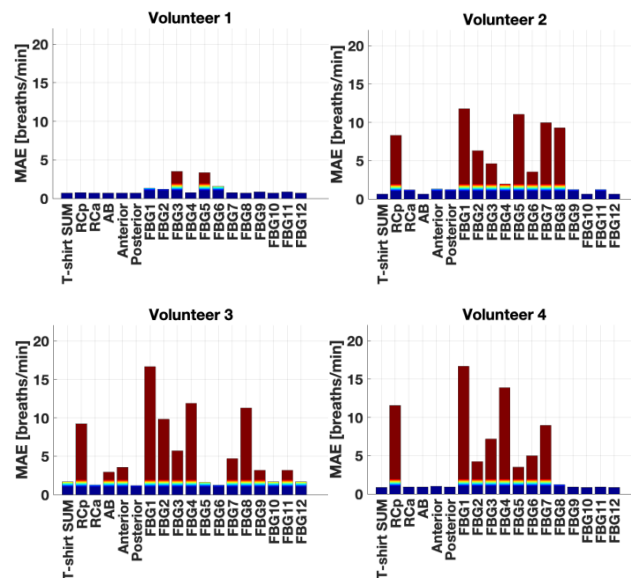


FIGURE 4:15. MAE values for the different sensors, the t-Shirt SUM, RCp, RCa, AB, Anterior, and Posterior, per each volunteer.

Focusing on the t-shirt SUM, Fig. 4:16 reports the 30 s – window f_R values of this signal and the reference instrument. A good overlap between reference values and the t-shirt was found in all the volunteers.

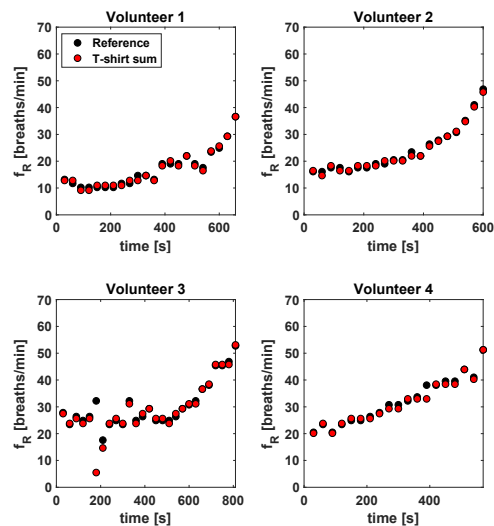


FIGURE 4:16. The 30 s – window f_R values of this signal and of the reference instrument.

Table 4:5 reports the MAE between the f_R values retrieved from t-shirt SUM, RCa, and AB signal against the reference values. t-shirt SUM showed a lower MAE than all the other combinations. RCa presented similar results, followed by AB. All these signals provide a robust estimation of f_R , with MAE values ranging from 0.66 bpm to 2.94 bpm.

TABLE 4:5

Volunteer	Average f_R MOD \pm LOAs [bpm]		MAE [bpm]
	Reference	<i>t-shirt SUM</i>	<i>t-shirt SUM</i>
		<i>RCa</i>	<i>RCa</i>
		<i>AB</i>	<i>AB</i>
1	16.9 \pm 7.0	16.8 \pm 7.0	0.70
		16.9 \pm 7.1	0.71
		16.8 \pm 7.1	0.70
2	24.0 \pm 8.8	23.8 \pm 8.5	0.66
		23.1 \pm 9.4	1.21
		23.8 \pm 8.54	0.66
3	30.4 \pm 8.5	29.2 \pm 9.9	1.68
		29.7 \pm 9.1	1.27
		28.0 \pm 10.6	2.94
4	33.5 \pm 10.5	33.0 \pm 10.4	0.86
		33.1 \pm 10.3	0.91
		32.9 \pm 10.5	0.91

Lastly, Table 4:6 shows the MOD and LOAs values obtained from the Bland-Altman analysis. We investigated these values considering f_R gathered from each sensor' signal, from the t-Shirt SUM, RCp, RCa, AB, Anterior and Posterior signals separately. Additionally, we investigated the performances for each volunteer as well as considering all the four volunteers' data (last column of Table 4:6).

These preliminary findings show that the sensors' location may be crucial to improve the performance of a device measuring f_R with strain sensors during cycling. The performance of the RCa and AB sensors was superior compared to those of the RCp sensors. These results may be attributed to the fact that during cycling, the hands are fixed on the handlebar, the trunk is inclined, and the muscles of the thorax are activated to stabilize the trunk, thus influencing the respiratory-related movements of the thorax. On the other hand, the RCp signal was obtained only from two sensors, while the RCa and AB signals were obtained from six and four sensors, respectively. This suggests that the number of sensors considered may have affected our results. Hence, the precise mechanisms underlying the observed differences between RCp, RCa, and AB sensors require further investigation. It is also interesting to highlight that the anterior and posterior parts of the trunk showed similar performances. This information is useful for the design of respiratory wearables, given that currently available devices often have sensors located in the anterior part only.

TABLE 4:6

	Bland-Altman analysis				
	MOD \pm LOAs				
	[bpm]				
	Vol.1	Vol.2	Vol.3	Vol.4	All together
t-shirt SUM	0.10 \pm 1.66	0.22 \pm 1.50	0.15 \pm 1.78	0.24 \pm 1.40	0.17 \pm 1.59
RCp	-0.06 \pm 1.81	-0.02 \pm 5.31	1.17 \pm 4.95	11.11 \pm 24.61	0.21 \pm 2.70
RCa	-0.07 \pm 1.81	-0.02 \pm 5.31	0.08 \pm 1.47	0.15 \pm 1.59	0.14 \pm 1.52
AB	0.10 \pm 1.66	0.22 \pm 1.50	0.39 \pm 2.72	0.33 \pm 1.47	0.17 \pm 1.53
Anterior	0.02 \pm 1.71	0.26 \pm 1.43	0.49 \pm 2.95	0.33 \pm 1.47	0.18 \pm 1.67
Posterior	0.10 \pm 1.66	0.26 \pm 1.44	0.081 \pm 1.47	0.15 \pm 1.59	0.14 \pm 1.52
FBG1	-0.17 \pm 1.81	11.75 \pm 21.49	16.33 \pm 26.01	16.33 \pm 2.89	7.02 \pm 18.43
FBG2	-0.33 \pm 1.78	0.60 \pm 4.63	2.79 \pm 9.86	0.62 \pm 2.55	0.58 \pm 3.78
FBG3	0.02 \pm 2.19	0.24 \pm 1.34	0.08 \pm 2.44	-0.29 \pm 2.27	0.02 \pm 2.13
FBG4	0.10 \pm 1.99	0.01 \pm 2.08	4.99 \pm 16.76	13.22 \pm 2.52	0.18 \pm 4.05
FBG5	-0.07 \pm 1.39	-1.89 \pm 30.40	0.08 \pm 1.47	-0.11 \pm 1.17	0.01 \pm 1.38
FBG6	0.11 \pm 1.97	0.37 \pm 1.30	0.08 \pm 1.60	-0.22 \pm 1.65	0.08 \pm 1.67
FBG7	0.02 \pm 1.78	0.77 \pm 6.65	0.57 \pm 2.68	2.67 \pm 11.84	0.22 \pm 3.23
FBG8	0.10 \pm 1.66	4.65 \pm 15.21	8.42 \pm 21.66	-0.59 \pm 3.35	0.01 \pm 2.26
FBG9	0.01 \pm 1.70	0.26 \pm 1.44	0.73 \pm 3.25	0.33 \pm 1.47	0.20 \pm 1.63
FBG10	0.10 \pm 1.66	0.22 \pm 1.50	0.15 \pm 1.78	0.24 \pm 1.40	0.17 \pm 1.59
FBG11	0.01 \pm 1.70	0.26 \pm 1.44	0.73 \pm 3.25	0.33 \pm 1.47	0.20 \pm 1.63
FBG12	0.10 \pm 1.66	0.22 \pm 1.50	0.15 \pm 1.78	0.24 \pm 1.40	0.17 \pm 1.59

4.1.1.2 Flexible sensors based on FBGs for respiratory and cardiac monitoring

There is a growing demand for strain sensors that can be used to instrument wearables for several applications ranging from clinical to sport and occupational settings. Among others, strain sensors based on FBGs encapsulated into flexible polymeric matrices have gained growing attention for cardiorespiratory monitoring thanks to the FBG intrinsic S_ϵ . In the following studies, custom wearable systems based on flexible sensors are presented.

Three specific wearable configurations are proposed:

Configuration 1: A wearable system instrumented by rectangular-shaped flexible sensors with a single FBG.

Configuration 2: A wearable system instrumented by dumbbell-shaped flexible sensors with a single FBG.

Configuration 3: A wearable system instrumented by a dumbbell-shaped flexible sensor with multiple FBGs.

Before assessing the capability of the developed wearables of cardiorespiratory monitoring, the design and the fabrication processes of the flexible sensors are described together with the results of their static and dynamic metrological characterization.

The metrological properties (e.g., sensitivity values and hysteresis behavior) are obtained since data given by the manufacturers are related to bare FBGs. When single or multiple FBGs are housed into soft matrices, the flexible material dampens the ϵ induced on the grating. The main influencing factors are matrix geometrical and mechanical properties of the matrix (e.g., dimensions, shape, and hardness), and the bonding strength at the fiber-matrix interface are the main factors that can positively/negatively affect the transmission. Therefore, for all the configurations, a metrological characterization of the developed flexible sensor has been performed to retrieve the sensor S_ϵ after the fabrication process. Moreover, the sensor response to a variety of parameters (i.e., environmental ΔT , ΔRH , and sweat) that can potentially influence the system performance in the scenarios of interest have been often investigated. In addition, the hysteresis errors (h_{err}) were evaluated to measure the energy dissipation of the sensor when subjected to period breathing and cardiac patterns. After finding out the static and dynamic characterizations of the flexible sensor, the wearable systems were developed by anchoring the encapsulated FBGs on elastic bands by using clips for Configuration 1, hooks and loops for Configuration 2, and on a stretchy t-shirt by using a medical tape for Configuration 3.

Design, fabrication, and metrological characterization

Focusing on the design of the proposed configurations:

- The flexible sensor is Configuration 1 consists of a rectangular-shaped matrix of 90 mm x 24 mm x 1 mm encapsulating an acrylate-recoated FBG sensor with a grating length of 10 mm commercialized by AtGrating Technologies. The rectangular shape was chosen since it is the most widely proposed in the state-of-the-art and easy to fabricate.
- The flexible sensor in Configuration 2 consists of a dumbbell-shaped matrix of 100 mm x 22 mm x 2 mm (with a narrow portion of 21 mm x 5 mm) encapsulating PI-recoated FBG with a grating length of 10 mm commercialized by Broptics Technology Inc. The sensor design was guided by the international standard ISO 37:2017 (Tensile Stress-Strain Properties of Vulcanized or Thermoplastic Rubber) [363]. Among various specimen size included in the standard, Type 1A has been chosen to fulfill the following requirements: *i)* the positioning of more sensors per band, one on the left side and the other one on the right side of both the thorax and the abdomen; *ii)* the well-anchorage of the sensors on the elastic bands through the dumbbell end wider than the narrow portion where the FBG is located. This solution prevents each sensor from mechanical damages which may occur during the bands dressing, improves the adhesion of the FBG to the band and, in turn, its compliance with the rib cage displacement
- The flexible sensor of Configuration 3 consists of a dumbbell-shaped matrix of 230 mm x 35 mm x 2 mm (with the narrow portion of 180 mm x 8 mm) encapsulating and an array of 4 FBGs with acrylate-recoating.

All the proposed systems were encapsulated into a frame of Dragon Skin™ 20 silicone rubber (Smooth-On, Inc. USA). Dragon Skin™ 20 has been chosen for its flexibility, stretchability, low tearing and distortion, and a wide range of service T (-53°C to 232°C) broadly covers the operating T values experienced in the application of interest [364].

The fabrication process of each flexible sensors consists of the following main steps:

1. Part A and Part B are mixed in an equal amount of weight (stoichiometric ratio 1A:1B, as suggested in the technical bulletin [364]);
2. The mixture was degassed using a vacuum chamber to promote the spillage of air trapped during mixing;
3. After vacuum degassing, the mixture was slowly poured into a custom 3D-printed mold (see Fig. 4:17) in which the FBG, placed at the midsection, is fully housed;

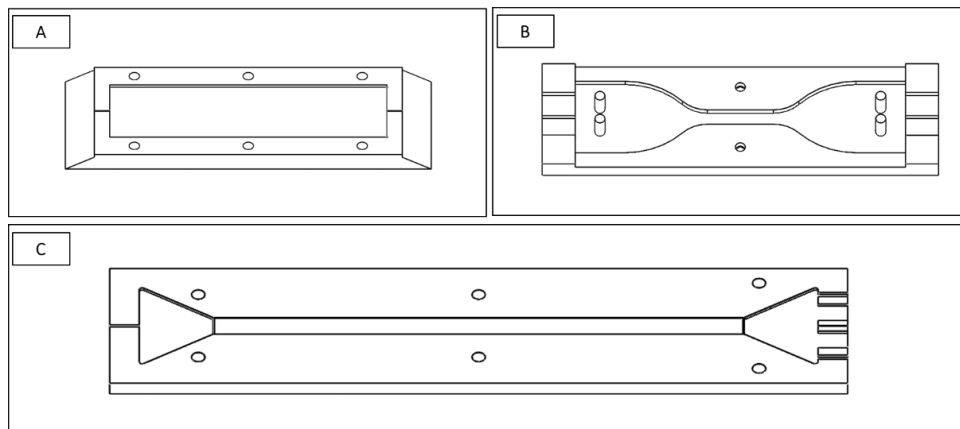


FIGURE 4.17: (A) The CAD of the mold used for the rectangular-shaped flexible sensor, (B) the one for the dumbbell-shaped sensor, and (C) the mold for the dumbbell-shaped sensors with 4 FBG.

4. Dragon Skin vulcanization was carried out at room T for four hours (as suggested in the technical bulletin [364]);
5. The flexible sensor was extracted from the mold.

Before investigating the performance of each wearable system in terms of cardiorespiratory monitoring, the response of the FBG-based flexible sensors to ϵ , under cyclic loading at velocities mimicking f_R and HR values and the influence of external agents (such as environmental ΔT and ΔRH , and sweating, for instance, caused by a high level of stress, anxiety, and intense workout) are assessed.

By way of example, the metrological characterization of the rectangular-shaped flexible sensor of Configuration 1 is described⁵ [365]. For all the other configurations, the same procedure was followed.

The characterization of the flexible sensor to controlled ϵ was performed by means of a tensile testing machine (Instron, mod. 3365). In particular, the static assessment was executed by positioning the sample between the lower base and the upper fixture of the machine at room T. A low displacement rate (i.e., $2 \text{ mm}\cdot\text{min}^{-1}$) was set to simulate quasi-static conditions, as well as $\epsilon\%_{\text{max}}$ of 2% in order to cover the ϵ range which could be experienced by the sensor in the applications of interest. The static assessment started from a resting position and ended at the position (l_{max}) corresponding to $\epsilon\%_{\text{max}}$. The ϵ applied by the testing machine to the polymeric

⁵ This work is an excerpt from "Wearable system based on flexible FBG for respiratory and cardiac monitoring" in which the Ph.D. candidate is the main author. doi: 10.1109/JSEN.2019.2916320

encapsulation (ϵ) was recorded at the sampling frequency of 10 Hz while the FBG outputs were collected by using an optical spectrum interrogator (si425, Micron Optics Inc., USA) at the sampling frequency of 250 Hz.

This mechanical test was implemented three times. The calibration curve ($\Delta\lambda_B$ vs. ϵ) was obtained by processing the collected data through a custom algorithm. The mean value of $\Delta\lambda_B$ and the related uncertainty was calculated across the three tests. The expanded uncertainty was estimated by multiplying the standard uncertainty with the coverage factor ($k=4.303$) obtained considering a t-student distribution with two degrees of freedom and a confidence level of 95% [366]. The calibration curve was calculated as the best fitting line considering the average $\Delta\lambda_B$ vs. ϵ . The S_ϵ of $0.125 \text{ nm}\cdot\text{m}\epsilon^{-1}$) was estimated as the slope of the best fitting line (see Fig. 4:18 a). The trade-off between the experimental data and the linear model was confirmed by the high value of the correlation coefficient ($R^2=0.994$).

Regarding the influence of ΔT , it was analyzed to estimate the S_T . The sensing element was positioned within a laboratory oven (PN120 Carbolite®) and exposed to ΔT of ~ 20 °C (T ranged from 26 °C to 46 °C). During tests, reference values of T were collected by a thermocouple (EL-USB-TC-LCD, EasyLog, Lascar Technology) at 10 Hz while the FBG at the sampling frequency of 1 Hz.

The value of S_T was also conceived as the slope of the best fitting line of the calibration curve $\Delta\lambda_B$ vs. ΔT . Results showed a value of S_T (i.e., $0.012 \text{ nm}\cdot\text{°C}^{-1}$) close to the value reported by the manufacturer for a nominal identical bare FBG (i.e., $S_T=0.010 \text{ nm}\cdot\text{°C}^{-1}$) as shown in Fig 4:18 b. The slight increase of sensitivity value can be due to the thermal expansion coefficient of the silicone-based elastomers larger than the one of the fiber silica. Thus, when exposed to ΔT , the polymeric matrix expands itself and, in turn, stretched the grating [367].

Concerning the influence of RH on the response of the sensing element, it was carried out by placing the piece within a custom climatic chamber. The output of a commercial RH sensor (HIH 4602A, Honeywell International Inc., Morristown-USA), used as a reference instrument, was collected by a DAQ (USB-6009, National Instruments) at the sampling frequency of 100 Hz, and RH ranged from 10% to 70%. The FBG outputs were collected simultaneously at the sampling frequency of 1 Hz. The T within the chamber was also measured by a thermocouple (EL-USB-TC-LCD, EasyLog, Lascar Technology) at the sampling frequency of 1 Hz. Results showed a non-linear response to ΔRH and S_{RH} almost negligible (Fig. 4:18 c). This result corroborates the fact that the influence of ΔRH on the sensor response is negligible. This is expected, considering that the Dragon Skin is a silicone rubber, commonly known for good hydrophobicity [368].

In addition, a set of experiments was performed to mimic challenging conditions the wearable system once worn, may be exposed to sweat. In order to simulate these conditions, the flexible FBG was immersed inside a plate filled with water. A nominal identical bare FBG was also tested to compare the two systems response and figure out whether the encapsulation influenced the flexible FBG response. The sensors' output was collected for ~ 1200 s after the immersion. The results showed no drifts of the outputs, corroborating the suitability of the proposed FBG sensor to work as a strain sensor in challenging conditions (see Fig. 4:18 d).

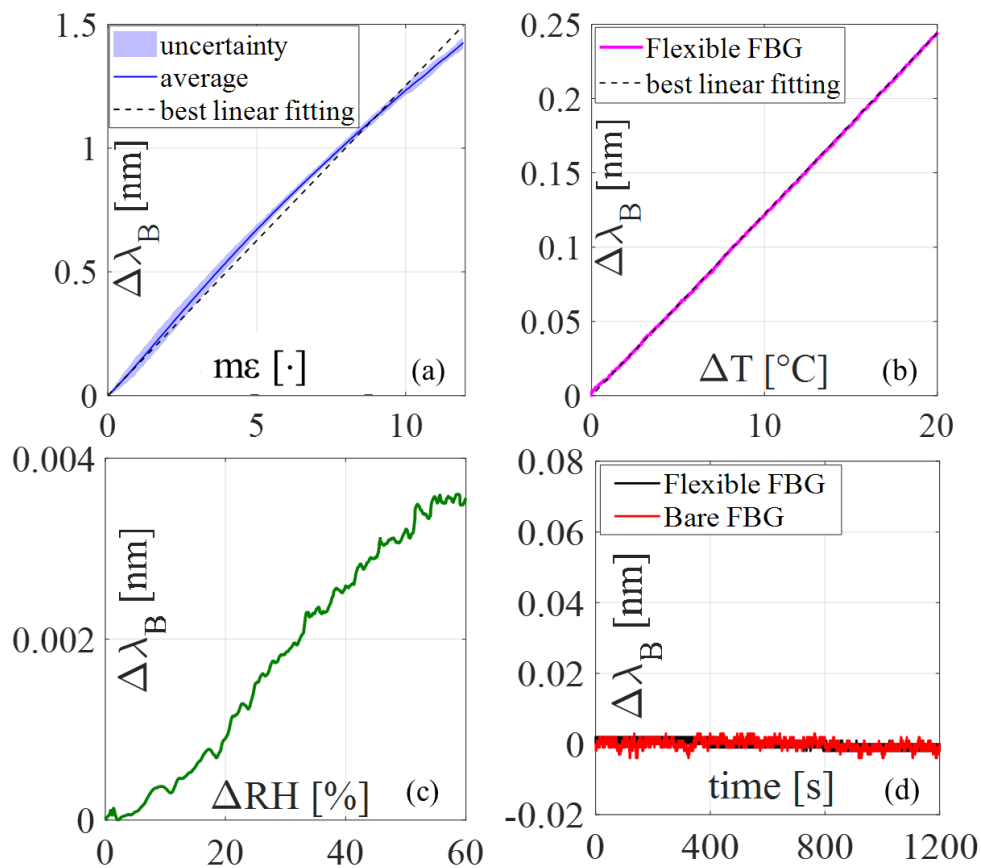


FIGURE 4:18. Results of metrological characterization: response to ϵ (a), T (b), RH (c), and water immersion (d).

Lastly, considering the periodical pattern of the respiratory and cardiac activities, the flexible sensors underwent two dynamic tests consisting of 10 hysteresis cycles at different velocities, which allow simulating f_R of 10 bpm and 20 bpm. For Configuration 2 also velocity simulating 36 bpm was added, and for Configuration 3, velocities simulating heart pumping at 30 bpm, 60 bpm, and 90 bpm were applied since this configuration is intended to be used especially for cardiac investigations (HR measurement and SCG monitoring).

Data from the tensile machine were at the sampling frequency of 100 Hz, while the FBG output was collected by an optical spectrum interrogator (si425, Micro Optics Inc.) at the sampling frequency of 250 Hz.

The h_{err} of each test was calculated starting from the difference between the value of FBG wavelength changes during the ascending and descending phases (i.e., $\Delta\lambda_B^{up}(\varepsilon) - \Delta\lambda_B^{down}(\varepsilon)$) of each hysteresis loop at the same ε (expressed in %); then, the maximum value of this difference was computed and divided by the $\Delta\lambda_B^{full-scale}$ of each loop as:

$$\%h_{err} = \frac{\max[\Delta\lambda_B^{up}(\varepsilon) - \Delta\lambda_B^{down}(\varepsilon)]}{\Delta\lambda_B^{full-scale}} \cdot 100$$

Equation 4:7

Results for the rectangular shape showed a $\%h_{err}^{max}$ of 21.4% and 26.7% for 10 bpm and 20 bpm, respectively (see Fig. 4:19). The $\%h_{err}^{max}$ values are quite large. These results can be explained considering the viscoelastic behavior of polymers [369].

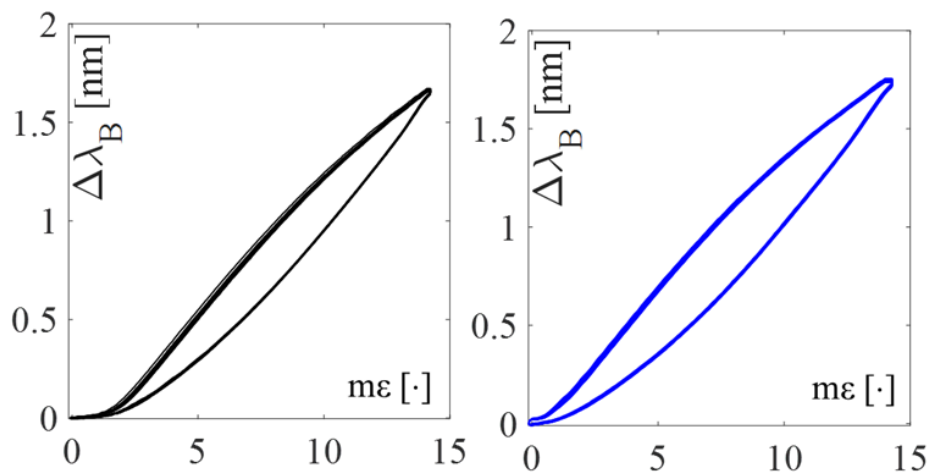


FIGURE 4:19. Hysteresis loops at velocities simulating 10 bpm (black loops) and 20 bpm (blue loops).

From the results of the metrological characterization, the influence of ΔT , ΔRH , and water immersion on the sensor response can be considered negligible for two main reasons: *i)* these parameters have a slower dynamic than the one related to the cardiorespiratory activity; *ii)* the silicone matrix shields the FBGs from environmental agents. In particular, the low thermal conductivity of silicone materials prevents the significant influence of ΔT on

the FBG output and the water-repelling capability protects the encapsulated sensors from the effect of RH or sweating. Hence, these sensing elements work as strain sensors.

The S_ϵ and the $\%h_{err}^{max}$ values for all the configurations are listed in Table 4:7.

TABLE 4:7

Configuration		S_ϵ [$nm \cdot m\epsilon^{-1}$]	h_{err}^{max} [%]		
			10 bpm	20 bpm	
1		0.125	21.4		26.7
			12 bpm	24 bpm	36 bpm
2		0.080	14.8	15.0	15.9
			30 bpm	60 bpm	90 bpm
3	FBG1	0.044	22.9	26.9	30.4
	FBG2	0.045	22.6	26.8	28.4
	FBG3	0.045	22.9	27.1	29.4
	FBG4	0.046	22.6	26.6	28.9

Configuration 1: A wearable system instrumented by rectangular-shaped flexible sensors with a single FBG⁶

The proposed study aimed to assess the capability of a wearable system consisting of two elastic bands instrumented by rectangular-shaped flexible sensors for cardiorespiratory monitoring. Firstly, tests were performed in a laboratory environment using a flowmeter and a PPG sensor as benchmarks for respiratory and cardiac activity, respectively. Then, the proposed wearable system was tested during sports activity (i.e., archery).

Two nominally identic rectangular-shaped flexible sensors were used to develop a smart textile consisting of two elastic bands (600 mm x 40 mm x 2.1 mm, 10 kg of resistance, and 100% of polyamide) worn around the thorax and the abdomen, respectively. The fit of each band was adjusted by the VELCRO® fastener. Each flexible sensor was anchored to the band using 4 automatic bottoms, one FBG in correspondence with the xiphoid process and the other one above the umbilicus. The use of anatomical landmarks allows the FBGs to be worn on the same measurement points. Each sensor consists of an FBG (Bragg wavelengths λ_B of 1541 nm

⁶ This work is an excerpt from "Cardio-Respiratory Monitoring in Archery Using a Smart Textile Based on Flexible Fiber Bragg Grating Sensors" in which the Ph.D. candidate is the main author. doi: <https://doi.org/10.3390/s19163581>

for the band around the thorax and 1545 nm for the band the abdomen, grating length of 10 mm, and reflectivity of 90%; AtGrating Technologies).

The smart textile was assessed firstly on nine healthy volunteers (four males and five females, anthropometric characteristics listed in Table 4:8, (C_T and C_A are the thoracic and abdominal circumferences) during tests carried out in a laboratory environment and then on two archers during the shooting in a real scenario.

TABLE 4:8

Volunteer	Age [years]	Height [cm]	Weight [kg]	C_T^1 [cm]	C_A^1 [cm]
1	28	182	70	82	74
2	22	168	74	60	80
3	30	163	81	62	84
4	29	180	82	69	91
5	26	153	69	48	71
6	22	166	67	58	76
7	27	173	82	71	90
8	25	160	74	60	78
9	22	172	67	55	72

Focusing on the laboratory tests, each participant was asked to perform a protocol consisting of three main phases: *i*) a short apnea useful to synchronize the reference instruments and the FBG outputs; *ii*) 16 quiet breaths; *iii*) a final apnea as long as each volunteer can.

The flexible sensors were positioned in correspondence with the xiphoid process and in correspondence with the umbilicus (see Fig. 4:20). Each FBG embedded into the smart textile (FBG^T for the band around the thorax and FBG^A for the band around the abdomen, *a* box in Fig. 4:20) was connected to an optical spectrum interrogator (si425, Micron Optics Inc., *b* box in Fig. 4:20) that worked at the sampling frequency of 250 Hz. The reference signal for the respiratory activity was collected by a commercial flow sensor (SpiroQuant P, EnviteC, *c* box in Fig. 4:20) connected to a differential pressure sensor (163PC01D75, Honeywell). The output of the reference system used for the respiratory monitoring was collected by using a DAQ (NI USB-6009, National Instrument, *d* box in Fig. 4:20) and a custom Virtual Instrument developed in LabVIEW® environment at the sampling frequency of 250 Hz. The reference system for the cardiac monitoring was a PPG sensor (*e* box in Fig. 4:20), placed on the index fingertip of the left hand, as in [354]. The PPG sensor was input into two other analog ports of the same DAQ used for the respiratory monitoring and collected at the sampling frequency of 250 Hz.

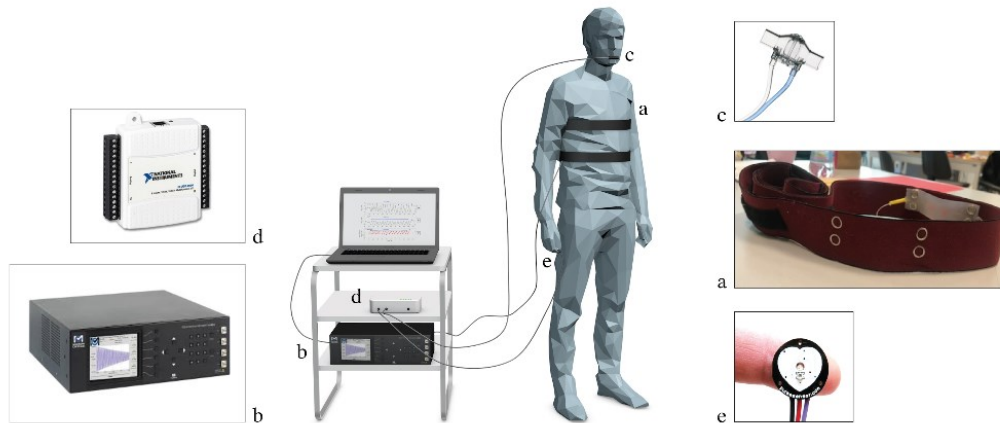


FIGURE 4:20. The experimental setup.

The collected data were analyzed to estimate f_R (during quiet breathing) and HR (during apnea). For each volunteer, data were processed following four main steps:

1. the outputs of the FBGs and the flow sensor were synchronized by selecting the first minimum points (i.e., starting points) after the starting apnea (see Fig. 4:21);
2. the quiet breathing stage was selected by cutting all the synchronized signals from the mentioned starting points and considering all the 16 breaths performed during the protocol (Fig. 4:21);
3. a filtering stage consisting of a second-order pass-band filter (lower cut-off frequency of 0.05 Hz and higher cut-off frequency of 0.5 Hz) was applied on both FBGs and flow sensor outputs;
4. a custom algorithm was used to select the maximum peaks of each signal (Fig. 4:22).

The respiratory periods (i.e., T_{R^A} and T_{C^T} for the band around the abdomen and the thorax, respectively, and $T_{R^{FLOW}}$ for the flow sensor) were calculated as the time interval between two consecutive maximum peaks. Then, the f_R values estimated by both the FBGs (i.e., f_{R^A} and f_{R^T}) and the flow sensor (i.e., $f_{R^{FLOW}}$) were calculated as the ratio between 60 and the respiratory period in order to express f_R in bpm.

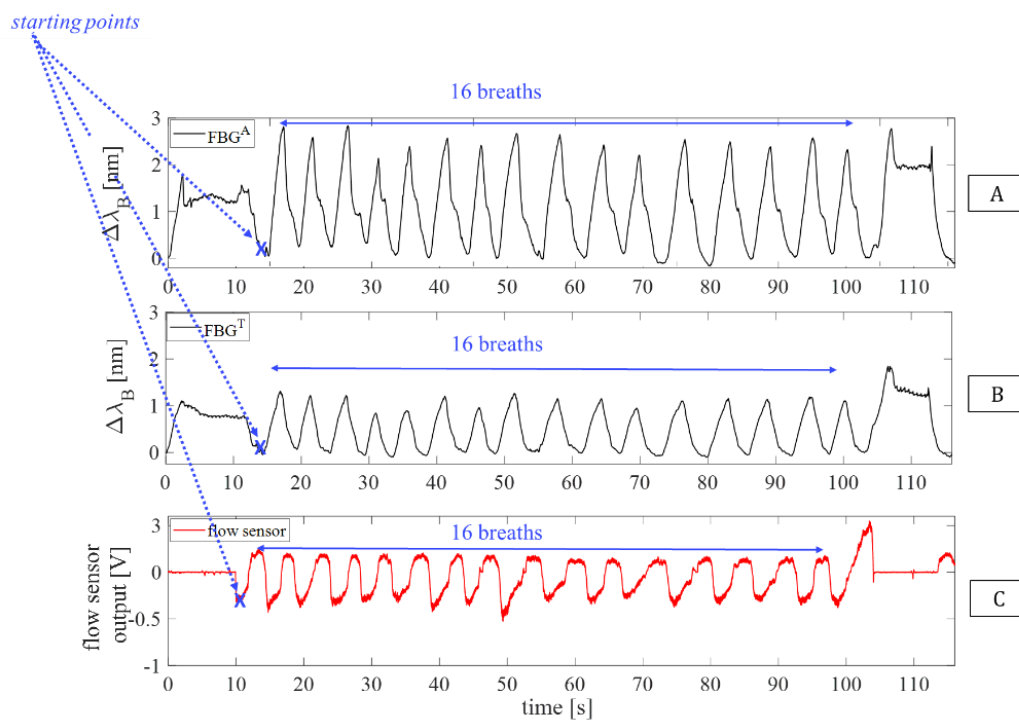


FIGURE 4:21. Signals collected during the experimental protocol by the FBG on(A) the abdomen, (B) THE thorax, and (C) the flow-meter.

The smart textile was assessed in terms of both breath-by-breath and mean f_R values. The Bland-Altman analysis was performed to describe the agreement between f_R values estimated by the proposed system and the reference one [370]. This analysis considered all the f_R values of the enrolled volunteers (*i.e.*, a total of 135 f_R values for each Bland-Altman analysis) for the calculation of MOD and LOAs. The mentioned analysis was performed considering the data provided by each flexible sensor. The mean absolute percentage error in the f_R estimation (*i.e.*, $MAPE^{f_R}$) was used to compare mean f_R values and was calculated as:

$$MAPE^{f_R} = \frac{1}{n} \cdot \sum \frac{|f_R^{smart_textile} - f_R^{reference}|}{f_R^{reference}} \cdot 100$$

Equation 4:8

with $f_R^{smart_textile}$ and $f_R^{reference}$ the values of the f_R obtained by the proposed system and the reference one, respectively.

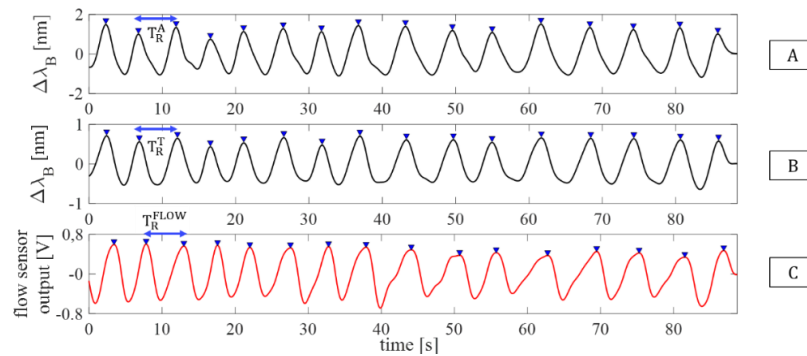


FIGURE 4:22. The peaks detection.

Results of the breath-by-breath analysis are shown in Fig. 4:23 and Table 4:9.

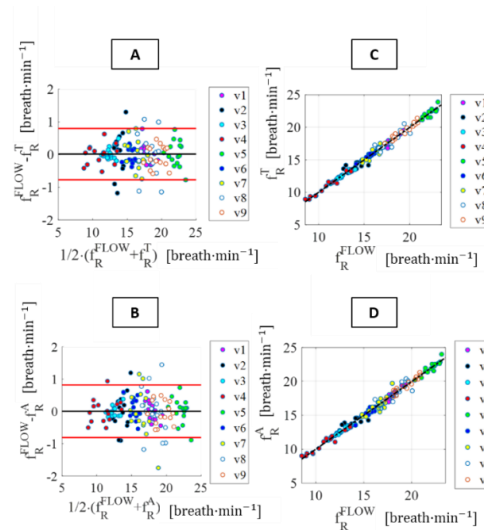


FIGURE 4:23. The Bland-Altman plots with the linear regression for breath-by-breath f_R estimation.

TABLE 4:9

	R^2	MOD [bpm]	LOAs [bpm]	MAPE f_R [%]
f_R^T	0.99	0.014	-0.804; 0.832	1.92
f_R^A	0.98	0.004	-0.811; 0.819	1.97

The good agreement between the f_r values measured by the proposed system and the reference one is confirmed by the high value of the correlation coefficient for both FBG^T and FBG^A and by the low value of both MOD and MAPE^{FR}.

The HR estimation during the apnea was performed by following four main phases:

1. for each trial, the first minimum points after the holding of breath were selected on the FBGs output to define the starting point of the apnea stage for the FBGs and the PPG sensor;
2. the same time interval (*i.e.*, 10 s) was chosen to estimate HR of all the volunteers during the apnea (see Fig. 4:24);
3. a fourth-order Butterworth pass-band filter with a lower cut-off frequency of 0.6 Hz and a higher cut-off frequency of 20 Hz was applied to the signals. This band of frequency was chosen according to the frequency components of vibrations induced on the chest wall by the blood flow ejection into the vascular bed [371];
4. a custom algorithm was used to select minimum peaks (blue markers in Fig. 4:25) on each filtered FBG signal. The beat-by-beat cardiac period (T_c) from the FBG outputs was calculated considering the minimum peaks, as the time elapsed between two consecutive minimum peaks (T_c^T and T_c^A from the band around the thorax and the abdomen, respectively). Minimum peaks were chosen because easier to be detected on the filtered FBG signals automatically. Beat-by-beat cardiac periods were calculated considering the time interval between two consecutive maximum peaks on the filtered PPG signal (T_c^{PPG}). The HR values (*i.e.*, HR^A , HR^T , and HR^{PPG}) were calculated as the ratio between 60 and T_c^T , T_c^A , and T_c^{PPG} ; in this way, HR is expressed in bpm.

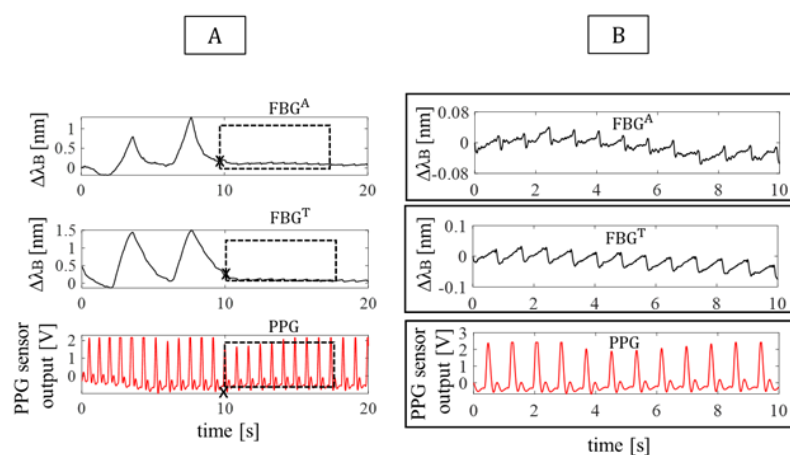


FIGURE 4:24. A zoom on the apnea stages collected by FBGs and PPG sensor.

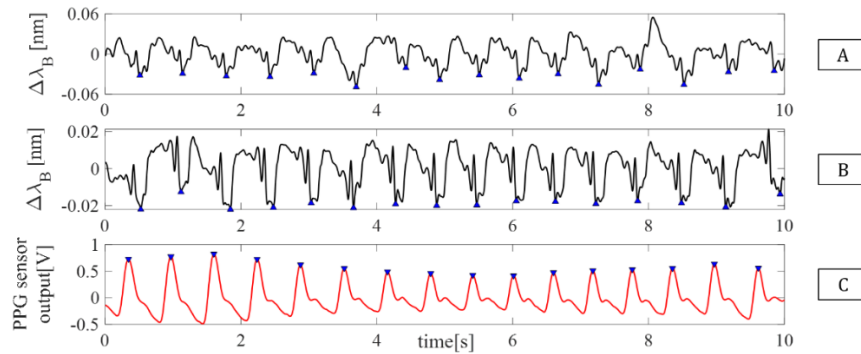


FIGURE 4:25. The peak detection.

The smart textile capability of monitoring HR was assessed in terms of beat-by-beat and mean HR values. The Bland-Altman analysis was performed comparing HR values estimated by the proposed system and the reference one, considering all the volunteers for a total number of 149 beats. The mean absolute percentage error (*i.e.*, $MAPE^{HR}$) was also calculated as follows:

$$MAPE^{HR} = \frac{1}{n} \cdot \sum \frac{|HR^{smart_textile} - HR^{reference}|}{HR^{reference}} \cdot 100$$

Equation 4:9

with $HR^{smart_textile}$ and $HR^{reference}$ values estimated by the smart textile and the PPG sensors, respectively. Results of the beat-by-beat analysis are shown in Fig. 4:26 and Table 4:10.

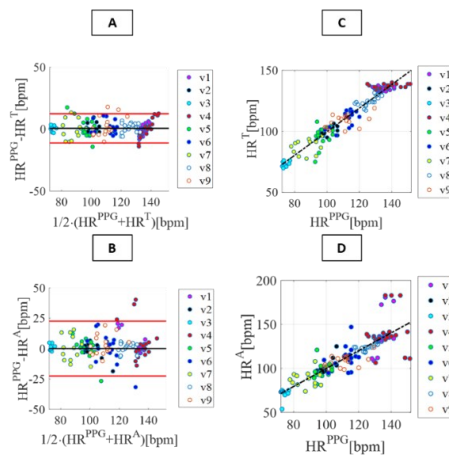


FIGURE 4:26. The Bland-Altman plots with the linear regression for beat-by-beat HR estimation

The good agreement between the f_r values measured by the proposed system and the reference one is confirmed by the high value of the correlation coefficient for FBGT and FBGA and the low value of both MOD and MAPE^{HR}.

TABLE 4:10

	R ²	MOD [bpm]	LOAs [bpm]	MAPE ^{f_r} [%]
HR ^A	0.76	0.059	- 22.54; + 22.65	5.74
HR ^T	0.91	0.664	-11.15; +12.48	3.92

After assessing the system performance in terms of the capability of cardiorespiratory monitoring in a laboratory environment, the proposed wearable system was also tested on two archers (a male and a female) for application in a sport setting. Their anthropometric characteristics are listed in Table 4:11.

TABLE 4:11

	Age [years]	Height [cm]	Weight [kg]	C _T [cm]	C _A [cm]	Experience [years]	Training frequency [days per week]
Archer 1	20	167	65	97	80	3	3
Archer 2	33	165	64	75	60	2	6

In archery, the control of breathing and heart beating is crucial to help the body to remain stable in the shooting position. To improve body stability, archers try to adopt similar breathing patterns and low heartbeat during each shot. The shooting action can be separated into three main phases: set-up, aiming, and release. During the set-up phase, shoulders are brought in line with the target, hips are rotated forward, and the hand position on the bow grip is set-up. During the aiming phase, the focus is completely diverted to the target, and the alignment of bow-sight-target is performed. The shooting of the arrow takes place in the release phase.

In these tests, the two archers were invited to perform two shooting sessions. Each session consists of six arrows to be shot in 5 minutes at designed 70 m targets. The first session is a practice round. In this round, the arrows are shot at the beginning and do not count as part of the score. Instead, the second one is a scoring round with an awardable maximum score of 60 points (10 points for arrow).

During each shooting session, archers wore the flexible sensors on the same positions investigated during tests on volunteers (see Figure 4:27). The optical spectrum interrogator (si425,

Micro Optics Inc.) for the acquisition of the FBGs output was placed at 3 m of distance from the archer. The sampling frequency was 250 Hz. Since the smart textile assessment was previously performed on volunteers during in-lab tests, no reference instruments were used during the shooting action to not impair the archer's movements.

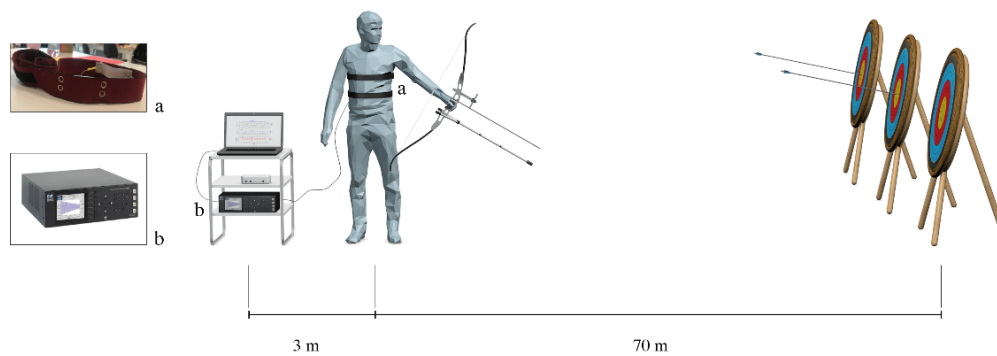


FIGURE 4:27. The experimental setup during shooting.

Changes of FBG^T and FBG^A output of the two practice shooting sessions are plotted in Fig. 4:28.

The analysis was performed by selecting FBG^T output because the respiratory acts and the shooting phases are clearly discernible, while FBG^A output has a more irregular trend (see Fig. 4:28). FBG^T output changes were analyzed following three main steps:

1. the six shooting actions were selected, as shown in Fig. 4:28;
2. for each shooting action, the signal related to the aiming phase was filtered, and its minimum peaks were detected to calculate the HR values (Fig. 4:29);
3. the signal related to the breathing activity which precedes the shooting actions was filtered, and its maximum peaks were detected to estimate the f_R values. The filtering stage, the peak detection algorithm, and the f_R and HR estimation were carried out as in Section 3. Results in terms of f_R and HR for all the four trials are summarized in Table 4:12.

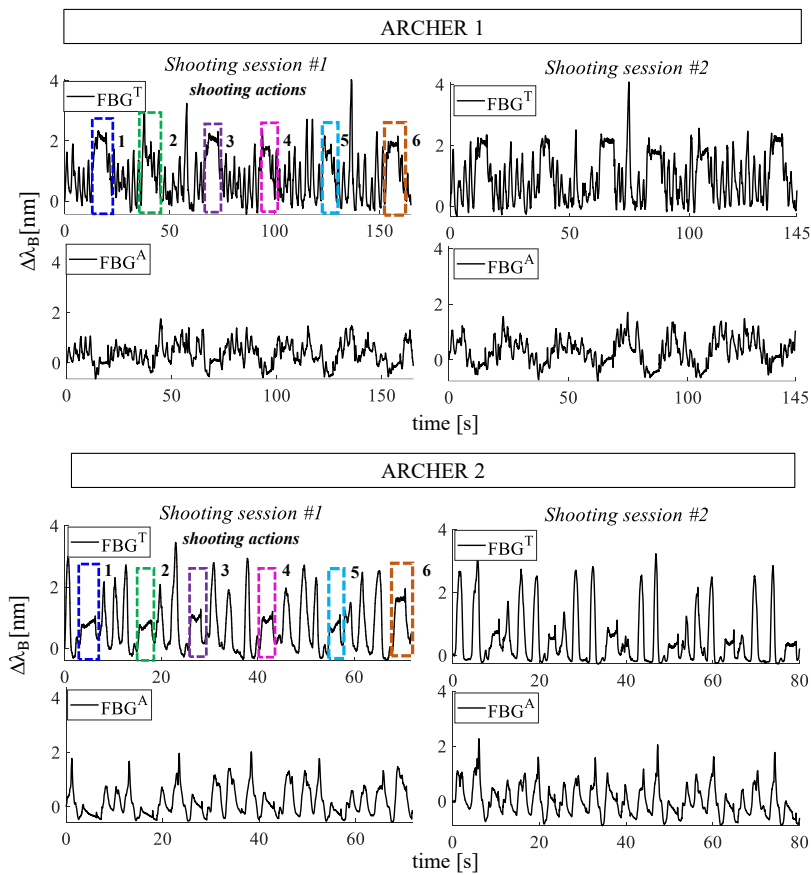


FIGURE 4:28. Shooting actions performed by archer 1 and archer 2.

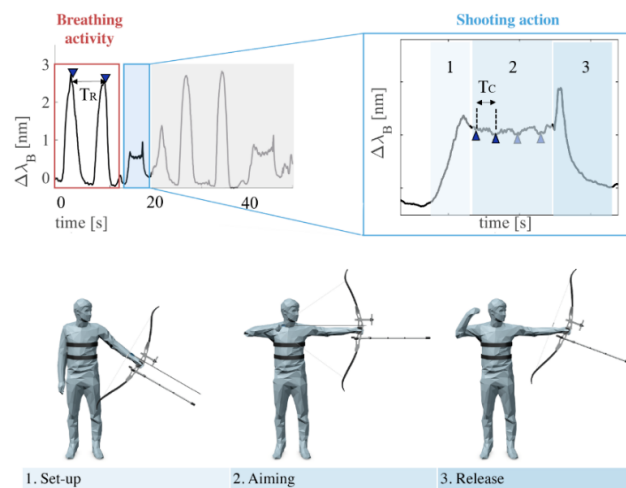


FIGURE 4:29. The phases of a single shooting action and the collected signal.

TABLE 4:12

	Shooting session #1						Shooting session #2					
shot	1	2	3	4	5	6	1	2	3	4	5	6
	f_R [bpm]						f_R [bpm]					
Archer 1	23.9	24.6	20.0	26.5	21.9	20.5	24.1	25.0	20.6	26.5	25.6	23.9
Archer 2	15.2	13.3	9.3	8.6	10.1	8.4	7.4	8.5	7.6	8.8	9.0	7.1
	HR [bpm]						HR [bpm]					
Archer 1	101.8	101.3	97.3	96.7	100.0	94.9	116.4	113.7	108.9	104.7	120.5	115.9
Archer 2	87.6	89.2	94.3	89.3	97.3	94.1	97.2	88.3	92.0	92.3	82.1	90.5

The main novelties of this investigation were the assessment of the custom wearable system on volunteers for monitoring of both respiratory and cardiac activities and its application in archery during shooting sessions. In the literature, FBGs encapsulated into flexible materials for cardiorespiratory monitoring were mainly proposed for clinical applications (e.g., during magnetic resonance exams). These technological solutions consist of FBG sensors encapsulated into polydimethylsiloxane, PDMS [372], polyvinyl chloride, PVC [229], and fiberglass[373]. In [372], an FBG was encapsulated into PDMS matrix (dimensions: 85 mm x 85 mm x 5 mm). Tests were carried out by positioning the sensing element on the back of two males and two females during MR examination. Results showed maximum relative errors of 4.41 % and 5.86% for respiratory and cardiac monitoring, respectively. In [22], an FBG was housed into fiberglass matrix (dimensions: 30 mm x 10 mm x 0.8 mm).

The accuracy of the proposed sensor was characterized by relative error < 4.64% for f_R and < 4.87% for HR. In the present study, tests performed on volunteers showed promising results in both the estimation of both f_R and HR (i.e., $MAPE^{f_R} \leq 1.97\%$ and $MAPE^{HR} \leq 5.74\%$). Focusing on the shooting sessions, results showed that the proposed system can detect all the six shooting actions and, in turn, monitor f_R during the breathing activity and HR during the aiming phase. In the literature, commercially available devices able to monitor only one of these parameters (f_R and HR) were used on archers [374] [2], [376], and [377]. All these studies showed that both f_R and HR are important, and they influence archers' performances.

Configuration 2: A wearable system instrumented by dumbbell-shaped flexible sensors with a single FBG⁷

The proposed study aimed to monitor f_R in an occupational setting while mimicking real working tasks. The f_R is considered one of the most reliable worker mental load and fatigue state indicators that may lead to work injuries. Monitoring this parameter through wearable devices represents an efficient solution for the maintenance of Occupational Health and Safety.

This study proposed a wearable system consisting of two elastic bands instrumented by four dumbbell-shaped flexible sensors. Each sensing element consists of a commercial PI-coated FBG encapsulated into a Dragon Skin™ 20 matrix. The choice of PI as fiber coating instead of acrylate is motivated by the higher flexibility and handiness of PI-recoated optical fiber [378]. The size and shape of the encapsulating matrix were chosen to enhance the flexible sensor sensitivity to uniaxial ϵ and improve the adhesion of the FBG to the band, resulting in a better compliance with the rib cage displacement. [379],

The anchorage of the flexible sensors to the band is performed thanks to two 3mm-diameter holes interspaced by 5 mm on the ends of the matrix. In this way, no matrix cracks and lacerations occur because of the implementation of a bonding mechanism (e.g., automatic buttons) after the polymer vulcanization. Each band has a length of 1 m with two Velcro® straps to make it suitable for different anthropometric characteristics. Two multiplexed flexible dumbbell-shaped sensors with λ_B values of 1549 nm and 1557 nm were anchored on each band using four hooks handsewn on the fabrics and two rectangular pad plates with two loops each. The rectangular-shaped pad plates are provided (55 mm x 10 mm x 2 mm) with two u-shaped loops (3 mm of diameter) to join a hook couple.

The hooks-and-loops anchoring system allows the flexible sensor to be placed on the band along a specific direction after its dressing around the chest (i.e., on the thorax and the abdomen). The locking of the flexible sensor to the pad plates is performed by clamping the matrix ends of each sensor between the pad plate in contact with the back surface (back pad plate in Fig. 4) of the sensor and an additional smaller rectangular plate (21 mm x 10 mm x 2 mm) on the front (front plate in Fig. 4:30).

⁷ This work is an excerpt from "A wearable system based on flexible sensors for unobtrusive respiratory monitoring in occupational settings" in which the Ph.D. candidate is the main author. doi: 10.1109/JSEN.2020.3036443

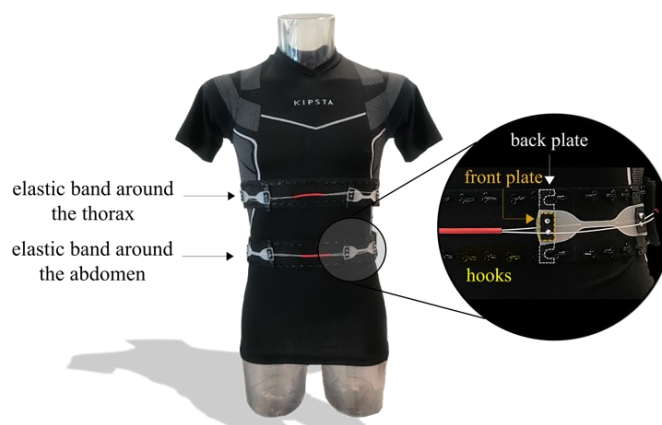


FIGURE 4:30. The wearable system with a zoomed detail of the anchoring system. The front rectangular plate is highlighted, the back-pad plate with U-shaped loops in dotted line, hooks in yellow.

The developed system was assessed on ten healthy volunteers with the following age and anthropometric features expressed as mean \pm standard deviation: age of 28 ± 4 years old, height of 165 ± 9 cm, body mass 61.5 ± 10.5 kg, and chest circumference 87.7 ± 9.7 cm.

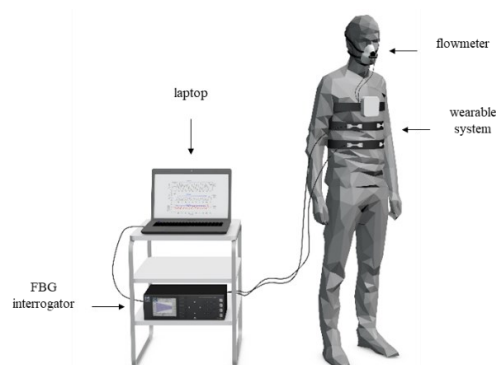


FIGURE 4:31. The experimental setup.

Each volunteer was invited to wear a tight shirt and stand still while an operator helped him/her to wear the wearable system. In particular, two stretchable elements were tightened with some Velcro strips around the subject's torso in thoracic and abdominal positions, respectively. Then, two sensing elements (each of which embeds two flexible sensors) were securely anchored upon the two elastic bands via the adjustable systems of hooks fixed at the extremities of the sensors. The experimental setup is shown in Fig. 4:31.

An FBG interrogator (Hyperion si255, Micron Optics) was used to collect FBGs outputs at the sampling frequency of 100 Hz. To assess the performances of the wearable system, we used as

a reference instrument a commercial variable orifice flowmeter (SpiroQuant P by EnviteC, Honeywell), which provides a restriction to the airflow allowing transducing the flowrate in a pressure drop between two static taps. The flowmeter has been coupled with a differential pressure sensor (163PC01D36, Honeywell), which transduces the pressure drop into a voltage. This voltage is then recorded using a custom electronic board embedding a 12-bit analog-to-digital converter (ADC MAX 1239 by Maxim), a microcontroller (STM32F446RET by STMicroelectronics), and a Bluetooth module (SPBT2632C2A by STMicroelectronics) for wireless data transmission at 100 Hz. The box containing the pressure sensor and the data acquisition board was placed in the sternal position with some stripes of adhesive polymeric tape, and the flowmeter was placed at the volunteer's mouth with the help of a commercial breathing mask.

To pilot the experimental protocol, two Graphical User Interfaces (GUIs) were developed in LabVIEW (National Instruments, TX, USA). The first GUI was used to synchronize and save the outputs readout of the wearable system, namely the FBGs, and the benchmark, namely the flowmeter. The other GUI has been implemented to make the experiment clearer to the participant and improve engagement during the test, guiding the subject to perform the current task associated with an image as a virtual instructor. The subject was then instructed on the movements to be executed and invited to follow the sequence of images displayed in the GUI. Two progress bars were used to indicate respectively, the number of tasks to complete the protocol and the remaining time to complete the current task.

The following trials were tested during five protocols (Fig. 4:32):

- 1st. A time interval of 60 s of eupnea and 60 s of tachypnea, both in standing, sitting, and supine static postures;
- 2nd. A time interval of 120 s of self-paced walking;
- 3rd. Cyclical changes of three different postures (i.e., standing, sitting, and prone), keeping each position for 30 s;
- 4th. Isolated upper limbs and trunk movements (i.e., frontal bending of the trunk, maximum right torsion of the trunk, maximum left torsion of the trunk, maximum arms up, lateral lifting of the arms, and frontal lifting of the arms), keeping each position for 10 s;
- 5th. Combination of different upper limbs and trunk movements consecutively performed (i.e., starting from a standing position, grab a target item laterally placed on the ground -on the left and the right-, move it frontally on a rack and then replace it back on the ground), repeating each cycle four times.

The experimental design of the presented protocol aimed at assessing the ability of the sensing system in tracking the subjects' breathing activity in selected static and dynamic conditions characterizing working settings. Specifically, trial 1 aims at evaluating f_R in the absence of body motions, while trials 2, 3, and 4 aim at estimating f_R during the execution of dynamic tasks. Finally, trial 5 aims at investigating the performances of the wearable in a real working scenario, mimicking some typical working tasks.

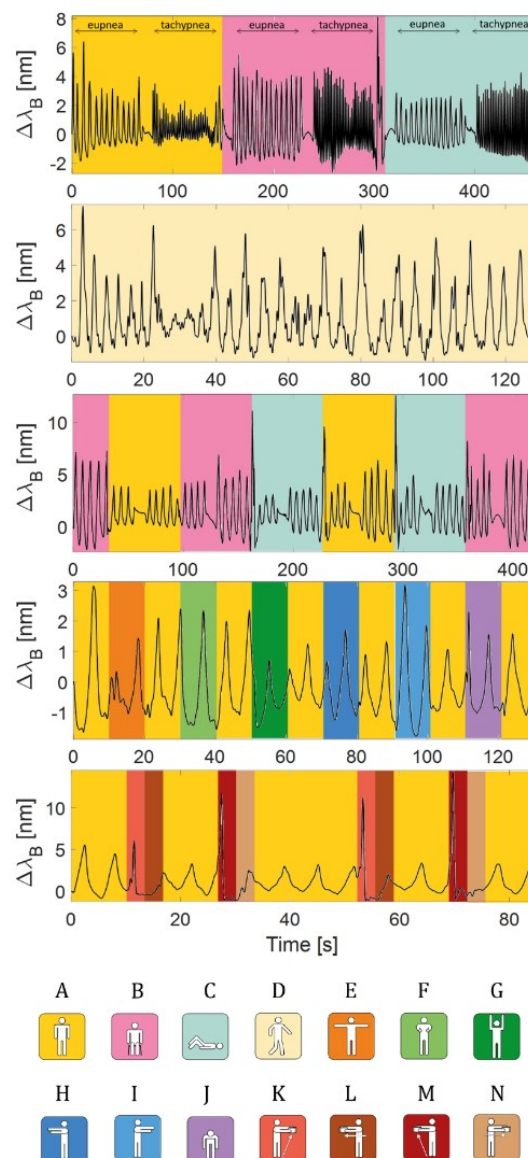


FIGURE 4.32. From top to bottom, the five designed protocols. Each box is colored as the icon representing the activity performed by the volunteer during the execution of the protocol. The activities are: A) standing, B) sitting, C) supine, D) walking, E) lateral lifting of the arms, F) front lifting of the arms, G) maximum arms up, H) maximum right torsion of the trunk, I) maximum left torsion of the trunk, J) front bending of the trunk, K) lifting an item from the ground on the left, L) lifting an item from the ground on the right, M) lifting an item from the ground on the right and N) moving the item from right to left.

The acquired data have been processed offline in MATLAB by the following steps:

1. The reference instrument signal has been filtered using a 3rd order Butterworth band-pass filter with a low cutoff frequency of 0.05 Hz and a high cut-off frequency of 2 Hz.
2. The 4 FBG signals have been summed together and then filtered using a 3rd order Butterworth bandpass filter with a low cutoff frequency of 0.05 Hz and a high cutoff frequency of 2 Hz.
3. f_R estimation. The f_R value has been estimated by identifying the inspiratory maxima peaks and then calculating the reciprocal of the averaged time differences between consecutive peaks, thus obtaining $f_R^{ref}(i)$ and $f_R^{FBG}(i)$

In this process, the detection of maxima peaks is crucial. Therefore, given the variability of the respiratory ranges within each trial, the identification of maxima peaks has been performed by considering a moving time window of 15 s for each sampling point (Fig. 4:33).

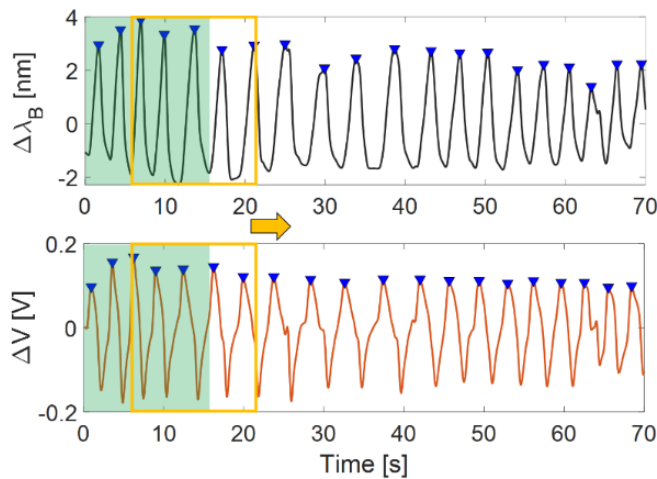


FIGURE 4:33. The moving window used to estimate f_R .

Therefore, identifying an instantaneous f_R value for both the reference and the wearable systems, which averaged in the i -th time window, allows obtaining $f_R^{ref}(i)$ and $f_R^{FBG}(i)$. Finally, we averaged $f_R^{ref}(i)$ and $f_R^{FBG}(i)$ obtaining $\overline{f_R^{ref}}$ and $\overline{f_R^{FBG}}$ for each protocol.

To assess the overall performance of the system for each protocol, we also calculated the mean $\overline{f_R^{ref}}$ and $\overline{f_R^{FBG}}$ among all volunteers. Results are listed in Table I in [380].

To evaluate the proposed wearable device's performance compared to the reference instrument, the percentage error ($\%e_{fR}$) has been computed as in the following equation.

$$\%e_{f_R} = \frac{\overline{f_R^{FBG}} - \overline{f_R^{ref}}}{\overline{f_R^{ref}}} \cdot 100$$

Equation 4:10

The average $\%e_{f_R}$ and the absolute percentage error $|\%e_{f_R}|$ have been computed for each subject and protocol. The overall results are listed in [380].

The proposed wearable system showed a proper match with the reference instrument as testified by both the $\overline{f_R^{ref}}$ and $\overline{f_R^{FBG}}$ values and the $\%e_{f_R}$ values. Indeed, the $\%e_{f_R}$ was lower than 5% in all volunteers except for volunteer 2 during the third protocol, in which the error was of 9.9%. Regarding the average errors, values ranging from -0.33 % and 3.38 %, and from 1.0 % and 4.2% were found for $\%e_{f_R}$ and $|\%e_{f_R}|$, respectively.

The main strengths of the proposed study rely on: *i)* the PI fiber recoating, which improves the robustness of the optical fiber and reduces the slippage between the coating and cladding than the acrylate one; *ii)* the dumbbell shape, which allows better adhesion of the sensing part to the band, a well-anchorage of the sensors through the wider matrix ends, a well-compliance to the chest wall displacement and the optimization of the tensile strength concentration in the narrow portion of the flexible matrix; *iii)* the good performance of the wearable system in the f_R estimation during simulating working activities.

The lower S_e value of the proposed sensor than the one of the FBG sensor encapsulated into a rectangular-shaped matrix (0.08 nm·mε⁻¹ vs. 0.20 nm·mε⁻¹) described in the previous works may be explained considering that there may be a weaker bonding between Dragon Skin™ and PI coating than between Dragon Skin™ and acrylate (i.e., materials used in [38]). However, the proposed sensors showed high inter-subject variability. Otherwise, S_T values are comparable. Lastly, lower $\%h_{err}$ values suggest a lower energy dissipation in the dumbbell-shaped one than in the rectangular.

The similar system proposed and tested on archers for respiratory and cardiac monitoring showed performance of the flexible rectangular-shaped sensors slightly higher than the ones of the wearable system proposed in this study (in the worst case, $\%e_{f_R} < 1.97$ % vs. 5%), but the scenario of interest is different. Indeed, in those experimental trials, f_R is monitored during a precision sport (i.e., archery), which requires stable chest maintenance and slow/quiet breathing with apnea stages during the arrow release. Otherwise, in this study, the system was tested during more challenging working activities where breathing-unrelated movements occur and may affect its performances.

Configuration 3: A wearable system instrumented by a dumbbell-shaped flexible sensor with multiple FBGs

The continuous monitoring of the patient's heart beating is very useful since cardiac diseases are the leading cause of death worldwide. In the last decades, electrocardiography and photoplethysmography have been used as dominant cardiac monitoring techniques. ECG electrodes greatly limit the user's mobility, while PPG sensors are very susceptible to motion artifacts caused by hand movements that affect the accuracy in HR estimation during daily routine activities. The proposed configuration was developed with the aim of using a flexible sensor as a promising alternative technique for recording the vibrations/displacements induced by the heart pumping on the chest surface.

The proposed wearable system consists of a custom-made fiber optic array of 4 FBGs equally spaced of 2 cm, and encapsulated in a flexible polymer. Each sensing element consists of an FBG with a different Bragg wavelength ($\lambda_B^{\text{FBG1}} = 1525$ nm, $\lambda_B^{\text{FBG2}} = 1533$ nm, $\lambda_B^{\text{FBG3}} = 1541$ nm, and $\lambda_B^{\text{FBG4}} = 1549$ nm, with a grating length of 10 mm).

The preliminary assessment of the system performance was performed on a healthy volunteer. He was asked to lay on a mattress in a supine position with the flexible sensor taped on a t-shirt with three electrodes placed underneath to collect the reference ECG signal. The SCG waveforms were recorded in twelve different measurement sites. Four sites were recorded simultaneously, so three different trials were carried out by positioning the sensor as in Fig.4:34 (i.e., horizontally on the sternum left side, vertically between the xiphoid process and the umbilicus, and horizontally above the umbilicus). Data from the flexible sensor were collected using an optical spectrum interrogator (si255 based on HYPERION platform; Micron Optics Inc.) at the sampling frequency of 1 kHz. Simultaneously, an AD8232 ECG sensor was used as a gold standard to record the ECG waveform.

During the experiments, the volunteer was invited to hold his breath for approximately 20 seconds after lung inflation at his maximum inspiration volume to emphasize the vibrations exclusively originated from the mechanical heart activity.

A custom algorithm was developed in MATLAB environment and used to synchronize and properly filter the collected data. A band-pass filter between 0.5 and 100 Hz was applied to the ECG signal, while the raw FBGs outputs were band-pass filtered in the range 20 Hz - 60 Hz to emphasize the mechanical activity of the cardiac aortic and mitral valves. The preliminary results showed the proposed solution's capability to detect SCG signals in all the measuring sites and the peaks related to the opening and closure of the aortic valve AO/AC, mitral valve

MO/MC, the isovolumetric moment IM and the rapid ejection RE are clearly identified. Further efforts will be devoted to enlarging the sample size, implement methods to identify mechanical events automatically, and estimate HR and HRV from SCG waveforms. Moreover, additional analysis will be carried out to investigate the influence of the measuring sites on the signal-to-noise ratio and cardiac events identification. The mechanical events identification coupled with the HR estimation (even collected by an ECG device) could open up new insight into the understanding of cardiac events and cardiovascular pathologies.

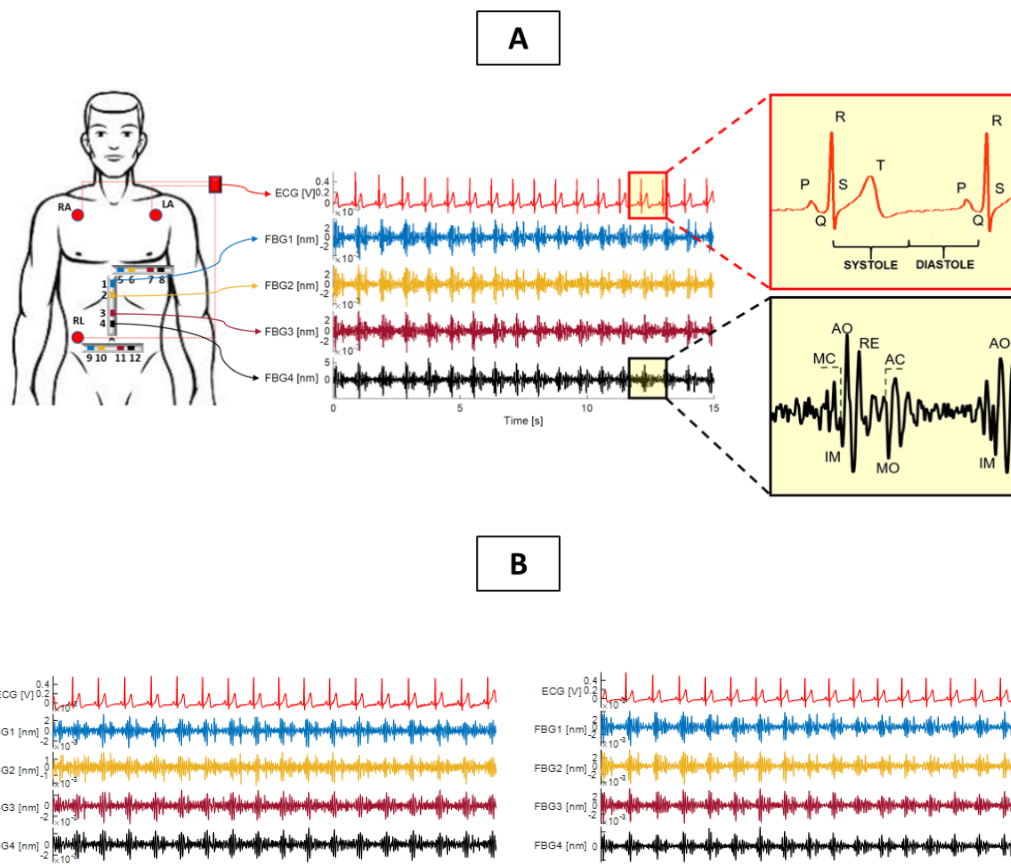


FIGURE 4.34. (A) The positioning of the ECG electrodes (RA, LA, and RL) and the flexible sensor (in the three positions: horizontally along the left side of the sternum, above the umbilicus, and vertically between the xiphoid process and the umbilicus). The ECG signal with the corresponding SCG signals recorded by the 4 FBGs is shown on the right with a zoom on two consecutive beats related to the ECG signals and the corresponding SCG signal with the proper fiducial points. (B) the signals collected when the sensor is placed vertically (on the left) and horizontally over the umbilicus (on the right).

4.1.2 Thermo-hygrometric conditions of respiratory gases

The development of FBG-based wearable systems for monitoring changes in thermo-hygrometric conditions of respiratory gases and from them f_R is based on the use of active coatings necessary for making FBGs sensitive to RH. This process is known as FBG functionalization.

Several materials have been proposed in the literature to coat optical gratings with thin active films. Among them, hygroscopic synthetic (e.g., PI, PMMA, SiO₂, TiO₂) and natural polymers (Agar, Agarose, and Chitosan) have been the most useful [239]. As for the encapsulated FBG, a metrological characterization of these sensing elements is mandatory after the fabrication processes to retrieve S_{RH} as well as the response times (τ_r , τ_s and τ^{63}) considering the dynamics of the phenomena under investigation.

The following section presents two configurations of systems based on functionalized FBGs:

Configuration 1: A smart needle encapsulating a 1 wt% agar-coated FBG for RH and f_R monitoring.

Configuration 2: An MR-compatible wearable system based on a silicone matrix encapsulating a 1 wt% agar-coated FBG for f_R monitoring.

To assess both these configurations' performances, a mechanical ventilator and a spirometer were used as reference instruments for Configuration 1 and a MoCap system for Configuration 2.

Before describing each configuration and the achieved results, a look inside at the design, the fabrication, and the metrological characterization of the functionalized FBGs is necessary. Moreover, the influences of coating polymer wt% and t_k on the sensor performances are also investigated. These results guided the development of a high performant sensing solution able to work in the breathing zone for respiratory monitoring.

Design, fabrication, and metrological characterization

Agar was chosen as an active coating in both the configuration thanks to its low tendency to evaporate, its biocompatibility, and its good adhesion to silica. Agar is made of agarose, the component with excellent gelling ability, and agarpectin, in different proportions, commonly 75% of agarose and 25% of agarpectin. Agarose is a linear and neutral polysaccharide whose

linear chains arrange themselves into double helixes. Three-quarters of hydroxyl groups in each helix structure can interact with other helixes or solvents through hydrogen bonds, while one-quarter is directed internally and can interact with water molecules trapped inside the helix. Agaropectin, instead, is characterized by poor gelling ability [381]. Agar is soluble in hot water, and the solution forms a gel on cooling to about 35–45 °C, which does not melt below 85°C [382].

The agar-based FBG functionalization was usually carried out, following four steps:

1. A bare FBG sensor is cleaned by using ethanol alcohol for enhancing the polymer adhesion to silica;
2. The sensor was placed into grooves of a 3D-printed mold. The straightness of the sensing part is important to achieve a uniform coating and to avoid polymer adhesions on the internal surface of the mold. Thus, FBG is keeping straight by two magnet clips that grasped the optical fiber on either side. Then, an adhesive tape is used to block the fiber tips, and the clips were removed; A negligible ε is induced;
3. The agar-based solutions are deposited on the FBG sensing part;
4. The drying process is carried out at controlled environmental conditions to avoid rapid changes in the drying kinetics, affecting the polymer cross-linking [383];
5. After 48h, the last two steps (3 and 4) were repeated to achieve better coverage.

Before developing systems of Configuration 1 and 2, the metrological properties of functionalized FBG should be retrieved, and the influences of wt% and tk on the sensor responses.

In my Ph.D. activity, the influence of two agar concentrations (i.e., 1wt% and 2wt% dissolved in distilled water) and four different tk values were investigated⁸.

The functionalization of FBGs was carried out by using two 3D-printed molds. Each mold is constituted of two parallelepiped-shaped molds in which FBGs were located (with $\lambda_B=1541$ nm for agar 1 wt% and $\lambda_B=1549$ nm for agar 2 wt%; all FBGs has a sensing length of 10 mm). The molds have different square cross-sections (i.e., 0.8mm x 0.8mm and 1.4mm x 1.4mm, respectively) for achieving different tk. Molds are made of ABS (Acrylonitrile Butadiene Styrene) [384].

After the fabrication process (steps 1-5, previously described), tk was evaluated using a digital microscope (i.e., Dino-Lite AM4515ZT with 1.3 Megapixels) as shown in Fig. 4:35. Three

⁸This work is an excerpt from "Agar-coated fiber Bragg grating sensor for relative humidity measurements: influence of coating thickness and polymer concentration nm" of which the Ph.D. candidate is the main author. doi: 10.1109/JSEN.2019.2892900

different points along the coated fiber were considered, and an average was calculated to obtain a tk value for each FBG. All tk values are listed in Fig. 4:35.

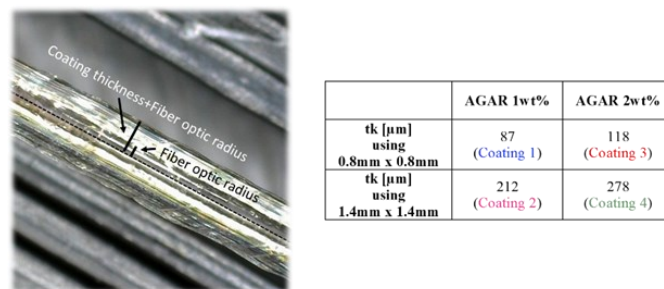


FIGURE 4:35. A digital microscope picture of the coated FBG sensor. All the coatings features are listed in the table.

The influence of tk and wt% was assessed by using the following experimental set-up: each FBG is interrogated by an optical spectrum interrogator (sm425, Micron Optics, Atlanta-USA) which works at a sampling frequency of 250 Hz. A capacitive-based RH sensor (HIH 4602A, commercialized by Honeywell International Inc., Morristown-USA) detects the reference RH values. Its output voltage is collected by a data acquisition card (DAQ NI USB-6009, National Instruments) at a sampling frequency of 250 Hz. Both FBGs and RH sensors are placed in a custom-made climatic chamber, adding a bare FBG for monitoring the ΔT during tests. The RH level inside the chamber ranges from RH<10% to RH>95%: the humidification of air is performed by forcing the air to flow inside the humidification chamber of a heated humidifier (red line in Fig. 4:36), while the dehumidification bypassing the humidifier (green line in Fig. 4:36) and forcing dry air to flow directly inside the climatic chamber.

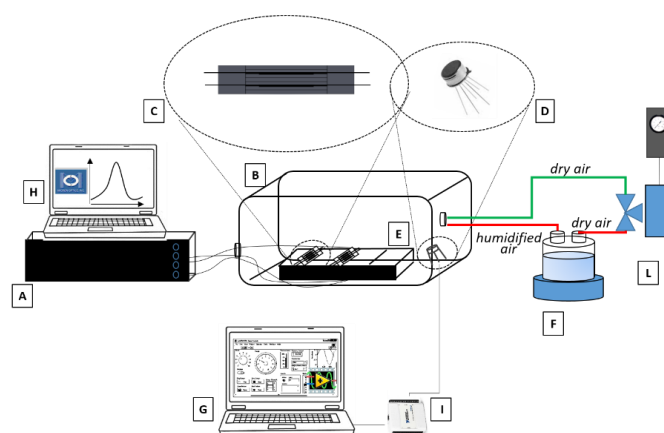


FIGURE 4:36. The experimental set-up. The optical spectrum analyzer (A), the climatic chamber (B), the molds (C), the capacitive-based RH sensor (D), the bare FBG (E), the humidifier (F), the laptop to check RH reference in LabVIEW environment inside the chamber during tests (G), the computer to check the FBG outputs during tests (H), DAQ (I), and the mass flow controller (L).

To retrieve S_{RH} , the static calibration of the four sensors was performed using the experimental set-up described in Fig. 4:36 applying RH values from 10% to 95%.

The step response was evaluated by exposing the agar-coated FBGs to RH step change ($\Delta RH \sim 26\%$) at a constant T of approximately 26 °C. Tests were performed bypassing the humidifier and forcing dry air inside the chamber. When RH reached a low value (about 10%), the chamber was opened, and sensors were exposed to the environmental condition (RH $\sim 32\%$). The acquisition lasted ~ 33 min to allow the FBG with higher agar wt% and thickest coating (i.e., Coating 4: 2 wt% and $t_k = 278 \mu m$) to reach the equilibrium (green curve in Fig. 4:37).

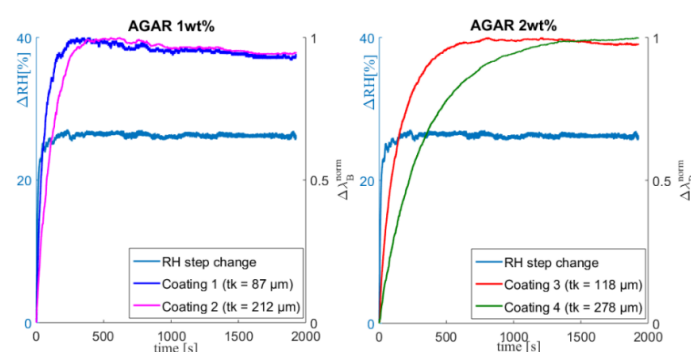


FIGURE 4:37. The RH step response of the four functionalized FBG with the reference.

Before investigating the effects of t_k and wt% on sensitivity and response time, the effect of the coating deposition process on the reflected FBGs spectra and their features were investigated.

A comparison between spectra collected before and after the coating deposition was performed. This analysis was based on the evaluation of the Full Width at Half Maximum (FWHM) for each functionalized-FBG to check the preservation of spectrum shape. Indeed, to work properly, FBGs must exhibit a narrow and symmetric bell-shaped spectrum centered at λ_B . However, coatings can introduce anisotropic radial compression, which could result in spectral broadening. For this reason, potential changes in the coated FBGs spectra were checked. Results showed FWHM of about 0.3 nm for Coatings 2 and 3 and FWHM of about 0.4 nm for Coatings 1 and 4 before the polymer deposition, while all FWHM increase up to about 0.5 nm for all coatings after deposition (see Fig. 4:38). Perhaps, no spectral broadening arose, and no evident changes in the spectral shape, which can cause problems on the spectrum interrogator detection of peaks, were found. Nevertheless, all λ_B peaks shift to lower values at the end of the drying process (from a minimum of 0.2 nm to a maximum of 1 nm with t_k).

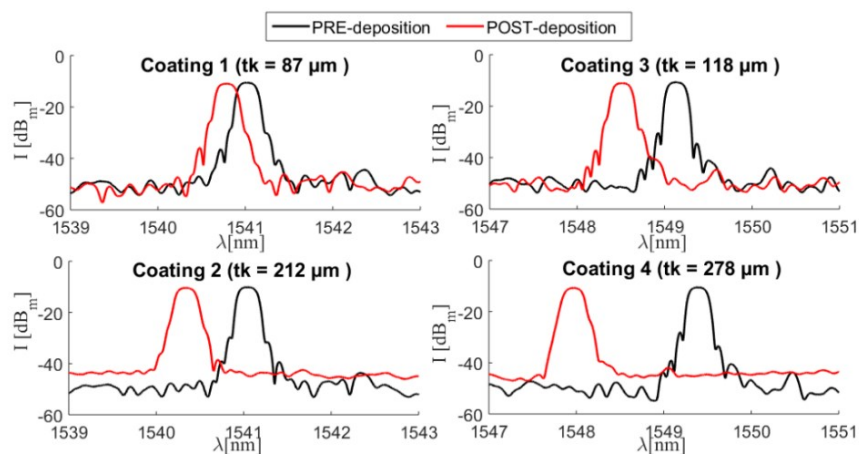


FIGURE 4:38. The 4 FBGs spectra before and after the functionalization.

Focusing on the metrological characterization, the static calibration of the four sensors showed a linear relationship between ΔRH and $\Delta \lambda_B$, as shown in Fig. 4:39. The linear fitting model implemented in MATLAB showed good values of the correlation between the experimental data and the model with correlation coefficients R^2 especially higher for agar concentration of 2wt% (for 1wt%: R^2 of 0.73 and 0.86 for Coating 1 and 2, respectively; for 2wt%: R^2 of 0.97 and 0.99 for Coating 3 and 4, respectively). The linear model was implemented after the T-induced shift compensation.

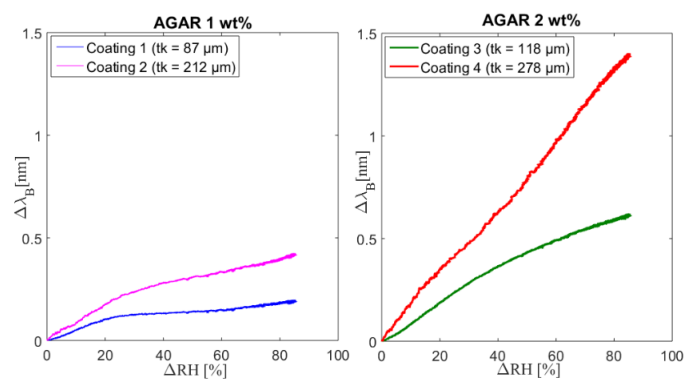


FIGURE 4:39. Plots show the agar-based FBGs responses to RH increase after the T compensation.

The detection of ΔT during the increase of RH was performed by using a bare FBG as a reference of T: a T increment of 2 °C was evaluated considering its S_T (i.e., 0.01 nm/°C), as shown in Fig. 4:40.

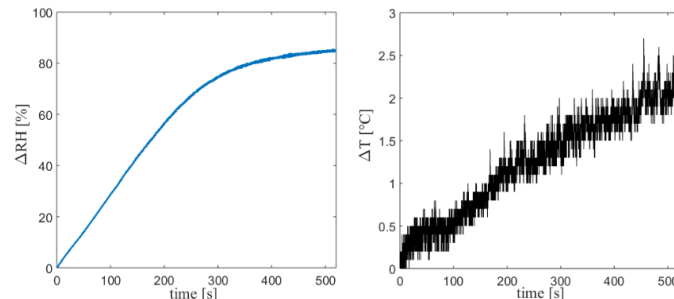


FIGURE 4:40. The reference ΔRH on the left and the bare FBG output (expressed as ΔT [°C]) over time on the right.

As evident, the sensors sensitivity increases with tk : at 1 wt%, $K_{RH}=0.0024 \text{ nm}\cdot\%^{-1}$ for Coating 1 (tk of 87 μm) and $K_{RH}=0.0052 \text{ nm}\cdot\%^{-1}$ for Coating 2 (tk of 212 μm); at 2 wt%, $K_{RH}=0.0076 \text{ nm}\cdot\%^{-1}$ for Coating 3 (tk of 118 μm) and $K_{RH}=0.0164 \text{ nm}\cdot\%^{-1}$ for Coating 4 (tk of 278 μm). Focusing on the influence of wt%, the analysis can be performed comparing Coating 2 with Coating 3. Although Coating 2 is thicker (tk of 212 μm) than Coating 3 (tk of 118 μm), it has lower sensitivity ($0.0052 \text{ nm}\cdot\%^{-1}$ vs. $0.0076 \text{ nm}\cdot\%^{-1}$) due to the lower concentration (1 wt% vs. 2 wt%). Results are summarized in Table 4:13 in terms of K_{RH} and S_{RH} and agreed with the theoretical analysis of the sensitivity dependence from coating geometrical and mechanical properties, as shown in (Eq 3:21). Indeed, the parameters under investigation play a crucial role mainly in the cross-section A_c and the Young modulus E_c . As experienced, a thicker tk leads to a bigger A_c , and a higher wt% leads to a higher E_c , resulting in an increase of sensitivity.

TABLE 4:13

	tk [μm]	K_{RH} [$\text{nm}\cdot\%^{-1}$]	S_{RH} [$\%^{-1}$]
Coating 1	87	0.0024	$1.56\cdot 10^{-6}\pm 4.0\cdot 10^{-9}$
Coating 2	212	0.0052	$3.38\cdot 10^{-6}\pm 7.0\cdot 10^{-9}$
Coating 3	118	0.0076	$4.91\cdot 10^{-6}\pm 6.0\cdot 10^{-9}$
Coating 4	278	0.0164	$10.59\cdot 10^{-6}\pm 10.0\cdot 10^{-9}$

For the response time estimation, an exponential fitting based on the bilayer model (Eq. 3:23) was applied to each step change response by setting $w_s=w_f=0.5$. The model showed a good agreement with the experimental data, as shown in Fig. 4:41, confirmed by the high values of R^2 (see Table 3). To simplify the comparison between sensors with different tk , we plotted the normalized Bragg wavelengths $\Delta\lambda_B^{\text{norm}}$ obtained by $\Delta\lambda_B/\Delta\lambda_B^{\text{max}}$ (i.e., the ratio between the Bragg wavelength shift from its initial value and the maximum wavelength shift induced by

RH change). Additionally, a global response time was evaluated by calculating τ^{63} , useful to immediately compare the systems' responses to a step change.

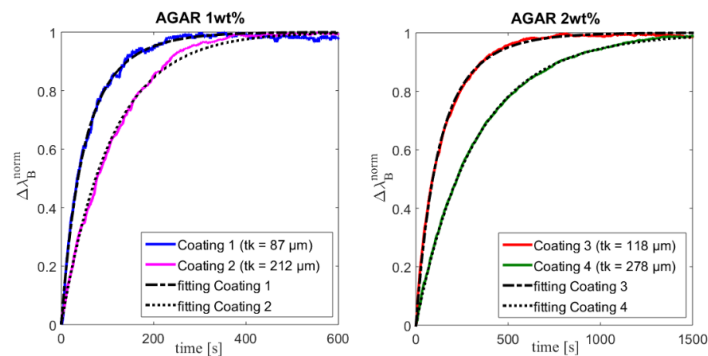


FIGURE 4:41. The fitting model of the step responses of all the four FBG sensors.

Results showed that τ^{63} increases with tk : at 1 wt% it was estimated as 56.7 s for Coating 1 ($tk=87 \mu\text{m}$) and 107.6 s for Coating 2 ($tk=212 \mu\text{m}$); at 2 wt% it was estimated as 143.4 s for Coating 3 ($tk=118\mu\text{m}$) and 328.7s for Coating 4 ($tk=278 \mu\text{m}$). The influence of wt% can be shown by comparing Coating 2 and Coating 3: in spite of Coating 2 thickness (thicker than Coating 3), Coating 3 showed a longer τ^{63} (143.4 s vs. 107.6 s). This result may be explained by the higher agar concentration of Coating 3 (2 wt% vs. 1 wt%).

The values of tk and wt% influence some material properties which play a crucial role on the dynamic response: the thicker the coating the bigger the radius, and the bigger the polymer concentration the lower its porosity (i.e., fraction of the volume of voids over the total volume). As a result, an increase in the response time is obtained. The main reason for this phenomenon is due to the coating radius influence on the diffusive processes (bigger is the radius largest is the time to reach the equilibrium [329]). At the same time, a reduction of polymer porosity causes a higher obstruction to water diffusion resulting in an increase in response time [385]. Results are summarized in Table 4:14.

TABLE 4:14

	tk [μm]	τ_f [s]	τ_s [s]	R^2	τ^{63} [s]
Coating 1	87	34.5	84.4	0.83	56.7
Coating 2	212	71.5	145.2	0.95	107.6
Coating 3	118	85.7	214.4	0.99	143.4
Coating 4	278	252.1	415.2	0.99	328.7

These findings suggest an easy control of wt% than tk during the fabrication process. Thus, the following configurations were fabricated using agar at controlled wt% (i.e., 1 wt%) instead of 2%, considering the faster dynamics and thin coating films.

The overall metrological properties of the following systems are listed in Table 4:15.

TABLE 4:15

Configuration	S_{RH} [nm·% ⁻¹]	τ^{63} [s]
1	0.008	90
2	0.016	72.4

Configuration 1: A smart needle encapsulating a 1wt% agar-coated FBG for RH and f_R monitoring⁹

This configuration was developed aiming at proposing a functionalized FBG-based system in an easy-to-use form (a needle) for monitoring both f_R and RH. The goal of this study is the assessment of the needle performances during mechanical ventilation in monitoring f_R and RH. The measurement of these two parameters may be useful because of their influence on the performance of heat wire humidifiers, which accomplishes the pivotal task of humidifying the air delivered by the mechanical ventilator. The performance deterioration increases the risk of endotracheal tube occlusion, patient's airway infections, and dehydration [386], [387].

The fabrication of the multi-sensitive system is described in detail in previous work [388]. A commercial FBG characterized by 10 mm-length of active part and λ_B of 1532 nm has been embedded inside a needle of 16 gauge of diameter for enhancing its usability, insertion into the breathing circuit, and sensor robustness. The needle surface has been pierced with ten holes to allow contact between the sensing part and the environment (Fig. 4:42). Then, among hygroscopic polymers, a solution of agar 1 wt% dissolved in distilled water has been deposited inside the holes for coating FBG and functionalizing the sensor active part as well to make the proposed system sensitive to RH.

⁹ This work is an excerpt from "Multi-sensitive FBG-based needle for both relative humidity and breathing rate monitoring" of which the Ph.D. candidate is the main co-author. doi: 10.1109/MeMeA.2018.8438658

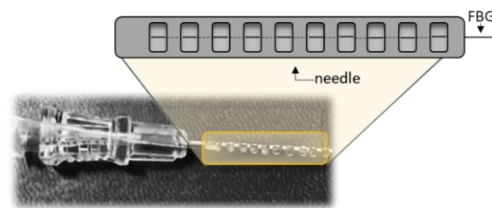


FIGURE 4.42. The developed needle instrumented with a functionalized FBG sensor.

The needle performances were first tested inside the Y-piece's inspiratory limb, commonly used for connecting the patient's upper airways to the breathing circuit. The T and the RH of air are conditioned by a commercial heated wire humidifier (MR850, Fisher & Paykel Healthcare-Auckland-New Zealand). This system works to keep the T of the air flowing through the Y-piece at approximately 40 °C. Then, the expired air flows back to the ventilator by the expiratory limb.

Regarding the f_R monitoring, a ventilator (Siemens SERVO 300A Ventilator) is used for performing eight tests by setting MV and f_R , and these values are considered as references. During these tests, the FBG-based needle is inserted inside the inspiratory limb, and the humidifier is used for keeping the T at ~40 °C (Fig. 4:43 B). Instead, the RH monitoring performed by FBG is performed by inserting a reference capacitive RH sensor (HIH 4602A, commercialized by Honeywell International Inc., Morristown-USA) in the inspiratory limb for checking the RH levels.

The experiment consists of three phases:

1. the ventilation is performed by delivering the dry air of the ventilator to the Y-piece (Fig. 4:43 A);
2. just after the acquisition is started, the heated wire humidifier is inserted in the inspiratory limb of the breathing circuit. In this way, the dry air delivered by the ventilator is humidified before reaching the Y-piece (Fig. 4:43 B). The ascending phase of RH starts, and it is stopped when RH value reaches ~90%;
3. the inspiratory limb is connected to the ventilator bypassing the humidifier assuming the beginning configuration (Fig. 4:43 A). Thus, dry air flows into the breathing circuit, and the descending phase of RH starts. Data from the RH sensor are collected using a data acquisition board (DAQ NI USB-6009, National Instruments) during these phases. The DAQ allows recording and plotting in real-time the RH changes in LabVIEW environment; in addition, it supplies the RH sensor at 5V.

The FBG-based needle is interrogated by an optical spectrum interrogator (si425, Micron Optics, Atlanta-USA) during both f_R and RH monitoring. The same system is used for collecting the FBG output changes due to the intermittency of the airflow and the RH changes.

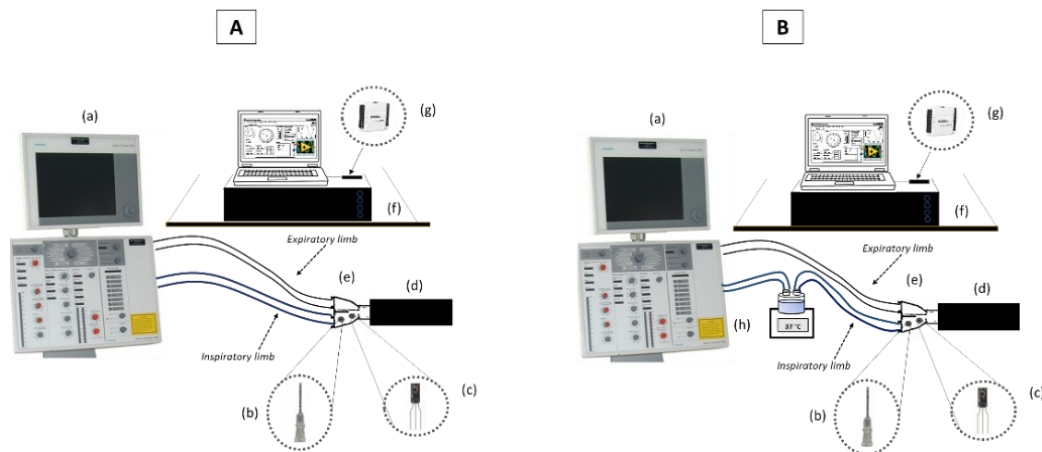


Figure 4:43. Experimental set-up of the first and third phases: the ventilator (a), the FBG-based needle (b), the capacitive RH sensor (c), the lung simulator (d), the Y-piece (e), the optical spectrum interrogator (f) and the DAQ (g). in fig. 3b experimental set-up of the second phase in which the humidifier (h) is added.

During mechanical ventilation, a patient requires ventilator support for breathing, and his upper airways are bypassed; thus, the dry air delivered by the ventilator must be humidified. This procedure is usually performed by a heated wire humidifier [389]. In this case, the monitoring of RH is crucial for avoiding respiratory infections and irritations [390]. In addition to that, as known, mechanical ventilation is characterized by an intermittent airflow supplied by the ventilator because, during the inspiratory phase, the airflow is present, while during the expiratory phase, is absent. It causes periodic fluctuations in the output of the FBG sensor when placed in the inspiratory limb of the Y-piece, probably due to mechanical ϵ induced by air that flows intermittently on the sensor. This period can be used to estimate f_R , crucial vital sign for providing oxygen needed for the tissue metabolism and removing carbon dioxide and metabolism waste products.

The assessment of the FBG-based needle for f_R monitoring was evaluated by performing data analysis in MATLAB environment. In order to get immediate comprehension of the data analysis procedure, a workflow is built and shown in Fig. 4:44.

At first, the whole pattern collected for each MV is split into five parts called 1st f_R , 2nd f_R , 3rd f_R , 4th f_R , and 5th f_R according to the f_R set for each MV. The numbers 1st, 2nd, 3rd, 4th, and 5th are referred to 8 bpm, 11 bpm, 14 bpm, 17 bpm, and 20 bpm, respectively. The MV subscripts,

instead, are referred to the values of MV set on the ventilator (i.e., 2, 4, 6, 8 according to 2L·min⁻¹, 4L·min⁻¹, 6L·min⁻¹ and 8 L·min⁻¹, respectively).

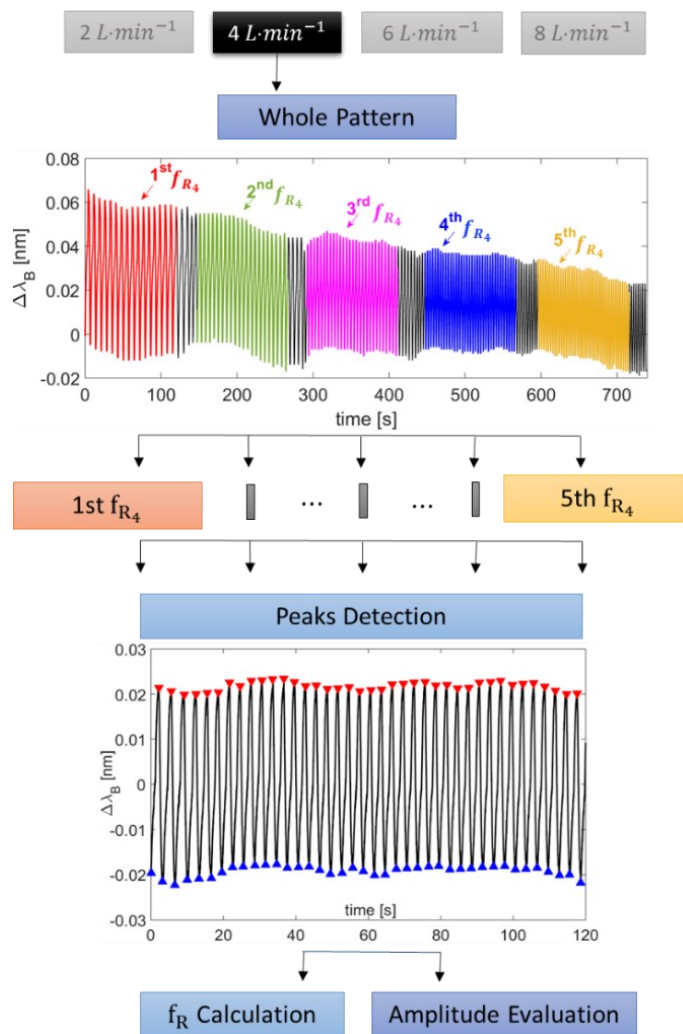


FIGURE 4.44. Data analysis workflow. Example of experiment performed at MV= 4L·min⁻¹. The 120s lasting signal which peak detection is applied on, refers to 5thf_{R4}.

Then, peak detection is performed by applying the *findpeaks* function in MATLAB. As a result, minimum and maximum peaks are highlighted on each 120s-lasting $i^{\text{th}}f_{R4}$ pattern, as shown in the workflow at the Peak Detection block. Starting from the respiratory period (T_R), evaluated as the time that elapses between two following maximum peaks, f_R is calculated as $60/T_R$. As previously described, two tests were carried out for each MV: one test during the first stage of the experiment and the other during the second stage. The same analysis was performed for

LD

each stage and, both of the f_R arrays referred to the same MV but based on data collected during different stages were concatenated. Moreover, the amplitude of each $i^{th}f_R$ pattern was evaluated as the $\Delta\lambda_B$ between a minimum peak and the following maximum one. Then, the concatenation of these arrays was executed as well. This last analysis showed the $\Delta\lambda_B$ - f_R relationship.

Referring to the monitoring of RH, data collected by the optical spectrum interrogator and the DAQ were imported in MATLAB environment, and the capability of the FBG-based needle to follow the RH changes was investigated.

Results show that the proposed system is able to estimate f_R with high accuracy. In Table 4:16, f_R estimated by the system are expressed as mean \pm expanded uncertainty, after the array concatenations. The expanded uncertainty was evaluated using a Gaussian distribution because the sample sizes are always bigger than 30. The level of confidence was 95%, so a coverage factor of 1.96 was used, as reported in [391].

TABLE 4:16

	MV [L·min ⁻¹]			
	2	4	6	8
$f_{R\ needle}^a$	7.97±0.11	10.94±0.09	14.01±0.07	16.88±0.14
[bpm]	8.03±0.13	10.80±0.06	13.92±0.13	17.20±0.11
	8.30±0.03	11.18±0.34	13.80±0.06	17.01±0.07
	8.09±0.03	11.01±0.22	14.30±0.07	17.21±0.09
	19.97±0.08	20.20±0.16	19.87±0.10	20.07±0.14

^aReference f_R values are 8 bpm, 11 bpm, 14 bpm, 17 bpm and 20 bpm for first, second, third, fourth and fifth columns, respectively.

Then, the percentage errors (%e) were calculated as shown in Eq. 4:11, where $f_{Rreference}$ is the ventilator set f_R :

$$e\% = \frac{f_{Rneedle} - f_{Rreference}}{f_{Rreference}} \cdot 100 \quad (4)$$

Equation 4:11

Overall results of %e are shown in Table 4:17. The maximum %e of the system is 3.74% for $f_R = 8$ bpm at MV=6L·min⁻¹ followed by 2.17% for $f_R=14$ bpm at MV=8L·min⁻¹. Instead, the minimum %e referring to the absolute value is 0.06% for $f_R=17$ bpm at MV=6L·min⁻¹.

Focusing on the obtained results, there is no a marked difference among tests performed at set f_R and MV. However, a potential influence of the peak detection on %e is possible. Two factors can be in charge. On the one hand, high f_R values result in a decrease of the signal-to-noise ratio (SNR); on the other hand, low f_R values result in a smooth signal pattern. Both of these factors make the peak detection complex. According to this assumption, it reasonable that the highest

%e is related to the lowest f_R . It is also worthy to note that the ventilator accuracy is ± 0.5 bpm (i.e., the Servo 300A ventilator accuracy). The differences between the estimated BR and the one set by the ventilator (from -0.20 bpm to 0.30 bpm) are always comparable to the ventilator accuracy.

TABLE 4:17

	%e [%]			
	MV [L·min ⁻¹]			
	2	4	6	8
$f_{R\ needle}^a$	-0.38	0.36	3.74	1.19
[bpm]	-0.51	-1.79	1.66	0.13
	0.07	-0.54	-1.42	2.17
	-0.70	1.26	0.06	1.21
	-0.17	0.99	-0.67	0.34

^aReference f_R values are 8 bpm, 11 bpm, 14 bpm, 17 bpm and 20 bpm for first, second, third, fourth and fifth columns, respectively.

Lastly, it is important to underline how the signal amplitude analysis showed decreased FBG output amplitude (Amp) according to the increasing of f_R . This phenomenon can be explained considering a relationship between the amplitude of FBG output changes and the tidal volume (i.e., the volume of air ventilated during a single act). Keeping MV constant, the tidal volume (it can be calculated as MV/f_R) decreases with f_R ; the consequence is a decrease in the amplitude of FBG output changes. This phenomenon is immediately showed in Fig. 4:45, where the red line in the middle of each box is the sample median, and the whiskers, above and below, extend from each box to boundary lines at the 25th and the 75th percentiles, respectively.

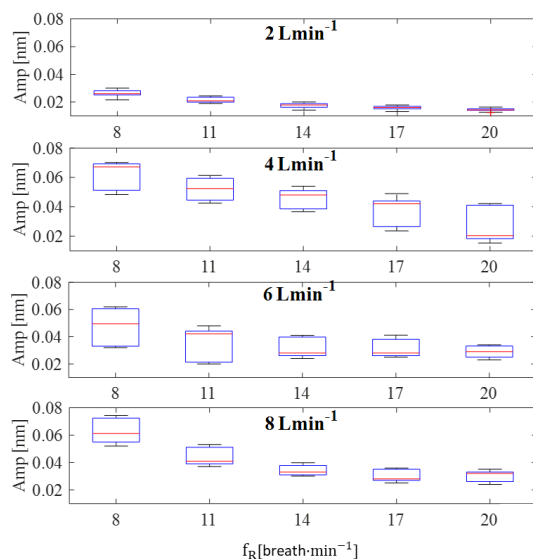


FIGURE 4:45. Whiskers plots: the red line in the middle of each box is the sample median, and the whiskers, above and below, extend from each box to boundary lines at the 25th and the 75th percentiles.

Regarding the monitor of RH, the FBG-based needle is able to follow cycle-by-cycle the RH changes allowing its measurement (Fig. 4:46). Results show that a $\Delta\lambda_B$ of 0.38 nm corresponds to a ΔRH of $\sim 70\%$ (i.e., from $\sim 20\%$ to $\sim 90\%$). Moreover, during the descending phase, it is possible to note small fluctuations in the $\Delta\lambda_B$ pattern, presumably caused by the intermittent airflows delivered by the mechanical ventilator.

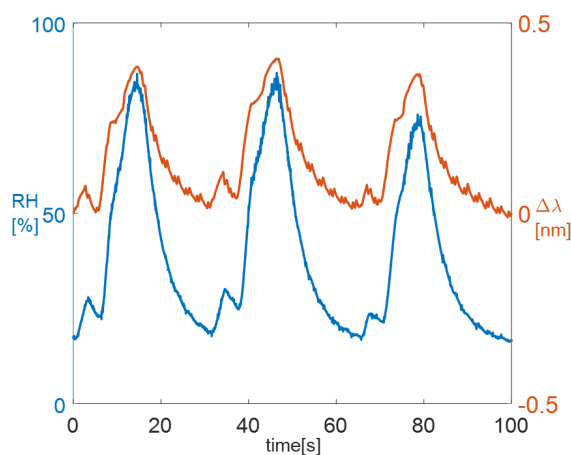


FIGURE 4:46. RH changes recorded by the reference instrument (blue line) and the FBG sensor (orange line).

Our system showed high performances in terms of f_R and RH changes monitoring, as previously described. The idea of housing an FBG inside a metallic structure (the needle) allows an easier insertion within the breathing circuit and easy handling as well, compared to [316]. This solution might be extremely useful for giving the control unit of the humidifier feedback of T during mechanical ventilation. Nowadays, this procedure is mainly based on electrical sensors like thermocouples or thermistors for adjusting the heat loss on the metallic plate and keeping the T of air that flows in the inspiratory limb at $\sim 37^\circ\text{C}$. However, the atmosphere during mechanical ventilation is potentially explosive, so that using these common electrical solutions is risky. Instead, the proposed solution will be intrinsically safe and compact, and it might be used in harsh environments without any risk.

According to the literature, other works show the simultaneous monitoring of more parameters by using FBG-based systems. Chen et al., for example, proposed a system made of two FBG sensors, one coated by polyimide for the RH measurement and the other one coated by acrylate for T monitoring [392]. The polyimide-coated-FBG experienced S_{RH} of $\sim 0.27 \text{ nm}/\%RH$, and RH

ranged from $\sim 10\%$ to $\sim 90\%$. Another FBG-based system for monitoring both ΔRH and ΔT is shown by Zhang et al. in [393]. Poly(methyl methacrylate, PMMA was used as a coating for the FBG functionalization because the PMMA high water affinity leads to a higher and quickly polymer swelling and, indirectly, increasing in $\Delta \lambda_B$. As expected, results showed S_{RH} of 1.6 nm/%RH in a range of RH between $\sim 50\%$ to $\sim 95\%$. Lastly, Hernandez et al. reported in [394] an FBG whose tip was coated by a mesoporous film, realizing a Fabry-Perot cavity made of 23 bilayers of Poly(allylamine hydrochloride-PAH) and SiO₂ nanoparticles for measuring T and RH during mechanical ventilation. The S_T of the FBG was 10 pm/°C while the S_{RH} was $-1.4 \cdot 10^{-12}$ W/%RH.

The same configuration was also tested on nine healthy volunteers¹⁰. The goal was to investigate the needle's ability for f_R monitoring on nine healthy volunteers, five females and four males (age from 23 to 26 years old), during spirometry, the most common pulmonary function test.

The FBG-based needle was inserted transversally to airflow direction through a plastic tube used for connecting the volunteers' mouth to a spirometer (SpiroLab III, MIR SpA, Rome, Italy), as shown in Fig. 1B. The spirometer signal was recorded by proprietary software (WinSpiro Pro, MIR SpA, Rome, Italy). Contemporary, an optical spectrum interrogator (si425, Micron Optics, Atlanta-USA) was used to interrogate the probe and record the back-reflected λ_B at a sampling frequency of 250 Hz.

Regarding the protocol, each volunteer was asked to perform a 60 s-lasting functional test. Before, a warming-up stage of 60 s was performed to help volunteers to feel more confident with the spirometer and more relaxed. Each test can be split into two phases: *i*) the apnea stage in which the volunteer is initially asked to hold his breath approximately for 8 seconds for the signals time-alignment and *ii*) the quiet breathing stage in which the volunteer is invited to breathe quietly.

Data collected by the spirometer and the FBG-based needle inside the tube were analyzed as follows:

1. The end of first expiration after the apnea phase is used as the point to cut the signals for data analysis (the green point on Fig. 4:47) at the end of the signals;
2. The signals are detrended (i.e., the mean is removed);

¹⁰ This work is an excerpt from "Polymer-coated fiber optic probe for the monitoring of breathing pattern and respiratory rate" in which the Ph.D. candidate is co-author. doi: 10.1109/EMBC.2018.8512566.

3. All the peaks are automatically detected on each signal by using a threshold algorithm based on [221], [355] to estimate the duration of each breath T_R ;
4. The instantaneous respiratory rate f_R is calculated as the ratio between 60 and the duration T_R ;

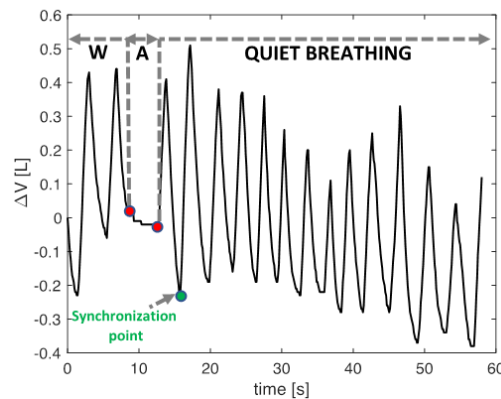


FIGURE 4:47. Data collected by the spirometer. W is a part of the warming-up stage (60 seconds in total), A is the apnea stage. Then, the quiet breathing stage is shown, together with the synchronization point at the end of the first expiration after the apnea.

An example of the two signals (spirometer and proposed FBG-based needle inside the tube) during quiet breathing is shown in Fig. 4:48.

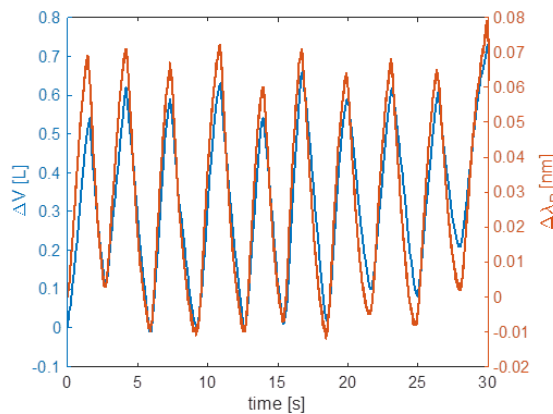


FIGURE 4:48. A 30-s window showing the signals collected by the spirometer (blue line, ΔV) and by the proposed probe (orange line, $\Delta\lambda_B$).

Considering all the f_R values estimated by each signal, the average value \bar{f}_R was calculated. From these values, the percentage error $\%e_{f_R}$ was estimated. Lastly, all the instantaneous f_R values gathered by the spirometer and the needle were compared with a Bland Altman analysis [362].

Results showed $\%e_{f_R}$ ranging from -0.56% to 1.43%, with the only exception of -2.07% for the Volunteer 8.

Bland-Altman analysis demonstrated the feasibility of the breath-by-breath monitoring of f_R : a MOD value of 0.06 bpm was found, while the LOAs were in the range ± 2.90 bpm (see Fig. 4:49)

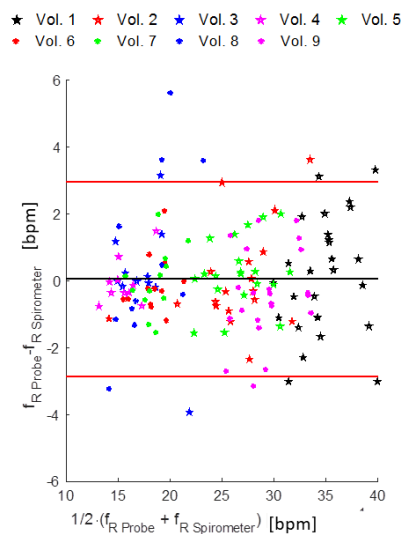


FIGURE 4:49. Bland-Altman plot. A colored symbol represents each volunteer. The black line represents the MOD value, while the upper and lower red line the upper and lower LOA, respectively.

Configuration 2: An MR-compatible wearable system based on a silicone matrix encapsulating a 1wt% agar-coated FBG for f_R monitoring¹¹

The most popular techniques for f_R monitoring are not usable in several clinical applications and unstructured environments. These issues have fostered a dramatic growth of interest for wearable systems devoted to monitor f_R . In this arena, FBGs have gained attention due to various benefits, including the MR compatibility. This configuration consists of a wearable device to monitor f_R from the nasal airflow. The sensing part is based on an FBG encapsulated into a polymeric matrix to improve its robustness, with the grating coated by agar to make the FBG sensitive to RH. The aims of the present work are: *i)* to design and fabricate an MR-compatible head-mounted wearable device, and *ii)* to perform a pilot study to assess the feasibility of the custom wearable device for monitoring f_R from the nasal airflow.

¹¹ This work is an excerpt from "A Magnetic Resonance-compatible wearable device based on functionalized fiber optic sensor for respiratory monitoring" in which the Ph.D. candidate is the main author. doi: 10.1109/JSEN.2020.2980940

The design of the proposed wearable device was driven by requirements of comfortability, unobtrusively, and MR-compatibility. It consists of two parts: Block A, which is the sensitive part, and Block B, which is the supporting one (see Fig. 4:50 A). Block A was fabricated as follows:

1. A commercial FBG sensor (λ_B of 1533 nm, grating length of 10 mm, At Grating Technologies) was encapsulated into a custom silicone brick (50 mm x 10 mm x 2 mm) made of Dragon Skin™ 20 (Smooth-On, USA), except for the grating (bare volume of 15 mm x 3 mm x 1.5 mm). The silicone rubber was cured for 4 h at room T, as suggested by the technical bulletin;
2. A 1 wt% solution of agar (commercialized by Sigma-Aldrich) was prepared by dissolving agar powder in distilled water at $T \sim 85$ °C. Then, the 1 wt% agar solution was deposited on the grating, and the drying process lasted 24 hours, at room T.

Regarding Block B, two 3D-printed sliding covers of PLA were used to connect Block A to a flexible polyvinylchloride (PVC) tube by a heat-shrink sheath made of Polyethylene (PE).

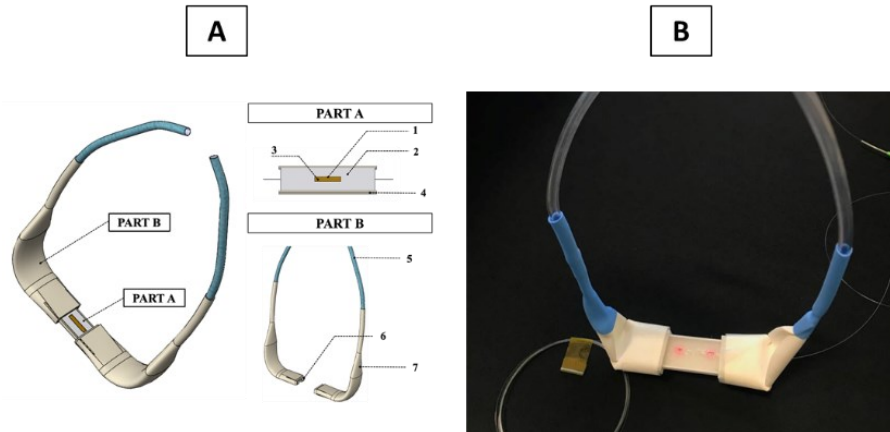


FIGURE 4:50. The MR-compatible wearable device. Block A shows the FBG (1), the agar-based matrix (2), the Dragon-Skin brick (3), and the PLA-based case (4). Block B shows the sliding covers (5), the heat-shrink sheath (6), and the flexible tube (7).

The wearable device is intended to be worn with the FBG sensor in Block A placed below the nostrils in the breathing zone and the PVB tube of Block B over the head and tightened by an adjustable piece at the back.

A pilot study was performed on six healthy volunteers (three males and three females, age 25-31 years old, body mass 48 kg - 85 kg, and height 163 cm - 182 cm) to assess the wearable

device's feasibility for monitoring f_R . An eight-camera MoCap system (D-Smart, BTS Bioengineering S.p.A., Milan, Italy) was used to record reference respiratory waveforms. On the torso of the participant, thirty-two IR-photo-reflective spherical markers (with a diameter of 15 mm) were positioned according to the protocol reported in [395], [396] (see Fig. 4:51 A, B, and C). The MoCap system records markers' trajectories to indirectly estimate f_R starting from the chest wall volume [397]. The sampling frequency was 60 Hz.

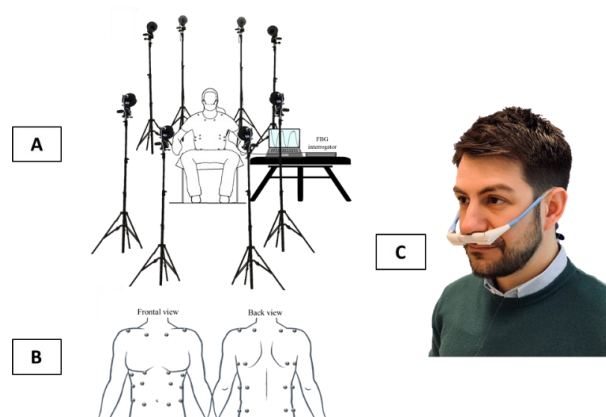


FIGURE 4:51. (A) The experimental setup; (C) the IR markers protocol; (D) the developed wearable system worn below the nostrils.

Each participant was invited to sit and wear the custom wearable device. Each participant performed a single trial which consists of three main phases: *i*) 10 s of apnea followed by 30 s of slow breathing; *ii*) 10 s of apnea followed by 30 s of normal breathing, and *iii*) 10 s of apnea followed by 30 s of fast breathing. Therefore, the proposed trials allow investigating the system performance. During the trial, a metronome was used to control the sb, nb, and fb.

The sensing element of Block A was exposed to the airflow (approximately 5 mm below the nostrils). The PVC tube of block B was snugly fitted over the ears and tight at the base of the skull. The output of the FBG-based sensing element was recorded by an optical interrogator (si255 based on Hyperion platform, Micron Optics, USA) at 100 Hz.

Data were collected using the wearable device and the MoCap, simultaneously. After 10 s of apnea (reported in Fig. 4:52), the slow breathing stage (green line), the normal breathing (blue line), and the fast breathing stage (red line) lasting 30 s are also clearly discriminated by both the proposed system and the reference one. Between each phase, there are 10 s of apnea, which can be identified by an interval of time where the systems' output is almost constant (shown in black line).

For each volunteer, the collected data were analyzed in MATLAB environment in five main steps:

1. Data collected by both the wearable device and the reference one were split into three signals according to the breathing stages performed by each volunteer;
2. A filtering stage was applied on the signals: a third-order Butterworth low pass filter with a cut-off frequency of 2 Hz for signals collected during sb and nb, and of 5 Hz for the one related to fast breathing;
3. All the signals were normalized;
4. A custom algorithm, described in detail in [398], was used to perform the peak detection on the normalized signal;
5. Since each maximum peak corresponds to the end of each inspiration, the time elapsed between consecutive peaks was calculated and considered equal to the respiratory period, T_R . The breath-by-breath f_R was estimated as $60/T_R$ (expressed in bpm).

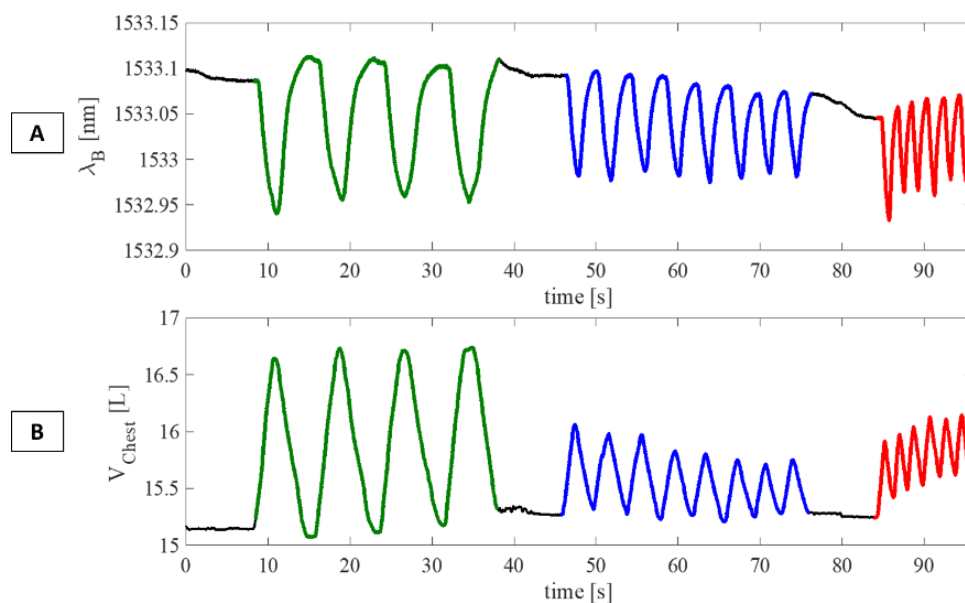


FIGURE 4:52. Results collected during the experiments on one of the volunteers: (A) the output of the wearable system and (B) the output of the MoCap system (V_{chest}). The green line is related to the slow breathing stage, the blue one to normal breathing stage, and the red one to the fast breathing stage. In black, the apnea stages.

The agreement between the breath-by-breath f_R values estimated by the wearable device and the ones by the reference system was evaluated considering all the three breathing stages (slow, normal, and fast breathing). The MPE and Bland-Altman analysis were performed.

The MPE (expressed in %) was calculated as follows:

$$MPE = \frac{1}{n} \cdot \sum \frac{f_R^{wearable_device} - f_R^{MoCap_system}}{f_R^{MoCap_system}} \cdot 100$$

Equation 4:12

Regarding the Bland Altman analysis, we calculated the MOD and LOAs according to [362].

All the MPE values are listed in Table 4:18.

TABLE 4:18

Breathing	MPE [%]					
	Vol 1	Vol 2	Vol 3	Vol 4	Vol 5	Vol 6
Slow	-0.48	-0.61	0.49	-1.06	-0.17	-2.29
Normal	-0.06	0.01	0.15	0.05	0.22	0.27
Fast	-0.17	-0.20	1.38	-0.39	-0.43	-1.55

MODs and LOAs are listed in Table 4:19, and Bland-Altman plots for each condition are reported in Fig. 4:53.

TABLE 4:19

Breathing	# breaths	MOD [bpm]	LOAs [bpm]
Slow	32	0.06	0.54
Normal	79	-0.02	0.33
Fast	109	0.31	4.89

Results showed a good agreement between the f_R values measured by the proposed system and the reference ones during slow, normal, and fsta breathing.

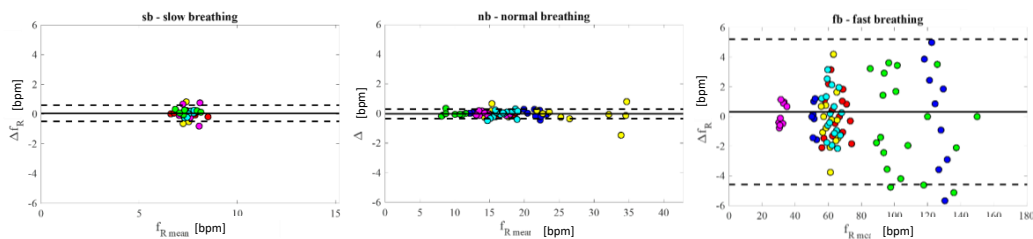


FIGURE 4:53. Bland-Altman plots related to slow breathing, normal breathing, and fat breathing. Each color represents one volunteer. The continuous black line is the MOD, while the dashed lines delimited the LOAs interval.

The novelty of this study relies on the use of agar as an active film to functionalize the grating encapsulated into Dragon Skin™ 20 to improve its usability. This configuration solution has a high S_{RH} and low τ^{63} with respect to the needle previously described [219] and [399]. Moreover, the new system showed better performance in terms of mean f_R estimation (maximum MPE value of 0.27 % vs. 2.07 %) and breath-by-breath analysis (MOD \pm LOAs of -0.02 ± 0.33 bpm vs. 0.06 ± 2.90 bpm).

In the literature, some wearable solutions have been proposed [400], [401], and [402]. In [401], a sensing probe embedding an FBG in the proximity of the fiber tip was proposed for RH measurement and tested on 20 volunteers showing its ability to follow the respiratory patterns without an analysis of the performance using a reference system. However, the use of a mask as FBG support can reduce the device's acceptability and comfortability. Indeed, intolerance, claustrophobia, and facial discomfort often fail to gain broader patients' acceptance, especially during long-term monitoring and chronic administration [403]. Moreover, considering the feeling of stress and anxiety experienced by patients during MRI, the mask can also act as an additional anxiety-inducing element [404]. Our system, otherwise, improves the wearability of the device and the usability of this kind of technological solution during MR procedures.

4.2 Wearables for joint motion detection

In this section, wearables developed for joint motions are presented. These systems exploit the mechanical coupling between the flexible sensors based on FBG and the body part in contact. (Fig. 4:54)

This research activity focused on the detection of motions of the spinal cord (i.e., the cervical and the back segment) since the main musculoskeletal disorders (MSD) whose population is affected are neck and low back pain. Their applications range from rehabilitation to occupation settings.

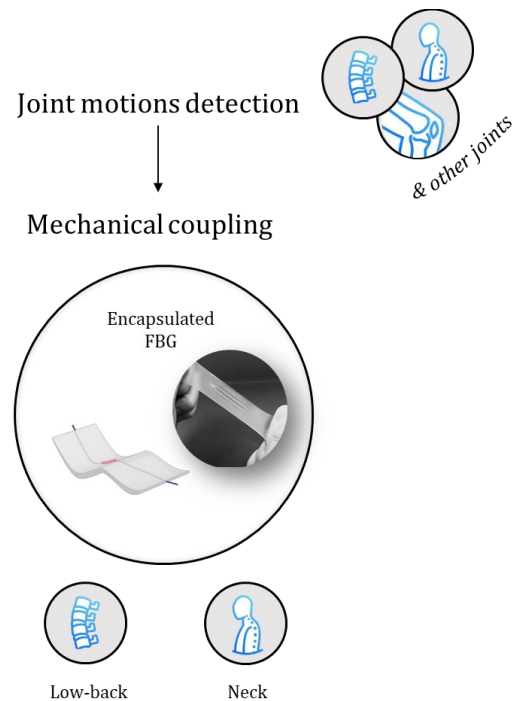


FIGURE 4:54. Wearables for joint motion detection: encapsulated FBGs have been used for the sensorization of wearable systems for neck and low back movements.

Two main configurations are proposed:

Configuration 1: A wearable system based on a rectangular-shaped flexible sensor directly stuck to the neck for monitoring F/E and AR movements.

Configuration 2: A wearable system based on a rectangular-shaped flexible sensor used to instrument an elastic band worn on the back for monitoring low back F/E movements.

The feasibility assessment of both these configurations was performed using a MoCap as a reference instrument. The achieved results are presented after describing the design, fabrication, and metrological characterization of the flexible sensors. As previously underlined, when the FBG is encapsulated into a polymeric matrix, its metrological properties as a strain sensor are investigated.

Design, fabrication, and metrological characterization

The design and the fabrication processes followed the same steps already described for the flexible sensors used in the cardiorespiratory monitoring (see Section 4.1.1.2 “Design, fabrication and metrological characterization”). The only difference relies on the 3D-printed molds used for the sensor in Configuration 2 while the sensing element used in Configuration 1 is the same involved during tests in both laboratory environment and archery.

Configuration 2 is based on a polymeric matrix with a rectangular shape (see Fig. 4:55) as Configuration 1 but smaller in length and width (90 mm x 24 mm vs. 55 mm x 20 mm) and thicker (1 mm vs. 2mm). Moreover, Dragon Skin™ 30 was used as silicone instead of Dragon Skin™ 20, resulting in lower sensor flexibility (hardness of 20 A vs. 30 A, expressed in Shore A scale) but higher robustness necessary in case of bigger joint bending and in turn, the higher ϵ applied on matrix during low-back F/E.

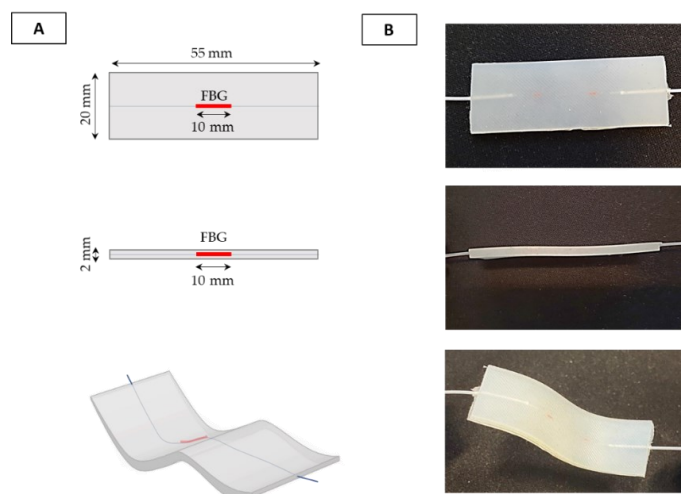


FIGURE 4:55. The flexible FBG-based sensing element. (A): Shape and size of the sensor in frontal view (up), lateral view (middle), and warped configuration (bottom); (B): Details of the sensor in frontal view (up), lateral view (middle), and warped configuration (bottom).

The investigation of the metrological properties followed the same procedure described for the flexible sensors used in cardiorespiratory monitoring. The S_ϵ values are $0.125 \text{ nm} \cdot \text{m}\epsilon^{-1}$ for Configuration 1 and $0.20 \text{ nm} \cdot \text{m}\epsilon^{-1}$ for Configuration 2, suggesting the influence of the matrix geometrical and mechanical properties as well as the bonding strength at the polymer-fiber interface.

Configuration 1: A wearable system based on a rectangular-shaped flexible sensor directly stuck to the neck for monitoring F/E and AR movements¹²

Neck pain is an MSD highly prevalent in office works [405], [406]. The 31% of computer workers in Europe experience neck pain [407]. It represents a socio-economic burden since it causes periods of absence from work, reduced productivity, and high utilization of health care services [407]–[409]. Bad postural habits and non-compliance of the workstation to ergonomics guidelines are the leading causes of neck pain. These factors may also alter respiratory functions. This configuration was developed to monitor neck F/E and AR together with f_R because prolonged head F/E and twisted neck are the main vicious computer workers' habits, and on f_R may be negatively influenced by job stress and wrong neck positions [410].

The proposed wearable system consists of two flexible sensors based on FBG technology (i.e., FBG1 and FBG2 with Bragg wavelength λ_B^{FBG1} of 1545 nm and λ_B^{FBG2} of 1541 nm, grating length of 10 mm and reflectivity of 90%; AtGrating Technologies, Shenzhen, China).

Sensor positioning was carefully evaluated to ensure high sensor capability in detecting and eliminating different neck movements and breathing activity. A polyacrylate bandage (100% polyester, Curafix® H, Lohmann & Rauscher, Padova, Italy) was used to allow a better adhesion and compliance to the skin. This bandage features adhesiveness, elasticity, and high breathability.

To detect F/E movements, FBG1 was positioned in correspondence with the cervical spine segment C1-C7, along the longitudinal direction starting from C7. For the AR monitoring, FBG2 was placed on the right side of the neck, horizontally to FBG1 beginning from the center of C6-C7 (Fig. 4:56 A). The positions were chosen to optimize the ϵ distribution along the FBG

¹² This work is an excerpt from "A Multi-Parametric Wearable System to Monitor Neck Movements and Respiratory Frequency of Computer Workers" in which the Ph.D. candidate is the main author. doi: <https://doi.org/10.3390/s20020536>

longitudinal direction. The F/E movements cause longitudinal ϵ on FBG1. The AR movements are mostly detected by the FBG2 as in Fig. 4:56 B and C.

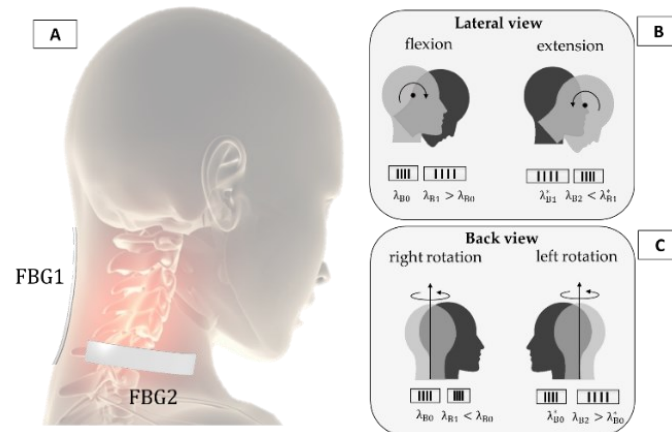


FIGURE 4:56. The FBG working principle when (A) attached to the neck for detecting (B) F/E and (C) left and right AR movements.

In this pilot study, a total of five healthy subjects (three males and two females) were enrolled. The subjects did not show any MSD or neck pain. Age and anthropometric measures (i.e., height, body mass, neck circumference) of each participant were collected before starting the experimental tests (Table 4:20).

TABLE 4:20

	Age [years]	Height [cm]	Body mass [kg]	Neck circumference [cm]
Vol. 1	23	183	125	46
Vol. 2	28	171	61	32
Vol. 3	27	178	85	38
Vol. 4	31	163	60	38
Vol. 5	39	171	71	43

Participants were asked to sit on an armless and height-adjustable chair, maintaining their feet on the floor, both hands on the knees, with hips and knees flexed at 90° (Fig. 4:57 A).

A MoCap system (Smart-D, BTS Bioengineering Corp., Milan, Italy) was used as a gold standard to assess the multi-parametric wearable system's capability to discriminate F/E and AR movements. Four spherical, infrared photo-reflective markers (15.2 mm in diameter) were placed on each subject, as shown in Fig. 4:58 A and B. In particular, the first marker is placed on the forehead (marker P1 in Fig. 4:58 A and B), the second marker on the C7 spinous process (marker P2 in Fig. 4:58 A and B), and the last two markers were placed in correspondence of

the acromioclavicular joints (P3' and P3'' in Fig. 4:57 B). 8 cameras collected the trajectories of the markers at a sampling rate of 60 Hz. An FBG interrogator (si255 based on HYPERION platform; Micron Optics Inc. USA) was used to record the FBGs output at a sampling rate of 1000 Hz.

After markers and FBGs positioning, the protocol was explained to each subject. Participants started with the head and neck in a neutral position and looking forward. Firstly, the participants were asked to perform F/E and AR movements, simultaneously recorded by the wearable and MoCap systems. Each participant performed: *i*) five F/E repetitions, followed by 30 s in the neutral position, and then five FE repetition (Fig. 4:57 B); *ii*) five AR repetitions to the right, followed by 30 s in the neutral position, and then by five AR repetition to the left (Fig. 4:57 B). An additional trial was executed to assess the multi-parametric wearable system's ability to monitor breathing activity (Fig. 4:57 C). During this trial, a commercial flowmeter (SpiroQuant P, EnviteC, Alter Hozhafen, Wismar, Germany) connected to a differential pressure sensor (163PC01D75, Honeywell, Minneapolis, Minnesota, USA) was used as a reference system. The output of the differential pressure sensor was collected through a DAQ (NI USB-6009, National Instrument, Rockville, Maryland, USA) and a custom Virtual Instrument developed in LabVIEW® environment at the sampling frequency of 250 Hz. The participants were asked to ventilate into a mouthpiece while performing two breathing patterns: 10 breaths of quiet breathing and ten breaths of tachypnea (in both cases, self-controlled breaths were performed); a 10 s stage of apnea (i.e., self-controlled breath-hold) was performed between the two breathing patterns (Fig. 4:57 D).

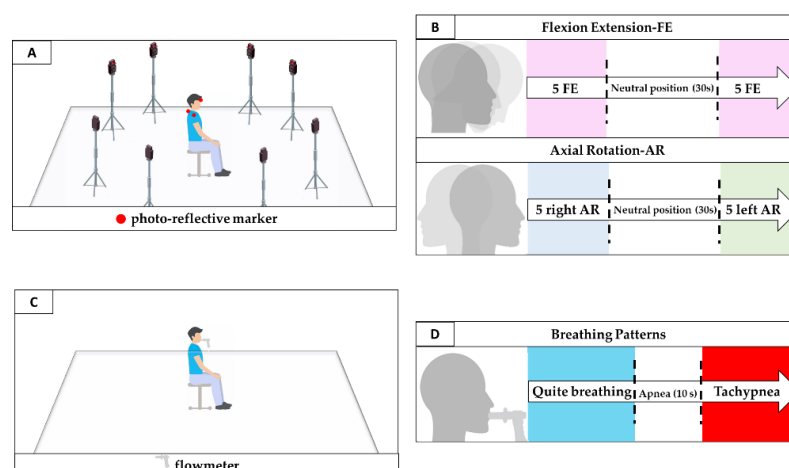


FIGURE 4:57. The experimental setup and performed protocol for (A and B) neck movements and (C and D) respiratory activity.

The number of F/E and AR repetitions was calculated from the raw data collected by the MoCap and the wearable systems. The 3D coordinates of the markers recorded by the MoCap system were used to carry out the reference signals by following these steps: *i)* the FE angle (α_{FE}) was estimated in the sagittal plane (i.e., y-z) as the angle between the vectors $\overrightarrow{P2P1}$ and \vec{u} (same direction of the y-axis), as shown in Fig. 4:58 A; *ii)* the AR angle (θ_{AR}) was estimated in the transverse plane (i.e., x-z), as the angle between the vectors $\overrightarrow{P2P3'}$ and \vec{v} (the same trend may be obtained by considering the vectors $\overrightarrow{P2P3''}$ and \vec{v}), as shown in Fig. 4:58 B. The θ_{AR} decreases during the right rotation (clockwise) and increases during the left rotation (counter-clockwise).

Regarding the wearable system, the analysis of the neck movements' detection was performed as follows: *i)* the changes of FBG1 output were used to evaluate FE movements since the chin lowered down toward the chest causes a longitudinal deformation of FBG1; *ii)* the changes of FBG2 output were considered to evaluate AR movements, as the right and left rotations of the head around its vertical line (y-axis in Fig. 4:58 A) causes a longitudinal deformation of FBG2. Trends of signals collected by the MoCap system are shown in Fig. 4:58 C and D, and the ones collected by the wearable system are shown in Figure 4:58 E and F.

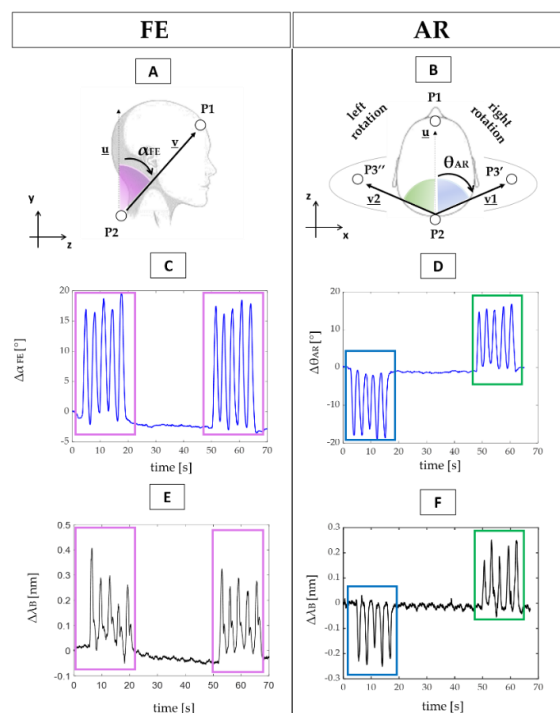


FIGURE 4:58 (A) The α_{FE} and (B) the θ_{AR} angles formed in the sagittal and transverse plane; (C) reference output changes over time during F/E and (D) AR repetitions; (E) FBGs outputs changes over time during F/E and (F) AR repetitions.

To assess the capability of the proposed system to detect neck movements on different planes, the collected data were processed by following two main steps:

1. The outputs of both the wearable and the MoCap system were normalized and plotted over time to evaluate trend similarity between signals;
2. The F/E and AR repetitions were detected by using a custom peak detection algorithm in MATLAB environment. F/E movements were detected by considering the maximum peaks of both MoCap and FBG1 signals: when α_{FE} increases during the neck flexion (signal provided by the MoCap) FBG1 is strained with a consequent rise of λ_B (Fig. 4:59 A and B). Right AR movements were detected by considering the minimum peaks of both MoCap and FBG2 signals: when θ_{AR} decreases during the right AR (signal provided by the MoCap) FBG2 is compressed with a consequent decrement of λ_B (Fig. 4:59 C). These data were collected during the first 5 AR repetitions; left AR movements were detected by considering the maximum peaks of both MoCap and FBG2 signals because when θ_{AR} increases during the left AR (signal provided by the MoCap) FBG2 is strained with a consequent increment of λ_B (Fig. 4:59 B). These data were collected during the last 5 AR repetitions.

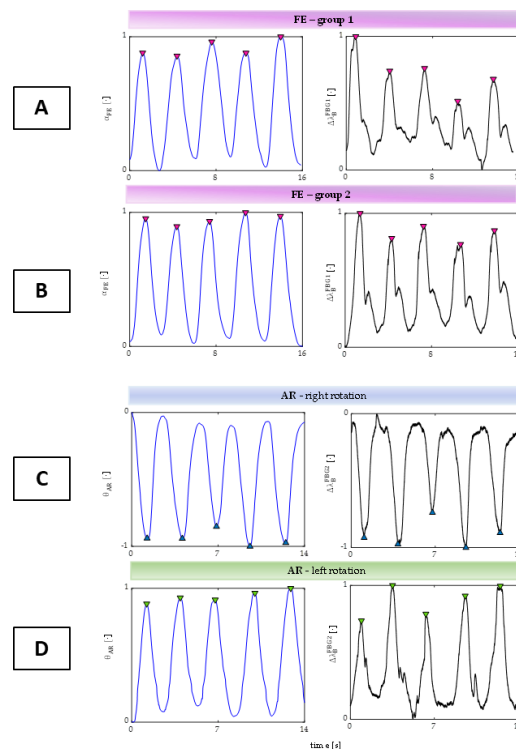


FIGURE 4:59. (A) The peak detection during the first group 5 F/E, (B) the second group 5 F/E right, (C) right AR repetitions, (D) left AR repetitions

Results showed that the proposed wearable system followed both F/E and AR movements and detected the repetitions, as shown in Fig. 4:60.

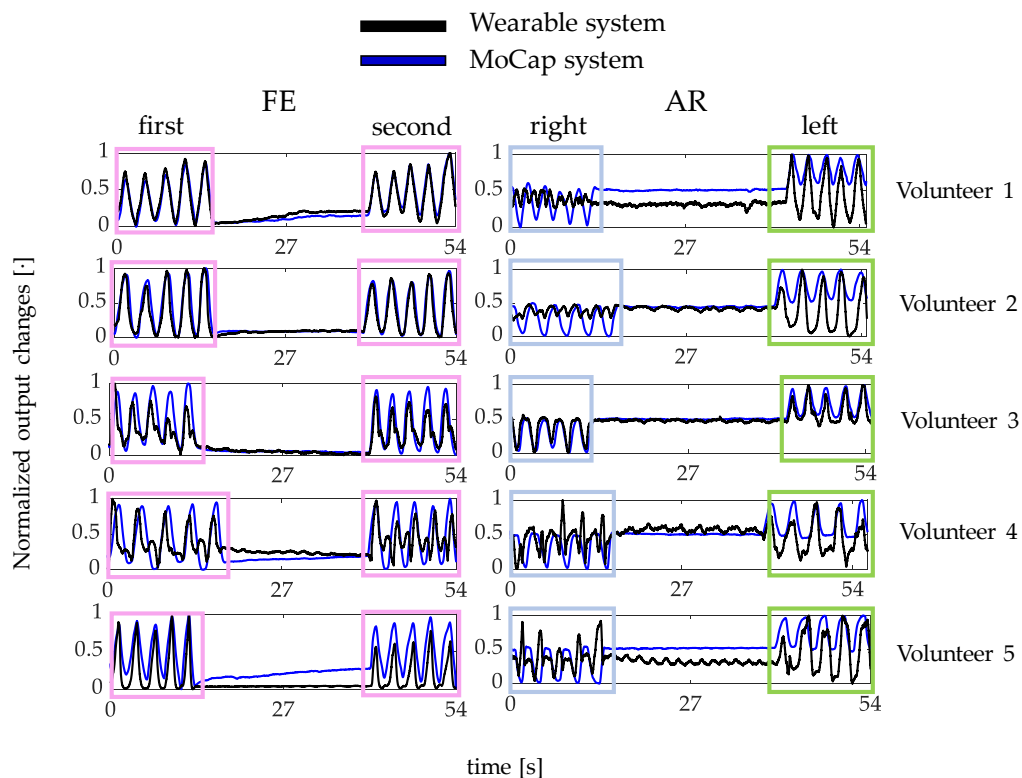


FIGURE 4:60. The output changes of both the wearable (black line) and the MoCap system (blue line) collected during F/E and AR repetitions.

In particular, the wearable system showed good performance in detecting F/E and left AR repetitions. Indeed, the $\Delta\lambda_B^{FBG1}$ and $\Delta\lambda_B^{FBG2}$ patterns matched the MoCap ones (pink and light blue boxes in Fig. 4:60). On the contrary, $\Delta\lambda_B^{FBG2}$ pattern during the right AR movements did not always match the reference signal (blue box in Fig. 4:60).

Focusing on f_R , the assessment of the proposed wearable system was performed by using the flowmeter as a reference instrument and following six main steps:

1. The outputs of the wearable system and the flowmeter were normalized in amplitude and split into quiet breathing-related signals and tachypnea-related ones (i.e., $FBG1_{qb}$, $FBG2_{qb}$, $FLOW_{qb}$, $FBG1_{tc}$, $FBG2_{tc}$, and $FLOW_{tc}$), as shown in Fig. 4:61;

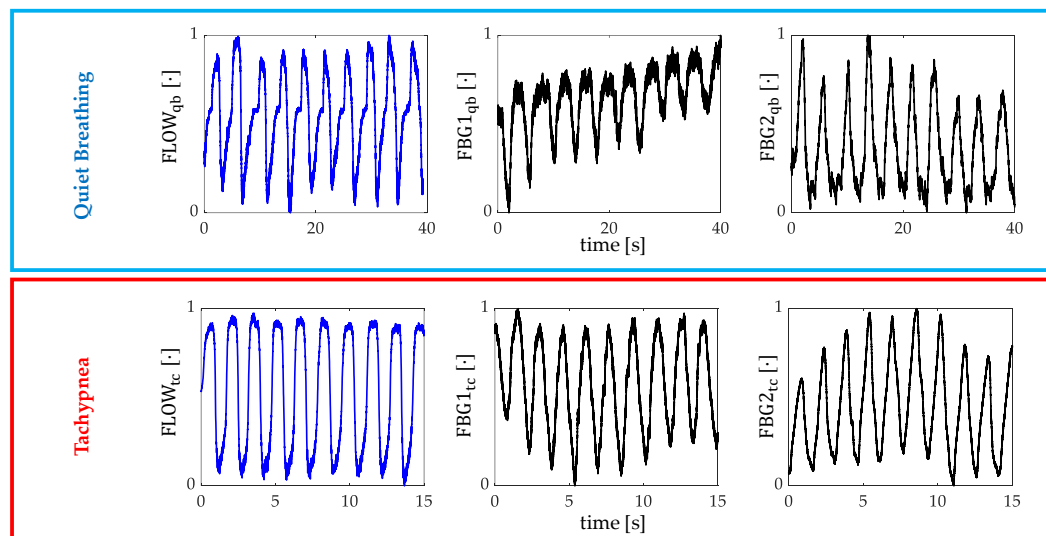


FIGURE 4.61. Signals collected by the flowmeter (blue trend) and by the FBGs (black trend) during both quiet breathing (light blue box) and tachypnea (red box).

2. The signs of both $FBG1_{qb}$ and $FBG1_{tc}$ were reversed since the $FBG1$ was compressed during the inspiration (when the volume of lungs increases) and tensioned during the expiration (when the volume of lungs decreases). This step was not implemented on the $FBG2$ output since its trend in time matches one of the reference system;
3. A third-order Butterworth low pass filter was applied on signals collected during quiet breathing (cut-off frequency of 0.5 Hz) and during tachypnea (cut-off frequency of 3 Hz);
4. Spectral analysis in terms of power spectral density (PSD) was performed on the filtered signals, and the maximum frequency (f_0) of both the reference and the wearable systems signals were evaluated (Figure 7);
5. Peak detection was performed by using *findpeaks* in MATLAB environment: the input parameter related to minimum peaks distance was set starting from the value of f_0 (Fig. 4:62);
6. The respiratory periods of each breath (i.e., T_R^i) were computed as the time elapsed between two consecutive maximum peaks of the signal provided by $FBG1$, $FBG2$, and the flowmeter, see Fig. 4:62. The f_R^i values during both quiet breathing and tachypnea were estimated as $60/T_R^i$ and expressed as bpm.

The assessment of the wearable system in the estimation of f_R during both quiet breathing and tachypnea was performed using three parameters:

1. In terms of percentage error ($\%e_{f_R}$) as in:

$$\%e_{f_R} = \frac{\overline{f_R}^{FBG} - \overline{f_R}^{FLOW}}{\overline{f_R}^{FLOW}} \cdot 100$$

Equation 4:13

where $\overline{f_R}$ is the mean value of f_R ;

2. In terms of absolute percentage errors for a breath-by-breath analysis:

$$|\%e_{f_R}^i| = \frac{|f_R^{iFBG} - f_R^{iFLOW}|}{f_R^{iFLOW}} \cdot 100$$

Equation 4:14

where f_R^{iFBG} and f_R^{iFLOW} are the values of the i^{th} f_R estimated either by FBG1 or FBG2 and by the flowmeter;

3. By calculating the mean value of the breath-by-breath absolute percentage errors (i.e., MAPE) for each volunteer as in:

$$|\%e_{f_R}^i| = \frac{1}{n} \cdot \sum \frac{|f_R^{FBG} - f_R^{FLOW}|}{f_R^{FLOW}} \cdot 100$$

Equation 4:15

All signals involved in the peak detection of the breathing analysis are shown in Fig. 4:63. The peak detection allowed estimating f_R in all volunteers but one (for FBG1 output changes of Volunteer 1 during both quiet breathing and tachypnea). The $\overline{f_R}$ with the $\%e_{f_R}$ are listed in Table 4:21.

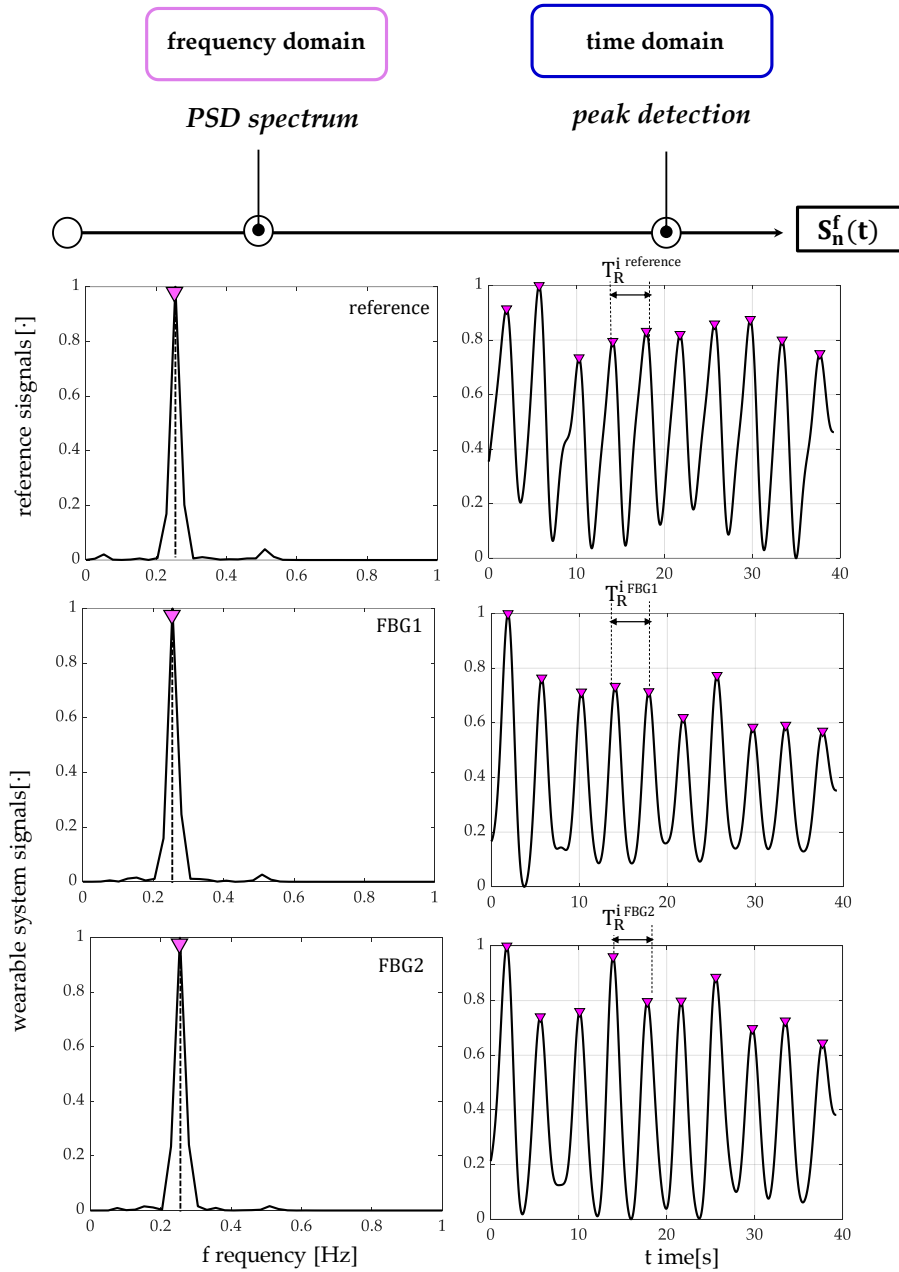


FIGURE 4:62. An example of signals processing performed for the f_R estimation from data recorded by the flowmeter and the wearable systems, during quiet breathing. The PSD spectra over frequency [Hz] and the peak detection over time [s] are shown for both the reference system and the proposed wearable system based on two flexible sensors (FBG1 and FBG2). The $S_n^f(t)$ signals are filtered and normalized.

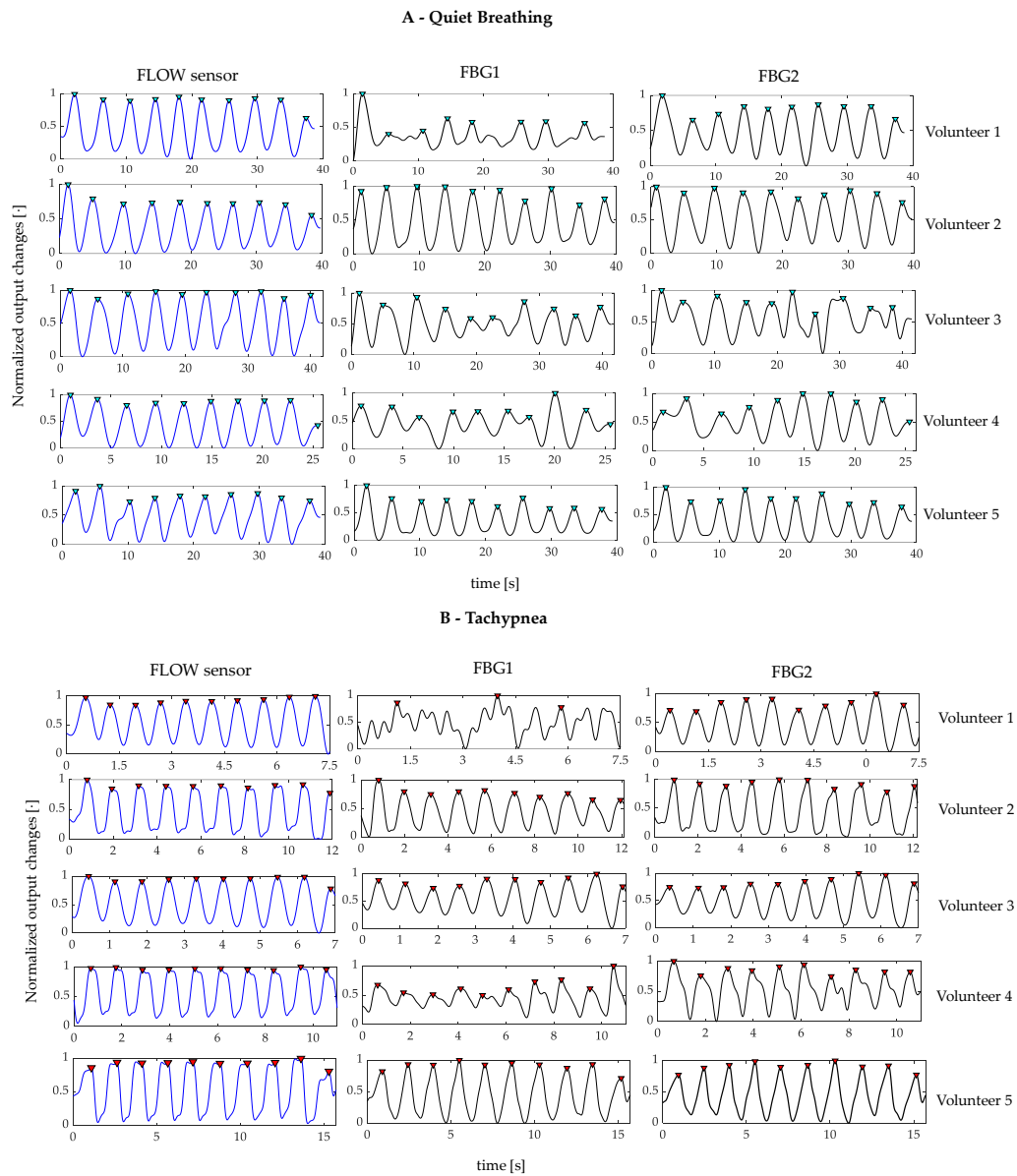


FIGURE 4.63. (A) signals collected by the flowmeter (blue line) and the FBGs (black line) for each volunteer during quiet breathing and (B) during tachypnea. All the signals are synchronized, filtered, and normalized. The detected peaks are highlighted by using red markers.

The e_p , the MAPE, and the $|e_p|$ values are listed in Tables 4:22 and 4:23. The e_{FR}^{FBG1} are always $\leq 1.53\%$ and $\leq 0.71\%$, whereas the $e_{FR}^{FBG2} \leq 6.09\%$ and $\leq 1.90\%$, during quiet breathing and tachypnea, respectively. The $MAPE^{FBG1}$ errors are always $\leq 12.87\%$ and $\leq 5.86\%$, and $MAPE^{FBG2}$ always $\leq 15.36\%$ and $\leq 4.90\%$, during quiet breathing and tachypnea, respectively. Data from FBG1 for Volunteer 1 were discarded.

TABLE 4:21

Quiet Breathing [bpm]			
Volunteer	\bar{f}_R^{FBG1}	\bar{f}_R^{FLOW}	\bar{e}_{fR}^{FBG1} [%]
1	-	15.37	-
2	14.47	14.63	-1.09
3	14.36	14.14	1.53
4	22.36	22.09	1.22
5	15.15	15.22	-0.45
	\bar{f}_R^{FBG2}	\bar{f}_R^{FLOW}	\bar{e}_{fR}^{FBG2} [%]
1	15.30	15.37	-0.48
2	14.65	14.63	0.15
3	15.00	14.14	6.09
4	22.40	22.09	1.40
5	15.10	15.22	-0.79
Tachypnea [bpm]			
Volunteer	\bar{f}_R^{FBG1}	\bar{f}_R^{FLOW}	\bar{e}_{fR}^{FBG1} [%]
1	-	83.62	-
2	48.65	48.80	-0.32
3	83.28	83.87	-0.71
4	54.53	54.58	-0.09
5	37.88	38.09	-0.56
	\bar{f}_R^{FBG2}	\bar{f}_R^{FLOW}	\bar{e}_{fR}^{FBG2} [%]
1	82.02	83.62	-1.90
2	48.46	48.80	-0.72
3	82.98	83.87	-1.05
4	54.99	54.58	0.75
5	38.01	38.09	-0.19

TABLE 4:22

Volunteer	Quiet Breathing									MAPE ^{FBG1} [%]
	e ^{fbg1} [%]									
1	-	-	-	-	-	-	-	-	-	-
2	10.40	0.34	0.28	0.19	0.58	1.91	2.24	2.93	3.22	2.45
3	16.66	10.88	2.28	4.97	10.26	7.75	13.7	5.62	8.17	8.92
4	12.32	7.11	14.04	13.51	10.17	28.65	1.24	15.56	13.21	12.87
5	0.21	8.24	4.48	5.92	0.91	3.56	6.58	4.71	1.04	1.47
	e ^{fbg2} [%]									MAPE ^{FBG2} [%]
1	5.28	3.76	0.20	2.18	4.75	4.19	1.33	4.92	4.33	3.44
2	2.69	0.86	2.06	1.14	0.97	2.09	0.19	6.76	4.42	2.36
3	29.36	12.12	4.05	3.63	17.35	27.82	8.21	15.75	19.93	15.36
4	15.34	16.03	4.22	0.85	7.36	3.46	3.33	0.16	1.35	5.79
5	2.53	1.52	0.95	1.95	~0	0.41	2.31	2.89	1.23	1.53

TABLE 4:23

	Tachypnea										
Volunteer	$e_{r^{FBG1}}$ [%]										$MAPE^{FBG1}$ [%]
1	-	-	-	-	-	-	-	-	-	-	-
2	3.74	0.65	3.11	3.34	7.56	6.21	4.64	11.54	3.75		4.95
3	1.69	2.70	1.71	0.55	3.72	4.09	~0	5.82	1.16		2.38
4	2.95	9.77	4.48	18.86	0.37	1.46	1.44	5.35	8.10		5.86
5	0.52	1.06	0.77	1.84	0.50	0.73	0.24	1.31	2.11		1.01
	$e_{r^{FBG2}}$ [%]										$MAPE^{FBG2}$ [%]
1	6.95	2.26	0.56	2.72	2.63	3.68	1.63	2.81	5.13		3.15
2	4.07	0.97	3.67	2.52	3.34	0.96	0.97	6.69	3.45		2.96
3	8.85	7.14	0.55	~0	1.12	1.14	0.55	1.11	7.41		3.10
4	6.41	2.47	9.92	5.24	5.43	2.11	6.23	6.29	~0		4.90
5	0.52	1.33	0.26	1.84	0.49	~0	1.72	1.02	0.72		0.88

This configuration is the first wearable system that monitors the above-mentioned parameters, which significantly expands our explorative study on a single FBG-based wearable system [411]. Indeed, the presence of 2 FBGs allowed the new system to monitor both neck movements and fR. Also, we performed a quantitative assessment of system performances on five volunteers by using reference systems during each trial.

Regarding the neck movements' detection, the proposed wearable system showed good performance in following both F/E and left AR movements and detect the repetitions, while some limitations resulted in the right AR detection. These findings could be explained considering different working conditions of FBG2 during AR repetitions: the grating is tensioned during left AR and compressed during right AR, which causes a partial adherence of FBG2 to the neck surface due to the friction shear stress between the skin and the contacting wearable system. Consequently, the asymmetric sensor arrangements can cause small distortions of the reflection spectrum [412].

In the literature, the neck movements' detection was mainly performed by using wearable systems based on electric sensors (e.g., inertial sensors [413], accelerometers [414], and piezoresistive sensors [415]). Two inertial sensors were proposed to evaluate F/E, AR, and lateral bending (LB) of patients treated with cervical arthrodesis [413]. Sensors were placed on the forehead and the sternum, respectively, and an optoelectronic system was used as a reference instrument. Differently from our system, such wearable inertial sensors required a pre-calibration to align the sensor axis with the segment anatomical frame. Moreover, the measurement units were not located on the neck but single points of other anatomical segments. A 3-axis accelerometer was placed on the forehead to monitor cervical postures [414]. Only F/E movements were monitored, but no reference instrument was used to assess such capability. The

flexible encapsulation of our sensors allows for multi-point positioning and better compliance with the neck anatomy with respect to these solutions based on accelerometers or inertial sensors. A wearable system based on six piezoresistive sensors was proposed to monitor F/E, AR, and LB movements [415]. As our system, the sensing elements detected neck movements from the induced ϵ , being in direct contact with the skin. Each movement was monitored by using a couple of sensors on the opposite sides of the neck, whereas we used only one FBG for F/E and one FBG for AR. Our choice was motivated by the desire to enhance system wearability and comfortability. Results in the literature [415] suggested that placing sensors diametrically opposite on the neck can allow monitoring both right and left AR movements despite the higher amount of wires.

The high sensitivity of the custom-made flexible FBGs allows our system the monitoring of f_R from the neck. Our findings suggest a good accuracy in f_R monitoring in terms of mean and breath-by-breath values in all trials except for Volunteer 1, presumably because of a non-well adherence of the sensing element to the skin due to a more prominent C1-C7 cervical segment and skin surface properties. For all the other volunteers, both FBG1 and FBG2 were able to detect f_R values. They showed comparable results in terms of mean and breath-by-breath values during both quiet breathing and tachypnea (i.e., $\%e_{FR} \leq 6.09\%$ vs. $\leq 1.90\%$, $|\%e_{FR}| \leq 29.36\%$ vs. $\leq 18.86\%$, and MAPE $\leq 15.36\%$ vs. $\leq 5.86\%$ during quiet breathing and tachypnea, respectively). In the literature, only a few studies investigated the possibility of monitoring respiratory activity by using acoustic sensors in contact with the neck [416], [417]. An acoustic sensor was attached to the anterior lateral base of the neck to measure the sounds coming from the flow of air in the trachea [416]. However, these acoustic systems, usually employed in sound-controlled environments, need to reject noises related to heartbeat, muscle activations, and swallowing [418].

Configuration 2: A wearable system based on a rectangular-shaped flexible sensor used to instrument an elastic band worn on the back for monitoring low back F/E movements¹³

Low back pain (LBP) is one of the MSD that most affects workers. As it causes exploitation of the National Health Service and absenteeism in workplaces, LBP constitutes a relevant socio-economic burden. In such a scenario, prompt detection of wrong seating postures can be useful

¹³ This work is an excerpt from "A Wearable Device Based on a Fiber Bragg Grating Sensor for Low Back Movements Monitoring" in which the Ph.D. candidate is co-author. doi: <https://doi.org/10.3390/s20143825>

to prevent the occurrence of this disorder. This configuration is a novel wearable device embedding an FBG sensor to detect low back F/E movements and ROMs in seated subjects.

Four healthy volunteers (two males and two females) with no history of back disorders were enrolled. The main population characteristics, expressed as mean \pm standard deviation, are: age of 28.4 ± 0.5 years old, height of 175.2 ± 4.4 cm, body mass 67 ± 11.7 kg, and chest circumference 94.4 ± 9.5 cm. Each subject wore the elastic structure over a tight t-shirt and was invited to sit on a stool placed at the center of the four-camera MoCap recording area (about 3 m³ of calibrated volume) and maintain a straight posture. In line with the protocol proposed in [419], 11 photo-reflective passive markers with a diameter of 18 mm were positioned on specific body landmarks (i.e., C7, T1, T4, T7, T10, L1, L3, L4, L5, right and left shoulder) using a bi-adhesive tape (see Fig. 4:64 A). The FBG-based flexible sensor was then fixed with bi-adhesive tape for textiles upon the elastic wearable structure, in correspondence with the lumbar area between the subject's L1 and L5 lumbar vertebrae, as shown in Fig. 4:64 A. The volunteer was instructed to follow the protocol that consisted of executing four consecutive back flexions followed by four consecutive extensions two times, for an overall of sixteen F/E movements per trial. Each volunteer repeated the protocol twice; a total amount of eight trials was collected. During the trials, the outputs of both the wearable system and the MoCap system were acquired. An optical spectrum interrogator (si255, Micron Optics Inc., Atlanta, GA, USA) was used to collect the FBG outputs at a sampling rate of 100 Hz, while the positions in time of the photo-reflective markers were collected by the MoCap at the sampling frequency of 60 Hz and processed with dedicated software (i.e., OEP-Smart, BTS Bioengineering Corp., Milan, Italy) to obtain the trajectories of the F/E movements. The entire experimental set-up is shown in Fig. 4:64 B.

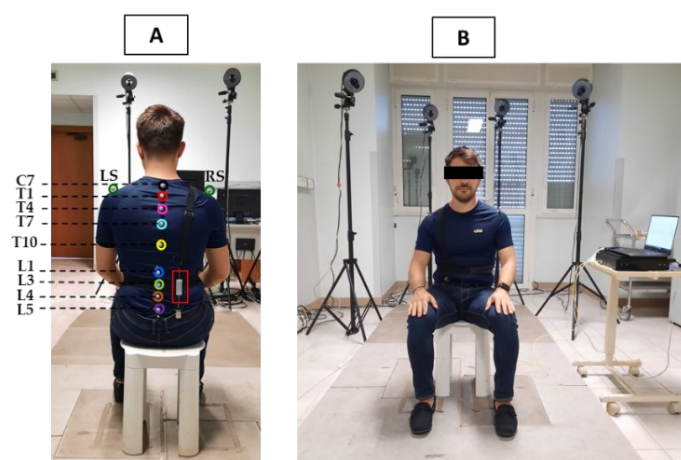


FIGURE 4:64. (A) the markers placement and (B) the experimental setup.

Per each trial, from markers' trajectories, the distance between markers L1 and L3 (d_{L3-L1} , see Figure 6) was calculated as in the following formula:

$$d_{L3-L1} = \sqrt{(x_{L3} - x_{L1})^2 + (y_{L3} - y_{L1})^2} \quad (3)$$

Equation 4:16

where x_{L3} and x_{L1} are the x -axis coordinates of L3 and L1, respectively and y_{L3} and y_{L1} the y -axis coordinates. The Δd_{L3-L1} was then calculated as

$$\Delta d_{L3-L1} = d_{L3-L1} - d_{L3-L1}|_{t=0} \quad (4)$$

Equation 4:17

This value allowed us to quantify the relative distance between L1 and L3 (expressed in cm) during F/E movements.

Referring to a single trial, the first maximum peaks recognized both on the $\Delta \lambda_B$ and on the Δd_{L3-L1} signals were used to synchronize the wearable device and the MoCap. Then, the $\Delta \lambda_B$ and Δd_{L3-L1} data recorded during the first flexion movement were used to calibrate the wearable device output for reconstructing the L1-L3 displacements from $\Delta \lambda_B$ (to obtain $\Delta d_{\Delta \lambda}$).

Since the linear relationship between the ε and the $\Delta \lambda_B$, a least-squares linear regression was carried out to accomplish this task, considering the Δd_{L3-L1} as predictor variables and $\Delta \lambda_B$ as response variables as in Eq. 4:18,

$$y = \alpha + \beta x + \zeta \quad (5)$$

Equation 4:18

where α is the y -intercept (fixed at 0), β the slope (or regression coefficient), and ζ the error term.

To quantify the goodness of regression, the coefficient of determination R^2 was calculated.

The obtained calibration coefficient β was then applied to the whole signal $\Delta\lambda_B$ to obtain $\Delta d_{\Delta\lambda_B}$ signal as in the following equation:

$$\Delta d_{\Delta\lambda_B} = \beta \Delta\lambda_B$$

Equation 4:19

To quantify the difference between the distance Δd_{L3-L1} and the reconstructed distance $\Delta d_{\Delta\lambda_B}$ the $MAE_{\Delta d}$ coefficient was calculated as in the following equation:

$$MAE_{\Delta d} = \frac{\sum_{i=1}^N |\Delta d_{\Delta\lambda_B} - \Delta d_{L3-L1}|}{N}$$

Equation 4:20

Additionally, the lumbar angle (θ) was calculated considering the trajectories of L1, L3, and L4 as shown in Fig. 4:65. In particular, θ was obtained as the angle among two vectors ($\overrightarrow{L1L3}$ and $\overrightarrow{L3L4}$) at each instant:

$$\theta = \cos^{-1} \left(\frac{\overrightarrow{L1L3} \cdot \overrightarrow{L3L4}}{\|\overrightarrow{L1L3}\| \cdot \|\overrightarrow{L3L4}\|} \right)$$

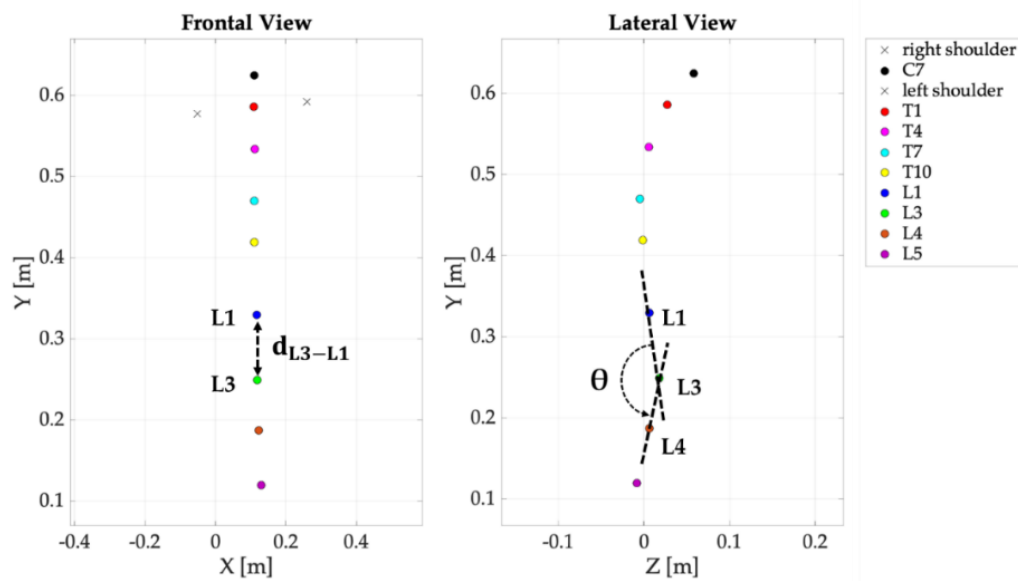


FIGURE 4:65. The distance d_{L3-L1} (left image) and the lumbar angle θ (right image) retrieved from markers' trajectories.

In Figure 4:66, the trends in time of the wearable output ($\Delta\lambda_B$), the distance between L1 and L3 (Δd_{L3-L1}) and the lumbar angle θ evaluated for each trial are reported. It is possible to observe that the FBG and the reference system outputs show good agreement. In fact, as visible from the $\Delta\lambda_B$ and the Δd_{L3-L1} trends, the wearable device was able to follow the volunteers' movements for the entire duration of the trials. In particular, the system succeeded in following the protocol even during the pauses between each set of flexions and extensions and during the execution of minimal movements (see Figure 7, Trial 6), which confirms the high sensitivity of the flexible sensor. The trends in time of θ are used as a further reference to evaluate the amplitude of the F/E movements performed during the protocol's execution. Moreover, F/E are clearly distinguishable: flexions are defined as the signal peaks (which are the portions of the signal between two consecutive minimum points starting from the first recorded value), while the extensions are defined as the signal valleys (which are the signals included between two successive maximum points starting from the first recorded value). For every trial, eight flexions and extensions can be counted, with a total amount of sixteen F/E movements, as expected. The widest $\Delta\lambda_B$ excursion that occurs during the trials is about 2 nm. It is worth noting that such strain condition was widely evaluated during the mechanical characterization of the flexible sensor.

Here below, Table 4:24 summarizes the β regression and the R^2 coefficients related to the regression procedures.

TABLE 4:24

Trial	#1	#2	#3	#4	#5	#6	#7	#8
β [cm·nm ⁻¹]	1.38	2.10	2.78	1.08	1.43	0.32	1.45	1.84
R^2	0.92	0.78	0.89	0.66	0.91	0.93	0.88	0.88

As shown in the table, the β differs trial by trial from 0.32 cm·nm⁻¹ to 2.78 cm nm⁻¹; all the R^2 values denote moderate to good quality of regression.

Table 4:25 reports the range of Δd_{L3-L1} calculated from data recorded by the MoCap together with the MAE_{Δd}. The maximum value of MAE_{Δd} was 0.33 cm (~16% on the Δd_{L3-L1} the amplitude of 2.02 cm, as in Figure 4:66 (a).

TABLE 4:25

Trial	#1	#2	#3	#4	#5	#6	#7	#8
MAE _{Δd} [cm]	0.33	0.18	0.21	0.14	0.14	0.07	0.28	0.29

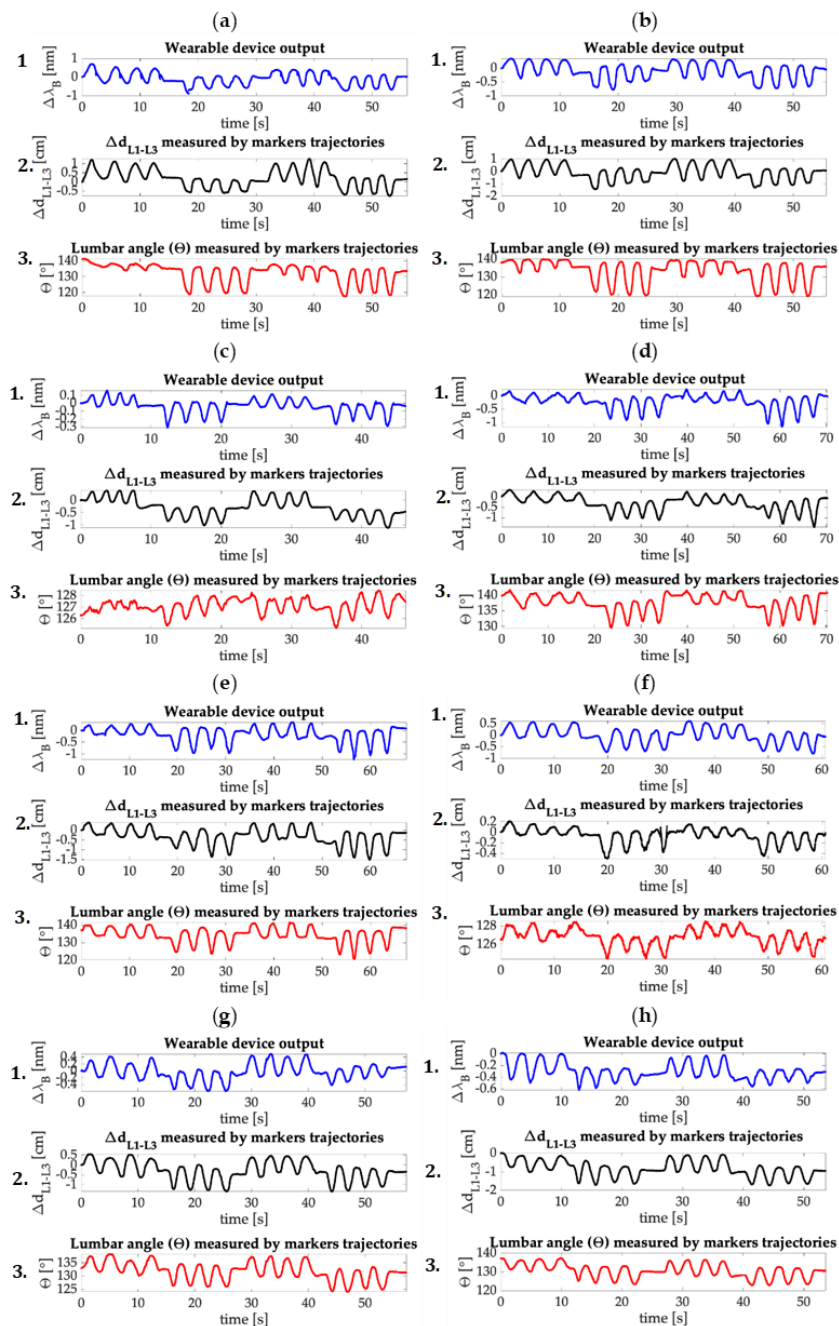


FIGURE 4:66. (1) The wearable output ($\Delta\lambda_B$), (2) the distance between L1 and L3 (Δd_{L3-L1}) and (3) the lumbar angle (θ) trends obtained per each trial. (a): Trial 1; (b): Trial 2; (c): Trial 3; (d): Trial 4; (e): Trial 5; (f): Trial 6; (g): Trial 7; (h): Trial 8.

In Fig. 4:67, the distance between L1 and L3 evaluated by the MoCap system (Δd_{L3-L1}) and the reconstructed distance ($\Delta d_{\Delta\lambda B}$) are shown for each trial. Once again, it is possible to appreciate the concordance of the two signals over time. Also in this case, F/E movements are clearly

LD

distinguishable, as well as the minimal movements and the pauses performed between each set of flexions and extensions.

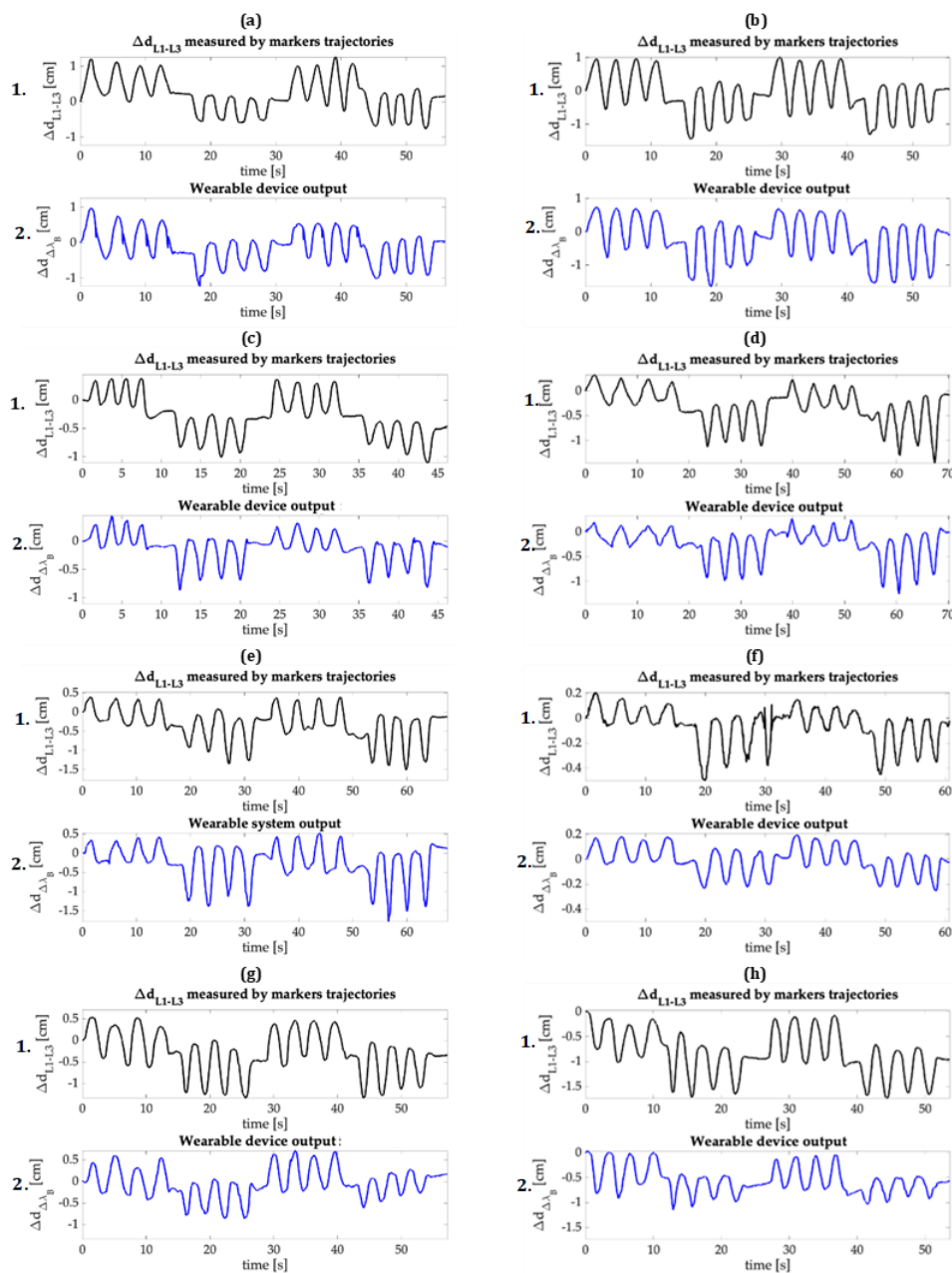


FIGURE 4.67. (1) The distance between L1 and L3 evaluated by the MoCap (Δd_{L1-L3}) and (2) the reconstructed distance ($\Delta d_{\Delta A, B}$) obtained per each trial. (a): Trial 1; (b): Trial 2; (c): Trial 3; (d): Trial 4; (e): Trial 5; (f): Trial 6; (g): Trial 7; (h): Trial 8.

The strength of the presented wearable device relies on the high sensitivity of the flexible sensor that permits continuous lumbar monitoring over time (even in case of pauses between

the F/E movements or minimal motions), as well as the distinction of flexion and extension phases. Moreover, the design of the structure allows the proposed solution to be easily worn over any type of garment, while its lightness and compactness permit the use of the device for the entire working day. Furthermore, thanks to the adjustable elastic suspender, the smart wearable can fit any body shape and size.

The proposed device lays the basis for the development of FBG-based wearables for workers' safety monitoring and could carry the research one step forward in occupational health. In clinical practice, one of the most reliable and accurate techniques to detect lumbar ROMs is the use of radiography [420], [421]. In fact, intervertebral angles can be identifiable by evaluating the radiographic images of subjects' back in F/E postures. Unfortunately, the disadvantages brought by such practice are several, as it is time-consuming and too invasive due to repeated X-ray exposures. Therefore, in the last decades, clinicians have been moving towards the use of ever safer, less invasive, and immediate techniques and devices (e.g., goniometers [422], MoCap systems [421]) and wearable instrumented by MEMS accelerometers and piezoresistive textiles [423], strain gauge sensors [424], and FOSs-based systems [425]–[427] technologies. Thanks to its flexibility, although the proposed configuration reached MAE values higher than 2% and was assessed in sitting positions, it is unobtrusive and compliant with the natural spinal curvature, so easily acceptable for the users in the working scenario. Besides, the optical signal is not affected by noises and electromagnetic interferences, permitting large-scale employment even in challenging and harsh environments (e.g., in the presence of strong electromagnetic fields).

4.3 Wearables for sensorimotor behavioral assessment

In the following section, the design of an FBG-based smart device for measuring palmar grasps of newborn infants is proposed. This is the first device based on FBG proposed in the literature for this aim.

It consists of a cylindrical-shaped structure filled by a flexible polymer encapsulating an FBG sensor (see Fig. 4:68). The mechanical coupling between the hand and the device is described using F and P exerted.

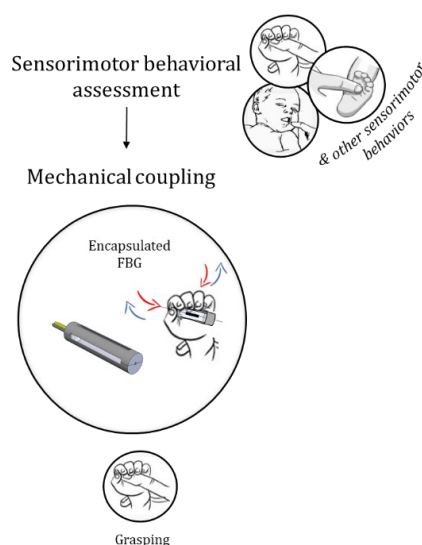


FIGURE 4:68. Wearables for sensorimotor behavioral assessment: for grasping investigations, encapsulated FBG are used to fill greppable/graspable tools.

A description of this FBG-based system focusing on the design, fabrication, metrological characterization, and results of the preliminary tests during grasping is presented below.

An fMRI compatible smart device for measuring palmar grasping in newborns¹⁴

Grasping is one of the first dominant motor behaviors that enable the interaction of a newborn infant with its surroundings. Although atypical grasping patterns are considered predictive of neuromotor disorders and injuries, their clinical assessment suffers from examiner subjectivity, and the neuropathophysiology is poorly understood. Therefore, the combination of technology with fMRI may help to precisely map the brain activity associated with grasping and thus provide important insights into how functional outcomes can be improved following

¹⁴ This work is an excerpt from "An fMRI Compatible Smart Device for Measuring Palmar Grasping Actions in Newborns" in which the Ph.D. candidate is the main author. doi: <https://doi.org/10.3390/s20216040>

cerebral injury. The present study aims to develop an FBG-based measuring system (hereinafter called the smart graspable device - SGD) to detect newborns' grasping actions. Firstly, the design, the fabrication, and the metrological characterization are proposed. Finally, two preliminary trials were carried out to investigate the performances of the proposed device when used by a preterm infant in the neonatal intensive care unit and an adult during an fMRI experiment.

Design, fabrication, and metrological characterization

Designing a sensing device able to detect natural grasping actions and work simultaneously within an fMRI experiment is very challenging. Furthermore, there are additional constraints set by the target population (i.e., preterm and term newborn infants), which are not fulfilled by the majority of devices currently proposed in the literature [348], [428]. Also, the electromagnetic field inside the MRI environment can affect the working capability of most electronic devices proposed for grasp measurements and can induce currents in metal loops leading to infant contact burns [429], [430]. In the same way, ferromagnetic elements widely used as components of graspable electronic devices may cause artifacts on the MRI images themselves, affecting diagnostic image quality [431].

As newborn infants are inherently uncooperative subjects, a further requirement of the device is that their natural movements can be safely measured under natural conditions [348], [432]. The proposed tool should be small and light-weight to allow handling by a newborn infant, and its shape should be appropriate to improve engagement and encourage palmar grasping [433]. Moreover, high sensitivity to a low range of loads is necessary to detect the hand closure of a newborn infant, as well as being biocompatible and easily cleaned reduce the risk of cross-infection between subjects [434], [435].

To meet all of these technical and clinical requirements, an FBG sensor was chosen as the sensing element. A flexible and non-toxic silicone rubber (i.e., Dragon Skin™ 10) was used as a squeezable matrix to encapsulate the FBG sensor [379]. Lastly, a polylactic acid (PLA) structure characterized by a linkage mechanism filled with the soft silicone was designed according to the index finger dimensions of an adult human as this is typically used to insert into the infant's palm to elicit the grasping reflex. The proposed solution is highly sensitive, robust, safe, affordable, and infant-friendly.

The idea behind the system design and manufacturing was based on the need for it to be sensitive enough to detect F_{ext} applied by the infant and able to transduce F_{ext} into grating ϵ measured by the FBG sensor. At the same time, the device should be robust and safe enough to be handled and grasped by a newborn infant in a variety of settings.

The medium consists of a PLA-based structure characterized by a linkage mechanism and filled by flexible silicone (i.e., Dragon Skin™ 10). The transduction mechanism exploits four-bar linkages hinged to the PLA structure ends to convert the applied F_{ext} into ϵ via the silicone squeezing and releasing. When the newborn infant grasps the device, the silicone squeezes, and the FBG is strained; and is then unstrained once the SGD is rereleased (see Fig. 3:22).

The PLA structure is a hollow cylinder made up of two semi-cylindrical pieces (see Figure 4:69 A and 4:69 B). Each piece is constituted of two end parts perpendicularly spaced by two bar linkages (40 mm of length, 4.2 mm of width, and 1 mm of depth). The bar linkages are hinged along the ends with a uniform interval of 60° to form a symmetrical structure (Fig. 4:69 A, top and front views). One semi-cylinder has a 10-mm length conduit to accommodate the jacket (yellow cable in Fig. 4:69 B). The jacket is the last layer of protection of the optical fiber from the end of the PLA structure to the interrogation unit.

The outer diameter of the PLA structure is 12 mm, and its overall length is 50 mm, which corresponds roughly to the dimensions of a human finger. The sensing element embedded into the PLA structure consists of an FBG sensor (λ_B of 1547 nm and grating length of 10 mm, commercialized by AtGrating Technologies, Shenzhen, China) configured with the middle part of the optical fiber encapsulated into a Dragon Skin™ 10 silicone matrix.

The encapsulation was fabricated as follows:

1. The optical fiber was tightly suspended inside the PLA structure by firmly gluing its two ends inside the small grooves fabricated at the center of the structure ends. This configuration utilized a pre-tension to keep the FBG in a stretched state in order to improve its resolution and sensitivity (stage 1 in Fig. 4:69 B);
2. The PLA structure was placed inside a mold to allow the cavity to fill without any silicone spilling. The silicone rubber was synthesized by mixing A and B liquid components of Dragon Skin™ polymer at a ratio of 1:1; the mix was degassed and poured into the cavity (stage 2 in Fig. 4:69 B);

3. A curing process of 5h was carried out at room T, as suggested in the technical bulletin [379], to allow the silicone rubber vulcanization before extracting the SGD from the mold (stage 3 in Fig. 4: 69 B).

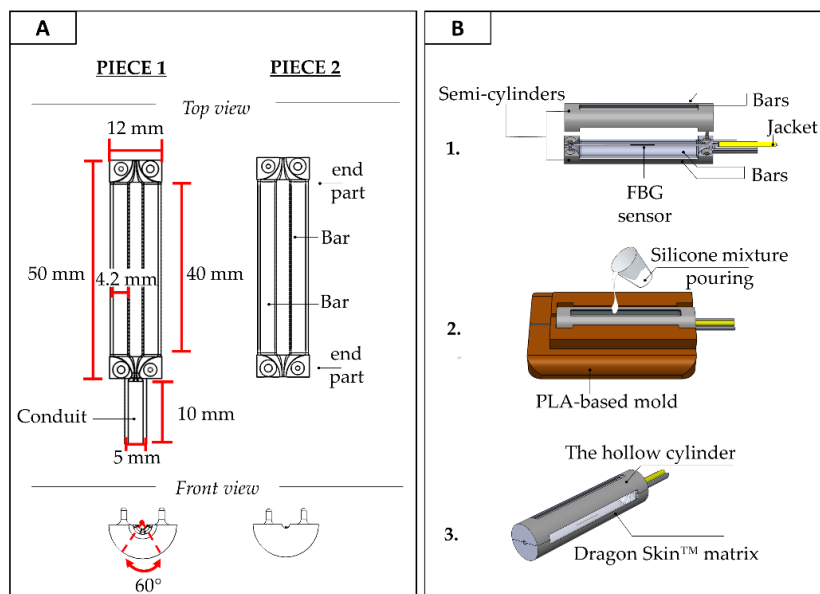


FIGURE 4:69. (A) The geometrical features of SGD; (B) the main manufacturing steps: the FBG sensor positioning (step 1), the silicone mixture pouring (step 2), and the SGD removed from the mold after the rubber vulcanization (step 3).

Two nominally identical SGDs (from now on referred to as SGD¹ and SGD²) were developed following the same manufacturing stages previously described.

To improve the SGDs usability during fMRI, both the devices were also designed to be able to instrument an already existing fMRI-compatible robotic interface for conducting experiments with newborn infants described in [436], [437]. This interface was designed to accommodate the infant's forearm on a central non-sensitive platform and to passively guide the flexion and extension of the infant's wrist while the hand was wrapped around a bar. The instrumentation of the robotic interface with the proposed SGD was performed by switching the non-sensitized handlebar with the SGD, so allowing the investigation of brain activity related to grasping and spontaneous movements (Fig. 4:70 A and B). Two temporary PLA-based anchoring systems were fabricated to fit the SGD to the robotic interface (see Fig. 4:70 A). The anchoring mechanism was designed to allow quick and easy fitting of the SGD according to the fMRI investigation being performed.

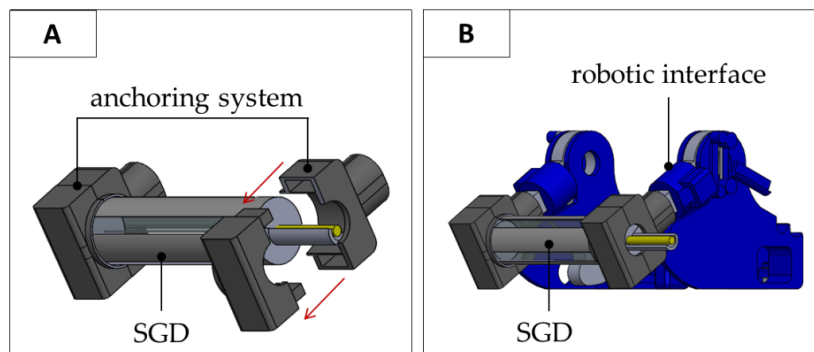


FIGURE 4:70. (A) A detail of the anchoring system elements designed to allow fitting of the SGD within an already existing robotic interface; (B) the SGD together with the robotic interface.

Before developing the proposed system, the compression behaviors of Dragon Skin™ silicones with different harnesses were investigated in order to define the one which better meets the technical requirements of the proposed sensing solution.

The mechanical properties of Dragon Skin™ 10 Medium, 20, and 30 were investigated in terms of σ - ε properties. To better quantify the compression behavior of Dragon Skin™ silicones, the Young modulus E (expressed in MPa) was calculated to drive the selection of the material, which better satisfies all the requirements mentioned above. Considering the scenario of interest and target population, the application of low squeezing F will induce a compression on the silicone rubber with ε values lower than 10% of the rubber sample (l_0). Thus, the σ - ε relationship can be described by Hooke's law [438]:

$$\sigma = E \varepsilon$$

Equation 4:21

Where σ is the external F applied to the sample per its cross-sectional area - A and ε is calculated as $(l-l_0) / l_0$.

The standard ISO 7743:2017 (Rubber, vulcanized, or thermoplastic - Determination of compression stress-strain properties) was used for defining the dimensions of the cylindrical pieces used for the compression tests. The test piece B (method C) with a diameter of 17.8 ± 0.2 mm and a height of 25.0 ± 0.2 mm was chosen [439]. Dragon Skin™ 10 Medium, 20, and 30 were poured into a cylindrical mold designed in Solidworks (Dassault Systemes, Tennessee, USA) and 3D printed using PLA. As suggested by the technical bulletin, the curing process was

carried out at room T for 5 h, 4 h, and 16 h for Dragon Skin™ 10, 20, and 30, respectively. A total of fifteen specimens were fabricated, five pieces for each hardness level.

Compression tests were carried out using the Instron machine (Instron mod. 3365, load cell with a range of measurement of ± 10 N, an accuracy of 0.02 N, and a resolution of 10^{-5} N) to apply controlled ε values (from 0% to 25% of l_0 as suggested by the standard ISO 7743:2017) in a quasi-static condition (at a low displacement rate of $2 \text{ mm}\cdot\text{min}^{-1}$). The static assessment of each specimen was executed by positioning the cylinder-shaped sample between the lower and the upper plates of the machine, as shown in Fig. 4:71. A total of five repetitive compression tests were carried out at room T for a total of twenty tests per sample. The loads and the displacements applied by the compression machine to the specimen were recorded at a sampling frequency of 100 Hz using Bluehill Universal software (Instron®, Torino, Italy).

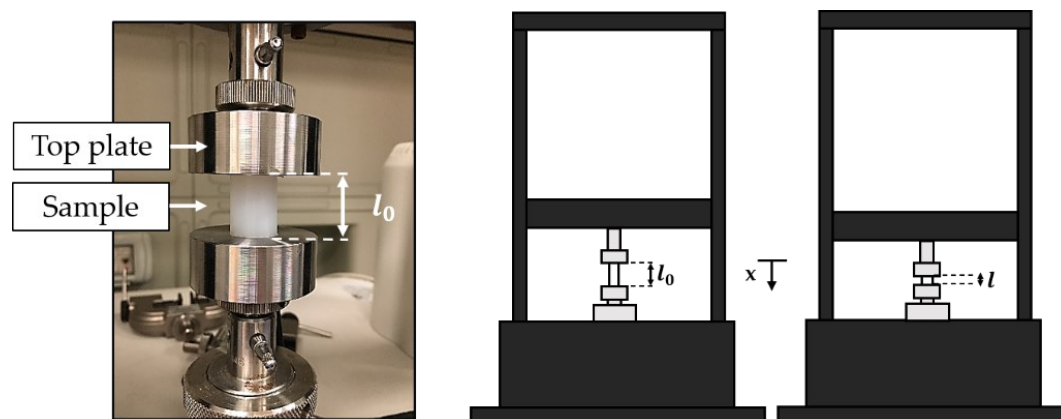


FIGURE 4:71. Setup of the compression tests: the cylinder-shaped sample between the lower and the upper plates of the Instron machine and the initial sample length before (l_0) and during the compression (l) are illustrated. The top plate moves at constant speed parallel to the x-axis.

The σ - ε relationships of each Dragon Skin™ material were obtained by processing the collected data through a custom algorithm. The mean value of experimental σ (σ_{exp}) and the repeatability of the system response was determined by calculating the related uncertainty across the twenty tests by considering a t-student reference distribution with 19 degrees of freedom and a level of confidence of 95% [366]. The best fitting line of the calibration curve was obtained, and its angular coefficient was calculated to estimate E. Lastly, the linearity error was calculated by using Eq. 4:22 in terms of the maximum linearity error ($\% u_{L,\text{max}}$):

$$\% u_L^{max} = \{ \max [\sigma_{exp}(\epsilon) - \sigma_{th}(\epsilon)] \cdot \sigma_{exp}^{-1} \} 100$$

Equation 4:22

Where σ_{exp}^{fs} is the full-scale output range, $\sigma_{exp}(\epsilon)$ the experimental stress experienced by the sample at a specific ϵ , and $\sigma_{th}(\epsilon)$ is the theoretical stress obtained by the linear model at the same ϵ value.

Results showed E values of 0.24 MPa, 0.47 MPa, and 0.74 MPa, for Dragon Skin™ 10, 20, and 30, respectively (see Fig. 4:72). The R² values higher than 0.98 were found for all the responses, and linearity errors of 5.7%, 7.8%, and 8.9% were obtained for Dragon Skin™ 10, 20, and 30, respectively. As expected, Dragon Skin™ 10 is more flexible than Dragon Skin™ 20 and Dragon Skin™ 30. In particular, the E value of Dragon Skin™ 10 is approximately half that of Dragon Skin™ 20 (i.e., 0.24 MPa vs. 0.47 MPa) and one-third that of Dragon Skin™ 30 (i.e., 0.24 MPa vs. 0.74 MPa). The high R² values (for all tests R² > 0.98) indicate good agreement between the experimental data and the linear model. Moreover, the Dragon Skin™ 10 response showed the best linear behavior as testified by the % u_L^{max} value (i.e., 5.7%), which is lower than the ones of Dragon Skin™ 20 (i.e., 7.8%) and Dragon Skin™ 30 (i.e., 8.9%), as shown in the respective plots in Fig. 4:72. Finally, Dragon Skin™ 10 showed the best results in terms of uncertainty (maximum uncertainty of 0.004 MPa) when compared to Dragon Skin™ 20 (i.e., 0.01 MPa) and Dragon Skin™ 30 (i.e., 0.007 MPa).

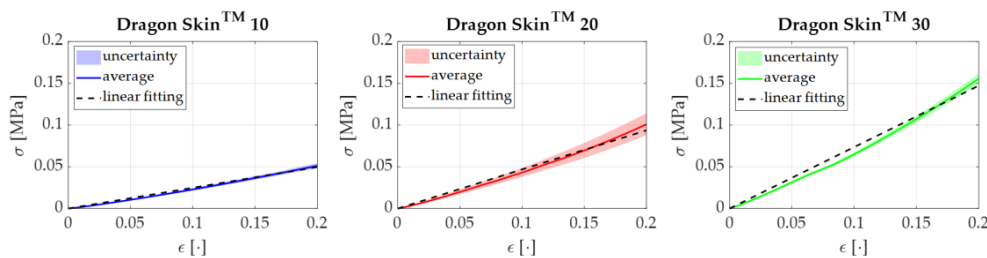


FIGURE 4:72. The σ - ϵ relationships for Dragon Skin™ 10, 20, and 30 are shown in blue, red, and green, respectively. In particular, the continuous lines represent the average σ_{exp} values, the shaded areas the related uncertainties, and the black dotted lines the σ_{th} values obtained by the best linear fitting model.

These findings demonstrated that Dragon Skin™ 10 is best suited to meet the technical requirements of the SGD; particularly given the expected low ranges of F_{ext} applied by newborn infants, which would likely require high flexibility, Dragon Skin™ 10 allow the SGD to be easily squeezed by a newborn for the F_{ext} transduction into grating ϵ .

After that, the two SGDs were fabricated by filling the cylindric-shaped structure with Dragon Skin™10 and, their metrological properties were investigated.

To estimate SGD sensitivity to $F_{\text{ext}} (S_F)$, compression tests were performed by using a tensile testing machine (Instron, mod. 3365, load cell with a range of measurement of ± 10 N, an accuracy of 0.02 N, and a resolution of 10^{-5} N).

Each sensor (i.e., SGD¹ and SGD²) was placed on the lower base of the machine blocked to the support place by using the 3D-printed clamps. External loads in the range ~ 0 N - 2 N were applied on each bar of the SGD at a low compression rate of $2 \text{ mm}\cdot\text{min}^{-1}$ to simulate quasi-static conditions (see Fig. 4:73).

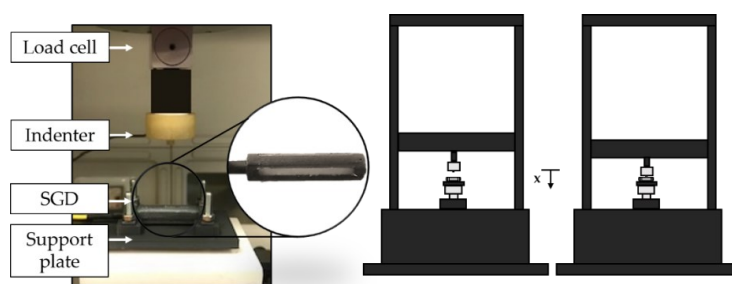


FIGURE 4:73. The SGD in the blocking system, the load cell, and the mechanical indenter are shown in the picture. A schematic representation of the SGD between the lower and the upper plates of the Instron machine is illustrated. The top plate moves at constant speed parallel to the x-axis.

The load was applied to the center of each bar by using a mechanical indenter (5 mm diameter). A total of five compression tests were performed on each of the four bars for a total of 20 tests. Once the five tests related to a single bar ended, the SGD was rotated of 90° along its longitudinal axis, re-blocked to the support, and the second bar was loaded. The same procedure was repeated for the remaining two bars. The S_F value of each SGD was found, averaging the twenty responses of all the bars to the applied loads. During each test, the output from the tensile machine was collected at a sampling frequency of 100 Hz. The $\Delta\lambda_B$ values were simultaneously recorded using the optical spectrum interrogator (si255, Hyperion Platform, Micro Optics Inc., Atlanta, GA, USA) at the same sampling frequency.

The calibration curve ($\Delta\lambda_B$ vs. F_{ext}) was obtained by processing the collected data through a custom algorithm. The average value of $\Delta\lambda_B$ and the related uncertainty were calculated across the twenty tests by considering a t-student reference distribution with 19 degrees of freedom and a level of confidence of 95%. The best fitting line of the calibration curve was

computed, and its angular coefficient was calculated to find out the S_F value for SGD^1 and SGD^2 (see Fig. 4:74).

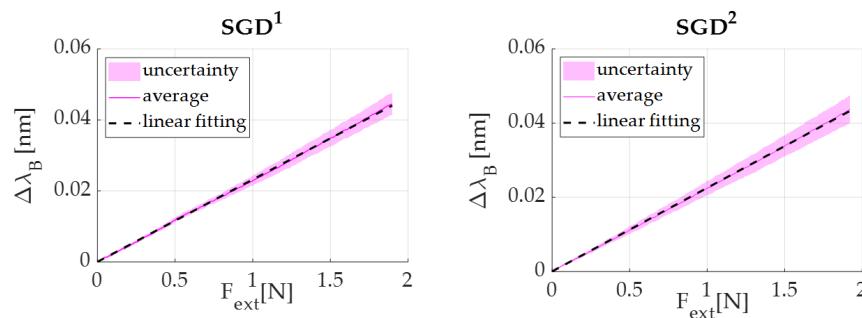


FIGURE 4:74. The $\Delta\lambda_B$ vs. F_{ext} of SGD^1 and SGD^2 : in continuous magenta lines the average $\Delta\lambda_B$ vs. F_{ext} responses, in the shaded magenta area the related uncertainties and in dotted black lines the best linear fitting.

Results showed S_F value of $\sim 0.23 \text{ nm}\cdot\text{N}^{-1}$ for both the devices suggesting a good reproducibility of the fabrication process. Moreover, $R^2 > 0.99$ indicated excellent agreement between the experimental data and the linear fitting model.

Preliminary trials

After the metrological characterization, the proposed SGDs performance was investigated in a real scenario. Two explorative tests were performed with a newborn infant and an adult subject. Given the high agreement in S_F value between SGD^1 and SGD^2 , SGD^1 was used for the following tests and for simplicity, is now referred to as SGD. First, an explorative test was performed on a healthy newborn infant in the neonatal intensive care unit of St. Thomas Hospital (London, UK) to test the compatibility of the SGD and assess its ability to detect a newborn infant's grasp. A further explorative trial within an fMRI experiment was then carried out to validate the device performances inside the MRI scanner and confirm that activation within the brain areas associated with the grasping action detected by SGD could be identified with fMRI.

To assess the capability of SGD to detect grasping behavior in newborn infants, three healthy infants were recruited at St Thomas' Hospital (London, UK). Of them, only one infant (gestational age at birth: 36 weeks + 6 days, postmenstrual age at the time of recording: 37 weeks + 2 days) was in a suitable awake state at the time of the recording. The study was approved by the NHS research ethics committee (REC code: 12/LO/1247), and informed written consent was obtained from parents before participation. Under the supervision of a physician,

a neonatal physiotherapist handled the SGD and applied light pressures on the infant's palm to induce hand closure around the device and elicit grasping behavior. Data from the SGD were collected using the FBG interrogator (si425, Micron Optics Inc., Atlanta, GA, USA) at a sampling frequency of 250 Hz. A video used as reference was simultaneously recorded using a camera (Handycam, Sony, Minato-ku, Tokyo JP). After data acquisition, the physiotherapist and the physician checked the recorded video to identify the time windows corresponding to the newborn infant's grasping action. A total of five grasping events were identified. A total of five grasping events were identified (see Fig. 4:75 A).

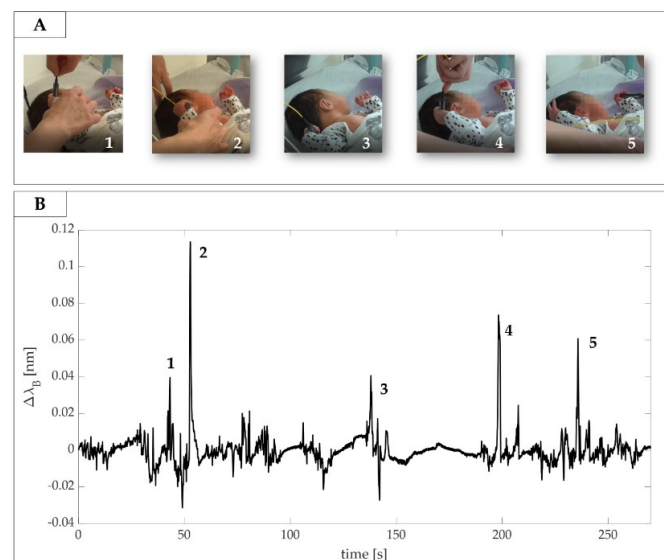


FIGURE 4:75. (A) Video frames of grasping actions identified by the clinicians; (B) the related signals collected by the SGD. Grasps actions are enumerated from 1 to 5.

Those time windows were then used to highlight changes in the SGD output associated with grasping actions. The signal showed evident peaks during this specific time window related to presumed SGD squeezing and releasing actions (see Fig. 4:75 B). Results showed $\Delta\lambda_B$ values ranging from 0.04 nm to 0.11 nm that corresponds to F ranging from ~ 0.17 N to ~ 0.48 N.

The second trial was performed on a healthy volunteer (32 years old, adult female volunteer) inside a 3 Tesla MRI scanner (Philips Achieva, Best, NL) located at St Thomas Hospital with a 32-channel receive head coil. High-resolution structural T1-weighted and T2-weighted images were acquired for image registration purposes. BOLD contrast fMRI data with an EPI

GRE sequence with parameters: x/y/z resolution: 3.5 mm x 3.5 mm x 6 mm; TR: 1500ms; TE: 45ms; FA 90°.

The subject was studied with her right hand fitted inside the instrumented robotic interface described in [436], [437] with the right index and middle fingers strapped to the SGD on the handlebar. The subject was then asked to use their two fingers to apply a short F on the SGD at spontaneous and random times during an acquisition session lasting 225 s (corresponding to 150 images). The SGD signal was collected using the FBG interrogator (si425, Micron Optics Inc., Atlanta, GA, USA) at a sampling frequency of 250 Hz, and the recording started synchronously with the fMRI image acquisition so that the timing of the task could be related to the fMRI time series. The task was designed to simulate a situation in which the experimenter is unaware of the timing of the task inside the scanner, as would be in the case of studying spontaneous motor behavior in infants, but can obtain this information from the output of the SGD. The experimental set-up and data flow are shown in Fig. 4:76.

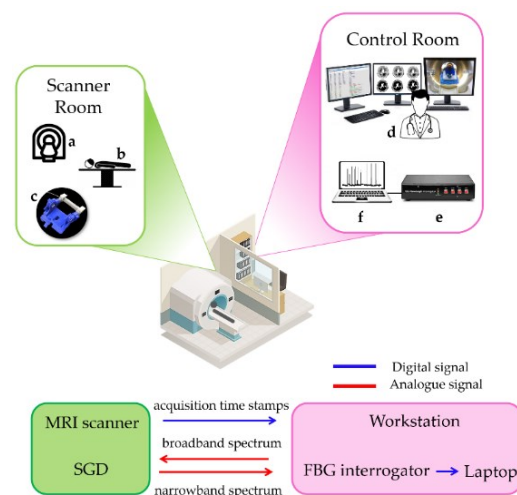


FIGURE 4:76. Experimental set-up of fMRI trial with the data flow: the MRI scanner (a), the patient (b) and the robotic interface instrumented by the SGD (c) in the scanner room, and the workstation (d), the FBG interrogator (e) and the laptop (f) in the control room. Digital and analogue data flows between the scanner and control rooms are shown using blue and red arrows, respectively.

The acquisition volume trigger markers (via a TTL pulse) were transmitted to the scanner workstation and used offline to synchronize the fMRI data with the signal recorded by the SGD. Data from the SGD were analyzed in MATLAB environment. As shown in Fig. 4:77 A, the device was able to detect the F applied by the subject without prior knowledge of its timing (i.e., 26 actions in the SGD output across the period of acquisition) from which the event-related occurrence of the task could be defined for the fMRI data analysis. In order to identify which voxels of the brain images were active during the task, it is possible to use a simple general linear

model (GLM) to fit the BOLD time series within each voxel with a temporal model of the predicted activation and the strength of each fit is used to generate a z-statistics map across the whole brain. The predicted activation used as a model is built as the convolution of the experimental design (a vector that represents the timing of action vs. rest) and the haemodynamic response function (HRF) that acts as a temporal smoothing kernel. The SGD-derived task pattern was then expressed in a binary vector form (with 1's representing action and 0's representing rest) where the events were identified using the *findpeaks* function on the normalised SGD signal in MATLAB (see Fig. 4:77 A).

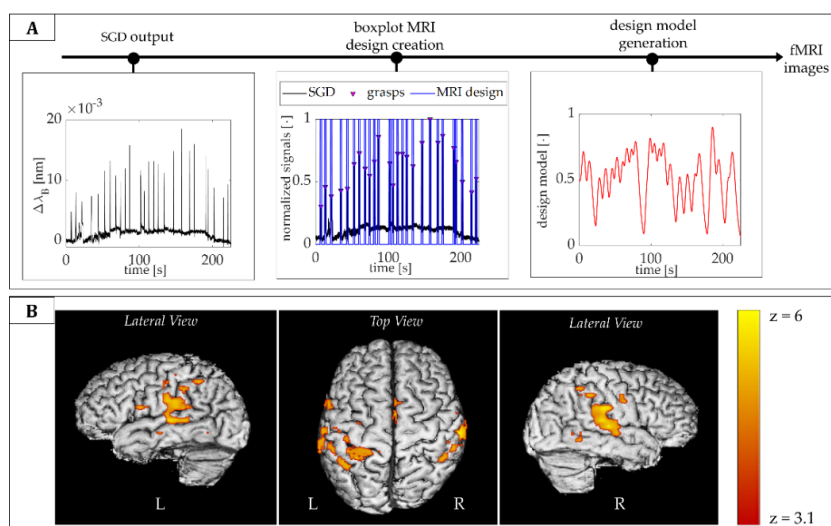


FIGURE 4:77. (A) The flow of data analysis. The peaks in $\Delta\lambda_B$ coming from the SGD were used to infer the timing of the action and create a boxplot MRI design. This was convolved with the HRF to generate the design model for the GLM. (B) Significant clusters of functional response to the task (in red and yellow) overlaid onto the subject's T1-weighted brain image.

Each event was represented by 8 ms centered at the peak of the action. The binary vector was then convolved with the canonical hemodynamic response function (HRF) to generate the design model for the general linear model fMRI analysis (see Fig. 4:77 A). MRI data were processed using tools implemented in the FMRIB Software Library (FSL) in [440] following a standard pipeline which included: high pass temporal filtering (with 0.02 Hz cut-off frequency), MCFLIRT rigid body motion correction, slice timing correction, brain extraction using BET, spatial smoothing (Gaussian of FWHM 5 mm), univariate general linear model (GLM) with additional six motion parameters derived from the rigid body motion correction as confound regressors, cluster correction (p threshold 0.05). As predicted, significant clusters of positive BOLD activity located in the primary contralateral (left) somatosensory and motor cortices and

supplementary motor area correlating to the task performed by the subject, and the main cluster of activation located at the hand knob on the precentral gyrus (see left - L and right - R lateral and top view on the 3D rendered brain images in Fig. 4:77 B).

To the best of our knowledge, the proposed SGD is the first fMRI-compatible device based on FBG able to detect and measure palmar grasp in preterm and term infants. The SGD is shaped and sized appropriately to be handled by a newborn infant's hand, easily squeezed, and able to detect low grasping F_{ext} . Furthermore, the FBGs' EMI compatibility ensures the safety and working capability both outside and inside the MRI environment. These preliminary validation experiments revealed that the SGD could work in both cases: on a non-collaborative subject (i.e., the newborn infant) and within the MRI environment.

In the literature, pioneering work describing grasping behavior in infants began in the 1930s [441]–[443]. These first studies were based on functional scales or on the direct observation of infant responses to light pressure applied on the palm [444]. These methods suffer from several limitations, including examiner subjectivity and incapability of quantifying grasping actions in terms of strength and duration. With the advancement of technological devices, novel methods emerged for assessing motor function in early infancy [351], [432], [435], [445]–[449]. In particular, grasping behavior has been studied in infants in terms of strength and holding time, with some studies proposing novel systems to investigate the relationship of these variables with intrinsic (e.g., infant sex [435], weight [434], preterm birth [450]) and extrinsic factors (e.g., object shape and texture [449]). Moreover, systems for objective assessment of grasping actions were developed to detect early abnormal neuromotor development and based on the premise that this could guide prompt intervention to improve functional outcome [447], [451]. The main findings of the state-of-the-art showed: *i*) a higher grasping strength and pronounced handedness symmetry in males more than females [435], *ii*) a decrease in holding time when the same object is repetitively put in the newborn infant's hand, and an increase when its shape and smoothness changes [449]; *iii*) longer holding times in preterm in comparison to term neonates with significant differences related to sex [435].

Existing technological tools developed for measuring grasping in newborn infants can be grouped into devices worn on the examiner's finger [351] or those that are directly handled by an infant. [351], [432], [446], [447]. Very few of these systems were also specifically designed to be used by newborn infants in the first days following birth. All of these systems are based on pressure transducers with electrical components (i.e., piezoresistive sensors [446], F sensing resistors – FSR [432], capacitive sensors [351], and conductive polymer layers [447]). These features do not allow their employment inside the MRI scanner. In contrast, our device

is designed to be directly handled by a newborn infant and can be used in fMRI owing to the FBG sensor EMI immunity and the SGD affordable shape.

In [446], as in our study, the device was designed to be directly grasped by a newborn infant without active involvement from the examiner during the experimental trial. An electrical sensing element (i.e., a piezoresistive pressure transducer) was used to develop a ring-shaped device consisting of a silicone-filled chamber hanged within a rigid case and connected to the transducer (total diameter of 93 mm). This allowed measuring infant grasping activity generated by chamber internal pressure changes due to the silicon squeezing. Our device differs as the proposed SGD is based on optical technology instead of electrical components, is softer (10A vs. 50A), and considerably lighter (8 g vs. 115 g). All of these features make our system more suitable for studying a broader range of infant populations, including preterm and term infants.

Indeed, this study was only a preliminary investigation. Future applications of the proposed SGDs will aim to investigate further the feasibility assessment in a broader range of newborn infants both inside and outside the MRI scanner. To improve the system usage, the SGD will be embodied into a wearable device for the fingers/palm of infants. In this way, the SGD can be easily employed inside the MR scan without any external clinical support. Moreover, wearable systems for left and right hands instrumented by the SGDs can be used together in longitudinal studies to study the emergence of hand dominance and (bi)manual grasping to investigate developmental motor disorders resulting from localized brain injury and provide new insights into behavioral neurophysiology and neuropathology.

Tesi di dottorato in Scienze e ingegneria per l'uomo e l'ambiente, di Daniela Lo Presti,
discussa presso l'Università Campus Bio-Medico di Roma in data 9/04/2021.
La disseminazione e la riproduzione di questo documento sono consentite per scopi di didattica e ricerca,
a condizione che ne venga citata la fonte.

LL

Chapter 5 Conclusion

The increase of the elderly population and the development of chronic diseases is leading to the growing market for wearable devices. Their application in SH, ranging from clinical to sport/fitness and occupational sectors, suggests the increasing immersion of wearables into daily life and their considerable impact on people's health, as described in Chapter 1.

Continuous monitoring of human activities can foster a culture of well-being pushing the disease treatment progression, a prompt patient assistance, and the development of patient-specific technological solutions. Focusing on their use as medical devices, wearables often require direct contact with skin or interact with a biological substance such as sweat and exhaled air; thus, they should meet stringent clinical (e.g., biocompatibility, EMI proof, high/low- T operating life, and high-pressure resistance) and technical requirements (e.g., user-friendly, highly reliable and accurate).

FBG sensing is a well-established technology that provides an accurate monitoring of the human health status showing advantages where the competitor electric sensors have difficulties (Chapter 2). Following this path, this thesis focused on the SH revolution and the role of FBGs-based wearable systems in the SH framework to answer the two questions proposed at the end of Chapter 1.

The first one was:

" What are the key elements to consider for the development of FBG-based wearables usable for SH applications?"

The FBGs advantages promote the use of this sensing technology for the development of wearables with medical potentialities. For instance, in all the previous study cases, the FBG small size, good metrological properties, and intrinsic biocompatibility resulted in key features where high performance, well body mechanical coupling, and fabrics integration were required. These benefits made these sensors particularly attractive for the development of

wearables employable in biomechanics, physiological monitoring, and sensorimotor behavioral assessment on newborns (see Chapter 4). At the same time, the possibility to perform high resolved and distributed measurements enabled the use of FBGs for monitoring chest wall vibrations, compartmental volumes after a pre-calibration and, vital parameters with higher reliability (as in some technological solutions described in Chapter 4).

Further investigations will mainly focus on the BCG/SCG extraction from the chest wall displacements by developing innovative sensors in terms of shape, mechanisms of adhesion to the body, and standard positioning. Moreover, arrays for low back measurements and spline shape reconstruction will also be considered as novel technological solutions for rehabilitation and occupational settings.

Some limitations related to this technology should also be underlined since they must be considered in the development of high-performant and robust medical wearable devices. First, an improvement of robustness is mandatory when FBGs are used to instrument wearable devices. Indeed, this technology requires body-contact and may be subjected to high ε (e.g., during joint bending) as described in Chapter 3. To meet these requirements, flexible and soft polymeric matrices have been used in the described works to encapsulate the grating and making FBGs more robust and easier to handle. Moreover, systems for making the wearable solutions able to fit different body shapes have been developed (e.g., Velcro straps and buttons) to make the FBG-based flexible sensors easily worn by subjects with different anthropometric (see Chapter 4).

Another important factor to underline is that these sensors need a physical connection between the interrogation unit and the optical fiber. Thus, during the design, it is important to consider additional wearable elements such as terminal boxes with patch panel faceplates. Inside the box, the optical cable ends, providing a patch point for a small number of connections to access the communication and interrogation equipment. This box is usually installed with adapters or pigtails with connectors and should also be positioned on the wearable system. One side of the panel is usually fixed, meaning that the fiber cables are not intended to be disconnected. On the other side of the panel, patch cords can be plugged in to establish the physical connection between the wearable system and the interrogator unit.

The second question was:

“Which main steps should be accomplished to translate such an optical technology from structured environments to clinical and everyday settings?”

The Healthcare 4.0 revolution has placed demands of systems conformally attached to human bodies minimalizing discomfort and promoting a great deal of sensing functionalities. The achievement of such high expectations requires the development of skin-like flexible sensors more comfortable and performant than those currently proposed in the state-of-the-art (Chapter 1). For this reason, a considerable amount of research has been dedicated to the fabrication and characterization of FBG-based sensors encapsulated into soft matrices.

Over the last years, several polymers have been investigated for grating encapsulations and fastener solutions have been proposed (e.g., buttons, straps, tapes), improving the FBGs use and acceptance for a broader range of population (Chapter 2). In this works, Dragon Skin silicones have been extensively used as flexible matrices due to their high flexibility and biocompatibility (Chapter 4).

Although the successful implementation of FBGs-based technologies in clinical trials and daily life activities has been proved both in this thesis than in the literature, there are still challenges to encounter and issues to overcome.

A limited amount of solutions are currently used in clinical practice [48], and no systems have been used for long-term monitoring in everyday settings. Some FBGs-based systems have been tested in clinical trials for biomechanics, and physiological monitoring [46], [355], patented surgical instruments have been proposed for tactile and shape sensing, and few solutions tested in scenarios mimicking real-life settings (Chapter 2 and Chapter 4).

To show the maturity of FBGs-based solutions described in Chapter 2, the technology readiness level (TRL) is illustrated in Fig. 5:1. All the implemented systems achieved a TRL ranging from 3 to 9. The highest level is around 3 for biosensing, 5 for both biomechanics and physiological monitoring where many wearable solutions are included, and 9 for MIS as commercial solutions certified EN60601 are available [204] (see Fig. 5:1).

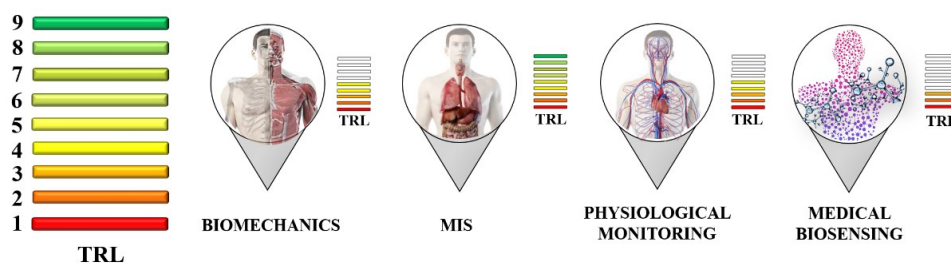


FIGURE 5:1. The TRL level of FBG-based systems for medical and healthcare applications.

Our custom technological solutions achieve a TRL around 5-6. Hence, more efforts should be made to translate these prototypes from laboratory settings to everyday life.

Unfortunately, the wide acceptance of FBGs-based wearables for uses in SH framework (for both clinical and everyday life settings) is still dampened by the need for both an interrogation unit and the physical connection between the interrogator and the optical fiber embedding the FBGs, as already described. Recently, steps forward have been taken to contain the optical interrogator bulkiness and related costs. Indeed, commercial solutions with package dimensions smaller than 40 mm x 40 mm x 50 mm and prices lower than \$ 7000 are available. The open challenge is to improve the performance of the miniaturized interrogators since they show lower resolution, lower interrogation speed, narrower wavelength bandwidth, and smaller number channels than the bulky interrogators. A miniaturized interrogation unit can also lead to a removal of the terminal boxes and, thus, to low overall encumbrance.

Another open challenge regards the development of even more realistic simulations for studying the polymeric matrix-fiber surface interaction. This knowledge may be useful to develop optimized, flexible sensors customized on the application of interest, finding the good trade-off between system structure robustness and performances. To date, no further models of this interaction are presented in the literature; hence, future works will be devoted to studying these bonding mechanisms and their modeling to develop optimized sensing solutions

Moreover, in a future perspective, improvements in the FBG inscription process, containment of FBG array dimensions, quality of multicore fiber technology, and T self-compensation will extend the potential market of FBG-based wearable devices in medicine and healthcare.

However, the considerable amount of attention given to FBGs in scientific papers and the growing market interest regarding their applications in healthcare (e.g., the increase of emerging and up-to-date sensing solutions for wearables and biosensing) underline the strong interest to fulfill the gap between research and everyday practice [49], [48].

Once the challenges above will be addressed and future trends realized, the next generation of medical devices will exploit the advantages of FBGs into portable solutions. The miniaturization of high-performant interrogation units and the development of optimized FBG-based sensing solutions, as well as the incorporation of wireless data communication modulus and the implementation of direct control strategies, will push the establishment of digital Health architectures also based on fiber optics. Such innovation will encourage the extensive use of FBG-based technology in SH framework, contributing to make it an effective integral part of medical devices and a novel healthcare system.

Tesi di dottorato in Scienze e ingegneria per l'uomo e l'ambiente, di Daniela Lo Presti,
discussa presso l'Università Campus Bio-Medico di Roma in data 9/04/2021.
La disseminazione e la riproduzione di questo documento sono consentite per scopi di didattica e ricerca,
a condizione che ne venga citata la fonte.

References

- [1] S. Tian, W. Yang, J. M. Le Grange, P. Wang, W. Huang, and Z. Ye, "Smart healthcare: making medical care more intelligent," *Glob. Heal. J.*, vol. 3, no. 3, pp. 62–65, 2019.
- [2] Health Services Delivery Programme and Division of Health Systems and Public Health, "Transforming health services delivery towards people-centred health systems," p. 23, 2014.
- [3] R. M. Epstein, K. Fiscella, C. S. Lesser, and K. C. Stange, "Analysis & commentary: Why the nation needs a policy push on patient-centered health care," *Health Affairs*, vol. 29, no. 8. Health Affairs, pp. 1489–1495, 02-Aug-2010.
- [4] E. Kanasi, S. Ayilavarapu, and J. Jones, "The aging population: demographics and the biology of aging," *Periodontology 2000*, vol. 72, no. 1. Blackwell Munksgaard, pp. 13–18, 01-Oct-2016.
- [5] "<https://www.who.int/news-room/fact-sheets/detail/ageing-and-health>."
- [6] S. Prasad, B. Sung, and B. B. Aggarwal, "Age-associated chronic diseases require age-old medicine: Role of chronic inflammation," *Preventive Medicine*, vol. 54, no. SUPPL. NIH Public Access, p. S29, 01-May-2012.
- [7] Y. A. Qadri, A. Nauman, Y. Bin Zikria, A. V. Vasilakos, and S. W. Kim, "The Future of Healthcare Internet of Things: A Survey of Emerging Technologies," *IEEE Communications Surveys and Tutorials*, vol. 22, no. 2. Institute of Electrical and Electronics Engineers Inc., pp. 1121–1167, 01-Apr-2020.
- [8] A. Kumar, R. Krishnamurthi, A. Nayyar, K. Sharma, V. Grover, and E. Hossain, "A Novel Smart Healthcare Design, Simulation, and Implementation Using Healthcare 4.0 Processes," *IEEE Access*, vol. 8, pp. 118433–118471, 2020.
- [9] J. Chen, C. D. Mullins, P. Novak, and S. B. Thomas, "Personalized Strategies to Activate and Empower Patients in Health Care and Reduce Health Disparities," *Heal. Educ. Behav.*, vol. 43, no. 1, pp. 25–34, 2016.
- [10] M. J. Rodrigues, O. Postolache, and F. Cercas, "Physiological and behavior monitoring systems for smart healthcare environments: A review," *Sensors (Switzerland)*, vol. 20, no. 8, pp. 1–26, 2020.
- [11] A. Holzinger, C. Röcker, and M. Ziefle, "From smart health to smart hospitals," *Lect. Notes Comput. Sci. (including Subser. Lect. Notes Artif. Intell. Lect. Notes Bioinformatics)*, vol. 8700, pp. 1–20, 2015.
- [12] A. Martinelli, A. Mina, and M. Moggi, "The Enabling Technologies of Industry 4.0: Examining the Seeds of the Fourth Industrial Revolution," *LEM Work. Pap. Ser.*, no. April, pp. 0–42, 2019.
- [13] D. Silvera-Tawil, M. S. Hussain, and J. Li, "Emerging technologies for precision health: An insight into sensing technologies for health and wellbeing," *Smart Heal.*, vol. 15, no. November 2019, p. 100100, 2020.
- [14] J. Wu, Y. Wang, L. Tao, and J. M. Peng, "Stakeholders in the healthcare service ecosystem," in *Procedia CIRP*, 2019, vol. 83, pp. 375–379.
- [15] D. T. HUNTER, "THE ROLE OF THE HOSPITAL IN A SICK SOCIETY.," *Can. Hosp.*, vol. 40, pp. 59–62, 1963.
- [16] M. Amiribesheli, A. Benmansour, and A. Bouchachia, "A review of smart homes in healthcare," *J. Ambient Intell. Humaniz. Comput.*, vol. 6, no. 4, pp. 495–517, 2015.
- [17] A. Lymberis, "Smart wearables for remote health monitoring, from prevention to rehabilitation: Current RandD, future challenges," *Proc. IEEE/EMBS Reg. 8 Int. Conf. Inf. Technol. Appl. Biomed. ITAB*, vol. 2003-Janua, pp. 272–275, 2003.
- [18] R. A. Hemker and L. A. Solomon, "Building a Physician Culture for Healthcare Transformation: A Hospital's Leadership Challenge," *Front. Health Serv. Manage.*, vol. 32, no. 3, pp. 3–14, Mar. 2016.
- [19] W. H. O. R. C. for the E. Mediterranean, "Technical discussions: The role of government in health development," *Training*, no. July, p. 19, 2006.
- [20] D. W. Bates, A. Heitmueller, M. Kakad, and S. Saria, "Why policymakers should care about 'big data' in healthcare," *Heal. Policy Technol.*, vol. 7, no. 2, pp. 211–216, 2018.
- [21] S. M. Greene, L. Tuzzio, and D. Cherkin, "A framework for making patient-centered care front and center.,"

References

- Perm. J.*, vol. 16, no. 3, pp. 49–53, 2012.
- [22] J. Wagner *et al.*, "Implementing risk stratification in primary care: Challenges and strategies," *J. Am. Board Fam. Med.*, vol. 32, no. 4, pp. 585–595, Jul. 2019.
- [23] C. Chen, E. W. Loh, K. N. Kuo, and K. W. Tam, "The Times they Are a-Changin' – Healthcare 4.0 Is Coming!," *J. Med. Syst.*, vol. 44, no. 2, pp. 2–5, 2020.
- [24] A. K. Yetisen, J. L. Martinez-Hurtado, B. Ünal, A. Khademhosseini, and H. Butt, "Wearables in Medicine," *Adv. Mater.*, vol. 30, no. 33, 2018.
- [25] H. Tankovska, "Global connected wearable devices 2016-2022 | Statista," *Statista*, 2020. [Online]. Available: <https://www.statista.com/statistics/487291/global-connected-wearable-devices/>. [Accessed: 21-Dec-2020].
- [26] L. Piwek, D. A. Ellis, S. Andrews, and A. Joinson, "The Rise of Consumer Health Wearables: Promises and Barriers," *PLoS Med.*, vol. 13, no. 2, pp. 1–9, 2016.
- [27] G. H. Williams, "The determinants of health: Structure, context and agency," *Sociology of Health and Illness*, vol. 25, no. SPEC. ISS. Blackwell Publishing Ltd, pp. 131–154, 01-Apr-2003.
- [28] J. F. Ha and N. Longnecker, "Doctor-patient communication: A review," *Ochsner Journal*, vol. 10, no. 1. Ochsner Clinic, L.L.C. and Alton Ochsner Medical Foundation, pp. 38–43, 2010.
- [29] C. Zeagler, "Where to wear it: Functional, technical, and social considerations in on-body location for wearable technology 20 years of designing for wearability," in *Proceedings - International Symposium on Wearable Computers, ISWC, 2017*, vol. Part F1305, pp. 150–157.
- [30] M. Amjadi, K. U. Kyung, I. Park, and M. Sitti, "Stretchable, Skin-Mountable, and Wearable Strain Sensors and Their Potential Applications: A Review," *Advanced Functional Materials*, vol. 26, no. 11. John Wiley & Sons, Ltd, pp. 1678–1698, 01-Mar-2016.
- [31] J. Guo *et al.*, "Wearable and Skin-Mountable Fiber-Optic Strain Sensors Interrogated by a Free-Running, Dual-Comb Fiber Laser," *Adv. Opt. Mater.*, vol. 7, no. 12, p. 1900086, Jun. 2019.
- [32] A. Nag, S. C. Mukhopadhyay, and J. Kosel, "Wearable Flexible Sensors: A Review," *IEEE Sensors Journal*, vol. 17, no. 13, pp. 3949–3960, 01-Jul-2017.
- [33] F. Xu and Y. Zhu, "Highly conductive and stretchable silver nanowire conductors," *Adv. Mater.*, vol. 24, no. 37, pp. 5117–5122, Sep. 2012.
- [34] C. S. Boland *et al.*, "Sensitive electromechanical sensors using viscoelastic graphene-polymer nanocomposites," *Science (80-.)*, vol. 354, no. 6317, pp. 1257–1260, Dec. 2016.
- [35] K. Y. Chun *et al.*, "Highly conductive, printable and stretchable composite films of carbon nanotubes and silver," *Nat. Nanotechnol.*, vol. 5, no. 12, pp. 853–857, 2010.
- [36] Z. F. Zhang, C. Zhang, X. M. Tao, G. F. Wang, and G. D. Peng, "Inscription of polymer optical fiber Bragg grating at 962 nm and its potential in strain sensing," *IEEE Photonics Technol. Lett.*, vol. 22, no. 21, pp. 1562–1564, 2010.
- [37] A. Stefani, W. Yuan, C. Markos, and O. Bang, "Narrow bandwidth 850-nm fiber Bragg gratings in few-mode polymer optical fibers," *IEEE Photonics Technol. Lett.*, vol. 23, no. 10, pp. 660–662, 2011.
- [38] L. Xu, N. Liu, J. Ge, X. Wang, and M. P. Fok, "Stretchable fiber-Bragg-grating-based sensor," *Opt. Lett.*, vol. 43, no. 11, p. 2503, Jun. 2018.
- [39] G. T. Kanellos, G. Papaioannou, D. Tsiokos, C. Mitrogiannis, G. Nianios, and N. Pleros, "Two dimensional polymer-embedded quasi-distributed FBG pressure sensor for biomedical applications," *Opt. Express*, vol. 18, no. 1, p. 179, Jan. 2010.
- [40] R. C. Da Silva Barros Allil and M. M. Werneck, "Optical high-voltage sensor based on fiber bragg grating and PZT piezoelectric ceramics," *IEEE Trans. Instrum. Meas.*, vol. 60, no. 6, pp. 2118–2125, Jun. 2011.
- [41] C. Yan *et al.*, "Highly stretchable piezoresistive graphene-nanocellulose nanopaper for strain sensors," *Adv. Mater.*, vol. 26, no. 13, pp. 2022–2027, Apr. 2014.

References

- [42] A. G. Leal-Junior, C. A. R. Diaz, L. M. Avellar, M. J. Pontes, C. Marques, and A. Frizera, "Polymer optical fiber sensors in healthcare applications: A comprehensive review," *Sensors (Switzerland)*, vol. 19, no. 14. MDPI AG, p. 3156, 18-Jul-2019.
- [43] W. He, D. Goodkind, and P. Kowal, "International Population Reports: An Aging World: 2015," *US Census Bur.*, p. P95, 2016.
- [44] D. Sharma, G. Singh Aujla, and R. Bajaj, "Evolution from ancient medication to human-centered Healthcare 4.0: A review on health care recommender systems," *Int. J. Commun. Syst.*, p. e4058, Sep. 2019.
- [45] V. Mishra, N. Singh, U. Tiwari, and P. Kapur, "Fiber grating sensors in medicine: Current and emerging applications," *Sensors Actuators, A Phys.*, vol. 167, no. 2, pp. 279–290, Jun. 2011.
- [46] E. Al-Fakih, N. A. A. Osman, and F. R. M. Adikan, "The use of fiber bragg grating sensors in biomechanics and rehabilitation applications: The state-of-the-art and ongoing research topics," *Sensors (Switzerland)*, vol. 12, no. 10. Molecular Diversity Preservation International, pp. 12890–12926, 25-Sep-2012.
- [47] Y. J. Rao, "Optical In-Fiber Bragg Grating Sensor Systems for Medical Applications," *J. Biomed. Opt.*, vol. 3, no. 1, p. 38, Jan. 1998.
- [48] R. Correia, S. James, S. W. Lee, S. P. Morgan, and S. Korposh, "Biomedical application of optical fibre sensors," *J. Opt.*, vol. 20, no. 7, p. 73003, 2018.
- [49] M. D. Al-Amri, M. El-Gomati, and M. S. Zubairy, *Optics in Our Time*. Springer International Publishing, 2016.
- [50] A. Othonos, K. Kalli, and G. E. Kohnke, "Fiber Bragg Gratings: Fundamentals and Applications in Telecommunications and Sensing," *Phys. Today*, vol. 53, no. 5, pp. 61–62, 2000.
- [51] A. D. Kersey *et al.*, "Fiber grating sensors," *J. Light. Technol.*, vol. 15, no. 8, pp. 1442–1462, Aug. 1997.
- [52] T. Erdogan, "Fiber grating spectra," *J. Light. Technol.*, vol. 15, no. 8, pp. 1277–1294, Aug. 1997.
- [53] D. Tosi, "Review and analysis of peak tracking techniques for fiber bragg grating sensors," *Sensors (Switzerland)*, vol. 17, no. 10. MDPI AG, p. 2368, 17-Oct-2017.
- [54] D. Tosi, "Review of chirped fiber bragg grating (CFBG) fiber-optic sensors and their applications," *Sensors (Switzerland)*, vol. 18, no. 7. MDPI AG, p. 2147, 04-Jul-2018.
- [55] G. Palumbo, D. Tosi, A. Iadicicco, and S. Campopiano, "Analysis and Design of Chirped Fiber Bragg Grating for Temperature Sensing for Possible Biomedical Applications," *IEEE Photonics J.*, vol. 10, no. 3, Jun. 2018.
- [56] S. Korganbayev *et al.*, "Detection of thermal gradients through fiber-optic Chirped Fiber Bragg Grating (CFBG): Medical thermal ablation scenario," *Opt. Fiber Technol.*, vol. 41, pp. 48–55, 2018.
- [57] P. Bettini, E. Guerreschi, and G. Sala, "Development and experimental validation of a numerical tool for structural health and usage monitoring systems based on chirped grating sensors," *Sensors*, vol. 15, no. 1, pp. 1321–1341, 2015.
- [58] J. Albert, L. Y. Shao, and C. Caucheteur, "Tilted fiber Bragg grating sensors," *Laser and Photonics Reviews*, vol. 7, no. 1. John Wiley & Sons, Ltd, pp. 83–108, 01-Jan-2013.
- [59] T. Guo, F. Liu, B.-O. Guan, and J. Albert, "Tilted fiber grating mechanical and biochemical sensors," *Opt. Laser Technol.*, vol. 78, pp. 19–33, 2016.
- [60] T. Guo, Á. González-Vila, M. Loyez, and C. Caucheteur, "Plasmonic optical fiber-grating immunosensing: a review," *Sensors*, vol. 17, no. 12, p. 2732, 2017.
- [61] A. Bekmurzayeva *et al.*, "Etched fiber Bragg grating biosensor functionalized with aptamers for detection of thrombin," *Sensors*, vol. 18, no. 12, p. 4298, 2018.
- [62] A. Iadicicco, A. Cusano, A. Cutolo, R. Bernini, and M. Giordano, "Thinned fiber Bragg gratings as high sensitivity refractive index sensor," *IEEE Photonics Technol. Lett.*, vol. 16, no. 4, pp. 1149–1151, 2004.
- [63] D. Tosi, E. Schena, C. Molardi, and S. Korganbayev, "Fiber optic sensors for sub-centimeter spatially resolved measurements: Review and biomedical applications," *Opt. Fiber Technol.*, vol. 43, pp. 6–19, 2018.

References

- [64] P. Saccomandi *et al.*, "Feedforward neural network for force coding of an MRI-compatible tactile sensor array based on fiber bragg grating," *J. Sensors*, vol. 2015, 2015.
- [65] L. Massari *et al.*, "A Machine-Learning-Based Approach to Solve Both Contact Location and Force in Soft Material Tactile Sensors," *Soft Robot*, p. soro.2018.0172, Dec. 2019.
- [66] T. W. Lu and C. F. Chang, "Biomechanics of human movement and its clinical applications," *Kaohsiung Journal of Medical Sciences*, vol. 28, no. 2 SUPPL. John Wiley & Sons, Ltd, pp. S13–S25, Feb-2012.
- [67] P. Roriz, A. Ramos, M. B. Marques, J. A. Simões, and O. Frazão, "A fiber optic buckle transducer for measurement of in vitro tendon strain," in *24th International Conference on Optical Fibre Sensors*, 2015, vol. 9634, p. 96342Q.
- [68] L. Ren, G. Song, M. Conditt, P. C. Noble, and H. Li, "Fiber Bragg grating displacement sensor for movement measurement of tendons and ligaments," *Appl. Opt.*, vol. 46, no. 28, pp. 6867–6871, Oct. 2007.
- [69] G. P. Behrmann, J. Hidler, and M. S. Mirotznik, "Fiber optic micro sensor for the measurement of tendon forces," *Biomed. Eng. Online*, vol. 11, no. 1, pp. 1–16, Oct. 2012.
- [70] M. Vilimek, "Using a fiber Bragg grating sensor for tendon force measurements," *J. Biomech.*, no. 41, p. S511, 2008.
- [71] M. J. Paulsen *et al.*, "Development and Ex Vivo Validation of Novel Force-Sensing Neochordae for Measuring Chordae Tendineae Tension in the Mitral Valve Apparatus Using Optical Fibers with Embedded Bragg Gratings," *J. Biomech. Eng.*, vol. 142, no. 1, Jan. 2020.
- [72] S. Iwanuma, R. Akagi, S. Hashizume, H. Kanehisa, T. Yanai, and Y. Kawakami, "Triceps surae muscle-tendon unit length changes as a function of ankle joint angles and contraction levels: The effect of foot arch deformation," *J. Biomech.*, vol. 44, no. 14, pp. 2579–2583, Sep. 2011.
- [73] S. Iwanuma *et al.*, "Longitudinal and transverse deformation of human Achilles tendon induced by isometric plantar flexion at different intensities," *J. Appl. Physiol.*, vol. 110, no. 6, pp. 1615–1621, 2011.
- [74] R. Akagi, S. Iwanuma, S. Hashizume, H. Kanehisa, T. Yanai, and Y. Kawakami, "In vivo measurements of moment arm lengths of three elbow flexors at rest and during isometric contractions," *J. Appl. Biomech.*, vol. 28, no. 1, pp. 63–69, Feb. 2012.
- [75] T. Fresvig, P. Ludvigsen, H. Steen, and O. Reikerås, "Fibre optic Bragg grating sensors: An alternative method to strain gauges for measuring deformation in bone," *Med. Eng. Phys.*, vol. 30, no. 1, pp. 104–108, Jan. 2008.
- [76] P. M. Talaia *et al.*, "Plated and intact femur strains in fracture fixation using fiber Bragg gratings and strain gauges," *Exp. Mech.*, vol. 47, no. 3, pp. 355–363, Jun. 2007.
- [77] A. Najafzadeh *et al.*, "Healing Assessment of Fractured Femur by Strain Measurement using Fibre Bragg Grating Sensors," in *2019 International Conference on Sensing and Instrumentation in IoT Era, ISSI 2019*, 2019.
- [78] V. Mishra *et al.*, "Fiber Bragg grating sensor for monitoring bone decalcification," *Orthop. Traumatol. Surg. Res.*, vol. 96, no. 6, pp. 646–651, Oct. 2010.
- [79] S. Umesh, S. Padma, S. Asokan, and T. Srinivas, "Fiber Bragg Grating based bite force measurement," *J. Biomech.*, vol. 49, no. 13, pp. 2877–2881, Sep. 2016.
- [80] A. Kalinowski *et al.*, "Optical Fiber Bragg Grating Strain Sensor for Bone Stress Analysis in Bovine During Masticatory Movements," *IEEE Sens. J.*, vol. 17, no. 8, pp. 2385–2392, Feb. 2017.
- [81] G. Marchi *et al.*, "Microindentation sensor system based on an optical fiber bragg grating for the mechanical characterization of articular cartilage by stress-relaxation," *Sensors Actuators, B Chem.*, vol. 252, pp. 440–449, Nov. 2017.
- [82] A. Aszodi *et al.*, "Cartilage microindentation using cylindrical and spherical optical fiber indenters with integrated Bragg gratings as force sensors," in *Optical Elastography and Tissue Biomechanics V*, 2018, vol. 10496, p. 34.
- [83] A. Javadzadeh Kalahrodi, G. Marchi, J. Möller, S. Nolte, and J. Roths, "2D stiffness mapping for localizing

References

- osteoarthritic degenerated cartilage by using a fast indentation system based on fiber Bragg gratings," in *Seventh European Workshop on Optical Fibre Sensors*, 2019, vol. 11199, p. 16.
- [84] G. Marchi *et al.*, "Fiberoptic microindentation technique for early osteoarthritis diagnosis: an in vitro study on human cartilage," *Biomed. Microdevices*, vol. 21, no. 1, pp. 1–9, Mar. 2019.
- [85] S. Umesh, S. Padma, T. Srinivas, and S. Asokan, "Fiber bragg grating goniometer for joint angle measurement," *IEEE Sens. J.*, vol. 18, no. 1, pp. 216–222, Jan. 2018.
- [86] S. Pant, S. Umesh, and S. Asokan, "Knee Angle Measurement Device Using Fiber Bragg Grating Sensor," *IEEE Sens. J.*, vol. 18, no. 24, pp. 10034–10040, Dec. 2018.
- [87] S. Umesh, S. Padma, S. Asokan, and T. Srinivas, "Fiber Bragg Grating based bite force measurement," *J. Biomech.*, vol. 49, no. 13, pp. 2877–2881, Sep. 2016.
- [88] R. P. Rocha, A. F. Silva, J. P. Carmo, and J. H. Correia, "FBG in PVC foils for monitoring the knee joint movement during the rehabilitation process," in *Proceedings of the Annual International Conference of the IEEE Engineering in Medicine and Biology Society, EMBS*, 2011, pp. 458–461.
- [89] Z. A. Abro, Y. F. Zhang, C. Y. Hong, R. A. Lakho, and N. L. Chen, "Development of a smart garment for monitoring body postures based on FBG and flex sensing technologies," *Sensors Actuators, A Phys.*, vol. 272, pp. 153–160, Apr. 2018.
- [90] Z. A. Abro, C. Hong, N. Chen, Y. Zhang, R. A. Lakho, and S. Yasin, "A fiber Bragg grating-based smart wearable belt for monitoring knee joint postures," *Text. Res. J.*, vol. 90, no. 3–4, pp. 386–394, Feb. 2020.
- [91] D. Lo Presti *et al.*, "Single-plane neck movements and respiratory frequency monitoring: A smart system for computer workers," in *2019 IEEE International Workshop on Metrology for Industry 4.0 and IoT, MetroInd 4.0 and IoT 2019 - Proceedings*, 2019, pp. 167–170.
- [92] D. Lo Presti *et al.*, "A multi-parametric wearable system to monitor neck movements and respiratory frequency of computer workers," *Sensors (Switzerland)*, vol. 20, no. 2, p. 536, Jan. 2020.
- [93] H. Cheng-Yu, Z. Ahmed Abro, Z. Yi-Fan, and R. Ahmed Lakho, "An FBG-based smart wearable ring fabricated using FDM for monitoring body joint motion," *J. Ind. Text.*, p. 152808371987020, Aug. 2019.
- [94] J. S. Kim *et al.*, "Wearable hand module and real-time tracking algorithms for measuring finger joint angles of different hand sizes with high accuracy using FBG strain sensor," *Sensors (Switzerland)*, vol. 20, no. 7, p. 1921, Mar. 2020.
- [95] M. F. Domingues *et al.*, "Energy-Aware Wearable E-Health Architecture Using Optical FBG Sensors for Knee Kinematic Monitoring," in *2018 IEEE Global Communications Conference, GLOBECOM 2018 - Proceedings*, 2018.
- [96] M. F. Domingues *et al.*, "Wearable ehealth system for physical rehabilitation: Ankle plantar-dorsi-flexion monitoring," in *2019 IEEE Global Communications Conference, GLOBECOM 2019 - Proceedings*, 2019.
- [97] P. W. Kong, C. C. Chan, M. L. Heng, Y. Liu, Y. Leow, and D. T. P. Fong, "Fiber Bragg Grating Sensors for Clinical Measurement of the First Metatarsophalangeal Joint Quasi-Stiffness," *IEEE Sens. J.*, vol. 20, no. 3, pp. 1322–1328, Feb. 2020.
- [98] A. F. Da Silva, A. F. Gonçalves, P. M. Mendes, and J. H. Correia, "FBG sensing glove for monitoring hand posture," *IEEE Sens. J.*, vol. 11, no. 10, pp. 2442–2448, 2011.
- [99] M. Zaltieri *et al.*, "Feasibility Assessment of an FBG-based Wearable System for Monitoring Back Dorsal Flexion-Extension in Video Terminal Workers," in *2020 IEEE International Instrumentation and Measurement Technology Conference (I2MTC)*, 2020, pp. 1–5.
- [100] C. R. Dennison, P. M. Wild, D. R. Wilson, and M. K. Gilbert, "An in-fiber Bragg grating sensor for contact force and stress measurements in articular joints," *Meas. Sci. Technol.*, vol. 21, no. 11, p. 115803, Oct. 2010.
- [101] C. R. Dennison *et al.*, "Ex vivo measurement of lumbar intervertebral disc pressure using fibre-Bragg gratings," *J. Biomech.*, vol. 41, no. 1, pp. 221–225, Jan. 2008.
- [102] S. Ambastha, S. Umesh, S. Dabir, and S. Asokan, "Comparison of Force Required for Lumbar Puncture with

References

- Different Gauges of Spinal Needle Using Fiber Bragg Grating Force Device," *IEEE Sens. J.*, vol. 18, no. 19, pp. 8028–8033, Oct. 2018.
- [103] S. Ambastha, S. Umesh, S. Dabir, and S. Asokan, "Spinal needle force monitoring during lumbar puncture using fiber Bragg grating force device," *J. Biomed. Opt.*, vol. 21, no. 11, p. 117002, Nov. 2016.
- [104] L. Mohanty and S. C. Tjin, "Pressure mapping at orthopaedic joint interfaces with fiber Bragg gratings," *Appl. Phys. Lett.*, vol. 88, no. 8, p. 083901, Feb. 2006.
- [105] L. Mohanty, S. C. Tjin, D. T. T. Lie, S. E. C. Panganiban, and P. K. H. Chow, "Fiber grating sensor for pressure mapping during total knee arthroplasty," *Sensors Actuators, A Phys.*, vol. 135, no. 2, pp. 323–328, Apr. 2007.
- [106] L. Armitage, G. Rajan, L. Kark, A. Simmons, and B. G. Prusty, "Simultaneous measurement of normal and shear stress using fiber bragg grating sensors in prosthetic applications," *IEEE Sens. J.*, vol. 19, no. 17, pp. 7383–7390, Sep. 2019.
- [107] A. Completo, F. Fonseca, C. Relvas, A. Ramos, and J. A. Simões, "Improved stability with intramedullary stem after anterior femoral notching in total knee arthroplasty," *Knee Surgery, Sport. Traumatol. Arthrosc.*, vol. 20, no. 3, pp. 487–494, Mar. 2012.
- [108] M. P. Whelan, R. P. Kenny, C. Cavalli, A. B. Lennon, and P. J. Prendergast, "Application of optical fibre Bragg grating sensors to the study of PMMA curing," 2000, p. 252.
- [109] C. Frias, O. Frazão, S. Tavares, A. Vieira, A. T. Marques, and J. Simões, "Mechanical characterization of bone cement using fiber Bragg grating sensors," *Mater. Des.*, vol. 30, no. 5, pp. 1841–1844, May 2009.
- [110] A. Ramos, M. W. Schiller, I. Abe, P. A. Lopes, and J. A. Simões, "Experimental Measurement and Numerical Validation of Bone Cement Mantle Strains of an In Vitro Hip Replacement Using Optical FBG Sensors," *Exp. Mech.*, vol. 52, no. 9, pp. 1267–1274, Jan. 2012.
- [111] A. Bimis and D. Karalekas, "Experimental evaluation of hardening strains in a bioceramic material using an embedded optical sensor," *Meccanica*, vol. 50, no. 2, pp. 541–547, Dec. 2015.
- [112] A. Bimis, D. Karalekas, N. Bouropoulos, D. Mouzakis, and S. Zaoutsos, "Monitoring of hardening and hygroscopic induced strains in a calcium phosphate bone cement using FBG sensor," *J. Mech. Behav. Biomed. Mater.*, vol. 60, pp. 195–202, Jul. 2016.
- [113] J. R. Galvão, C. R. Zamarreño, C. Martelli, J. C. Cardozo Da Silva, F. J. Arregui, and I. R. Matías, "Smart Carbon Fiber Transtibial Prosthesis Based on Embedded Fiber Bragg Gratings," *IEEE Sens. J.*, vol. 18, no. 4, pp. 1520–1527, Feb. 2018.
- [114] J. R. Galvao, C. R. Zamarreno, C. Martelli, J. C. Cardozo Da Silva, F. J. Arregui, and I. R. Matias, "Strain Mapping in Carbon-Fiber Prosthesis Using Optical Fiber Sensors," *IEEE Sens. J.*, vol. 17, no. 1, pp. 3–4, Jan. 2017.
- [115] J. Feng and Q. Jiang, "Slip and roughness detection of robotic fingertip based on FBG," *Sensors Actuators, A Phys.*, vol. 287, pp. 143–149, Mar. 2019.
- [116] L. Massari, C. M. Oddo, E. Sinibaldi, R. Detry, J. Bowkett, and K. C. Carpenter, "Tactile sensing and control of robotic manipulator integrating fiber Bragg grating strain-sensor," *Front. Neurobot.*, vol. 13, p. 8, Apr. 2019.
- [117] C. M. Oddo *et al.*, "Intraneural stimulation elicits discrimination of textural features by artificial fingertip in intact and amputee humans," *Elife*, vol. 5, no. MARCH2016, 2016.
- [118] A. Mazzoni *et al.*, "Morphological Neural Computation Restores Discrimination of Naturalistic Textures in Trans-radial Amputees," *Sci. Rep.*, 2020.
- [119] G. T. Kanellos, G. Papaioannou, D. Tsiokos, C. Mitrogiannis, G. Nianios, and N. Pleros, "Two dimensional polymer-embedded quasi-distributed FBG pressure sensor for biomedical applications," *Opt. Express*, vol. 18, no. 1, p. 179, Jan. 2010.
- [120] N. Pleros, G. T. Kanellos, and G. Papaioannou, "Optical fiber sensors in orthopedic biomechanics and rehabilitation," in *Final Program and Abstract Book - 9th International Conference on Information Technology and Applications in Biomedicine, ITAB 2009*, 2009.

References

- [121] G. T. Kanellos, D. Tsiokos, N. Pleros, G. Papaioannou, P. Childs, and S. Pissadakis, "Enhanced durability FBG-based sensor pads for biomedical applications as human-machine interface surfaces," in *2011 International Workshop on Biophotonics, BIOPHOTONICS 2011*, 2011.
- [122] E. A. Al-Fakih, N. A. Abu Osman, F. R. Mahamd Adikan, A. Eshraghi, and P. Jahanshahi, "Development and Validation of Fiber Bragg Grating Sensing Pad for Interface Pressure Measurements Within Prosthetic Sockets," *IEEE Sens. J.*, vol. 16, no. 4, pp. 965–974, Feb. 2016.
- [123] E. A. Al-Fakih, N. A. A. Osman, A. Eshraghi, and F. R. M. Adikan, "The capability of fiber Bragg grating sensors to measure amputees' trans-tibial stump/socket interface pressures," *Sensors (Switzerland)*, vol. 13, no. 8, pp. 10348–10357, Aug. 2013.
- [124] C. Tavares, M. F. Domingues, T. Paixão, N. Alberto, H. Silva, and P. Antunes, "Wheelchair pressure ulcer prevention using FBG based sensing devices," *Sensors (Switzerland)*, vol. 20, no. 1, p. 212, Dec. 2020.
- [125] K. Chethana, A. S. Guru Prasad, S. N. Omkar, B. Vadiraj, and S. Asokan, "Design and development of optical sensor based ground reaction force measurement platform for gait and geriatric studies," *Int. J. Mech. Aerosp. Ind. Mechatron. Manuf. Eng.*, vol. 10, no. 1, pp. 60–64, 2016.
- [126] Y. F. Zhang, C. Y. Hong, R. Ahmed, and Z. Ahmed, "A fiber Bragg grating based sensing platform fabricated by fused deposition modeling process for plantar pressure measurement," *Meas. J. Int. Meas. Confed.*, vol. 112, pp. 74–79, Dec. 2017.
- [127] J. Z. Hao *et al.*, "Design of a foot-pressure monitoring transducer for diabetic patients based on FBG sensors," in *Conference Proceedings - Lasers and Electro-Optics Society Annual Meeting-LEOS*, 2003, vol. 1, pp. 23–24.
- [128] R. Suresh, S. Bhalla, J. Hao, and C. Singh, "Development of a high resolution plantar pressure monitoring pad based on fiber Bragg grating (FBG) sensors," *Technol. Heal. Care*, vol. 23, no. 6, pp. 785–794, Oct. 2015.
- [129] T. C. Liang, J. J. Lin, and L. Y. Guo, "Plantar pressure detection with fiber bragg gratings sensing system," *Sensors (Switzerland)*, vol. 16, no. 10, p. 1766, Oct. 2016.
- [130] D. Vilarinho *et al.*, "POFBG-embedded cork insole for plantar pressure monitoring," *Sensors (Switzerland)*, vol. 17, no. 12, p. 2924, Dec. 2017.
- [131] C. Tavares *et al.*, "Gait shear and plantar pressure monitoring: A non-invasive OFS based solution for e-health architectures," *Sensors (Switzerland)*, vol. 18, no. 5, p. 1334, Apr. 2018.
- [132] Z. Hao, K. Cook, J. Canning, H. T. Chen, and C. Martelli, "3-D printed smart orthotic insoles: Monitoring a person's gait step by step," *IEEE Sensors Lett.*, vol. 4, no. 1, Jan. 2020.
- [133] M. F. Domingues *et al.*, "Insole optical fiber Bragg grating sensors network for dynamic vertical force monitoring," *J. Biomed. Opt.*, vol. 22, no. 9, p. 091507, Feb. 2017.
- [134] M. F. Domingues *et al.*, "Insole Optical Fiber Sensor Architecture for Remote Gait Analysis - An e-Health Solution," *IEEE Internet Things J.*, vol. 6, no. 1, pp. 207–214, Feb. 2019.
- [135] J. C. C. Silva, L. Carvalho, R. N. Nogueira, J. A. Simoes, J. L. Pinto, and H. J. Kalinowski, "FBG applied in dynamic analysis of an implanted cadaveric mandible," in *Second European Workshop on Optical Fibre Sensors*, 2004, vol. 5502, p. 226.
- [136] L. Carvalho, J. C. C. Silva, R. N. Nogueira, J. L. Pinto, H. J. Kalinowski, and J. A. Simões, "Application of Bragg grating sensors in dental biomechanics," *J. Strain Anal. Eng. Des.*, vol. 41, no. 6, pp. 411–416, Aug. 2006.
- [137] J. C. C. Silva *et al.*, "Fibre Bragg grating sensing and finite element analysis of the biomechanics of the mandible," in *17th International Conference on Optical Fibre Sensors*, 2005, vol. 5855, p. 102.
- [138] M. W. Schiller *et al.*, "On the use of FBG sensors to assess the performance of a dental implant system," in *Optics InfoBase Conference Papers*, 2006, p. ThE77.
- [139] H. J. Kalinowski, J. a Simões, J. L. Pinto, L. M. R. Carvalho, and R. N. Nogueira, "Probing Dental Biomechanics with Fibre Bragg Grating Sensors LOAD (N)," *Methods*, 2004.
- [140] M. S. Milczewski *et al.*, "FBG application in the determination of setting expansion of dental materials," in *17th International Conference on Optical Fibre Sensors*, 2005, vol. 5855, p. 387.

References

- [141] H. Ottevaere, M. Tabak, A. Fernandez Fernandez, F. Berghmans, and H. Thienpont, "Optical fiber sensors and their application in monitoring stress build-up in dental resin cements," in *Optical Fibers: Applications*, 2005, vol. 5952, p. 59520P.
- [142] S. C. Tjin, Y. K. Tan, M. Yow, Y. Z. Lam, and J. Hao, "Recording compliance of dental splint use in obstructive sleep apnoea patients by force and temperature modelling," *Med. Biol. Eng. Comput.*, vol. 39, no. 2, pp. 182–184, 2001.
- [143] M. S. Milczeswki, J. C. C. Silva, I. Abe, J. A. Simões, A. S. Paterno, and H. J. Kalinowski, "Measuring orthodontic forces with HiBi FBG sensors," in *Optics InfoBase Conference Papers*, 2006, p. TuE65.
- [144] M. S. Milczewski, H. J. Kalinowski, J. C. C. da Silva, I. Abe, J. A. Simões, and A. Saga, "Stress monitoring in a maxilla model and dentition," in *21st International Conference on Optical Fiber Sensors*, 2011, vol. 7753, p. 77534V.
- [145] L. Carvalho, P. Roriz, O. Frazão, and M. B. Marques, "Evaluation of the performance of orthodontic devices using FBG sensors," in *Journal of Physics: Conference Series*, 2015, vol. 605, no. 1, p. 12017.
- [146] A. A. G. Abushagur, N. Arsad, M. I. Reaz, and A. A. A. Bakar, "Advances in bio-tactile sensors for minimally invasive surgery using the fibre bragg grating force sensor technique: A survey," *Sensors (Switzerland)*, vol. 14, no. 4, pp. 6633–6665, Apr. 2014.
- [147] D. Tosi, E. Schena, C. Molardi, and S. Korganbayev, "Fiber optic sensors for sub-centimeter spatially resolved measurements: Review and biomedical applications," *Opt. Fiber Technol.*, vol. 43, pp. 6–19, Jul. 2018.
- [148] C. Shi *et al.*, "Shape sensing techniques for continuum robots in minimally invasive surgery: A survey," *IEEE Trans. Biomed. Eng.*, vol. 64, no. 8, pp. 1665–1678, Aug. 2017.
- [149] J. Konstantinova, A. Jiang, K. Althoefer, P. Dasgupta, and T. Nanayakkara, "Implementation of tactile sensing for palpation in robot-assisted minimally invasive surgery: A review," *IEEE Sens. J.*, vol. 14, no. 8, pp. 2490–2501, 2014.
- [150] Z. Wang, S. Wang, and S. Zuo, "A hand-held device with 3-DOF haptic feedback mechanism for microsurgery," *Int. J. Med. Robot. Comput. Assist. Surg.*, vol. 15, no. 5, Oct. 2019.
- [151] Z. Sun, M. Balicki, J. Kang, J. Handa, T. Russell, and I. Iordachita, "Development and preliminary data of novel integrated optical micro-force sensing tools for retinal microsurgery," in *Proceedings - IEEE International Conference on Robotics and Automation*, 2009, pp. 1897–1902.
- [152] I. Iordachita *et al.*, "A sub-millimetric, 0.25 mN resolution fully integrated fiber-optic force-sensing tool for retinal microsurgery," *Int. J. Comput. Assist. Radiol. Surg.*, vol. 4, no. 4, pp. 383–390, Apr. 2009.
- [153] X. He, J. Handa, P. Gehlbach, R. Taylor, and I. Iordachita, "A submillimetric 3-DOF force sensing instrument with integrated fiber bragg grating for retinal microsurgery," *IEEE Trans. Biomed. Eng.*, vol. 61, no. 2, pp. 522–534, Feb. 2014.
- [154] S. Sunshine *et al.*, "A force-sensing microsurgical instrument that detects forces below human tactile sensation," *Retina*, vol. 33, no. 1, pp. 200–206, Jan. 2013.
- [155] B. Gonenc *et al.*, "Preliminary evaluation of a micro-force sensing handheld robot for vitreoretinal surgery," in *IEEE International Conference on Intelligent Robots and Systems*, 2012, pp. 4125–4130.
- [156] A. Gijbels, E. B. Vander Poorten, P. Stalmans, and D. Reynaerts, "Development and experimental validation of a force sensing needle for robotically assisted retinal vein cannulations," in *Proceedings - IEEE International Conference on Robotics and Automation*, 2015, vol. 2015-June, no. June, pp. 2270–2276.
- [157] A. Gijbels, K. Willekens, L. Esteveny, P. Stalmans, D. Reynaerts, and E. B. Vander Poorten, "Towards a clinically applicable robotic assistance system for retinal vein cannulation," in *Proceedings of the IEEE RAS and EMBS International Conference on Biomedical Robotics and Biomechanics*, 2016, vol. 2016-July, pp. 284–291.
- [158] B. Gonenc, R. H. Taylor, I. Iordachita, P. Gehlbach, and J. Handa, "Force-sensing microneedle for assisted retinal vein cannulation," in *Proceedings of IEEE Sensors*, 2014, vol. 2014-Decem, no. December, pp. 698–701.

References

- [159] B. Gonenc, N. Tran, C. N. Riviere, P. Gehlbach, R. H. Taylor, and I. Iordachita, "Force-based puncture detection and active position holding for assisted retinal vein cannulation," in *IEEE International Conference on Multisensor Fusion and Integration for Intelligent Systems*, 2015, vol. 2015-Octob, pp. 322–327.
- [160] B. Gonenc, A. Chamani, J. Handa, P. Gehlbach, R. H. Taylor, and I. Iordachita, "3-DOF Force-Sensing Motorized Micro-Forceps for Robot-Assisted Vitreoretinal Surgery," *IEEE Sens. J.*, vol. 17, no. 11, pp. 3526–3541, Jun. 2017.
- [161] B. Gonenc, N. Patel, and I. Iordachita, "Evaluation of a Force-Sensing Handheld Robot for Assisted Retinal Vein Cannulation*," in *Proceedings of the Annual International Conference of the IEEE Engineering in Medicine and Biology Society, EMBS*, 2018, vol. 2018-July, pp. 1–5.
- [162] X. He *et al.*, "Force sensing micro-forceps with integrated fiber Bragg grating for vitreoretinal surgery," in *Optical Fibers and Sensors for Medical Diagnostics and Treatment Applications XII*, 2012, vol. 8218, p. 82180W.
- [163] I. Kuru *et al.*, "Force sensing micro-forceps for robot assisted retinal surgery," in *Proceedings of the Annual International Conference of the IEEE Engineering in Medicine and Biology Society, EMBS*, 2012, pp. 1401–1404.
- [164] X. He, M. Balicki, P. Gehlbach, J. Handa, R. Taylor, and I. Iordachita, "A multi-function force sensing instrument for variable admittance robot control in retinal microsurgery," in *Proceedings - IEEE International Conference on Robotics and Automation*, 2014, pp. 1411–1418.
- [165] A. Ebrahimi, N. Patel, C. He, P. Gehlbach, M. Kobilarov, and I. Iordachita, "Adaptive control of sclera force and insertion depth for safe robot-assisted retinal surgery," in *Proceedings - IEEE International Conference on Robotics and Automation*, 2019, vol. 2019-May, pp. 9073–9079.
- [166] C. He, N. Patel, A. Ebrahimi, M. Kobilarov, and I. Iordachita, "Preliminary study of an RNN-based active interventional robotic system (AIRS) in retinal microsurgery," *Int. J. Comput. Assist. Radiol. Surg.*, vol. 14, no. 6, pp. 945–954, Mar. 2019.
- [167] C. He *et al.*, "Toward Safe Retinal Microsurgery: Development and Evaluation of an RNN-Based Active Interventional Control Framework," *IEEE Trans. Biomed. Eng.*, vol. 67, no. 4, pp. 966–977, Apr. 2020.
- [168] C. Kim and C. H. Lee, "Development of a 6-DoF FBG force-moment sensor for a haptic interface with minimally invasive robotic surgery," *J. Mech. Sci. Technol.*, vol. 30, no. 8, pp. 3705–3712, Aug. 2016.
- [169] C. Lv, S. Wang, and C. Shi, "A High-Precision and Miniature Fiber Bragg Grating-Based Force Sensor for Tissue Palpation During Minimally Invasive Surgery," *Ann. Biomed. Eng.*, vol. 48, no. 2, pp. 669–681, Feb. 2020.
- [170] R. Xue, B. Ren, J. Huang, Z. Yan, and Z. Du, "Design and evaluation of FBG-based tension sensor in laparoscope surgical robots," *Sensors (Switzerland)*, vol. 18, no. 7, p. 2067, Jun. 2018.
- [171] P. S. Zarrin, A. Escoto, R. Xu, R. V. Patel, M. D. Naish, and A. L. Trejos, "Development of a 2-DOF Sensorized Surgical Grasper for Grasping and Axial Force Measurements," *IEEE Sens. J.*, vol. 18, no. 7, pp. 2816–2826, Apr. 2018.
- [172] P. S. Zarrin, A. Escoto, R. Xu, R. V. Patel, M. D. Naish, and A. L. Trejos, "Development of an optical fiber-based sensor for grasping and axial force sensing," in *Proceedings - IEEE International Conference on Robotics and Automation*, 2017, pp. 939–944.
- [173] K. S. Shahzada, A. Yurkewich, R. Xu, and R. V. Patel, "Sensorization of a surgical robotic instrument for force sensing," in *Optical Fibers and Sensors for Medical Diagnostics and Treatment Applications XVI*, 2016, vol. 9702, p. 97020U.
- [174] Y. Guo, J. Kong, H. Liu, H. Xiong, G. Li, and L. Qin, "A three-axis force fingertip sensor based on fiber Bragg grating," *Sensors Actuators, A Phys.*, vol. 249, pp. 141–148, Oct. 2016.
- [175] C. Shi, M. Li, C. Lv, J. Li, and S. Wang, "A High-Sensitivity Fiber Bragg Grating-Based Distal Force Sensor for Laparoscopic Surgery," *IEEE Sens. J.*, vol. 20, no. 5, pp. 2467–2475, Mar. 2020.
- [176] C. Huang, R. X. Huang, and Z. J. Qiu, "Natural orifice transluminal endoscopic surgery: New Minimally invasive surgery come of age," *World Journal of Gastroenterology*, vol. 17, no. 39, Baishideng Publishing Group Inc,

References

- pp. 4382–4388, 21-Oct-2011.
- [177] W. Lai *et al.*, “An Integrated Sensor-Model Approach for Haptic Feedback of Flexible Endoscopic Robots,” *Ann. Biomed. Eng.*, vol. 48, no. 1, pp. 342–356, Jan. 2020.
- [178] W. Lai *et al.*, “Force Sensing With 1 mm Fiber Bragg Gratings for Flexible Endoscopic Surgical Robots,” *IEEE/ASME Trans. Mechatronics*, vol. 25, no. 1, pp. 371–382, Feb. 2020.
- [179] W. Lai, L. Cao, Z. Xu, P. T. Phan, P. Shum, and S. J. Phee, “Distal end force sensing with optical fiber bragg gratings for tendon-sheath mechanisms in flexible endoscopic robots,” in *Proceedings - IEEE International Conference on Robotics and Automation*, 2018, pp. 5349–5355.
- [180] J. W. Arkwright *et al.*, “In-vivo demonstration of a high resolution optical fiber manometry catheter for diagnosis of gastrointestinal motility disorders,” *Opt. Express*, vol. 17, no. 6, p. 4500, Mar. 2009.
- [181] F. Bianchi *et al.*, “Endoscopic tactile instrument for remote tissue palpation in colonoscopic procedures,” in *2017 IEEE International Conference on Cyborg and Bionic Systems, CBS 2017*, 2017, vol. 2018-Janua, pp. 248–252.
- [182] J. H. Bae, C. J. Ploch, M. A. Lin, B. L. Daniel, and M. R. Cutkosky, “Display of needle tip contact forces for steering guidance,” in *IEEE Haptics Symposium, HAPTICS*, 2016, vol. 2016-April, pp. 332–337.
- [183] B. Carotenuto *et al.*, “Optical guidance systems for epidural space identification,” *IEEE J. Sel. Top. Quantum Electron.*, vol. 23, no. 2, Mar. 2017.
- [184] S. Elayaperumal, J. H. Bae, B. L. Daniel, and M. R. Cutkosky, “Detection of membrane puncture with haptic feedback using a tip-force sensing needle,” in *IEEE International Conference on Intelligent Robots and Systems*, 2014, pp. 3975–3981.
- [185] M. Ahmed, C. L. Brace, F. T. Lee, and S. N. Goldberg, “Principles of and advances in percutaneous ablation,” *Radiology*, vol. 258, no. 2. Radiological Society of North America, Inc., pp. 351–369, 01-Feb-2011.
- [186] E. Schena, D. Tosi, P. Saccomandi, E. Lewis, and T. Kim, “Fiber optic sensors for temperature monitoring during thermal treatments: An overview,” *Sensors (Switzerland)*, vol. 16, no. 7. MDPI AG, p. 1144, 22-Jul-2016.
- [187] P. Saccomandi, E. Schena, and S. Silvestri, “Techniques for temperature monitoring during laser-induced thermotherapy: An overview,” *International Journal of Hyperthermia*, vol. 29, no. 7. Informa Healthcare, pp. 609–619, 13-Nov-2013.
- [188] Y. J. Rao, D. J. Webb, D. A. Jackson, L. Zhang, and I. Bennion, “In-fiber bragg-grating temperature sensor system for medical applications,” *J. Light. Technol.*, vol. 15, no. 5, pp. 779–784, May 1997.
- [189] E. Samset, T. Mala, B. Edwin, I. Gladhaug, O. Soreide, and E. Fosse, “Validation of estimated 3D temperature maps during hepatic cryo surgery,” *Magn. Reson. Imaging*, vol. 19, no. 5, pp. 715–721, Jun. 2001.
- [190] N. T. Pham, S. L. Lee, S. Park, Y. W. Lee, and H. W. Kang, “Real-time temperature monitoring with fiber Bragg grating sensor during diffuser-assisted laser-induced interstitial thermotherapy,” *J. Biomed. Opt.*, vol. 22, no. 4, p. 045008, Apr. 2017.
- [191] D. Polito *et al.*, “A needlelike probe for temperature monitoring during laser ablation based on fiber Bragg grating: Manufacturing and characterization,” *J. Med. Devices, Trans. ASME*, vol. 9, no. 4, Dec. 2015.
- [192] F. M. Di Matteo *et al.*, “Feasibility of EUS-guided Nd:YAG laser ablation of unresectable pancreatic adenocarcinoma,” *Gastrointest. Endosc.*, vol. 88, no. 1, pp. 168-174.e1, Jul. 2018.
- [193] C. Cavaioia *et al.*, “Error of a temperature probe for cancer ablation monitoring caused by respiratory movements: Ex vivo and in vivo analysis,” *IEEE Sens. J.*, vol. 16, no. 15, pp. 5934–5941, Aug. 2016.
- [194] S. Ambastha, S. Pant, S. Umesh, V. Vazhayil, and S. Asokan, “Feasibility Study on Thermography of Embedded Tumor Using Fiber Bragg Grating Thermal Sensor,” *IEEE Sens. J.*, vol. 20, no. 5, pp. 2452–2459, Mar. 2020.
- [195] H. H. A. Raziff *et al.*, “A temperature-controlled laser hot needle with grating sensor for liver tissue tract ablation,” *IEEE Trans. Instrum. Meas.*, pp. 1–1, Mar. 2020.
- [196] E. De Vita *et al.*, “Multipoint temperature monitoring of microwave thermal ablation in bones through fiber

References

- bragg grating sensor arrays†," *Sensors (Switzerland)*, vol. 20, no. 11, p. 3200, Jun. 2020.
- [197] S. Korganbayev *et al.*, "Highly dense FBG arrays for millimeter-scale thermal monitoring during nanocomposite-enhanced laser ablation," in *Optical Sensing and Detection VI*, 2020, vol. 11354, p. 19.
- [198] E. Schena and L. Majocchi, "Assessment of temperature measurement error and its correction during Nd:YAG laser ablation in porcine pancreas," *Int. J. Hyperth.*, vol. 30, no. 5, pp. 328–334, Aug. 2014.
- [199] F. Manns, P. J. Milne, X. Gonzalez-Cirre, D. B. Denham, J. M. Parel, and D. S. Robinson, "In situ temperature measurements with thermocouple probes during laser interstitial thermotherapy (LITT): Quantification and correction of a measurement artifact," *Lasers Surg. Med.*, vol. 23, no. 2, pp. 94–103, Jan. 1998.
- [200] A. D. Reid, M. R. Gertner, and M. D. Sherar, "Temperature measurement artefacts of thermocouples and fluoroptic probes during laser irradiation at 810 nm," *Phys. Med. Biol.*, vol. 46, no. 6, p. N149, 2001.
- [201] G. Allegretti *et al.*, "Magnetic resonance-based thermometry during laser ablation on ex-vivo swine pancreas and liver," *Med. Eng. Phys.*, vol. 37, no. 7, pp. 631–641, Jul. 2015.
- [202] E. Schena *et al.*, "Experimental assessment of CT-based thermometry during laser ablation of porcine pancreas," *Phys. Med. Biol.*, vol. 58, no. 16, p. 5705, 2013.
- [203] S. Korganbayev *et al.*, "Detection of thermal gradients through fiber-optic Chirped Fiber Bragg Grating (CFBG): Medical thermal ablation scenario," *Opt. Fiber Technol.*, vol. 41, pp. 48–55, Mar. 2018.
- [204] "[Online] Available: <https://fbgs.com/solutions/shape-sensing/>."
- [205] M. Abayazid, M. Kemp, and S. Misra, "3D flexible needle steering in soft-tissue phantoms using Fiber Bragg Grating sensors," in *Proceedings - IEEE International Conference on Robotics and Automation*, 2013, pp. 5843–5849.
- [206] R. J. Roesthuis, M. Kemp, J. J. Van Den Dobbelsteen, and S. Misra, "Three-dimensional needle shape reconstruction using an array of fiber bragg grating sensors," *IEEE/ASME Trans. Mechatronics*, vol. 19, no. 4, pp. 1115–1126, 2014.
- [207] Z. Lunwei, Q. Jinwu, S. Linyong, and Z. Yanan, "FBG sensor devices for spatial shape detection of intelligent colonoscope," in *Proceedings - IEEE International Conference on Robotics and Automation*, 2004, vol. 2004, no. 1, pp. 835–840.
- [208] X. Yi, J. Qian, Y. Zhang, Z. Zhang, and L. Shen, "3-D Shape display of intelligent colonoscope based on FBG sensor array and binocular vision," in *2007 IEEE/ICME International Conference on Complex Medical Engineering, CME 2007*, 2007, pp. 14–19.
- [209] I. Floris, P. A. Calderón, S. Sales, and J. M. Adam, "Effects of core position uncertainty on optical shape sensor accuracy," *Meas. J. Int. Meas. Confed.*, vol. 139, pp. 21–33, Jun. 2019.
- [210] F. Khan, A. Denasi, D. Barrera, J. Madrigal, S. Sales, and S. Misra, "Multi-Core Optical Fibers with Bragg Gratings as Shape Sensor for Flexible Medical Instruments," *IEEE Sens. J.*, vol. 19, no. 14, pp. 5878–5884, Jul. 2019.
- [211] R. Xu, A. Yurkewich, and R. V. Patel, "Shape sensing for torsionally compliant concentric-tube robots," in *Optical Fibers and Sensors for Medical Diagnostics and Treatment Applications XVI*, 2016, vol. 9702, p. 97020V.
- [212] A. A. G. Abushagur, N. Arsad, M. I. Reaz, and A. A. A. Bakar, "Advances in bio-tactile sensors for minimally invasive surgery using the fibre bragg grating force sensor technique: A survey," *Sensors (Switzerland)*, vol. 14, no. 4, pp. 6633–6665, Apr. 2014.
- [213] N. J. van de Berg, J. Dankelman, and J. J. van den Dobbelsteen, "Design of an actively controlled steerable needle with tendon actuation and FBG-based shape sensing," *Med. Eng. Phys.*, vol. 37, no. 6, pp. 617–622, Jun. 2015.
- [214] S. Jäckle, T. Eixmann, H. Schulz-Hildebrandt, G. Hüttmann, and T. Pätz, "Fiber optical shape sensing of flexible instruments for endovascular navigation," *Int. J. Comput. Assist. Radiol. Surg.*, vol. 14, no. 12, pp. 2137–2145, Dec. 2019.

References

- [215] W. Q. Mok, W. Wang, and S. Y. Liaw, "Vital signs monitoring to detect patient deterioration: An integrative literature review," *Int. J. Nurs. Pract.*, vol. 21, no. S2, pp. 91–98, May 2015.
- [216] C. Massaroni, M. Zaltieri, D. Lo Presti, D., *et al.*, "Fiber Bragg Grating Sensors for Cardiorespiratory Monitoring: A Review," *IEEE Sens. J.*, pp. 1–1, Apr. 2020.
- [217] L. Dziuda, F. W. Skibniewski, M. Krej, and J. Lewandowski, "Monitoring respiration and cardiac activity using fiber Bragg grating-based sensor," *IEEE Trans. Biomed. Eng.*, vol. 59, no. 7, pp. 1934–1942, 2012.
- [218] J. Hao, M. Jayachandran, P. L. Kng, S. F. Foo, P. W. Aung Aung, and Z. Cai, "FBG-based smart bed system for healthcare applications," *Front. Optoelectron. China*, vol. 3, no. 1, pp. 78–83, Jan. 2010.
- [219] S. Iacoponi *et al.*, "Polymer-coated fiber optic probe for the monitoring of breathing pattern and respiratory rate," in *Proceedings of the Annual International Conference of the IEEE Engineering in Medicine and Biology Society, EMBS*, 2018, vol. 2018-July, pp. 1616–1619.
- [220] D. Lo Presti *et al.*, "Cardio-respiratory monitoring in archery using a smart textile based on flexible fiber bragg grating sensors," *Sensors (Switzerland)*, vol. 19, no. 16, p. 3581, Aug. 2019.
- [221] M. Ciocchetti *et al.*, "Smart textile based on fiber bragg grating sensors for respiratory monitoring: Design and preliminary trials," *Biosensors*, vol. 5, no. 3, pp. 602–615, Sep. 2015.
- [222] C. Massaroni *et al.*, "Design and preliminary assessment of a smart textile for respiratory monitoring based on an array of Fiber Bragg Gratings," in *Proceedings of the Annual International Conference of the IEEE Engineering in Medicine and Biology Society, EMBS*, 2016, vol. 2016-October, pp. 6054–6057.
- [223] G. Wehrle, P. Nohama, H. J. Kalinowski, P. I. Torres, and L. C. G. Valente, "A fibre optic Bragg grating strain sensor for monitoring ventilatory movements," *Meas. Sci. Technol.*, vol. 12, no. 7, pp. 805–809, 2001.
- [224] A. Grillet *et al.*, "Optical fiber sensors embedded into medical textiles for healthcare monitoring," in *IEEE Sensors Journal*, 2008, vol. 8, no. 7, pp. 1215–1222.
- [225] J. De Jonckheere *et al.*, "OFSETH: Smart medical textile for continuous monitoring of respiratory motions under magnetic resonance imaging," in *Proceedings of the 31st Annual International Conference of the IEEE Engineering in Medicine and Biology Society: Engineering the Future of Biomedicine, EMBC 2009*, 2009, pp. 1473–1476.
- [226] J. Witt *et al.*, "Medical textiles with embedded fiber optic sensors for monitoring of respiratory movement," *IEEE Sens. J.*, vol. 12, no. 1, pp. 246–254, 2012.
- [227] D. Lo Presti *et al.*, "Smart Textile Based on 12 Fiber Bragg Gratings Array for Vital Signs Monitoring," *IEEE Sens. J.*, vol. 17, no. 18, pp. 6037–6043, Sep. 2017.
- [228] D. Lo Presti, C. Massaroni, P. S. E. Schena, D. Formica, M. A. Caponero, and G. Di Tomaso, "Smart textile based on FBG sensors for breath-by-breath respiratory monitoring: Tests on women," in *MeMeA 2018 - 2018 IEEE International Symposium on Medical Measurements and Applications, Proceedings*, 2018.
- [229] A. F. Silva, J. P. Carmo, P. M. Mendes, and J. H. Correia, "Simultaneous cardiac and respiratory frequency measurement based on a single fiber Bragg grating sensor," *Meas. Sci. Technol.*, vol. 22, no. 7, p. 075801, Jul. 2011.
- [230] J. Nedoma *et al.*, "Validation of a novel fiber-optic sensor system for monitoring cardiorespiratory activities during mri examinations," *Adv. Electr. Electron. Eng.*, vol. 15, no. 3, pp. 536–543, Sep. 2017.
- [231] D. Lo Presti *et al.*, "Wearable system based on flexible fbg for respiratory and cardiac monitoring," *IEEE Sens. J.*, vol. 19, no. 17, pp. 7391–7398, Sep. 2019.
- [232] Ł. Dziuda, F. W. Skibniewski, M. Krej, and P. M. Baran, "Fiber Bragg grating-based sensor for monitoring respiration and heart activity during magnetic resonance imaging examinations," *J. Biomed. Opt.*, vol. 18, no. 5, p. 057006, May 2013.
- [233] Y. Zhao, K. Chen, and J. Yang, "Novel target type flowmeter based on a differential fiber Bragg grating sensor," *Measurement*, vol. 38, no. 3, pp. 230–235, 2005.
- [234] S. Ambastha, S. Umesh, U. Maheshwari K, and S. Asokan, "Pulmonary Function Test Using Fiber Bragg

References

- Grating Spirometer," *J. Light. Technol.*, vol. 34, no. 24, pp. 5682–5688, Dec. 2016.
- [235] J. Yang, X. Chen, and X. Dong, "Hot-wire Anemometer Based on Frosted Fiber Bragg Grating Coated with Silver Film," in *IOP Conference Series: Materials Science and Engineering*, 2020, vol. 711, no. 1, p. 12112.
- [236] R. Gao and D. Lu, "Temperature compensated fiber optic anemometer based on graphene-coated elliptical core micro-fiber Bragg grating," *Opt. Express*, vol. 27, no. 23, p. 34011, Nov. 2019.
- [237] Y. Liang, A. P. Mazzolini, and P. R. Stoddart, "Fibre bragg grating sensor for respiratory monitoring," in *ACOFT/AOS 2006 - Australian Conference on Optical Fibre Technology/Australian Optical Society*, 2006.
- [238] A. Manuĵo and T. Osuch, "Temperature fiber Bragg grating based sensor for respiration monitoring," in *Photonics Applications in Astronomy, Communications, Industry, and High Energy Physics Experiments 2017*, 2017, vol. 10445, p. 104451A.
- [239] D. Lo Presti, C. Massaroni, and E. Schena, "Optical Fiber Gratings for Humidity Measurements: A Review," *IEEE Sens. J.*, vol. 18, no. 22, pp. 9065–9074, Nov. 2018.
- [240] D. Lo Presti *et al.*, "Agar-Coated Fiber Bragg Grating Sensor for Relative Humidity Measurements: Influence of Coating Thickness and Polymer Concentration," *IEEE Sens. J.*, vol. 19, no. 9, pp. 3335–3342, May 2019.
- [241] G. Shafiq and K. C. Veluvolu, "Surface chest motion decomposition for cardiovascular monitoring," *Sci. Rep.*, vol. 4, no. 1, pp. 1–9, May 2014.
- [242] K. Chethana, A. S. Guru Prasad, S. N. Omkar, and S. Asokan, "Fiber bragg grating sensor based device for simultaneous measurement of respiratory and cardiac activities," *J. Biophotonics*, vol. 10, no. 2, pp. 278–285, Feb. 2017.
- [243] Ł. Dziuda and F. W. Skibniewski, "A new approach to ballistocardiographic measurements using fibre Bragg grating-based sensors," *Biocybern. Biomed. Eng.*, vol. 34, no. 2, pp. 101–116, Jan. 2014.
- [244] J. Nedoma, M. Fajkus, R. Martinek, and H. Nazeran, "Vital sign monitoring and cardiac triggering at 1.5 tesla: A practical solution by an mr-ballistocardiography fiber-optic sensor," *Sensors*, vol. 19, no. 3, p. 470, 2019.
- [245] S. Koyama, H. Ishizawa, K. Fujimoto, S. Chino, and Y. Kobayashi, "Influence of individual differences on the calculation method for FBG-type blood pressure sensors," *Sensors (Switzerland)*, vol. 17, no. 1, p. 48, Dec. 2017.
- [246] A. P. Avolio, M. Butlin, and A. Walsh, "Arterial blood pressure measurement and pulse wave analysis—their role in enhancing cardiovascular assessment," *Physiol. Meas.*, vol. 31, no. 1, p. R1, 2009.
- [247] C. J. Leitão *et al.*, "Arterial pulses assessed with FBG based films: a smart skin approach," in *Biophotonics: Photonic Solutions for Better Health Care VI*, 2018, vol. 10685, p. 31.
- [248] S. Pant, S. Umesh, and S. Asokan, "A Novel Approach to Acquire the Arterial Pulse by Finger Plethysmography Using Fiber Bragg Grating Sensor," *IEEE Sens. J.*, vol. 20, no. 11, pp. 5921–5928, Feb. 2020.
- [249] C. Leitão *et al.*, "Feasibility studies of Bragg probe for noninvasive carotid pulse waveform assessment," *J. Biomed. Opt.*, vol. 18, no. 1, p. 017006, Jan. 2013.
- [250] S. Padma, S. Umesh, T. Srinivas, and S. Asokan, "Carotid Arterial Pulse Waveform Measurements Using Fiber Bragg Grating Pulse Probe," *IEEE J. Biomed. Heal. Informatics*, vol. 22, no. 5, pp. 1415–1420, Sep. 2018.
- [251] D. Jia *et al.*, "A Fiber Bragg Grating Sensor for Radial Artery Pulse Waveform Measurement," *IEEE Trans. Biomed. Eng.*, vol. 65, no. 4, pp. 839–846, Apr. 2018.
- [252] S. Chino, H. Ishizawa, S. Hosoya, S. Koyama, K. Fujimoto, and T. Kawamura, "Research for wearable multiple vital sign sensor using fiber Bragg Grating-Verification of several pulsate points in human body surface," in *I2MTC 2017 - 2017 IEEE International Instrumentation and Measurement Technology Conference, Proceedings*, 2017.
- [253] Y. Haseda, J. Bonefacino, H. Y. Tam, S. Chino, S. Koyama, and H. Ishizawa, "Measurement of pulse wave signals and blood pressure by a plastic optical fiber FBG sensor," *Sensors (Switzerland)*, vol. 19, no. 23, p. 5088, Nov. 2019.
- [254] Y. Miyauchi, S. Koyama, and H. Ishizawa, "Basic experiment of blood-pressure measurement which uses FBG

References

- sensors," in *Conference Record - IEEE Instrumentation and Measurement Technology Conference*, 2013, pp. 1767–1770.
- [255] Y. Katsuragawa and H. Ishizawa, "Non-invasive blood pressure measurement by pulse wave analysis using FBG sensor," in *Conference Record - IEEE Instrumentation and Measurement Technology Conference*, 2015, vol. 2015-July, pp. 511–515.
- [256] S. Koyama, H. Ishizawa, A. Sakaguchi, S. Hosoya, and T. Kawamura, "Influence on calculated blood pressure of measurement posture for the development of wearable vital sign sensors," *J. Sensors*, vol. 2017, 2017.
- [257] A. van Brakel, P. L. Swart, A. A. Chtcherbakov, and M. G. Shlyagin, "Blood pressure manometer using a twin Bragg grating Fabry-Perot interferometer," in *Advanced Sensor Systems and Applications II*, 2005, vol. 5634, p. 595.
- [258] U. Sharath, R. Sukreet, G. Apoorva, and S. Asokan, "Blood pressure evaluation using sphygmomanometry assisted by arterial pulse waveform detection by fiber Bragg grating pulse device," *J. Biomed. Opt.*, vol. 18, no. 6, p. 067010, Jun. 2013.
- [259] H. Li, H. Yang, E. Li, Z. Liu, and K. Wei, "Wearable sensors in intelligent clothing for measuring human body temperature based on optical fiber Bragg grating," *Opt. Express*, vol. 20, no. 11, p. 11740, May 2012.
- [260] Q. Yu, Y. Zhang, Y. Dong, Y. P. Li, C. Wang, and H. Chen, "Study on optical fiber Bragg grating temperature sensors for human body temperature monitoring," in *2012 Symposium on Photonics and Optoelectronics, SOPO 2012*, 2012.
- [261] L. D'Acquisto, F. Scardulla, and S. Pasta, "Steam sterilization processes affect the stability of clinical thermometers: Thermistor and prototypal FBG probe comparison," *Opt. Fiber Technol.*, vol. 55, p. 102156, Mar. 2020.
- [262] W. Xu, D. Wang, D. Li, and C. C. Liu, "Recent developments of electrochemical and optical biosensors for antibody detection," *International Journal of Molecular Sciences*, vol. 21, no. 1. MDPI AG, p. 134, 24-Dec-2020.
- [263] C. Chen and J. Wang, "Optical biosensors: An exhaustive and comprehensive review," *Analyst*, vol. 145, no. 5. Royal Society of Chemistry, pp. 1605–1628, 07-Mar-2020.
- [264] X. D. Wang and O. S. Wolfbeis, "Fiber-Optic Chemical Sensors and Biosensors (2015-2019)," *Anal. Chem.*, vol. 92, no. 1, pp. 397–430, Jan. 2020.
- [265] B. N. Shivananju, M. Renilkumar, G. R. Prashanth, S. Asokan, and M. M. Varma, "Detection limit of etched fiber bragg grating sensors," *J. Light. Technol.*, vol. 31, no. 14, pp. 2441–2447, Jul. 2013.
- [266] M. Loyez *et al.*, "Rapid Detection of Circulating Breast Cancer Cells Using a Multiresonant Optical Fiber Aptasensor with Plasmonic Amplification," *ACS Sensors*, vol. 5, no. 2, pp. 454–463, Feb. 2020.
- [267] J. Lao *et al.*, "Gold Nanoparticle-Functionalized Surface Plasmon Resonance Optical Fiber Biosensor: In Situ Detection of Thrombin with 1 n-M Detection Limit," *J. Light. Technol.*, vol. 37, no. 11, pp. 2748–2755, Jun. 2019.
- [268] W. Hu, Y. Huang, C. Chen, Y. Liu, T. Guo, and B. O. Guan, "Highly sensitive detection of dopamine using a graphene functionalized plasmonic fiber-optic sensor with aptamer conformational amplification," *Sensors Actuators, B Chem.*, vol. 264, pp. 440–447, Jul. 2018.
- [269] A. Candiani *et al.*, "Optical fiber ring cavity sensor for label-free DNA detection," *IEEE J. Sel. Top. Quantum Electron.*, vol. 18, no. 3, pp. 1176–1183, 2012.
- [270] A. N. Chryssis, S. S. Saini, S. M. Lee, H. Yi, W. E. Bentley, and M. Dagenais, "Detecting hybridization of DNA by highly sensitive evanescent field etched core fiber Bragg grating sensors," *IEEE J. Sel. Top. Quantum Electron.*, vol. 11, no. 4, pp. 864–872, Jul. 2005.
- [271] A. Revzin, E. Maverakis, and H. C. Chang, "Biosensors for immune cell analysis-A perspective," *Biomicrofluidics*, vol. 6, no. 2, p. 021301, Apr. 2012.
- [272] B. Jiang *et al.*, "Graphene oxide-deposited tilted fiber grating for ultrafast humidity sensing and human breath monitoring," *Sensors Actuators, B Chem.*, vol. 293, pp. 336–341, Aug. 2019.

References

- [273] Y. Miao *et al.*, "Relative humidity sensor based on tilted fiber Bragg grating with polyvinyl alcohol coating," *IEEE Photonics Technol. Lett.*, vol. 21, no. 7, pp. 441–443, Apr. 2009.
- [274] C. Massaroni, D. Lo Presti, P. Saccomandi, M. A. Caponero, R. D'Amato, and E. Schena, "Fiber Bragg Grating Probe for Relative Humidity and Respiratory Frequency Estimation: Assessment during Mechanical Ventilation," *IEEE Sens. J.*, vol. 18, no. 5, pp. 2125–2130, Mar. 2018.
- [275] C. Massaroni *et al.*, "Multi-sensitive FBG-based needle for both relative humidity and breathing rate monitoring," in *MeMeA 2018 - 2018 IEEE International Symposium on Medical Measurements and Applications, Proceedings*, 2018.
- [276] S. P. Morgan *et al.*, "Optical fiber sensors for monitoring in critical care," in *Proceedings of the Annual International Conference of the IEEE Engineering in Medicine and Biology Society, EMBS*, 2019, pp. 1139–1143.
- [277] D. Lo Presti *et al.*, "A Magnetic Resonance-compatible wearable device based on functionalized fiber optic sensor for respiratory monitoring," *IEEE Sens. J.*, pp. 1–1, Mar. 2020.
- [278] V. Malachovská *et al.*, "Fiber-Optic SPR Immunosensors Tailored to Target Epithelial Cells through Membrane Receptors," *Anal. Chem.*, vol. 87, no. 12, pp. 5957–5965, Jun. 2015.
- [279] C. Caucheteur, V. Malachovska, C. Ribaut, and R. Wattiez, "[INVITED] Cell sensing with near-infrared plasmonic optical fiber sensors," *Opt. Laser Technol.*, vol. 78, pp. 116–121, Apr. 2016.
- [280] H. M. H. Hurks *et al.*, "Expression of epidermal growth factor receptor: risk factor in uveal melanoma," *Invest. Ophthalmol. Vis. Sci.*, vol. 41, no. 8, pp. 2023–2027, 2000.
- [281] Y. Shevchenko, T. J. Francis, D. A. D. Blair, R. Walsh, M. C. Derosa, and J. Albert, "In situ biosensing with a surface plasmon resonance fiber grating aptasensor," *Anal. Chem.*, vol. 83, no. 18, pp. 7027–7034, Sep. 2011.
- [282] X. Chen *et al.*, "In-situ detection of small biomolecule interactions using a plasmonic tilted fiber grating sensor," *J. Light. Technol.*, vol. 37, no. 11, pp. 2792–2799, Jun. 2019.
- [283] B. Jiang *et al.*, "Label-free glucose biosensor based on enzymatic graphene oxide-functionalized tilted fiber grating," *Sensors Actuators, B Chem.*, vol. 254, pp. 1033–1039, Jan. 2018.
- [284] B. Luo, Z. Yan, Z. Sun, Y. Liu, M. Zhao, and L. Zhang, "Biosensor based on excessively tilted fiber grating in thin-cladding optical fiber for sensitive and selective detection of low glucose concentration," *Opt. Express*, vol. 23, no. 25, p. 32429, Dec. 2015.
- [285] C. Brüser, C. H. Antink, T. Wartzek, M. Walter, and S. Leonhardt, "Ambient and unobtrusive cardiorespiratory monitoring techniques," *IEEE Rev. Biomed. Eng.*, vol. 8, pp. 30–43, 2015.
- [286] H. Liu, J. Allen, D. Zheng, and F. Chen, "Recent development of respiratory rate measurement technologies," *Physiological Measurement*, vol. 40, no. 7. Institute of Physics Publishing, 02-Aug-2019.
- [287] M. J. Tipton, A. Harper, J. F. R. Paton, and J. T. Costello, "The human ventilatory response to stress: rate or depth?," *J. Physiol.*, vol. 595, no. 17, pp. 5729–5752, 2017.
- [288] C. Massaroni, A. Nicolò, D. Lo Presti, M. Sacchetti, S. Silvestri, and E. Schena, "Contact-based methods for measuring respiratory rate," *Sensors (Switzerland)*, vol. 19, no. 4. Multidisciplinary Digital Publishing Institute, p. 908, 21-Feb-2019.
- [289] A. Nicolò, C. Massaroni, and L. Passfield, "Respiratory Frequency during Exercise: The Neglected Physiological Measure," *Front. Physiol.*, vol. 8, p. 922, Dec. 2017.
- [290] A. Nicolò, M. Montini, M. Girardi, F. Felici, I. Bazzucchi, and M. Sacchetti, "Respiratory frequency as a marker of physical effort during high-intensity interval training in soccer players," *Int. J. Sports Physiol. Perform.*, 2020.
- [291] J. Z. Liu, T. H. Dai, T. H. Elster, V. Sahgal, R. W. Brown, and G. H. Yue, "Simultaneous measurement of human joint force, surface electromyograms, and functional MRI-measured brain activation," *J. Neurosci. Methods*, vol. 101, no. 1, pp. 49–57, Aug. 2000.
- [292] J. Hogan, "Why don't nurses monitor the respiratory rates of patients?," *Br. J. Nurs.*, vol. 15, no. 9, pp. 489–

References

- 492, 2006.
- [293] A. F. Smith and J. Wood, "Can some in-hospital cardio-respiratory arrests be prevented? A prospective survey," *Resuscitation*, vol. 37, no. 3, pp. 133–137, Jun. 1998.
- [294] A. Nicolò, M. Girardi, I. Bazzucchi, F. Felici, and M. Sacchetti, "Respiratory frequency and tidal volume during exercise: differential control and unbalanced interdependence," *Physiol. Rep.*, vol. 6, no. 21, Nov. 2018.
- [295] A. Nicolò and M. Sacchetti, "A new model of ventilatory control during exercise," *Exp. Physiol.*, vol. 104, no. 9, pp. 1331–1332, Sep. 2019.
- [296] C. Deaton, E. S. Froelicher, L. H. Wu, C. Ho, K. Shishani, and T. Jaarsma, "The global burden of cardiovascular disease," *Eur. J. Cardiovasc. Nurs.*, vol. 10, no. SUPPL. 2, pp. S5–S13, Jun. 2011.
- [297] J. Achten and A. E. Jeukendrup, "Heart rate monitoring: Applications and limitations," *Sports Medicine*, vol. 33, no. 7. Springer, pp. 517–538, 23-Sep-2003.
- [298] M. Buchheit, "Monitoring training status with HR measures: Do all roads lead to Rome?," *Front. Physiol.*, 2014.
- [299] S. Cook, M. Togni, M. C. Schaub, P. Wenaweser, and O. M. Hess, "High heart rate: a cardiovascular risk factor?," *Eur. Heart J.*, vol. 27, no. 20, pp. 2387–93, Oct. 2006.
- [300] J. F. Thayer, F. Åhs, M. Fredrikson, J. J. Sollers, and T. D. Wager, "A meta-analysis of heart rate variability and neuroimaging studies: Implications for heart rate variability as a marker of stress and health," *Neuroscience and Biobehavioral Reviews*. 2012.
- [301] A. B. OTIS, W. O. FENN, and H. RAHN, "Mechanics of breathing in man," *J. Appl. Physiol.*, vol. 2, no. 11, pp. 592–607, May 1950.
- [302] L. B. Rowell and others, *Human cardiovascular control*. Oxford University Press, USA, 1993.
- [303] O. T. Inan *et al.*, "Ballistocardiography and Seismocardiography: A Review of Recent Advances," *IEEE J. Biomed. Heal. Informatics*, vol. 19, no. 4, pp. 1414–1427, 2015.
- [304] I. Sadek, J. Biswas, and B. Abdulrazak, "Ballistocardiogram signal processing: a review," *Heal. Inf. Sci. Syst.*, vol. 7, no. 1, Dec. 2019.
- [305] P. K. Jain, A. K. Tiwari, and O. L. Bhagat, "Seismocardiography: An alternate method to estimate electro-mechanical window," in *2016 International Conference on Systems in Medicine and Biology, ICSMB 2016*, 2017, pp. 136–139.
- [306] A. Taebi, B. E. Solar, A. J. Bomar, R. H. Sandler, and H. A. Mansy, "Recent Advances in Seismocardiography," *Vibration*, vol. 1, no. September 2017, pp. 64–86, 2018.
- [307] V. L. Petrovic, M. M. Jankovic, A. V. Lupsic, V. R. Mihajlovic, and J. S. Popovic-Bozovic, "High-Accuracy Real-Time Monitoring of Heart Rate Variability Using 24 GHz Continuous-Wave Doppler Radar," *IEEE Access*, vol. 7, pp. 74721–74733, 2019.
- [308] W. Q. Lindh, *Delmar's comprehensive medical assisting: administrative and clinical competencies*. Delmar's, 2010.
- [309] J. Wang, X. Wang, L. Chen, J. Huangfu, C. Li, and L. Ran, "Noncontact distance and amplitude-independent vibration measurement based on an extended dacm algorithm," *IEEE Trans. Instrum. Meas.*, vol. 63, no. 1, pp. 145–153, Jan. 2014.
- [310] J. Park *et al.*, "Polyphase-Basis Discrete Cosine Transform for Real-Time Measurement of Heart Rate with CW Doppler Radar," *IEEE Trans. Microw. Theory Tech.*, vol. 66, no. 3, pp. 1644–1659, Mar. 2018.
- [311] M. Nosrati and N. Tavassolian, "High-Accuracy Heart Rate Variability Monitoring Using Doppler Radar Based on Gaussian Pulse Train Modeling and FTFR Algorithm," *IEEE Trans. Microw. Theory Tech.*, vol. 66, no. 1, pp. 556–567, Jan. 2018.
- [312] T. Allsop *et al.*, "Cardiac-induced localized thoracic motion detected by a fiber optic sensing scheme," *J. Biomed. Opt.*, vol. 19, no. 11, p. 117006, Nov. 2014.

References

- [313] J. Gomez-Clapers, A. Serra-Rocamora, R. Casanella, and R. Pallas-Areny, "Towards the standardization of ballistocardiography systems for J-peak timing measurement," *Meas. J. Int. Meas. Confed.*, vol. 58, pp. 310–316, Dec. 2014.
- [314] Y. Liu, Z. Guo, Y. Zhang, K. S. Chiang, and X. Dong, "Simultaneous pressure and temperature measurement with polymer-coated fibre Bragg grating," *Electron. Lett.*, vol. 36, no. 6, p. 564, 2000.
- [315] L. Jin *et al.*, "An embedded FBG sensor for simultaneous measurement of stress and temperature," *IEEE Photonics Technol. Lett.*, vol. 18, no. 1, pp. 154–156, 2006.
- [316] C. Massaroni, M. A. Caponero, R. D'Amato, D. Lo Presti, and E. Schena, "Fiber bragg grating measuring system for simultaneous monitoring of temperature and humidity in mechanical ventilation," *Sensors (Switzerland)*, vol. 17, no. 4, p. 749, Apr. 2017.
- [317] M. S. Islam, G. Paul, H. X. Ong, P. M. Young, Y. T. Gu, and S. C. Saha, "A review of respiratory anatomical development, air flow characterization and particle deposition," *International Journal of Environmental Research and Public Health*, vol. 17, no. 2. MDPI AG, 02-Jan-2020.
- [318] K. Schmidt-Nielsen, F. R. Hainsworth, and D. E. Murrish, "Counter-current heat exchange in the respiratory passages: Effect on water and heat balance," *Respir. Physiol.*, vol. 9, no. 2, pp. 263–276, May 1970.
- [319] "Respiratory Humidification Products." [Online]. Available: <https://live.wilamed.de/Products/atemgasbefeuchtung-2/?lang=en>. [Accessed: 24-Dec-2020].
- [320] J. Ma, J. Dong, Y. Shang, K. Inthavong, J. Tu, and D. O. Frank-Ito, "Air conditioning analysis among human nasal passages with anterior anatomical variations," *Med. Eng. Phys.*, vol. 57, pp. 19–28, Jul. 2018.
- [321] J. Wen, K. Inthavong, J. Tu, and S. Wang, "Numerical simulations for detailed airflow dynamics in a human nasal cavity," *Respir. Physiol. Neurobiol.*, vol. 161, no. 2, pp. 125–135, Apr. 2008.
- [322] K. Kumahata, F. Mori, S. Ishikawa, and T. Matsuzawa, "Nasal flow simulation using heat and humidity models," *J. Biomech. Sci. Eng.*, vol. 5, no. 5, pp. 565–577, 2010.
- [323] A. J. Bates *et al.*, "Dynamics of airflow in a short inhalation," *J. R. Soc. Interface*, vol. 12, no. 102, 2014.
- [324] C. Y. Lee and C. R. Wilke, "Measurements of Vapor Diffusion Coefficient," *Ind. Eng. Chem.*, vol. 46, no. 11, pp. 2381–2387, Nov. 1954.
- [325] D. Lo Presti *et al.*, "Fiber bragg gratings for medical applications and future challenges: A review," *IEEE Access*, vol. 8, pp. 156863–156888, 2020.
- [326] N. A. David, P. M. Wild, and N. Djilali, "Parametric study of a polymer-coated fibre-optic humidity sensor," *Meas. Sci. Technol.*, vol. 23, no. 3, p. 035103, 2012.
- [327] P. Kronenberg, P. K. Rastogi, P. Giaccari, and H. G. Limberger, "Relative humidity sensor with optical fiber Bragg gratings," *Opt. Lett.*, vol. 27, no. 16, pp. 1385–1387, 2002.
- [328] A. J. Swanson, S. G. R. Photonics, S. J. Photonics, R. D. B. Photonics, and M. D. H. B. Photonics, "Physical Development of novel polymer coating for FBG based relative humidity sensing," *Sensors Actuators, A Phys.*, vol. 249, pp. 217–224, 2016.
- [329] T. L. Yeo, T. Sun, K. T. V. Grattan, D. Parry, R. Lade, and B. D. Powell, "Characterisation of a polymer-coated fibre Bragg grating sensor for relative humidity sensing," *Sensors Actuators, B Chem.*, vol. 110, no. 1, pp. 148–156, 2005.
- [330] E. Davies *et al.*, "Original article Dynamics of water in agar gels studied using low and high resolution 1 H NMR spectroscopy," pp. 2502–2507, 2010.
- [331] A. Tözeren, *Human body dynamics: classical mechanics and human movement*. Springer Science & Business Media, 1999.
- [332] G. Cai, J. Wang, K. Qian, J. Chen, S. Li, and P. S. Lee, "Extremely Stretchable Strain Sensors Based on Conductive Self-Healing Dynamic Cross-Links Hydrogels for Human-Motion Detection," *Adv. Sci.*, vol. 4, no. 2, Feb. 2017.
- [333] D. Schofield, S. Kelly, R. Shrestha, E. Callander, M. Passey, and R. Percival, "The impact of back problems on retirement wealth," *Pain*, vol. 153, no. 1, pp. 203–210, Jan. 2012.

References

- [334] D. J. Schofield *et al.*, "Lost productive life years caused by chronic conditions in australians aged 45-164 years, 2010-2030," *Med. J. Aust.*, vol. 203, no. 6, pp. 260.e1-260.e6, Sep. 2015.
- [335] M. Jang, J. S. Kim, S. H. Um, S. Yang, and J. Kim, "Ultra-high curvature sensors for multi-bend structures using fiber Bragg gratings," *Opt. Express*, vol. 27, no. 3, p. 2074, Feb. 2019.
- [336] M. Ha and D. Han, "The relationship between knee joint angle and knee flexor and extensor muscle strength," *J. Phys. Ther. Sci.*, vol. 29, no. 4, pp. 662-664, 2017.
- [337] A. I. Faisal, S. Majumder, T. Mondal, D. Cowan, S. Naseh, and M. J. Deen, "Monitoring methods of human body joints: State-of-the-art and research challenges," *Sensors (Switzerland)*, vol. 19, no. 11, pp. 1-39, 2019.
- [338] G. L. Smidt, "Biomechanical analysis of knee flexion and extension," *J. Biomech.*, vol. 6, no. 1, pp. 79-92, Jan. 1973.
- [339] Y. Yakut and A. Tuncer, "Architecture of human joints and their movement," in *Comparative Kinesiology of the Human Body*, Elsevier, 2020, pp. 47-57.
- [340] K.-N. An, "Kinematic analysis of human movement," *Ann. Biomed. Eng.*, vol. 12, no. 6, pp. 585-597, 1984.
- [341] A. Grassi, F. Cecchi, M. Maselli, M. Roling, C. Laschi, and M. Cianchetti, "Warp-Knitted Textile as a Strain Sensor: Characterization Procedure and Application in a Comfortable Wearable Goniometer," *IEEE Sens. J.*, vol. 17, no. 18, pp. 5927-5936, Sep. 2017.
- [342] M. Maselli, E. Mussi, F. Cecchi, M. Manti, P. Tropea, and C. Laschi, "A wearable sensing device for monitoring single planes neck movements: Assessment of its performance," *IEEE Sens. J.*, vol. 18, no. 15, pp. 6327-6336, Aug. 2018.
- [343] B. L. Riemann and S. M. Lephart, "The sensorimotor system, part I: The physiologic basis of functional joint stability," *Journal of Athletic Training*, vol. 37, no. 1. Association, Inc, pp. 71-79, 2002.
- [344] E. Thelen, D. M. Fisher, and R. Ridley-Johnson, "The relationship between physical growth and a newborn reflex," *Infant Behav. Dev.*, vol. 7, no. 4, pp. 479-493, Oct. 1984.
- [345] R. Mowbray, J. M. Gottwald, M. Zhao, A. P. Atkinson, and D. Cowie, "The development of visually guided stepping," *Exp. Brain Res.*, vol. 237, no. 11, pp. 2875-2883, Nov. 2019.
- [346] M. C. Allen and A. J. Capute, "The evolution of primitive reflexes in extremely premature infants," *Pediatr. Res.*, vol. 20, no. 12, pp. 1284-1289, 1986.
- [347] M. V. M. Moraes, E. Tudella, J. Ribeiro, T. S. Beltrame, and R. J. Krebs, "Reliability of the M-FLEX™: Equipment to measure palmar grasp strength in infants," *Infant Behav. Dev.*, vol. 34, no. 2, pp. 226-234, Apr. 2011.
- [348] A. G. Allievi, T. Arichi, A. L. Gordon, and E. Burdet, "Technology-aided assessment of sensorimotor function in early infancy," *Frontiers in Neurology*, vol. 5, no. OCT. Frontiers Research Foundation, p. 197, 01-Oct-2014.
- [349] E. Mercuri, D. Ricci, M. Pane, and G. Baranello, "The neurological examination of the newborn baby," in *Early Human Development*, 2005, vol. 81, no. 12, pp. 947-956.
- [350] T. H. Glick, "Toward a more efficient and effective neurologic examination for the 21st century," in *European Journal of Neurology*, 2005, vol. 12, no. 12, pp. 994-997.
- [351] T. Muhammad, J. S. Lee, Y. B. Shin, and S. Kim, "A wearable device to measure the palmar grasp reflex of neonates in neonatal intensive care unit," *Sensors Actuators, A Phys.*, vol. 304, p. 111905, Apr. 2020.
- [352] H.-J. Sheng, M.-Y. Fu, T.-C. Chen, C.-M. Lin, W.-F. Liu, and S.-S. Bor, "High-sensitivity pressure sensor based on a fiber Bragg grating," in *Industrial and Highway Sensors Technology*, 2004, vol. 5272, p. 248.
- [353] D. Lo Presti *et al.*, "An fmri compatible smart device for measuring palmar grasping actions in newborns," *Sensors (Switzerland)*, vol. 20, no. 21, pp. 1-16, Oct. 2020.
- [354] D. Lo Presti *et al.*, "Smart Textile Based on 12 Fiber Bragg Gratings Array for Vital Signs Monitoring," *IEEE Sens. J.*, vol. 17, no. 18, pp. 6037-6043, Sep. 2017.
- [355] C. Massaroni *et al.*, "Design and Feasibility Assessment of a Magnetic Resonance-Compatible Smart Textile Based on Fiber Bragg Grating Sensors for Respiratory Monitoring," *IEEE Sens. J.*, vol. 16, no. 22, pp. 8103-

References

- 8110, Nov. 2016.
- [356] Ł. Dziuda, F. W. Skibniewski, M. Krej, and P. M. Baran, "Fiber Bragg grating-based sensor for monitoring respiration and heart activity during magnetic resonance imaging examinations," *J. Biomed. Opt.*, vol. 18, no. 5, p. 057006, May 2013.
- [357] Y. Retory, P. Niedzialkowski, C. De Picciotto, M. Bonay, and M. Petitjean, "New respiratory inductive plethysmography (RIP) method for evaluating ventilatory adaptation during mild physical activities," *PLoS One*, vol. 11, no. 3, 2016.
- [358] C. Massaroni *et al.*, "Optoelectronic Plethysmography in Clinical Practice and Research: A Review," *Respiration*, vol. 93, no. 5. Karger Publishers, pp. 339–354, 2017.
- [359] A. P. Silvatti, K. J. Sarro, P. Cerveri, G. Baroni, and R. M. L. Barros, "A 3D kinematic analysis of breathing patterns in competitive swimmers," *J. Sports Sci.*, vol. 30, no. 14, pp. 1551–1560, 2012.
- [360] C. Massaroni *et al.*, "Smart textile for respiratory monitoring and thoraco-abdominal motion pattern evaluation," *J. Biophotonics*, vol. 11, no. 5, 2018.
- [361] C. Massaroni *et al.*, "Validation of a Wearable Device and an Algorithm for Respiratory Monitoring During Exercise," *IEEE Sens. J.*, vol. 19, no. 12, pp. 4652–4659, 2019.
- [362] D. G. Altman and J. M. Bland, "Measurement in Medicine : the Analysis of Method Comparison Studies," *Stat.*, vol. 32, pp. 307–317, 1983.
- [363] BS ISO 37, *BS ISO 37:2011 - Rubber, vulcanized or thermoplastic — Determination of tensile stress-strain properties*. 2011.
- [364] "<https://www.smooth-on.com/products/dragon-skin-20/>."
- [365] D. Lo Presti *et al.*, "Wearable system based on flexible FBG for respiratory and cardiac monitoring," *IEEE Sens. J.*, pp. 1–1, 2019.
- [366] R. Willink and R. Willink, "Guide to the Expression of Uncertainty in Measurement," in *Measurement Uncertainty and Probability*, no. September, 2013, pp. 237–244.
- [367] A. Leal-Junior, J. Casas, C. Marques, M. J. Pontes, and A. Frizera, "Application of Additive Layer Manufacturing Technique on the Development of High Sensitive Fiber Bragg Grating Temperature Sensors," *Sensors (Basel)*, vol. 18, no. 12, p. 4120, Nov. 2018.
- [368] H. Sun, Y. Wang, J. Chen, and H. Hillborg, "Silicone rubber with improved hydrophobicity," in *Annual Report - Conference on Electrical Insulation and Dielectric Phenomena, CEIDP*, 2015, vol. 2015-Decem, pp. 241–244.
- [369] A. G. Leal, A. Frizera, and M. J. Pontes, "Hysteresis compensation technique for POF curvature sensors," in *25th International Conference on Optical Fiber Sensors*, 2017, vol. 10323, p. 103232U.
- [370] J. Martin Bland and D. G. Altman, "STATISTICAL METHODS FOR ASSESSING AGREEMENT BETWEEN TWO METHODS OF CLINICAL MEASUREMENT," *Lancet*, vol. 327, no. 8476, pp. 307–310, Feb. 1986.
- [371] T. Allsop *et al.*, "Cardiac-induced localized thoracic motion detected by a fiber optic sensing scheme," *J. Biomed. Opt.*, vol. 19, no. 11, p. 117006, Nov. 2014.
- [372] J. Nedoma *et al.*, "Validation of a novel fiber-optic sensor system for monitoring cardiorespiratory activities during mri examinations," *Adv. Electr. Electron. Eng.*, vol. 15, no. 3, pp. 536–543, Oct. 2017.
- [373] J. Nedoma, M. Fajkus, R. Martinek, and H. Nazeran, "Vital sign monitoring and cardiac triggering at 1.5 tesla: A practical solution by an mr-ballistocardiography fiber-optic sensor," *Sensors (Switzerland)*, vol. 19, no. 3, p. 470, Jan. 2019.
- [374] M. N. Mohamed, W. M. N. Wan Norman, A. Linoby, M. H. Sariman, and M. Z. Mohd Azam, "Breathing Pattern Influence to the Shooting Performance," in *Proceedings of the International Colloquium on Sports Science, Exercise, Engineering and Technology 2014 (ICoSSEET 2014)*, Singapore: Springer Singapore, 2014, pp. 321–333.
- [375] F. M. Clemente, M. S. Couceiro, and R. Mendes, "Study of the Heart Rate and Accuracy Performance of Archers SEE PROFILE," 2016.

References

- [376] D. Keast and B. Elliott, "Fine body movements and the cardiac cycle in archery," *J. Sports Sci.*, vol. 8, no. 3, pp. 203–213, Dec. 1990.
- [377] M. N. Mohamed, W. M. N. Wan Norman, A. Linoby, M. H. Sariman, and M. Z. Mohd Azam, "The Importance of Being Calm: The Impact of Heart Rate Towards Performance," in *Proceedings of the International Business Management and Computing Research Colloquium (BMCRC) 2016, Raub, Malaysia, 25 May 2016*, 2016.
- [378] M. Drissi-Habti, V. Raman, A. Khadour, and S. Timorian, "Fiber optic sensor embedment study for multi-parameter strain sensing," *Sensors (Switzerland)*, vol. 17, no. 4, p. 667, Mar. 2017.
- [379] Smooth-On, "Dragon Skin® High Performance Silicone Rubber," *Smooth-On*, 2015. [Online]. Available: <https://www.smooth-on.com/product-line/dragon-skin/>. [Accessed: 23-Jul-2020].
- [380] J. Di Tocco *et al.*, "A wearable system based on flexible sensors for unobtrusive respiratory monitoring in occupational settings," *IEEE Sens. J.*, pp. 1–1, Nov. 2020.
- [381] O. Access, F. Chiavaioli, F. Baldini, S. Tombelli, C. Trono, and A. Giannetti, "Biosensing with optical fiber gratings," vol. 6, no. 4, pp. 663–679, 2017.
- [382] F. Galatas and R. Armise, "4 Agar."
- [383] M. Laguna and J. Estella, "Effects of aging and drying conditions on the structural and textural properties of silica gels," vol. 102, pp. 274–282, 2007.
- [384] Z. Weng, J. Wang, T. Senthil, and L. Wu, "Institute of Research on the Structure of Matter , Chinese Academy of Sciences ," *JMADE*, 2016.
- [385] R. Armisen, "Agar and agarose biotechnological applications," *Hydrobiologia*, vol. 221, no. 1, pp. 157–166, 1991.
- [386] R. D. Branson, "The effects of inadequate humidity,," *Respir. Care Clin. N. Am.*, vol. 4, no. 2, pp. 199–214, Jun. 1998.
- [387] C. Losquadro, P. Saccomandi, C. Massaroni, and E. Schena, "Performances of heated wire humidifiers during adult mechanical ventilation: Estimation of the amount of condensation," in *2016 IEEE International Symposium on Medical Measurements and Applications (MeMeA)*, 2016, pp. 1–5.
- [388] C. Massaroni, S. Member, D. Lo Presti, S. Member, and P. Saccomandi, "Fiber Bragg grating probe for relative humidity and respiratory frequency estimation : assessment during mechanical ventilation," vol. 1748, no. c, 2017.
- [389] D. Todd, J. Boyd, J. Lloyd, and E. John, "Inspired gas humidity during mechanical ventilation: Effects of humidification chamber, airway temperature probe position and environmental conditions," *J. Paediatr. Child Health*, vol. 37, no. 5, pp. 489–494, Oct. 2001.
- [390] I. Air, B. Munksgaard, and I. Air, "Significance of humidity and temperature on skin and upper airway symptoms," pp. 344–352, 2003.
- [391] B. N. Taylor and C. E. Kuyatt, "United States Department of Commerce Guidelines for Evaluating and Expressing the Uncertainty of NIST Measurement Results," 1994.
- [392] Q. Chen and P. Lu, "Fiber Bragg Gratings and Their Applications as Temperature and Humidity Sensors," *At. Mol. Opt. Phys. New Res.*, pp. 235–260, 2008.
- [393] C. Zhang, W. Zhang, D. J. Webb, and G.-D. Peng, "Optical fibre temperature and humidity sensor," *Electron. Lett.*, vol. 46, no. 9, p. 643, 2010.
- [394] O. F. Sensors and M. June, "Sergiy (2016) Simultaneous temperature and humidity measurements in a mechanical ventilator using an optical fibre sensor . In : Sixth European Workshop on Simultaneous temperature and humidity measurements in a," 2016.
- [395] S. J. Cala *et al.*, "Chest wall and lung volume estimation by optical reflectance motion analysis," *J. Appl. Physiol.*, vol. 81, pp. 2680–2689, 1996.
- [396] C. Massaroni *et al.*, "Comparison of marker models for the analysis of the volume variation and thoracoabdominal motion pattern in untrained and trained participants," *J. Biomech.*, vol. 76, pp. 247–252,

References

- 2018.
- [397] C. Massaroni, G. Senesi, E. Schena, and S. Silvestri, "Analysis of breathing via optoelectronic systems: comparison of four methods for computing breathing volumes and thoraco-abdominal motion pattern," *Comput. Methods Biomech. Biomed. Engin.*, 2017.
- [398] C. Massaroni *et al.*, "Respiratory Monitoring during Physical Activities with a Multi-Sensor Smart Garment and Related Algorithms," *IEEE Sens. J.*, vol. 20, no. 4, pp. 2173–2180, 2020.
- [399] C. Massaroni, D. Lo Presti, P. Saccomandi, M. A. Caponero, R. D'Amato, and E. Schena, "Fiber Bragg Grating Probe for Relative Humidity and Respiratory Frequency Estimation: Assessment during Mechanical Ventilation," *IEEE Sens. J.*, vol. 18, no. 5, pp. 2125–2130, 2018.
- [400] F. U. Hernandez *et al.*, "Simultaneous temperature and humidity measurements in a mechanical ventilator using an optical fibre sensor," in *Sixth European Workshop on Optical Fibre Sensors*, 2016, vol. 9916, p. 99160C.
- [401] S. P. Morgan *et al.*, "Optical fiber sensors for monitoring in critical care," 2019, pp. 1139–1143.
- [402] B. Jiang *et al.*, "Graphene oxide-deposited tilted fiber grating for ultrafast humidity sensing and human breath monitoring," *Sensors Actuators B Chem.*, vol. 293, pp. 336–341, 2019.
- [403] J. L. Nixon *et al.*, "Exploring the prevalence and experience of mask anxiety for the person with head and neck cancer undergoing radiotherapy," *J. Med. Radiat. Sci.*, vol. 65, no. 4, pp. 282–290, Dec. 2018.
- [404] K. J. Kieran and J. A. Brunbergz, "Adult claustrophobia, anxiety and sedation in MRI," *Magn. Reson. Imaging*, vol. 15, no. 1, pp. 51–54, 1997.
- [405] R. C. Ailneni, K. R. Syamala, I.-S. Kim, and J. Hwang, "Influence of the wearable posture correction sensor on head and neck posture: Sitting and standing workstations," *Work*, vol. 62, no. 1, pp. 27–35, Feb. 2019.
- [406] D. F. Barbieri, D. Srinivasan, S. E. Mathiassen, and A. B. Oliveira, "Variation in upper extremity, neck and trunk postures when performing computer work at a sit-stand station," *Appl. Ergon.*, vol. 75, pp. 120–128, 2019.
- [407] S. Bevan, "Economic impact of musculoskeletal disorders (MSDs) on work in Europe," *Best Practice and Research: Clinical Rheumatology*, vol. 29, no. 3. Elsevier, pp. 356–373, 2015.
- [408] M. B. Näf, A. S. Koopman, S. Baltrusch, C. Rodriguez-Guerrero, B. Vanderborght, and D. Lefebvre, "Passive back support exoskeleton improves range of motion using flexible beams," *Front. Robot. AI*, vol. 5, no. JUN, 2018.
- [409] D. Jun, M. Zoe, V. Johnston, and S. O'Leary, "Physical risk factors for developing non-specific neck pain in office workers: a systematic review and meta-analysis," *Int. Arch. Occup. Environ. Health*, vol. 90, no. 5, pp. 373–410, 2017.
- [410] A. H. Kahlaee, L. Ghamkhar, and A. M. Arab, "The Association between Neck Pain and Pulmonary Function: A Systematic Review," *American Journal of Physical Medicine and Rehabilitation*, vol. 96, no. 3. LWW, pp. 203–210, 2017.
- [411] D. Lo Presti *et al.*, "Single-plane neck movements and respiratory frequency monitoring: a smart system for computer workers," in *2019 II Workshop on Metrology for Industry 4.0 and IoT (MetroInd4. 0&IoT)*, 2019, pp. 167–170.
- [412] S. Takahashi, J. Z. Hao, Y. W. A. Lee, Z. Cai, T. T. Do, and B. Y. R. Ng, "Effect of bending methods on FBG lateral force sensor," *Electron. Lett.*, vol. 41, no. 23, pp. 1270–1271, 2005.
- [413] C. Duc, P. Salvia, A. Lubansu, V. Feipel, and K. Aminian, "A wearable inertial system to assess the cervical spine mobility: Comparison with an optoelectronic-based motion capture evaluation," *Med. Eng. Phys.*, vol. 36, no. 1, pp. 49–56, 2014.
- [414] Y. Wang *et al.*, "An intelligent wearable device for human's cervical vertebra posture monitoring," in *2018 40th Annual International Conference of the IEEE Engineering in Medicine and Biology Society (EMBC)*, 2018, pp. 3280–3283.
- [415] M. Maselli, E. Mussi, F. Cecchi, M. Manti, P. Tropea, and C. Laschi, "A wearable sensing device for monitoring

References

- single planes neck movements: Assessment of its performance," *IEEE Sens. J.*, vol. 18, no. 15, pp. 6327–6336, 2018.
- [416] G. Sierra *et al.*, "Comparison of respiratory rate estimation based on tracheal sounds versus a capnograph," in *Annual International Conference of the IEEE Engineering in Medicine and Biology - Proceedings*, 2005.
- [417] O. Mimoz, T. Benard, A. Gaucher, D. Frasca, and B. Debaene, "Accuracy of respiratory rate monitoring using a non-invasive acoustic method after general anaesthesia," *Br. J. Anaesth.*, 2012.
- [418] P. Corbishley and E. Rodríguez-Villegas, "Breathing detection: Towards a miniaturized, wearable, battery-operated monitoring system," *IEEE Trans. Biomed. Eng.*, vol. 55, no. 1, pp. 196–204, 2008.
- [419] N. Chockalingam, P. H. Dangerfield, G. Giakas, and T. Cochrane, "Study of marker placements in the back for opto-electronic motion analysis," *Stud. Health Technol. Inform.*, pp. 105–109, 2002.
- [420] H. T. Ma, Z. Yang, J. F. Griffith, P. C. Leung, and R. Y. W. Lee, "A new method for determining lumbar spine motion using Bayesian belief network," *Med. Biol. Eng. Comput.*, vol. 46, no. 4, pp. 333–340, 2008.
- [421] R. Lee, "Measurement of movements of the lumbar spine," *Physiother. Theory Pract.*, vol. 18, no. 4, pp. 159–164, 2002.
- [422] A. F. Kachingwe and B. J. Phillips, "Inter-and intrarater reliability of a back range of motion instrument," *Arch. Phys. Med. Rehabil.*, vol. 86, no. 12, pp. 2347–2353, 2005.
- [423] R. Bartalesi, F. Lorussi, D. De Rossi, M. Tesconi, and A. Tognetti, "Wearable monitoring of lumbar spine curvature by inertial and e-textile sensory fusion," in *2010 Annual International Conference of the IEEE Engineering in Medicine and Biology*, 2010, pp. 6373–6376.
- [424] M. Suter, P. Eichelberger, J. Frangi, E. Simonet, H. Baur, and S. Schmid, "Measuring lumbar back motion during functional activities using a portable strain gauge sensor-based system: A comparative evaluation and reliability study," *J. Biomech.*, vol. 100, pp. 1–14, 2020.
- [425] J. M. Williams, I. Haq, and R. Y. Lee, "Dynamic measurement of lumbar curvature using fibre-optic sensors," *Med. Eng. Phys.*, vol. 32, no. 9, pp. 1043–1049, Nov. 2010.
- [426] B. A. Cloud, K. D. Zhao, R. Breighner, H. Giambini, and K.-N. An, "Agreement between fiber optic and optoelectronic systems for quantifying sagittal plane spinal curvature in sitting," *Gait Posture*, vol. 40, no. 3, pp. 369–374, 2014.
- [427] L. E. Dunne, P. Walsh, B. Smyth, and B. Caulfield, "Design and evaluation of a wearable optical sensor for monitoring seated spinal posture," in *2006 10th IEEE International Symposium on Wearable Computers*, 2006, pp. 65–68.
- [428] R. Gassert, E. Burdet, and K. Chinzei, "MRI-compatible robotics," in *IEEE Engineering in Medicine and Biology Magazine*, 2008, vol. 27, no. 3, pp. 12–14.
- [429] M. F. Dempsey, B. Condon, and D. M. Hadley, "MRI safety review," *Seminars in Ultrasound CT and MRI*, vol. 23, no. 5. W.B. Saunders, pp. 392–401, 01-Oct-2002.
- [430] M. F. Dempsey and B. Condon, "Thermal injuries associated with MRI," *Clinical Radiology*, vol. 56, no. 6. Elsevier, pp. 457–465, 01-Jun-2001.
- [431] K. Krupa and M. Bekiesińska-Figatowska, "Artifacts in magnetic resonance imaging," *Polish J. Radiol.*, vol. 80, no. 1, pp. 93–106, Feb. 2015.
- [432] F. Cecchi *et al.*, "Design and development of 'biomechatronic gym' for early detection of neurological disorders in infants," in *2010 Annual International Conference of the IEEE Engineering in Medicine and Biology Society, EMBC'10*, 2010, pp. 3414–3417.
- [433] J. G. Hall, G. F. I. Ursula, and J. E. Allanson, "Handbook of Normal Physical," *Meas. Oxford Oxford Med. Publ.*, 1989.
- [434] M. Molina and F. Jouen, "Manual cyclical activity as an explanatory tool in neonates," *Infant Behav. Dev.*, vol. 27, no. 1, pp. 42–53, Feb. 2004.
- [435] M. Molina and F. Jouen, "Modulation of the palmar grasp behavior in neonates according to texture

References

- property," *Infant Behav. Dev.*, vol. 21, no. 4, pp. 659–666, 1998.
- [436] A. G. Allievi, A. Melendez-Calderon, T. Arichi, A. D. Edwards, and E. Burdet, "An fMRI compatible wrist robotic interface to study brain development in neonates," *Ann. Biomed. Eng.*, vol. 41, no. 6, pp. 1181–1192, 2013.
- [437] S. Dall'Orso, J. Steinweg, A. G. Allievi, A. D. Edwards, E. Burdet, and T. Arichi, "Somatotopic mapping of the developing sensorimotor cortex in the preterm human brain," *Cereb. Cortex*, vol. 28, no. 7, pp. 2507–2515, Jul. 2018.
- [438] P. Mazurek, S. Vudayagiri, and A. L. Skov, "How to tailor flexible silicone elastomers with mechanical integrity: A tutorial review," *Chemical Society Reviews*, vol. 48, no. 6. Royal Society of Chemistry, pp. 1448–1464, 21-Mar-2019.
- [439] Iso, "ISO 7743:2011 Rubber, vulcanized or thermoplastic -- Determination of compression stress-strain properties," *Standards*, 2011. [Online]. Available: <https://www.iso.org/standard/72784.html>. [Accessed: 25-Aug-2020].
- [440] M. Jenkinson, C. F. Beckmann, T. E. J. Behrens, M. W. Woolrich, and S. M. Smith, "Review FSL," *Neuroimage*, vol. 62, no. 2, pp. 782–790, Aug. 2012.
- [441] H. M. Halverson, "An experimental study of prehension in infants by means of systematic cinema records.," *Genet. Psychol. Monogr.*, 1931.
- [442] H. M. Halverson, "A further study of grasping," *J. Gen. Psychol.*, vol. 7, no. 1, pp. 34–64, 1932.
- [443] H. M. Halverson, "Studies of the grasping responses of early infancy: I," *Pedagog. Semin. J. Genet. Psychol.*, vol. 51, no. 2, pp. 371–392, 1937.
- [444] C. Amiel-Tison, G. Barrier, S. M. Shnider, S. C. Hughes, and S. J. Stefani, "A new neurologic and adaptive capacity scoring system for evaluating obstetric medications in full-term newborns," *Anesthesiol. J. Am. Soc. Anesthesiol.*, vol. 53, no. 3 Suppl, pp. S322--S322, 1980.
- [445] H. Forssberg, H. Kinoshita, A. C. Eliasson, R. S. Johansson, G. Westling, and A. M. Gordon, "Development of human precision grip - II. Anticipatory control of isometric forces targeted for object's weight," *Exp. Brain Res.*, vol. 90, no. 2, pp. 393–398, 1992.
- [446] M. Del Maestro, F. Cecchi, S. M. Serio, C. Laschi, and P. Dario, "Sensing device for measuring infants' grasping actions," *Sensors Actuators, A Phys.*, vol. 165, no. 2, pp. 155–163, Feb. 2011.
- [447] F. Cecchi *et al.*, "A mechatronic toy for measuring infants' grasping development," in *Proceedings of the 2nd Biennial IEEE/RAS-EMBS International Conference on Biomedical Robotics and Biomechatronics, BioRob 2008*, 2008, pp. 397–401.
- [448] M. Molina and F. Jouen, "Weight perception in 12-month-old infants," *Infant Behav. Dev.*, vol. 26, no. 1, pp. 49–63, Feb. 2003.
- [449] M. Molina, C. Sann, M. David, Y. Touré, B. Guillois, and F. Jouen, "Active touch in late-preterm and early-term neonates," *Dev. Psychobiol.*, vol. 57, no. 3, pp. 322–335, Apr. 2015.
- [450] F. Lejeune, F. Audeoud, L. Marcus, A. Streri, T. Debillon, and E. Gentaz, "The manual habituation and discrimination of shapes in preterm human infants from 33 to 34+6 post-conceptual age," *PLoS One*, vol. 5, no. 2, p. e9108, Feb. 2010.
- [451] G. Cioni *et al.*, "Early neurological signs in preterm infants with unilateral intraparenchymal echodensity," *Neuropediatrics*, vol. 31, no. 05, pp. 240–251, 2000.

Ph.D. candidate publications

Peer Reviewed Journals (J)

-2020-	
J1	Lo Presti, D. , Massaroni, C., Leitão, et al. (2020). Fiber Bragg Gratings for Medical Applications and Future Challenges: A Review. <i>IEEE Access</i> , 8, 156863-156888.
J2	Di Tocco, J*, Lo Presti* , D., Zaltieri, M., D'Alesio, G., Filosa, M., Massari, L., ... & Schena, E. (2020). A wearable system based on flexible sensors for unobtrusive respiratory monitoring in occupational settings. <i>IEEE Sensors Journal</i> . * equal contribution
J3	Massaroni, C., Zaltieri*, M., Lo Presti* , D. et al. (2020). Fiber Bragg Grating Sensors for Cardiorespiratory Monitoring: A Review. <i>IEEE Sensors Journal</i> . * equal contribution
J4	Lo Presti, D. , Massaroni, C., Zaltieri, et al. (2020). A Magnetic Resonance-compatible wearable device based on functionalized fiber optic sensor for respiratory monitoring. <i>IEEE Sensors Journal</i> .
J5	Lo Presti, D. , Dall'Orso, S., Muceli, S., et al. (2020). An fMRI Compatible Smart Device for Measuring Palmar Grasping Actions in Newborns. <i>Sensors</i> , 20(21), 6040.
J6	Zaltieri, M., Massaroni, C., Lo Presti, D. , et al. (2020). A Wearable Device Based on a Fiber Bragg Grating Sensor for Low Back Movements Monitoring. <i>Sensors</i> , 20(14), 3825.
J7	Lo Presti, D. , Carnevale, A., D'Abbraccio, J., et al. (2020). A Multi-Parametric Wearable System to Monitor Neck Movements and Respiratory Frequency of Computer Workers. <i>Sensors</i> , 20(2), 536.
-2019-	
J8	Lo Presti, D. , Massaroni, C., D'Abbraccio, J., et al. (2019). Wearable system based on flexible FBG for respiratory and cardiac monitoring. <i>IEEE Sensors Journal</i> , 19(17), 7391-7398.
J9	Carnevale, A., Longo, U. G., Schena, E., Massaroni, C., Lo Presti, D. , et al. (2019). Wearable systems for shoulder kinematics assessment: A systematic review. <i>BMC Musculoskeletal Disorders</i> , 20(1), 546.
J10	Massaroni, C., Di Tocco, J., Bravi, M., Carnevale, A., Lo Presti, D. , et al. (2019). Respiratory Monitoring During Physical Activities With a Multi-Sensor Smart Garment and Related Algorithms. <i>IEEE Sensors Journal</i> , 20(4), 2173-2180.
J11	Massaroni, C., Di Tocco, J., Lo Presti, D. , et al. (2019). Smart textile based on piezoresistive sensing elements for respiratory monitoring. <i>IEEE Sensors Journal</i> , 19(17), 7718-7725.
J12	Lo Presti, D. , Massaroni, C., Piemonte, V., et al. (2019). Agar-coated fiber Bragg grating sensor for relative humidity measurements: Influence of coating thickness and polymer concentration. <i>IEEE Sensors Journal</i> , 19(9), 3335-3342.
J13	Lo Presti, D. , Romano, C., Massaroni, C., et al. (2019). Cardio-respiratory monitoring in archery using a smart textile based on flexible fiber Bragg grating sensors. <i>Sensors</i> , 19(16), 3581.
J14	Massaroni, C., Lo Presti, D. , Formica, D., et al. (2019). Non-contact monitoring of breathing pattern and respiratory rate via RGB signal measurement. <i>Sensors</i> , 19(12), 2758.
J15	Massaroni, C., Nicolò, A., Lo Presti, D. , et al. (2019). Contact-based methods for measuring respiratory rate. <i>Sensors</i> , 19(4), 908.
-2018-	

Tesi di dottorato in Scienze e ingegneria per l'uomo e l'ambiente, di Daniela Lo Presti, discussa presso l'Università Campus Bio-Medico di Roma in data 9/04/2021. La disseminazione e la riproduzione di questo documento sono consentite per scopi di didattica e ricerca, a condizione che ne venga citata la fonte.

Ph.D. candidate publications

J16	Lo Presti, D. , Massaroni, C., & Schena, E. (2018). Optical fiber gratings for humidity measurements: A review. <i>IEEE Sensors Journal</i> , 18(22), 9065-9074.
J17	Schena, E., Saccomandi, P., Tosi, D., Davrieux, F., Gassino, R., Massaroni, C., Lo Presti, D. , et al. (2018). Solutions to Improve the Outcomes of Thermal Treatments in Oncology: Multipoint Temperature Monitoring. <i>IEEE Journal of Electromagnetics, RF and Microwaves in Medicine and Biology</i> , 2(3), 172-178.
J18	Massaroni, C., Venanzi, C., Silvatti, A. P., Lo Presti, D. , et al. (2018). Smart textile for respiratory monitoring and thoraco-abdominal motion pattern evaluation. <i>Journal of biophotonics</i> , 11(5), e201700263.
J19	Massaroni, C., Lo Presti, D. , Saccomandi, P., et al. (2018). Fiber Bragg grating probe for relative humidity and respiratory frequency estimation: assessment during mechanical ventilation. <i>IEEE Sensors Journal</i> , 18(5), 2125-2130.
J20	Massaroni, C., Lopes, D. S., Lo Presti, D. , et al. (2018). Contactless monitoring of breathing patterns and respiratory rate at the pit of the neck: A single camera approach. <i>Journal of Sensors</i> , 2018.
-2017-	
J21	Lo Presti, D. , Massaroni, C., Formica, D., et al. (2017). Smart textile based on 12 fiber Bragg gratings array for vital signs monitoring. <i>IEEE Sensors Journal</i> , 17(18), 6037-6043.
J22	Massaroni, C., Caponero, M. A., D'Amato, R., Lo Presti, D. , et al. (2017). Fiber Bragg grating measuring system for simultaneous monitoring of temperature and humidity in mechanical ventilation. <i>Sensors</i> , 17(4), 749.
J23	Massaroni, C., Lo Presti, D. , Saccomandi, P., et al. (2018). Fiber Bragg grating probe for relative humidity and respiratory frequency estimation: assessment during mechanical ventilation. <i>IEEE Sensors Journal</i> , 18(5), 2125-2130.

Conference Proceedings (CP)

-2020-	
CP1	Zaltieri, M., Di Tocco, J., Lo Presti, D. , et al. (2020, June). A Test Bench to Assess Systems for Respiratory Monitoring of Workers. In <i>2020 IEEE International Workshop on Metrology for Industry 4.0 & IoT</i> (pp. 182-186). IEEE.
CP2	Massaroni, C., Nicolò, A., Lo Presti, D. , et al. (2020, June). Respiratory monitoring during cycling exercise: performance assessment of a smart t-shirt embedding fiber optic sensors. In <i>2020 IEEE International Workshop on Metrology for Industry 4.0 & IoT</i> (pp. 49-53). IEEE.
CP3	Zaltieri, M., Lo Presti, D. , Massaroni, C., et al. (2020, June). An FBG-based Smart Wearable Device for Monitoring Seated Posture in Video Terminal Workers. In <i>2020 IEEE International Workshop on Metrology for Industry 4.0 & IoT</i> (pp. 713-717). IEEE.
CP4	Carnevale, A., Massaroni, C., Lo Presti, D. , et al. (2020, June). Wearable stretchable sensor based on conductive textile fabric for shoulder motion monitoring. In <i>2020 IEEE International Workshop on Metrology for Industry 4.0 & IoT</i> (pp. 106-110). IEEE.
CP5	Resta, P., Lo Presti, D. , Schena, E., et al. (2020, June). A wearable system for knee flexion/extension monitoring: design and assessment. In <i>2020 IEEE International Workshop on Metrology for Industry 4.0 & IoT</i> (pp. 273-277). IEEE.
CP6	Zaltieri, M., Lo Presti, D. , Massaroni, C., et al. (2020, May). Feasibility assessment of an FBG-based wearable system for monitoring back dorsal flexion-extension in video terminal workers. In <i>2020 IEEE International Instrumentation and Measurement Technology Conference (I2MTC)</i> (pp. 1-5). IEEE.
CP7	Massaroni, C., Di Tocco, J., Sabbadini, R., Carnevale, A., Lo Presti, D. , et al. (2020, May). Influence of torso movements on a multi-sensor garment for respiratory monitoring during walking and running activities. In <i>2020 IEEE International Instrumentation and Measurement Technology Conference (I2MTC)</i> (pp. 1-6). IEEE.
-2019-	
CP8	Massaroni, C., Di Tocco, J., Lo Presti, D. , et al. (2019, June). Influence of motion artifacts on a smart garment for monitoring respiratory rate. In <i>2019 IEEE International Symposium on Medical Measurements and Applications (MeMeA)</i> (pp. 1-6). IEEE.

Tesi di dottorato in Scienze e ingegneria per l'uomo e l'ambiente, di Daniela Lo Presti, discussa presso l'Università Campus Bio-Medico di Roma in data 9/04/2021. La disseminazione e la riproduzione di questo documento sono consentite per scopi di didattica e ricerca, a condizione che ne venga citata la fonte.

Ph.D. candidate publications

CP9	Lo Presti, D. , Massaroni, C., Di Tocco, J., et al. (2019, June). Cardiac monitoring with a smart textile based on polymer-encapsulated FBG: influence of sensor positioning. In <i>2019 IEEE International Symposium on Medical Measurements and Applications (MeMeA)</i> (pp. 1-6). IEEE.
CP10	Romano, C., Lo Presti, D. , Schena, E., et al. (2019, June). A wearable system based on fiber Bragg grating for monitoring respiratory and heart activity of archers. In <i>2019 IEEE International Symposium on Medical Measurements and Applications (MeMeA)</i> (pp. 1-6). IEEE.
CP11	Lo Presti, D. , Massaroni, C., Di Tocco, J., et al. (2019, June). Single-plane neck movements and respiratory frequency monitoring: A smart system for computer workers. In <i>2019 II Workshop on Metrology for Industry 4.0 and IoT (MetroInd4.0&IoT)</i> (pp. 167-170). IEEE.
-2018-	
CP12	Iaconi, S., Massaroni, C., Lo Presti, D., et al. (2018, July). Polymer-coated fiber optic probe for the monitoring of breathing pattern and respiratory rate. In <i>2018 40th Annual International Conference of the IEEE Engineering in Medicine and Biology Society (EMBC)</i> (pp. 1616-1619). IEEE.
CP13	Molinari, N., Massaroni, C., Lo Presti, D., et al. (2018, July). Wearable textile based on silver plated knitted sensor for respiratory rate monitoring. In <i>2018 40th Annual International Conference of the IEEE Engineering in Medicine and Biology Society (EMBC)</i> (pp. 2865-2868). IEEE.
CP14	Evangelisti, E., Schena, E., Massaroni, C., Lo Presti, D., et al. (2018, June). Experimental analysis of the influencing factors on the response of a tool for epidural space detection. In <i>2018 IEEE International Symposium on Medical Measurements and Applications (MeMeA)</i> (pp. 1-5). IEEE.
CP15	Lo Presti, D., Massaroni, C., Schena, E., et al. (2018, June). Smart textile based on FBG sensors for breath-by-breath respiratory monitoring: tests on women. In <i>2018 IEEE International Symposium on Medical Measurements and Applications (MeMeA)</i> (pp. 1-6). IEEE.
CP16	Massaroni, C., Lo Presti, D., Losquadro, C., et al. (2018, June). Multi-sensitive FBG-based needle for both relative humidity and breathing rate monitoring. In <i>2018 IEEE International Symposium on Medical Measurements and Applications (MeMeA)</i> (pp. 1-6). IEEE.
-2017-	
CP17	Lo Presti, D., Massaroni, C., Saccomandi, P., et al. (2017, July). A wearable textile for respiratory monitoring: Feasibility assessment and analysis of sensors position on system response. In <i>Conference proceedings: Annual International Conference of the IEEE Engineering in Medicine and Biology Society. IEEE Engineering in Medicine and Biology Society. Annual Conference</i> (Vol. 2017, pp. 4423-4426).